



**HAL**  
open science

# Etude spectroélectrochimique de la réactivité de la cytochrome bd oxydase et des systèmes apparentés avec de petites molécules

Iryna Makarchuk

► **To cite this version:**

Iryna Makarchuk. Etude spectroélectrochimique de la réactivité de la cytochrome bd oxydase et des systèmes apparentés avec de petites molécules. Autre. Université de Strasbourg, 2022. Français. NNT : 2022STRAF063 . tel-04189434

**HAL Id: tel-04189434**

**<https://theses.hal.science/tel-04189434>**

Submitted on 28 Aug 2023

**HAL** is a multi-disciplinary open access archive for the deposit and dissemination of scientific research documents, whether they are published or not. The documents may come from teaching and research institutions in France or abroad, or from public or private research centers.

L'archive ouverte pluridisciplinaire **HAL**, est destinée au dépôt et à la diffusion de documents scientifiques de niveau recherche, publiés ou non, émanant des établissements d'enseignement et de recherche français ou étrangers, des laboratoires publics ou privés.

**ÉCOLE DOCTORALE DES SCIENCES CHIMIQUES**

**UMR 7140, Chimie de la matière complexe**

**THÈSE** présentée par :

**Iryna MAKARCHUK**

soutenue le : **5 Décembre 2022**

pour obtenir le grade de : **Docteur de l'université de Strasbourg**

Discipline/ Spécialité : Chimie

**Étude spectroélectrochimique de la réactivité  
de la cytochrome *bd* oxydase et des systèmes  
apparentés avec de petites molécules**

Spectroelectrochemical study of the cytochrome *bd* oxidase  
and related systems reactivity with small molecules

**THÈSE dirigée par :**

**Prof. Dr. HELLWIG Petra**

Professeur, Université de Strasbourg

**Dr. MELIN Frédéric**

Maître de Conférences, Université de Strasbourg

**RAPPORTEURS :**

**Prof. Dr. LEMAÎTRE Frédéric**

Professeur, Sorbonne Université

**Dr. LÉGER Christophe**

Directeur de recherches, Université Aix-Marseille

---

**AUTRES MEMBRES DU JURY :**

**Prof. Dr. SAVINOVA Elena**

Professeur, Université de Strasbourg

**Prof. Dr. BALD Dirk**

Directeur de recherches, Vrije Universiteit  
Amsterdam



*“Science and everyday life cannot and should not be separated.*

*Science, for me, gives a partial explanation for life.*

*In so far as it goes, it is based on **fact, experience and experiment.**”*

Rosalind Franklin



## Acknowledgements

I would like to express special gratitude to my thesis advisors Prof. Dr. Petra Hellwig and Dr. Frédéric Melin. Not only for the mentorship and endless support but for giving me an opportunity to work on this interesting project in the Laboratory of Bioelectrochemistry and Spectroscopy. Thank you for the guidance, scientific discussions, corrections and remarks, encouragement, and all the expertise I have learnt from you over these three years.

I thank Prof. Dr. Frédéric Lemaitre, Dr. Christophe Leger, Prof. Dr. Elene Savinova, and Prof. Dr. Dirk Bald for kindly accepting to be members of my thesis committee and their interest in this work.

I would like to express my gratitude to Prof. Dr. Thorsten Friedrich from the University of Freiburg for the fruitful collaboration and the opportunity to visit his laboratory. As well a big thanks to the members of his research group: Jan Kägi, Dr. Daniel Wohlwend, Caroline Harter, Dr. Franziska Hoerer, Luca Mérono, for the consultation and sharing knowledge in the protein preparation methodology.

I am grateful to Prof. Dr. Pia Ädelroth in Stockholm University and the PhD student from her group Sofia Appelgren who provided us with the protein samples of cNOR and helped with the discussion.

This project could have not been possible without the funding granted by the IDEX International Doctoral Program of the University of Strasbourg.

I would like to thank Dr. Zahia Boubegtiten for her advice, endless patience with all the puzzling moments in the laboratory, for friendship and kindness.

I am grateful for the group meetings and objectivity to all members of our research team: Dr. Youssef El Khoury, Dr. Nicolas Javahiraly, Dr. Fatima Omeis, Dr. Filipa Seica, Krongkarn Sirinukunwattana, Raaif Siddeque, Aleksei Kuznetsov, Ariadna Murillo Bello, all the master students and my best friend for life Tatjana Gerasimova. I warmly thank Tatjana for being a big part of my life during this journey in Strasbourg: for the late nights at work, for Covid restriction announcements meetings, our moments at the conference, for the unexpected and well-planned travels, for the funny adventures and sad moments, thank you sweetie.

I would like to thank my dearest friends I met on the way: Filipa for believing in me and for unconditional support, Michael and Renato for the advice and inspiration, without you my three years of PhD would not be so memorable. Thanks to all international team of StrasAIR: Nizami, Rokas, Lisa, Liuda, Guido, Andrei, Viktoriia for the events, conferences and every Café Linguistique we organized together. And of course, I am endlessly grateful to my partner Ivan Khariushin for his encouragement, exceptional patience and support during the period of writing and ability to make me smile even on the worst days.

Last but not the least, I would like to thank my parents, Svitlana and Serhii, for their unconditional love and warm-hearted words of support I receive over the distance and hurdles of war that separate us. I dedicate this to my family and the brave people of Ukraine that fight for freedom and human rights at this very moment. Слава Україні та вічна пам'ять героям!



# Table of contents

Abbreviations and Acronyms .....	11
Résumé .....	13
List of presentations.....	25
List of publications .....	26
List of figures.....	27
List of schemes .....	33
List of tables .....	33
Chapter I Introduction: getting inside the protein world.....	35
1.1 Cell bioenergetics: oxidative phosphorylation .....	37
1.2 From redox chain to respiration: function of membrane complexes.....	38
1.3 Classification and structure of Complex IV .....	40
1.3.1 Superfamily of heme-copper oxidases (HCOs) .....	42
1.3.2 The family of NOR oxidases .....	44
1.3.3 Superfamily of cytochrome <i>bd</i> oxidases: structural diversity and mechanism.....	46
1.4 The state of art: role of nitric oxide in pathogen virulence.....	50
1.4.1 Denitrification chain of bacteria .....	51
1.4.2 Mechanism of NO binding with different oxidases .....	52
1.5 Inhibitors towards cytochrome <i>bd</i> oxidase for the perspective drug design.....	57
1.6 Aims of the project.....	61
Chapter II Techniques of analysis.....	63
2.1 Direct electrochemistry .....	65
2.1.1 The protein film voltammetry .....	66
2.1.2 Theories behind electron kinetics in proteins .....	69
2.1.3 Electron transfer mechanism of immobilized enzymes .....	70
2.1.4 Immobilization and signal enhancement strategies .....	71
2.1.5 Steady-state electrochemistry .....	74
2.2 Inhibition of protein activity as method of characterization.....	76
2.3 UV-Vis spectroscopy .....	80
2.3.1 UV-vis spectroscopy for proteins .....	82
2.3.2 UV-Vis potentiometric titration .....	84
2.4 Infrared spectroscopy .....	85
2.4.1 Infrared spectroscopy of proteins: Amide I and Amide II region.....	87
2.4.2 FTIR differential spectroscopy coupled to electrochemistry .....	88



2.5 Raman spectroscopy of heme proteins .....	89
Chapter III Cytochrome <i>bd</i> -I oxidase of <i>E. coli</i> inhibition assay with Aurachins .....	91
3.1 Electrochemical sensor for cytochrome protein inhibition study .....	93
3.1.1 Morphological study of the electrode modified with gold nanoparticles by scanning electron microscopy SEM .....	93
3.1.2 The choice of the thiols and lipids for cytochrome <i>bd</i> -I oxidase immobilization.....	96
3.2 Inhibition screening of cytochrome <i>bd</i> -I oxidase with Aurachin D derivatives.....	100
3.2.1 Activity screening by the electrochemical sensor with immobilized <i>bd</i> -I oxidase.....	100
3.2.2 Inhibition screening of Aurachin D synthetic analogues .....	102
3.2.3 Effect of the ubiquinol on the inhibition assay .....	106
3.2.4 Concentration dependent study to determine half-inhibitory constant of the lead compounds	106
3.3 Conclusions .....	108
Chapter IV Insight in reactivity of <i>E. coli</i> <i>bd</i> oxidases with molecular oxygen .....	111
4.1 Characterization of <i>bd</i> -I and <i>bd</i> -II oxidases from <i>E. coli</i> .....	113
4.1.1 UV-Vis and FTIR spectroscopic characterization of homologues <i>bd</i> oxidases.....	114
4.1.2 Potentiometric titration of cytochrome <i>bd</i> -II oxidase .....	117
4.1.3 Protein film voltammetry of <i>bd</i> -I and <i>bd</i> -II oxidases .....	120
4.2 The influence of the Glu445 and Arg448 residues on cyt <i>bd</i> -I oxidase catalytic properties.....	123
4.2.1 Spectral characterization of E445D and R448N variants .....	124
4.2.2 Oxygen electrocatalytic reaction and NO reactivity of the variants of cytochrome <i>bd</i> -I oxidase .....	126
4.2.3 UV-Vis redox titration of the E445D and R448N variants.....	127
4.3 Conclusions .....	131
Chapter V Reactivity of <i>bd</i> oxidases with nitric oxide .....	133
5.1 Nitric oxide binding to the cytochrome <i>bd</i> -I oxidase from <i>E. coli</i> .....	135
5.1.1 The oxygen electrocatalysis inhibition of cytochrome <i>bd</i> -I oxidase by nitric oxide .....	135
5.1.2 UV-Vis spectroscopy of the cytochrome <i>bd</i> -I oxidase in the presence of NO .....	137
5.2 Characterization of NO-binding to the homologues <i>bd</i> oxidases from <i>E. coli</i> .....	138
5.2.1 Electrocatalytic inhibition of cytochrome <i>bd</i> -II activity by NO .....	138
5.2.2 Following the spectral signature of the NO binding reaction for <i>bd</i> -II oxidase .....	140
5.2.3 pH-dependent kinetics of NO release in reduced and oxidized states .....	141
5.3 The role of Asp58 and Glu58 in <i>bd</i> -I and <i>bd</i> -II oxidases for NO-binding .....	145
5.3.1 The spectral characterization of the Asp58Glu and Asp58Leu cytochrome <i>bd</i> -I variants .....	146
5.3.2 NO binding of the mutated D58E and E58D <i>bd</i> -I and <i>bd</i> -II oxidases .....	149
5.4 Conclusions .....	152

Chapter VI Spectroelectrochemical characterization of cNOR from <i>Paracoccus denitrificans</i> and the Fe <sub>B</sub> lacking variant.....	153
6.1 Spectral characterization of cNOR WT and Fe <sub>B</sub> depleted enzyme .....	155
6.1.1 UV-Vis spectroscopy of cNOR in the thin-layer electrochemical cell .....	155
6.1.2 FTIR difference spectroscopy of WT and Variant.....	157
6.1.3 Raman spectroscopy of cNOR WT and Fe <sub>B</sub> deficient enzyme films and solution .....	159
6.2 Electrochemical study of cNOR WT and Fe <sub>B</sub> lacking enzyme .....	163
6.2.1 Potentiometric titration of cNOR WT and Fe <sub>B</sub> lacking enzyme .....	163
6.2.2 Probing electrocatalytic activity of cNOR on carbon electrodes .....	166
6.3 Conclusions .....	171
Annex.....	173
A. Instrumentation.....	173
A.1 Electrochemical equipment .....	173
A.2 Clark electrode .....	174
A.3 Thin-layer electrochemical cell .....	175
A.4 UV-vis spectrometer.....	176
A.5 Fourier transform IR spectrometer .....	176
A.6 Raman spectrometer .....	178
B. Protocols .....	179
B.1 Preparation and purification of the studied protein samples.....	179
B.1.1 Production and of the <i>E. coli</i> cytochrome <i>bd</i> -I and <i>bd</i> -II oxidase.....	179
B.1.2 Purification and generation of mutants E445D and R448N of cyt <i>bd</i> -I oxidase .....	179
B.1.3 Production and of the D58E and D58L variants of the cytochrome <i>bd</i> -I and E58D mutants of the <i>bd</i> -II oxidase .....	179
B.1.4 The preparation and purification of cNOR from <i>P. denitrificans</i> .....	180
B.2 Catalytic activity measurement in solution for <i>bd</i> oxidases and its mutants .....	181
B.2.1 NADH oxidase activity of the <i>bd</i> oxidases measured in membranes.....	181
B.2.2 The duroquinol: oxygen oxidoreductase activity of isolated <i>bd</i> oxidases.....	181
B.3 Protein film voltammetry immobilization protocols.....	181
B.3.1 Protein sample pretreatment for the PFV .....	181
B.3.2 Pretreatment of the gold rotating electrodes.....	183
B.3.3 Preparation of gold NPs with average diameter of 14-16 nm .....	183
B.3.4 Immobilization protocol for <i>bd</i> -I and <i>bd</i> -II on the gold disk electrode.....	183
B.3.5 Immobilization protocol for cNOR on the glassy carbon electrode.....	184
B.3.6 Inhibition assay with Aurachin derivatives for cytochrome <i>bd</i> -I oxidase.....	184

B.3.7 Inhibition of the oxygen reduction catalytic reaction of <i>bd</i> oxidases by nitric oxide.....	184
B.4 Spectroelectrochemistry in the thin-layer cell .....	185
B.4.1 The working electrode (semitransparent gold grid) modification .....	185
B.4.2 The conditions of the potentiometric titrations .....	185
B.4.3 Red-ox induced FTIR spectroscopy conditions .....	185
B.5 Spectroscopic study of proteins .....	186
B.5.1 MAHMA NONOate kinetics .....	186
B.5.2.NO binding experiment for <i>bd</i> oxidases .....	187
B.5.3 Pretreatment of the cNOR samples for Raman spectroscopy .....	187
C. Materials .....	188
C.1 Chemicals .....	188
C.2 Mediators for the electrochemical cell.....	188
C.3 Software.....	189
D.1 Abbreviations and structures of 20 common amino acids.....	190
E.1 The titration curves of the E445D variant of the cytochrome <i>bd</i> -I oxidase .....	191
References.....	193

## Abbreviations and Acronyms

---

<b>ATP</b>	adenosine triphosphate
<b>CE</b>	counter electrode
<b>CQ</b>	caldariella quinone
<b>Cryo-EM</b>	cryo electron microscopy
<b>CV</b>	cyclic voltammogram
<b>cyt</b>	cytochrome
<b>DDM</b>	n-Dodecyl $\beta$ -D-maltoside
<b>DET</b>	direct electron transfer
<b>DMSO</b>	dimethyl sulfoxide
<b>ET</b>	electron transfer
<b>FIR</b>	far infrared
<b>FTIR</b>	Fourier-transform infrared spectroscopy
<b>GCE</b>	glassy carbon electrode
<b>GNPs</b>	gold nanoparticles
<b>HCOs</b>	heme-copper oxidases
<b>HQNO</b>	2-heptyl-4-quinolinol 1-oxide
<b>HT</b>	hexanthiol-1
<b>IC<sub>50</sub></b>	half maximal inhibitory concentration
<b>IR</b>	infrared
<b><math>K_I^{app}</math></b>	apparent inhibition constant
<b>MAHMA</b>	6-(2-Hydroxy-1-methyl-2-nitrosohydrazino)-N-methyl-1-
<b>NONOate</b>	hexanamine
<b>MCH</b>	6-mercapto-1-hexanol
<b>MET</b>	mediated electron transfer
<b>MHA</b>	6-mercaptohexanoic acid
<b>MIR</b>	mid infrared
<b>MK</b>	menaquinone
<b>MOPS</b>	3-(N-morpholino)propanesulfonic acid
<b>MPA</b>	3-mercaptopropionic acid
<b>MUA</b>	11-mercaptoundecanoic acid
<b>NADH</b>	nicotinamide adenine dinucleotide

<b>NDH</b>	NADH dehydrogenase
<b>NIR</b>	near infrared
<b>NOR</b>	nitric oxide reductase
<b>PDB</b>	protein data bank
<b>PE</b>	1,2-dimyristoyl-sn-glycero-3-phosphoethanolamine
<b>PFV</b>	protein film voltammetry
<b>PG</b>	1,2-dioleoyl-sn-glycero-3-phosphoglycerol
<b>PGE</b>	pyrolytic graphite electrode
<b><i>pmf</i></b>	proton motive force
<b>ptBLM</b>	protein tethered bilayer lipid membrane
<b>RDE</b>	rotating disk electrode
<b>RE</b>	reference electrode
<b>RNS</b>	reactive nitrogen species
<b>ROS</b>	reactive oxygen species
<b>RR</b>	resonance Raman
<b>Q / QH<sub>2</sub></b>	quinone / quinol
<b>SAM</b>	self assembled monolayer
<b>SEM</b>	scanning electron microscopy
<b>SHE</b>	standard hydrogen electrode
<b>TM helix</b>	transmembrane helix
<b>UQ</b>	ubiquinone
<b>UV</b>	ultraviolet
<b>Vis</b>	visible
<b>WE</b>	working electrode

### Introduction

On estime qu'environ 80% des futures cibles des produits pharmaceutiques seront des protéines membranaires<sup>1</sup>. Elles participent aux multiples fonctions essentielles des cellules vivantes, telles que le transport, la signalisation et la respiration. Cette thèse se concentre sur deux enzymes de la chaîne respiratoire bactérienne : la cytochrome *bd* oxydase (cyt *bd*-I et cyt *bd*-II) d'*Escherichia coli* et la NO réductase dépendante au cytochrome c (cNOR) de *Paracoccus denitrificans*.

Les cytochromes *bd* oxydases constituent une famille unique de protéines membranaires que l'on trouve uniquement dans la chaîne respiratoire des procaryotes, y compris plusieurs agents pathogènes tels que *Escherichia coli*, *Mycobacterium tuberculosis*, *Salmonella* et *Klebsiella pneumoniae*, qui sont à l'origine d'un certain nombre de maladies potentiellement mortelles<sup>2,3</sup>. Les cytochromes *bd* oxydases catalysent la réduction de l'oxygène moléculaire au niveau de l'hème d couplée à l'oxydation du quinol au niveau du site de liaison Q<sup>4</sup>. Il semblerait que les *bd* oxydases jouent également un rôle crucial dans la protection des bactéries contre le stress oxydant, ainsi que dans leur virulence, leur adaptabilité et leur résistance aux antibiotiques<sup>5</sup>. Une compréhension approfondie de ce mécanisme enzymatique pourrait conduire à la découverte d'inhibiteurs spécifiques de ces enzymes qui pourraient devenir de futurs antibiotiques avec un nouveau mode d'action. *E. coli* contient deux cytochromes *bd* oxydases très comparables, *bd*-I et *bd*-II<sup>6</sup>. Malgré leur grande similitude de séquence et de structure, il existe des différences dans le canal d'accès de l'oxygène au site actif, qui peuvent entraîner des différences dans la liaison de la protéine aux petites molécules (O<sub>2</sub>, NO, CO et H<sub>2</sub>S).

La cNOR est impliquée dans l'étape importante de la respiration anaérobie des bactéries dénitrifiantes. Elle assure la réduction catalytique de l'oxyde nitrique toxique en oxyde nitreux, cependant, trois mécanismes catalytiques possibles ont été proposés, où le rôle du centre Fe<sub>B</sub> est toujours en discussion<sup>7,8</sup>. Cette étude vise à comprendre le rôle du centre du fer non hémique dans le cycle catalytique des cNOR. Dans ce but, l'enzyme sans Fe<sub>B</sub> a été obtenue en supprimant les protéines chaperons NorQ et NorD dans le gène, ce qui a entraîné l'absence du centre de fer non hémique<sup>9</sup>.

Le principal objectif de ce projet est d'élucider le mécanisme de réaction catalytique des protéines membranaires mentionnées ci-dessus avec de petites molécules en appliquant la voltammétrie à film protéique (VFP) et des méthodes spectroscopiques avancées couplées à l'électrochimie.

Les protéines d'intérêt (cyt *bd* oxydase, cNOR) ont été immobilisées sur la surface d'électrodes afin d'étudier leur réaction avec différents substrats en conditions catalytiques et non catalytiques. Il a été nécessaire dans un premier temps d'optimiser le protocole d'immobilisation afin d'obtenir un capteur électrochimique sensible<sup>10</sup>. La modification avec une seule portion de solution de nanoparticules d'or de 15 nm entraîne la formation d'une structure hautement poreuse avec une augmentation de huit fois la surface électrochimiquement active. En fonction de la quantité résiduelle de phospholipides après chaque purification de l'enzyme, le protocole de modification de l'électrode doit être adapté. Les films de protéines les plus stables et la meilleure activité catalytique ont été obtenus ici avec un mélange de thiols non chargés, 1-hexanthiol et 6-mercaptohexan-1-ol sur la surface d'or et l'ajout de 2,5% de lipide zwitterionique PE.

La cellule électrochimique en couche mince a été utilisée pour étudier les changements de conformation qui se produisent pendant la réaction d'oxydoréduction induite par l'application d'un potentiel<sup>11</sup>. Cette approche nous permet aussi de déterminer les potentiels d'oxydoréduction des cofacteurs de la protéine et d'extraire des informations sur les réactions de transfert de protons couplées qui se produisent dans le cycle catalytique.

### **Comparaison des fonctions catalytiques des cytochromes *bd-I* et *bd-II* et criblage d'inhibiteurs dérivés de l'aurachine D contre la cyt *bd-I***

Les spectres différentiels UV-Vis et FTIR induits par électrochimie de la cyt *bd-II* ressemblent à ceux de la *bd-I* d'*E. coli*, ce qui suggère un environnement similaire des hèmes dans les deux enzymes. Un léger décalage des nombres d'onde des bandes dans la région de l'amide I (1695-1610 cm<sup>-1</sup>) et de l'amide II (1575-1480 cm<sup>-1</sup>) est observé. Des différences plus évidentes ont été observées dans la région des résidus acides, ce qui suggère des modifications de la structure de la cyt *bd-II*. Lors d'un titrage potentiométrique dans la cellule à couche mince, l'observation la plus frappante a été le potentiel extrêmement élevé de l'hème *d* pour la cyt *bd-II* qui était presque 200 mV plus élevé que celui de la cyt *bd-I*. Cela pourrait expliquer pourquoi

la cyt bd-II a une activité duroquinol:dioxygène oxydoréductase 2,5 fois plus lente que celle de l'enzyme *bd-I*.

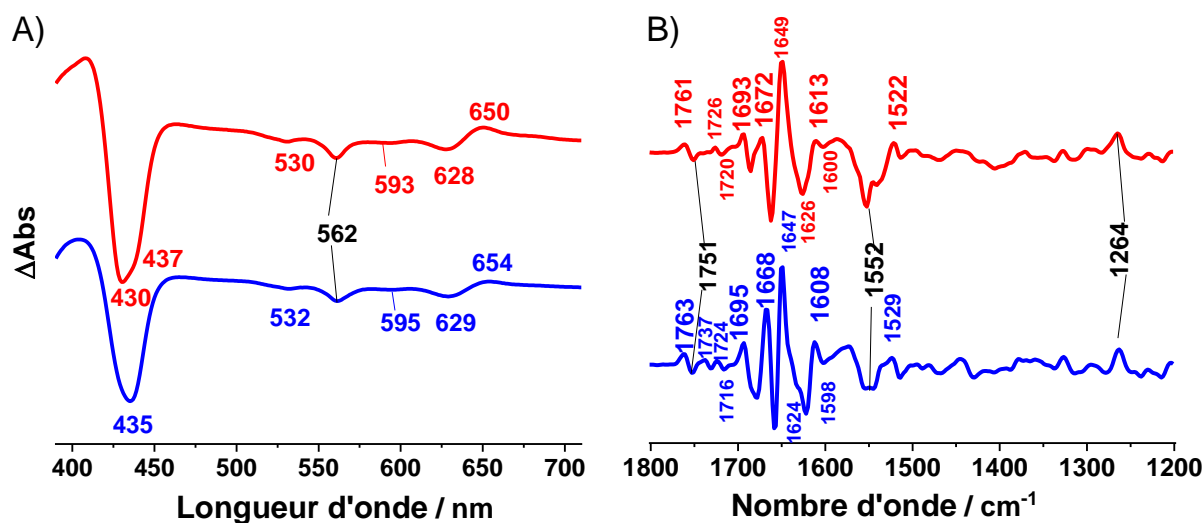


Figure 1. Caractérisation spectrale de l'oxydase *bd-I* (rouge) et *bd-II* (bleu) : Spectre différentiel UV Vis air-oxydé moins dithionite-réduit (A) ; Spectre différentiel FTIR Ox-red (B).

Pour mieux comprendre la fonction de l'hème  $b_{595}$  à haut spin, dont le rôle dans le centre catalytique dihémique a longtemps été contesté<sup>12</sup>, on a procédé à une mutation dirigée du résidu Glu455, le ligand confirmé de cet hème<sup>3,13</sup>. Les études électrocatalytiques ont montré que les variants Glu455Asp et Arg448Asn sont encore aptes à réagir avec l'oxygène et à fixer et libérer un substrat gazeux tel que l'oxyde nitrique. On a également constaté que les potentiels d'équilibre des trois hèmes,  $b_{558}$ ,  $b_{595}$  et  $d$ , sont fortement décalés dans ces mutants jusqu'à 200 mV par rapport à ceux de l'enzyme sauvage (tableau 1).

Tableau 1. Potentiels redox des hèmes des diverses *bd* oxydases de *E. coli* étudiées ici, déterminés dans un tampon phosphate (KPi pH 7, 0,02% DDM) par titrage potentiométrique, l'erreur standard de la méthode est de 20 mV.

Enzyme	Potentiel vs SHE / mV	
Type sauvage, <i>bd-I</i> <sup>14</sup>	+258 ( <i>d</i> )	+168 ( $b_{595}$ ) +176 ( $b_{558}$ )
Type sauvage, <i>bd-II</i>	+432 ( <i>d</i> )	+237 ( $b_1, b_2$ )
Variante Glu445Asp de <i>bd-I</i>	+310 ( <i>d</i> )	+276 ( $b_{595}$ ) +124 ( $b_{558}$ )
Variante Arg448Asn de <i>bd-I</i>	+446 ( <i>d</i> )	-86 ( $b_{595}$ ) +174 ( $b_{558}$ )



Les mutants Glu445Asp (E445D) et Arg448Asn (R448N) montrent encore un turnover de  $41 \pm 2 \%$  et  $20 \pm 4 \%$ , respectivement dans les tests d'activité réalisés avec une électrode de Clark. Les variants E445D et R448N ont été immobilisés avec succès sur l'électrode à nanoparticules d'or pour des études électrocatalytiques. Ces enzymes sont capables de catalyser la réduction d'oxygène, cependant, les voltammogrammes des deux variants (courbes bleues sur la figure 2) ont été fortement modifiés, à la fois en forme et en amplitude par rapport à la *bd-I* oxydase de type sauvage. Néanmoins, comme le type sauvage, E445D et R448N sont inhibés rapidement et de manière réversible lors de l'addition de NO. Ces résultats suggèrent que l'hème *b*<sub>595</sub> ne contribue pas à la réduction de l'oxygène, et que le cytochrome *bd* est actif même si le transfert d'électrons est moins favorable.

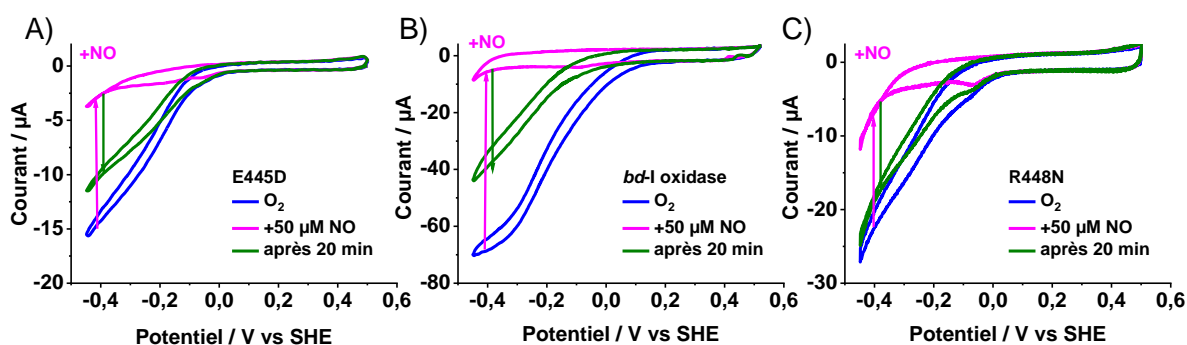


Figure 2. L'effet de l'inhibition du NO sur la réduction électrocatalytique de l'O<sub>2</sub> de type sauvage et des variantes *bd-I* oxydase (A), E445D (B) et R448N (C) sur une électrode en or modifiée avec des NP d'or et des thiols SAM à pH 7 avec 2,5 % de PE. Conditions : tampon phosphate pH 7 saturé d'air, vitesse de balayage 0,02 V/s, vitesse de rotation 1000 tr/min.

Le capteur électrochimique optimisé a été utilisé avec succès pour le criblage d'inhibiteurs de la *cyt bd-I* oxydase dérivés de l'alcaloïde naturel Aurachine D. Pour identifier les inhibiteurs les plus actifs, un criblage rapide à une concentration de 10 µM et une analyse dose-dépendante ont été effectués. Les quinolones avec des substituants alkyle et iodure en C-2 et C-3 ont une activité inhibitrice supérieure à 10 %, ce qui semble confirmer la présence de résidus hydrophobes dans la poche de liaison de la quinone. Cette étude a également montré que la longueur de la chaîne isoprénoïde joue un rôle crucial sur l'inhibition dans les analogues synthétisés de l'Aurachine D. L'activité d'inhibition la plus élevée a été observée pour le composé AD-2 avec deux unités isoprénoïdes, mais pas pour l'Aurachine D (AD-3), comme cela a été montré précédemment dans la littérature<sup>15</sup>. Dans l'étude concentration-dépendante, la plus basse IC<sub>50</sub> à 1.1 µM a également été trouvée pour la molécule AD-2 révélant que le site de liaison au quinol préfère les quinolones avec un long substituant lipophile en position C-3,

mais pas trop volumineux comme pour AD-4. En outre, il a été démontré que les composés les plus actifs AD-2 et AD-3 agissent comme des inhibiteurs compétitifs, leur pouvoir d'inhibition étant plus bas lorsque la quantité d'ubiquinol, le substrat naturel, est plus élevée dans l'échantillon de protéine. Tous ces résultats ouvrent la voie au développement futur de nouveaux médicaments antimicrobiens contre les bactéries pathogènes exprimant la cytochrome *bd-I* oxydase.

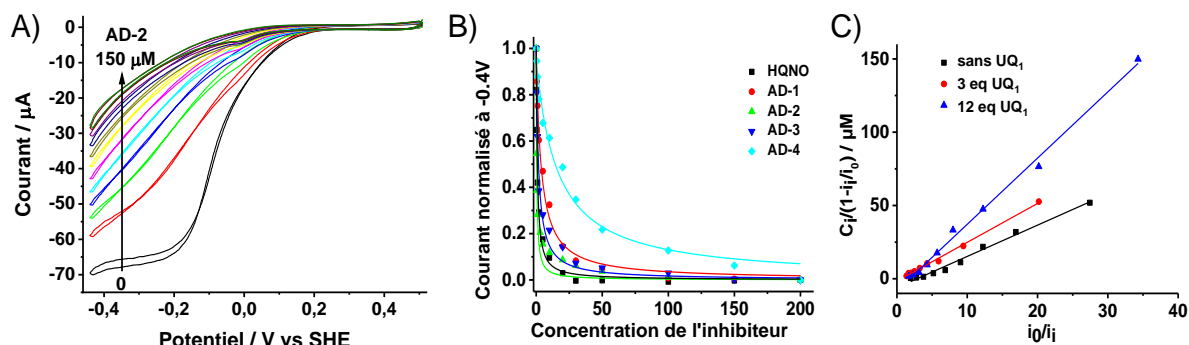


Figure 3. Effet de l'ajout d'aliquotes d'AD-2 sur les voltammogrammes de la protéine (A) ; tracé du courant normalisé ( $i/i_0$ ) à -0,4 V en fonction de la concentration des dérivés synthétiques de l'aurachine D (AD-1 à 4) et de HQNO (B). Graphiques de Henderson obtenus pour AD-2 à trois quantités différentes d'ubiquinone-1 (C). Conditions : tampon pH 7 saturé d'air, vitesse de balayage : 0.02 V/s, vitesse de rotation de l'électrode : 1000 rpm.

## La réactivité des cytochromes *bd-I* et *bd-II* oxydases avec le monoxyde d'azote

La réduction catalytique du dioxygène a lieu au niveau de l'hème de type *d* à haut-spin dans toutes les *bd* oxydases, et cet hème est également le site de liaison de petites molécules non chargées telles que CO, H<sub>2</sub>S et NO, qui sont impliquées dans la signalisation cellulaire. Dans le cas de l'oxyde nitrique, il est produit par l'hôte dans les systèmes biologiques comme mécanisme de défense contre les pathogènes microbiens envahissants. Par conséquent, les bactéries infectieuses virulentes ont développé des mécanismes qui permettent la respiration bactérienne sous stress nitrosant. En particulier, il a été démontré que les *bd* oxydases améliorent la survie bactérienne chez *E. coli* en cas de stress oxydant et nitrosant<sup>16</sup>. Par conséquent, la compréhension de la liaison du NO avec les cytochromes *bd* oxydases aidera à évaluer l'importance de cette réaction pour la pathogénicité microbienne.

Dans le présent travail, la liaison et la réactivité des cyt *bd-I* et *bd-II* vis-à-vis du NO ont été comparés. Ces expériences nous ont permis de conclure que la réactivité de l'oxyde

nitrique à l'état réduit et oxydé des oxydases *bd* d'*E. coli* est uniquement liée à la liaison à l'hème *d* (Figure 4).

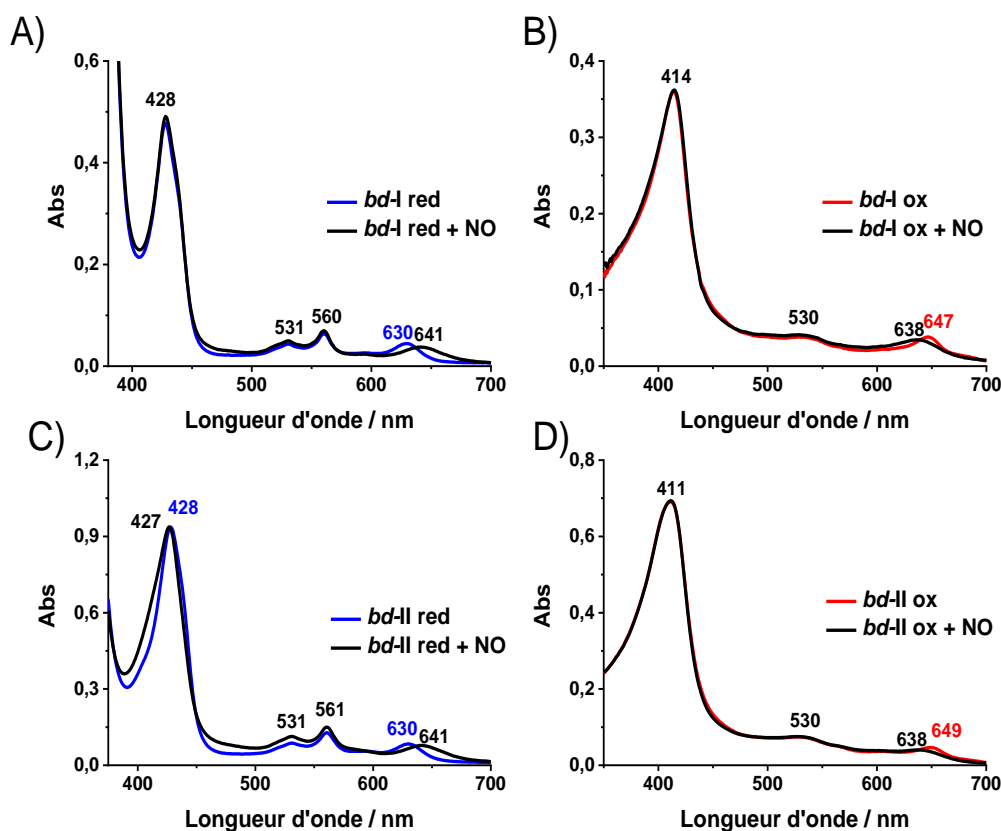


Figure 4. Spectres UV-Vis des *bd-I* et *bd-II* à l'état réduit (A, C) et oxydé (B, D) lors de l'ajout de 1:100 équivalents de NO à l'échantillon à pH 7.

La libération de NO par les cyt *bd-I* et *bd-II* a été étudiée dans une large gamme de pH physiologique de 6 à 8 par des méthodes électrochimiques et spectroscopiques. Il a été démontré que lorsque le NO est ajouté, il entre en compétition avec l'oxygène moléculaire au niveau du site actif et inhibe immédiatement l'activité de l'oxydoréductase à pH 7, comme le prouve la voltammétrie à film protéique. Cependant, l'inhibition du NO s'inverse avec le temps, jusqu'à 70 % de récupération pour les protéines immobilisées sur les électrodes modifiées avec des nanoparticules d'or. À pH 8, le NO agit comme un inhibiteur puissant, ce qui est en accord avec les expériences UV-Vis, où lors de l'augmentation du pH la libération de NO est ralentie pour la *bd-I*, et bloquée pour la *bd-II* (Figure 5).

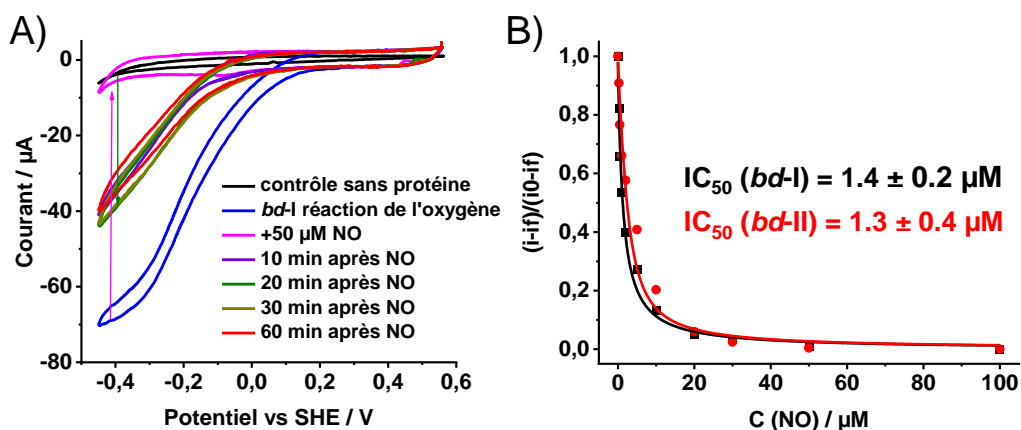
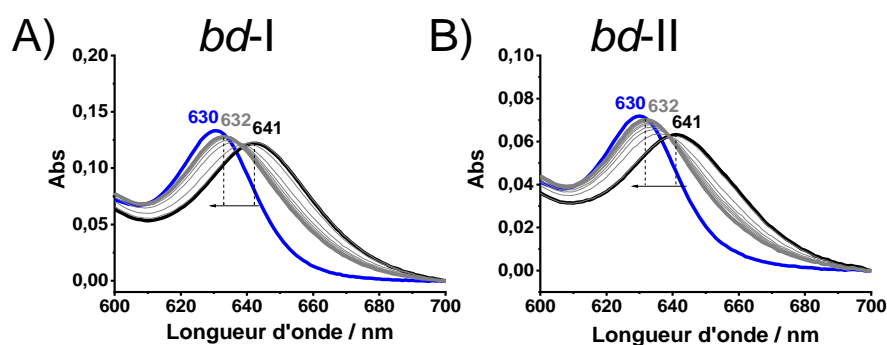


Figure 5. Réduction électrocatalytique de  $O_2$  par la *cyt bd-I* oxydase sur une électrode d'or modifiée avec des NPs d'or et des SAM thiols à pH 7 avec 2,5 % de PE (courbe bleue), inhibition de la catalyse de  $O_2$  par le NO (courbe rose) et libération de NO en fonction du temps (A) ; détermination de la  $IC_{50}$  du NO pour les oxydases *cyt bd-I* (courbe noire) et *bd-II* (courbe rouge) (B). Conditions : tampon phosphate pH 7 saturé d'air, vitesse de balayage 0.02V/s, vitesse de rotation 1000 rpm.

La réactivité du NO a été étudiée dans des variants des *cyt bd-I* et *bd-II* où des échanges Asp→Glu et Glu→Asp, respectivement, en position 58 dans la sous-unité CydB ont été réalisés (Fig. 6). Dans le variant D58E de la *bd-I* et le variant E58D de la *bd-II*, seul l'hème *d* se lie au substrat, entraînant le déplacement bathochrome de 630 à 641 nm comme dans les enzymes de type sauvage. Cependant, à pH 6,5 et 7, le NO n'a été que partiellement libéré de l'enzyme, ce qui a entraîné un petit décalage vers 636/638 nm. Dans la plage de pH 7,5-8, on n'observe pas de libération de NO pendant plus d'une heure. On peut en conclure que chez ces mutants, NO est resté principalement lié au site actif, l'hème *d*. La libération de NO du site actif est perturbée dans les deux variants, et les résultats suggèrent aussi que le résidu acide en 58ème position dans la sous-unité CydB participe au transport des protons vers le site actif. Auparavant, seuls les résidus de CydA étaient considérés pour expliquer la réactivité des oxydases *bd*.



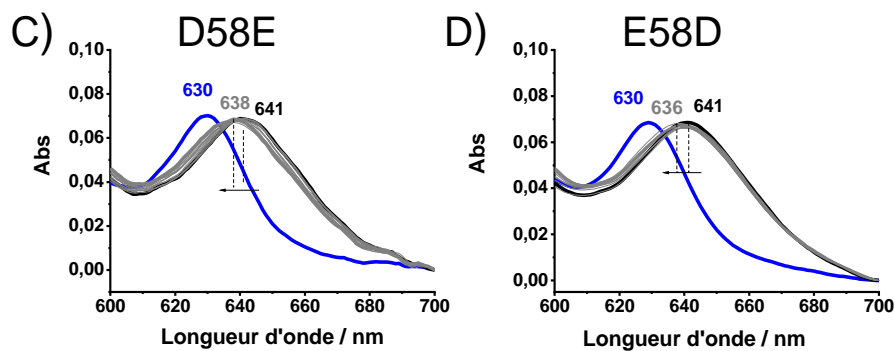


Figure 6. Liaison et libération du NO pH-dépendante dans l'hème d à l'état réduit pour la *bd-I* (A), la *bd-II* (B), le variant D58E de la *bd-I* (C) et le variant E58D de la *bd-II* (D) à pH 7; protéine réduite (bleu), hème complexe d-NO (noir), état final 60 min après la liaison de NO (gris).

De plus, dans les spectres FTIR des variants D58E et D58L de la cyt *bd-I*, les changements les plus importants sont observés dans la région de 1700 à 1800  $\text{cm}^{-1}$  où les modes vibrationnels des résidus acides protonés sont attendus. Les bandes à 1726  $\text{cm}^{-1}$  et à 1761/1751  $\text{cm}^{-1}$  étaient clairement détectables dans les spectres du type sauvage et du variant D58E mais absentes dans le variant D58L. Pour le variant D58E la nouvelle bande à 1741/1731  $\text{cm}^{-1}$  est apparue probablement suite à l'échange Asp→Glu.

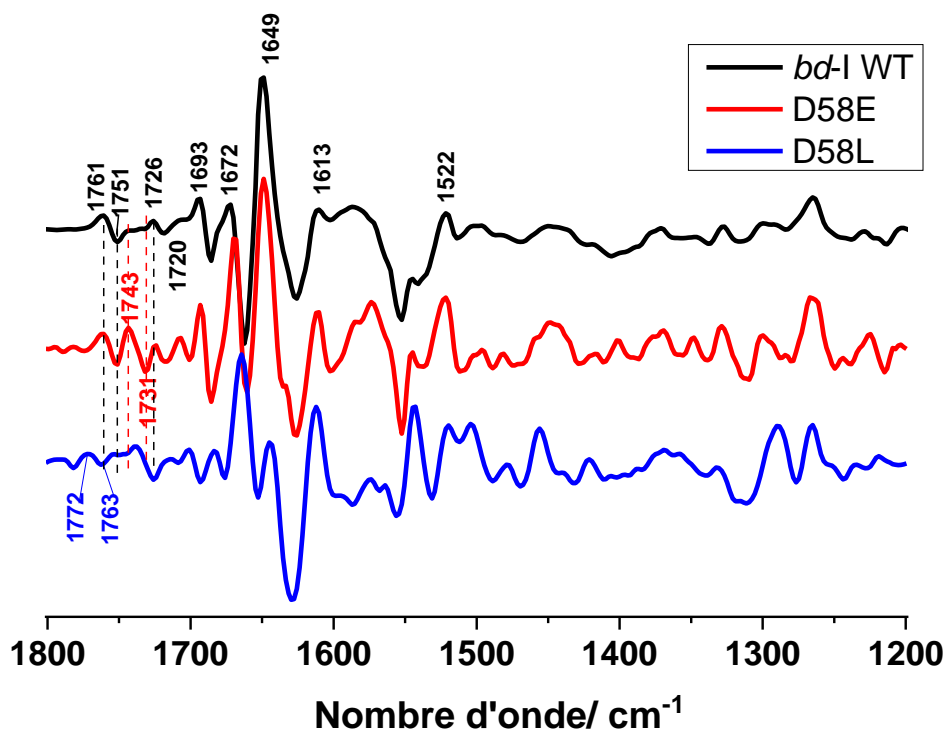


Figure 7. Spectres de différence FTIR oxydés-moins réduits de la cyt *bd-I* de type sauvage (noir) et des variants D58E (rouge) et D58L (bleu).

## Caractérisation spectroélectrochimique de la cNOR de *P. denitrificans*

La caractérisation spectrale de la cNOR de *Paracoccus denitrificans* par spectroscopies UV-Vis, IR et Raman a été faite pour le type sauvage et le variant dépourvu de Fe<sub>B</sub>. L'intégrité structurale de la protéine a été confirmée par les spectres UV-Vis, montrant la présence des trois hèmes. L'analyse des signaux dans la région de l'amide I dans les spectres infrarouges différentiels a confirmé l'environnement similaire des cofacteurs de l'hème dans les deux enzymes, mais des différences significatives ont été observées dans la région des modes vibrationnels des résidus acides Glu/Asp protonés. Ces différences indiquent un changement du microenvironnement en réponse à l'absence du centre de fer non hémique dans le site actif.

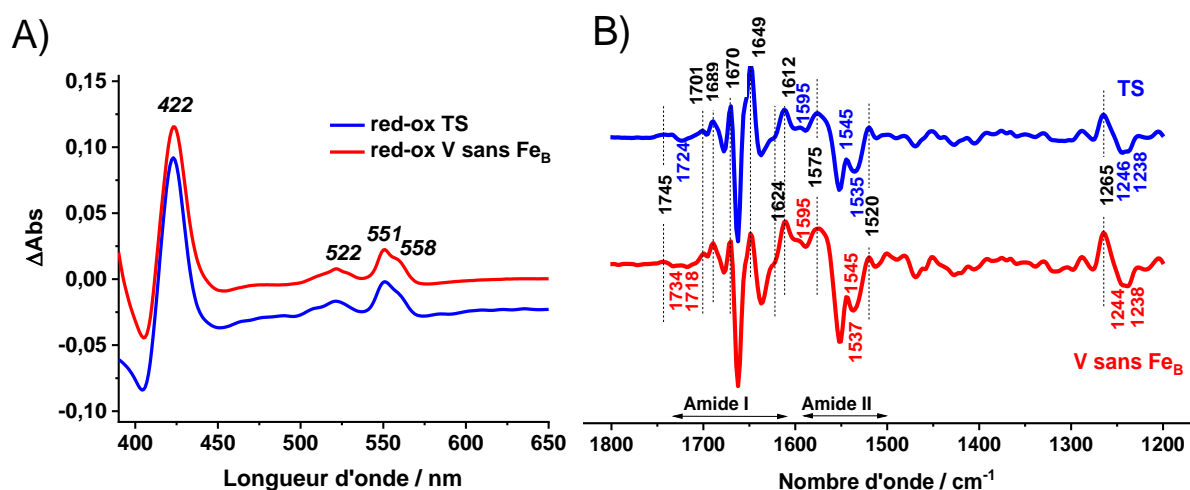


Figure 8. Caractérisation spectrale de la cNOR type sauvage (rouge) et du variant dépourvu de Fe<sub>B</sub>, (bleu) : Spectre différentiel UV Vis air-oxydé moins dithionite-réduit (A) ; Spectre différentiel FTIR Ox-red (B).

Les méthodes électrochimiques nous ont permis de déterminer les potentiels des hèmes du type sauvage et du variant dépourvu de Fe<sub>B</sub>. Un potentiel redox négatif de -50 mV et -64 mV vs SHE a été déterminé pour l'hème b<sub>3</sub> dans les échantillons du type sauvage et du variant, respectivement. Un effet significatif de l'absence du Fe<sub>B</sub> sur le potentiel redox de l'hème c était inattendu, mais il peut être dû à des changements de conformation induits par l'élimination du centre de fer non hémique.

Tableau 2. Potentiels redox des hèmes de la cNOR de type sauvage et du variant dépourvu de Fe<sub>B</sub>, déterminés dans un tampon phosphate (KPi pH 7.5, 0,02% DDM) par titrage potentiométrique, l'erreur standard de la méthode est de 20 mV.

Potentiel vs SHE / mV	Variant sans Fe <sub>B</sub> , cNOR	Type sauvage, cNOR
hème b <sub>3</sub>	-64	-50
hème c	+133	+246
hème b	+320	+356

L'étude électrochimique a montré que le transfert direct d'électrons pour la cNOR immobilisée sur l'électrode en carbone vitreux était atteint dans le type sauvage et le variant dépourvu de Fe<sub>B</sub>. En conséquence, dans des conditions non catalytiques, les potentiels redox formels des deux centres métalliques de la protéine ont été déterminés, donnant +0,290 V pour l'hème *c* et -0,158 V vs SHE pour l'hème *b*<sub>3</sub>. Des valeurs similaires ont été obtenues pour la protéine sans Fe<sub>B</sub>.

L'activité électrocatalytique en présence d'oxygène et d'oxyde nitrique a été étudiée par voltammétrie cyclique. Il a été observé que l'absence du centre de fer non hémique ne perturbe pas la liaison de l'oxygène dans le variant, ce qui est en accord avec les mesures d'activité de ces enzymes<sup>17</sup>. Les résultats électrochimiques ont également montré que le type sauvage et le variant sans Fe<sub>B</sub> sont tous les deux très actifs sur l'électrode avec des turnovers ( $k_{cat}$ ) de  $2859 \pm 712$  unités/s et  $2842 \pm 961$  unités/s, respectivement. Étant donné que même en l'absence de Fe<sub>B</sub>, la réduction catalytique de NO a toujours lieu, ces résultats sont en faveur des mécanismes catalytiques trans et cis:*b*<sub>3</sub>, où l'une ou l'autre ou les deux molécules de NO se lieraient à l'hème *b*<sub>3</sub>. Cependant, l'activité catalytique extrêmement élevée pour les deux protéines immobilisées peut être liée à la configuration de l'expérience où, en cas d'orientation favorable sur la surface de l'électrode, les électrons peuvent être directement transférés au site actif, évitant la chaîne de transfert d'électrons naturelle. Il faudrait donc étudier la réaction électrocatalytique des protéines immobilisées en contrôlant mieux l'orientation de la protéine sur la surface de l'électrode, par exemple, en utilisant l'His-Tag sur la surface de la protéine. Il est important de noter que l'inhibition de l'état oxydé de l'enzyme par le NO n'est pas observée ici car dans les expériences réalisées, la protéine est maintenue à l'état réduit par le potentiel appliqué, ce qui n'est pas le cas dans les tests d'activité traditionnels<sup>18</sup>.

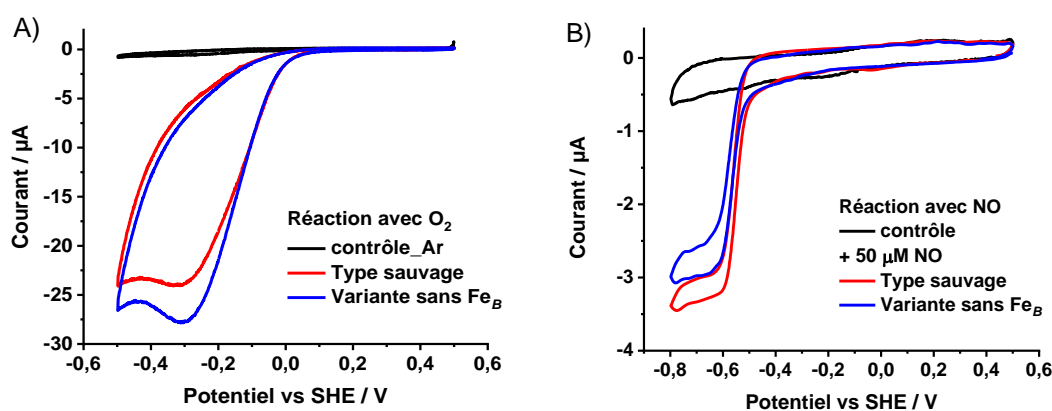


Figure 4. Voltammogrammes cycliques de la cNOR type sauvage (ligne rouge) et du variant sans Fe<sub>B</sub> (ligne bleue) immobilisée sur l'électrode de carbone vitreux en présence de O<sub>2</sub> (A) et NO (B), la ligne noire montre la réponse de la protéine sans aucun substrat dans l'atmosphère anaérobie, conditions expérimentales : 0.02 V/s, 1000 rpm, pH 7.5 KPi.

## Conclusions générales

Ce projet a porté dans un premier temps sur la comparaison des propriétés spectroscopiques et électrochimiques des oxydases *bd-I* et *bd-II* de *E. coli* en relation avec les différences structurales. Le capteur électrochimique optimisé dans cette étude a été utilisé pour le criblage d'inhibiteur de la *cyt bd* oxydase dans une bibliothèque de petites molécules de type quinol. Ces résultats ont permis d'élaborer des stratégies pour le développement d'une nouvelle génération de médicaments antibactériens contre les pathogènes qui dépendent de la cytochrome *bd* oxydase pour leur survie.

Les résultats obtenus ici ont également contribué à la connaissance du mécanisme de réaction au NO de ces enzymes procaryotes, en donnant des informations précieuses sur le caractère dépendant du pH de la libération du NO à partir du site actif. En outre, ces résultats ouvriront de nouvelles perspectives sur la compréhension du rôle de ces enzymes dans la haute tolérance d'*E. coli* au stress nitrosant.

La caractérisation structurale et électrochimique de la cNOR de type sauvage et du variant dépourvu de  $Fe_B$  a mis en lumière le rôle du centre redox du fer non hémique dans la réduction catalytique du NO. Cette information est pertinente pour la compréhension du rôle évolutif du cNOR qui s'est révélé capable de réduire le NO même si le cofacteur  $Fe_B$  est absent.





## List of presentations

---

30 August - 4 September 2020 – 71th annual meeting of the International society of electrochemistry, Belgrad Serbia, <https://annual71.ise-online.org/>, (oral communication):

Iryna Makarchuk, Alexander Theßeling, Hamid Nasiri, Andreas Speicher, Thorsten Friedrich, Petra Hellwig, Frédéric Melin, Development of a Bioelectrochemical Sensor Based on Cytochrome *bd* Oxidase.

1-15 July 2021 - CSAC2021: 1st international electronic conference on the chemical biosensors and analytical chemistry, <https://csac2021.sciforum.net/>, (poster):

Iryna Makarchuk, Anton Nikolaev, Alexander Thesseling, Lisa Dejon, Daniel Lamberty, Laura Stief, Andreas Speicher, Thorsten Friedrich, Petra Hellwig, Hamid R. Nasiri, Frederic Melin, The Inhibition Study of Cytochrome *bd* Oxidase Using the Enzyme-Based Electrochemical Sensor, DOI: 10.3390/CSAC2021-10555

21-24 September 2021 – 21st edition of the congress of Groupe Français de Bioénergétique GFB, <https://premc.org/gfb2021/>, (oral communication):

Iryna Makarchuk, J. Kagi, T. Gerasimova, T. Friedrich, P. Hellwig, F. Melin, The study of a ligand-binding reaction of cytochrome *bd* oxidase with NO.

10-15 July 2022 – ICPP 2022: 12th International Conference of porphyrines and phtalocyanines, Madrid Spain, <http://www.icpp-spp.org/>, (poster):

Iryna Makarchuk, Jan Kagi, Tatjana Gerasimova, Daniel Wohlwend, Thorsten Friedrich, Frédéric Melin, Petra Hellwig, The small molecules reactivity of homologous cytochrome *bd* oxidases from *E. coli*.

20-25 August 2022 – EBEC 2022: 21st edition of the European conference on Bioenergetics, Aix-en-Provence, France, <https://ebec2022.org/>, (poster):

Iryna Makarchuk, Jan Kagi, Tatjana Gerasimova, Daniel Wohlwend, Thorsten Friedrich, Frédéric Melin, Petra Hellwig, Spectroelectrochemical study of NO binding of cytochrome *bd*-I and *bd*-II oxidases from *E. coli*, S3. P20, DOI: 10.1016/j.bbabi.2022.148690

## List of publications

---

A. Nikolaev, I. Makarchuk, A. Thesseling, et al, Stabilization of the highly hydrophobic membrane protein, cytochrome *bd* oxidase, on metallic surfaces for direct electrochemical studies, *Molecules*, 25 (2020), 3240, DOI: 10.3390/molecules25143240

I. Makarchuk, A. Nikolaev, A. Thesseling, L. Dejon, D. Lamberty, L. Stief, A. Speicher, T. Friedrich, P. Hellwig, H.R. Nasiri, F. Melin, Identification and optimization of quinolone-based inhibitors against cytochrome *bd* oxidase using an electrochemical assay, *Electrochimica Acta*, 381 (2021), 138293, ISSN 0013-4686, DOI: 10.1016/j.electacta.2021.138293

I. Makarchuk, A. F. Santos Seica, F. Melin, P. Hellwig, Probing the reaction of membrane proteins via infrared spectroscopies, plasmonics, and electrochemistry, *Current Opinion in Electrochemistry*, 30 (2021), 100770, DOI: 10.1016/j.coelec.2021.100770

A. Grauel, J. Kägi, T. Rasmussen, I. Makarchuk, S. Oppermann, A. Moumbock, D. Wohlwend, R. Müller, F. Melin, S. Günther, P. Hellwig, B. Böttcher, T. Friedrich, Structure of *Escherichia coli* cytochrome *bd*-II type oxidase with bound aurachin D, *Nature Communications*, 12 (2021), 6498, DOI: 10.1038/s41467-021-26835-2

J. Kägi, I. Makarchuk, D. Wohlwend, F. Melin, T. Friedrich, P. Hellwig, *E. coli* cytochrome *bd*-I requires Asp58 in the CydB subunit for catalytic activity, *FEBS Letters*, (2022), 1-7, DOI: 10.1002/1873-3468.14482

I. Makarchuk, J. Kägi, T. Gerasimova, D. Wohlwend, T. Friedrich, F. Melin, P. Hellwig, Electrocatalytic and kinetic characterization of the NO binding to *bd*-I and *bd*-II oxidase from *E. coli* reveals the dependence on Asp/Glu58B, *BBA* (**submitted**)

I. Makarchuk, T. Gerasimova, J. Kägi, D. Wohlwend, F. Melin, T. Friedrich, P. Hellwig, Mutation of heme *b*<sub>595</sub> ligands shifts redox potential by 200 mV without inactivating *E. coli* *bd*-I oxidase, *Bioelectrochemistry* (**submitted**)

## List of figures

Figure 1.1. Schematic representation of the mitochondrial respiratory chain: Complex I (PDB: 4WZ7), Complex II (PDB: 2WDV), Complex III (PDB: 2A06), Complex IV (PDB: 3ASO) – heme-copper oxidases in mitochondria (HCOs) terminal acceptor in the electron transfer chain which reduces O <sub>2</sub> to H <sub>2</sub> O .....	37
Figure 1.2. Structures of the A-, B-, and C-type HCOs and nitric oxide reductase containing main catalytic subunit (green) and auxiliary subunits (red and blue). The schematic representation of the proton channels for different types of HCOs: copper and iron ions are represented as black and red sphere, respectively, and hemes are shown as sticks (orange).....	42
Figure 1.3. Crystal structure of cNOR (A) with the binuclear active site (B) from <i>P. aeruginosa</i> (PDB: 3O0R), composed of two subunits NorB (blue) and NorC (green) .....	45
Figure 1.4. Structures of bacterial cytochrome <i>bd</i> oxidases: (A) <i>bd</i> oxidase of <i>G. thermodenitrificans</i> (PDB: 5DOQ) with subunit CydA (light beige), CydB (red), and CydS (dark red); (B) <i>E. coli bd-I</i> (PDB: 6RKO in green colours) with subunit CydA, CydB, CydX, and CydY; (C) <i>bd-II</i> oxidase from <i>E. coli</i> (PDB: 7OSE in blue colours, pdb: 7OY2 in grey tones) with subunit AppC (homologue to CydA), AppB (homologue to CydB), and AppX (homologous to CydS/X), 7OSE has been solved with the inhibitor aurachin D (AurD) bound to the Q-loop; (D) The mycobacterial <i>bd</i> oxidase ( <i>M. smegmatis</i> , PDB: 7D5I, in yellow colours, <i>M. tuberculosis</i> , PDB: 7NKZ, in orange and salmon) with subunit CydA and CydB .....	47
Figure 1. 5. (A) Triangular heme arrangement in <i>G. thermodenitrificans</i> , hemes <i>b</i> <sub>558</sub> and <i>b</i> <sub>595</sub> (light beige sticks) are found in a plane, while heme <i>d</i> sits orthogonally on top (grey sticks). (B) The superposition of the heme arrangement in <i>E. coli bd-I</i> (green sticks), <i>E. coli bd-II</i> (blue sticks), <i>bd</i> from <i>M. smegmatis</i> (yellow sticks), and <i>bd</i> from <i>M. tuberculosis</i> (red sticks). Molecular oxygen shown in red spheres, reproduced from reference <sup>109</sup> ). (C) Redox potentials obtained from spectro-electrochemical titrations of cyt <i>bd</i> from <i>E. coli</i> and <i>G. thermodenitrificans</i> at pH 7 (vs SHE). .....	48
Figure 1.6. The denitrification chain in <i>Paracoccus denitrificans</i> . Denitrification-specific enzymes are in green and blue colors: AP (PDB: 4U4W), NAR (PDB: 1R27), NOR (PDB: 5GUW), N <sub>2</sub> OR (PDB: 1FWX), NIR (PDB: 1AOF) whereas enzymes also involved in aerobic respiration complex I (PDB: 4WZ7), complex III (PDB: 2A06) and ATP synthase (PDB: 5LQY) are shown in different colors. .51	
Figure 1.7. NO reductase activity of purified mycobacterial cytochrome <i>bcc-aa3</i> supercomplex. Four aliquots of 2.1 μM NO (1.8 μL of 1.8 mM NO each) were sequentially added to degassed buffer containing dithiothreitol (5 mM), MD menadione (0.26 mM) as the reducing system, and glucose (5 mM) and glucose oxidase (16 units/mL) to scavenge residual O <sub>2</sub> in the 1.5-mL reaction chamber, where pre-reduced cytochrome <i>bcc-aa3</i> (200 nM) was added .....	54
Figure 1.8. Oxygraphic traces showing NO inhibition of <i>E. coli</i> cytochrome <i>bd-I</i> and bovine CcO, and activity recovery after addition of oxy-haemoglobin ( <i>HbO2</i> ) to scavenge free NO.....	56
Figure 1.9. Structures of the potent inhibitors of the cytochrome <i>bd</i> oxidase activity. ....	59
Figure 2.1. The biological redox scale at pH 7 .....	65
Figure 2.2. a) Cyclic voltammetry for the adsorbed redox couple, displaying reversible electron transfer; b)electron transfer coupled to catalytic reaction in the presence of the substrate (stationary electrochemistry) .....	66
Figure 2.3. a) Cyclic voltammograms of cytochrome <i>c</i> at pH 7.0 with a scan rate of 100 mVs <sup>-1</sup> ; b) Trumpet plots, cathodic (circle) and anodic (square) potentials were determined from voltammograms at each scan rate .....	67

Figure 2.4. Models of the structure a) cytochrome <i>c</i> peroxidase <sup>195</sup> and b) <i>D. fructosovorans</i> NiFe hydrogenase, showing the two proteins assembled in the heterodimer (light blue and green), the buried active site (AS), the three lined-up iron-sulfur (FeS) clusters used for transferring electrons.	68
Figure 2.5. Direct and mediated electron transfer in protein voltammetry.	70
Figure 2.7. a) Catalytic current measured for cytochrome <i>ba</i> <sub>3</sub> adsorbed at a rotating gold nanoparticles electrode as a function of rotation speed ; b) Koutecky-Levich plot showing small but nonzero intercept at infinite rotation rate, allowing one to estimate $k_{cat}$ .	75
Figure 2.8. The model Henderson plots at different concentration of substrate for competitive (A) and uncompetitive (B) inhibition.	79
Figure 2.9. a) The electromagnetic spectrum showing the boundaries between different regions and the type of atomic or molecular transition responsible for the change in energy; b) Jablonski diagram of the possible transitions that can occur after a molecule has been photoexcited.	81
Figure 2.10. Structures of the hemes found in enzymes of the respiratory chain.	82
Figure 2.11. Differential red-ox spectra of the UV/Visible spectra of cytochrome <i>aa</i> <sub>3</sub> oxidase from <i>P. denitrificans</i> , cytochrome <i>bo</i> <sub>3</sub> oxidase from <i>E. coli</i> , cytochrome <i>ba</i> <sub>3</sub> oxidase from <i>T. thermophilus</i> , cytochrome <i>cbb</i> <sub>3</sub> oxidase from <i>P. stutzeri</i> , and cytochrome <i>bd</i> -I oxidase from <i>E. coli</i> .	83
Figure 2.12. a) Differential red-ox spectra of the UV-Vis potentiometric titration of cis-trans isomerase from <i>Pseudomonas aeruginosa</i> ; b) Fitting with modified Nernst equation for determination of the mid-point potential of the red-ox active cofactors of the protein.	84
Figure 2.13. A typical mid-IR transmission spectrum showing in a schematic way typical absorptions lines associated to vibrational modes of molecules.	86
Figure 2.14. A typical FTIR spectrum of a protein in phosphate buffer showing the Amide I and Amide II bands at $\sim 1650\text{ cm}^{-1}$ and $\sim 1540\text{ cm}^{-1}$ , respectively. (Inset) Expanded view of the Amide I band, which can be deconvoluted into its secondary structure components.	87
Figure 2.15. Schematic representation of the spectra of the oxidized and reduced forms (a) and redox-induced difference spectrum of the cytochrome <i>c</i> oxidase from <i>P. denitrificans</i> for the full potential step from -0.5 to 0.5 V vs. a Ag/AgCl reference electrode (b).	89
Figure 3.1. SEM images of the electrode surface after single deposition of the gold nanoparticles at 1 $\mu\text{M}$ (a) and evaluation of the of ligaments size at 100 nm scale (b).	94
Figure 3.2. Cyclic voltammograms of a modified NPs electrode (red curve) and a flat gold electrode (black curve) with the same geometric area in 0.1 M $\text{H}_2\text{SO}_4$ solution at scan rate of 0.1 $\text{V}\cdot\text{s}^{-1}$ .	94
Figure 3.3. The evaluation of rugosity at 10 $\mu\text{m}$ scale of 3D gold nanoparticle electrode (a) and electrodes after overnight incubation with neutral thiols (b) and negatively charged thiols (c).	95
Figure 3.4. Evaluation of porosity at the 200 nm scale of 3D gold nanoparticle electrode after 1h incubation with neutral thiols (a) and negatively charged thiols (b).	96
Figure 3.5. Structure of the lipids probed for the protein film stability examination.	96
Figure 3.6. Voltammograms obtained for cytochrome <i>bd</i> oxidase with added 2.5% PE (a) and 2.5% PG (b) on gold NPs modified with HT/MCH (1/1) (black trace), HT/MCH/MPA (1/1/1) (red trace), HT/MCH/MHA (1/1/1) (blue trace) and HT/MCH/MUA (1/1/1) (pink trace).	97
Figure 3.7. Two consecutive voltammograms obtained for cytochrome <i>bd</i> oxidase modified with HT/MCH SAM and with 2.5% PE (a), 2.5% PG (b) and with 1.25% PE + 1.25% PG (c) incubated with protein solution.	98

Figure 3.8. Cyclic voltammogrammes of the cytochrome <i>bd-I</i> oxidase oxigen reduction (black curves) alone and after addition of the 50 $\mu$ M HQNO a), nalidixic acid b), and 2-bromo-1,4 naphtoquinone c) (red curves), grey curves represent control voltammograms before protein immobilization. ....	101
Figure 3.9. Control cyclic voltamograms in the absence of protein (grey curves) and effect of the added 50 $\mu$ M HQNO a), nalidixic acid b), and 2-bromo-1,4 naphtoquinone c) (red curves). ....	101
Figure 3.10. Structures of the Auchin D analogues tested in the inhibition study towards <i>bd-I</i> oxidase immobilized on gold electrode. ....	103
Figure 3.11 Inhibition of <i>bd-I</i> oxidase activity upon introducing 10 $\mu$ M AD-2 solution in DMSO (green curve) after verifying the stability of the electrode signal by 3 subsequent CVs (red, blue and pink curve), the control CV without added protein is showed in black. ....	104
Figure 3.12 Log P values calculated for the series compounds varied in the length of isoprenyl chain in C-3 position. ....	105
Figure 3.13. a) Concentration dependent inhibition of the <i>bd-I</i> oxidase immobilized on gold 3D electrode by AD-2; b) Henderson plots obtained for the AD-2 at different amount of ubiquinol in protein sample. ....	106
Figure 3.14. a) Inhibition effect of the AD-2 on the activity of <i>bd-I</i> oxidase immobilized on the nanostructured elecctrode; b) Plot of the normalized current at -0.4V versus the concentration of Aurachin D derivatives and HQNO. Conditions: air-saturated pH 7 phosphate buffer, scan rate 0.02V/s, rotation speed 1000 rpm. ....	107
Figure 4.1. Differences in the proton channel of homologues <i>bd</i> oxidases: a) shows the short channel in <i>bd-II</i> (pdb code: 7OY2) that begins at the end of the large, hydrophilic cavity, b) the longer proton pathway along a series of titratable amino acid residues in <i>bd-I</i> (pdb code: 6RKO); c) comparison of the active sites of <i>bd-I</i> and <i>bd-II</i> oxidases from <i>E. coli</i> . Subunit <i>cydA</i> is shown in blue, <i>cydB</i> in green, putative proton pathways are indicated by red arrows that connect titratable residues. ....	114
Figure 4.2. Dithionite-reduced minus air-oxidized difference UV-Vis spectra of the <i>bd-I</i> (red) and <i>bd-II</i> (blue) oxidase. ....	114
Figure 4.3. Ox-red induced FTIR difference spectra of the <i>bd-I</i> (red) and <i>bd-II</i> (blue) oxidase from <i>E. coli</i> . ....	115
Figure 4.4. a) Example of the reductive titration of <i>bd-II</i> in the range of +700/-300 mV vs SHE; b) The differential spectra at +350 mV vs. SHE compared with full red-ox spectra. ....	117
Figure 4.5. a) The evolution of the absorbance of <i>bd-II</i> in Soret band (435 nm) versus applied potential; b) Determination of the hemes b potential from differential UV/Vis spectra at 562 nm; c) Determination of the heme d potential from differential UV/Vis spectra at 629 nm; d) The reductive and oxidative titration for the determination of the redox potential of the heme <i>d</i> . ....	118
Figure 4.6. Voltammogrammes obtained for cytochrome <i>bd-II</i> oxidases incubated with 2.5% PE (red curve), 2.5% PG (blue curve) and the mixture of 1.25% PE and 1.25% PG (green curve) on gold NPs modified with HT/MCH thiols. Experimental conditions: air-saturated pH 7 phosphate buffer, scan rate 0.02V/s, rotation speed 1000 rpm. ....	120
Figure 4.7. Voltammogrammes obtained for cytochrome <i>bd-I</i> (a) and <i>bd-II</i> (b) oxidases incubated with 2.5% PE and 2.5% PG respectively on gold NPs modified with HT/MCH thiols. Experimental conditions: air-saturated pH 7 phosphate buffer, scan rate 0.02V/s, rotation speed 1000 rpm. ....	121
Figure 4.8. The pH-dependent oxygen catalysis of cytochrome <i>bd-I</i> (a) and <i>bd-II</i> (b) oxidases incubated with 2.5% PE and 2.5% PG, respectively, on gold NPs modified with HT/MCH thiols. Experimental conditions: air-saturated pH 7 phosphate buffer, scan rate 0.02V/s, rotation speed 1000 rpm. ....	122

Figure 4.9. Duroquinol: oxygen oxidoreductase activities of cyt <i>bd-I</i> (black) and <i>bd-II</i> (red) as a function of pH measured with a Clark electrode (Freiburg University). .....	122
Figure 4.10. Active site of cytochrome <i>bd-I</i> oxidase of <i>E. coli</i> . (A) Coordination geometry of Glu445 <sup>A</sup> and Arg448 <sup>A</sup> at heme b <sub>595</sub> in subunit CydA, Hydrogen bond angles (°) and distances (Å) are indicated. (B) Heme arrangement in CydA with Fe-Fe distances between the hemes given in Å. Trp441 <sup>A</sup> serving as electron shuttle between hemes b <sub>558</sub> and b <sub>595</sub> is additionally shown. A dioxygen molecule is coordinated by the active site heme <i>d</i> . .....	123
Figure 4.11. Dithionite-reduced minus air-oxidized UV-vis difference spectra of cyt <i>bd-I</i> oxidase (black) and the E445D (blue) and R448N (pink) variants. ....	124
Figure 4.12. FTIR ox-red differential spectra of WT cyt <i>bd-I</i> oxidase and mutants E445D, R448N (+500/-500 mV vs Ag/AgCl). ....	125
Figure 4.13. Voltammograms of the cyt <i>bd-I</i> wild type (black) and the E445D (blue) and R448N (pink) variants in air-saturated pH 7 phosphate buffer; scan rate: 0.02V/s, rotation speed: 1000 rpm. ....	126
Figure 4.14. The effect of NO inhibition on the electrocatalytic O <sub>2</sub> reduction of the wild type <i>bd-I</i> oxidase (a), E445D (b) and R448N (c) variants on a gold electrode modified with gold NPs and SAM thiols at pH 7 with 2.5 % PE. Conditions: air-saturated pH 7 phosphate buffer, scan rate 0.02V/s, rotation speed 1000 rpm. ....	127
Figure 4.15. a) Oxidative titration of <i>bd-I</i> R448N variant in the range of +700/-300 mV vs. SHE, b) The differential absorbance of <i>bd-I</i> R448N at Soret band, 430 nm, plotted versus applied potential, c) Determination of the hemes <i>b</i> potential from differential UV/Vis spectra at 561 nm with modified Nernst equation, d) Determination of the heme <i>d</i> potential from differential UV/Vis spectra at 629 nm with modified Nernst equation. ....	128
Figure 4.16. a) Example of the reductive titration of <i>bd-I</i> R448N variant in the range of +700/-300 mV vs. SHE, b) The differential absorbance of <i>bd-I</i> R448N at Soret band, 430 nm, plotted versus applied potential, c) Determination of the hemes <i>b</i> potential from differential UV/Vis spectra at 561 nm with modified Nernst equation, d) Determination of the heme <i>d</i> potential from differential UV/Vis spectra at 629 nm with modified Nernst equation. ....	129
Figure 4.17. Summarized potentiometric titrations of <i>bd-I</i> R448N in reductive (blue) and oxidative (red) directions. ....	129
Figure 5.1 a) Electrocatalytic reduction of O <sub>2</sub> by the cyt <i>bd-I</i> oxidase (a) on a gold electrode modified with gold NPs and SAM thiols at pH 7 with 2.5 % PE (blue curve), NO inhibition of O <sub>2</sub> catalysis (pink curve) and NO release over time; b) Determination of the IC <sub>50</sub> of NO for the cyt <i>bd-I</i> oxidase. Conditions: air-saturated pH 7 phosphate buffer, scan rate 0.02V/s, rotation speed 1000 rpm. ....	136
Figure 5.2. UV-Vis spectra of the <i>bd-I</i> in reduced (a) and oxidized (b) state upon addition of 1:100 equivalent of NO to the sample at pH 7. ....	137
Figure 5.3. Superposition of <i>bd-II</i> with <i>bd-I</i> structures from <i>E. coli</i> (a) and top view (b). The homologous subunits of <i>E. coli</i> <i>bd-I</i> are all shown in gray, the heme groups are shown in yellow and ubiquinone-8 in red. ....	138
Figure 5.4. a) Electrocatalytic O <sub>2</sub> reduction by cyt <i>bd-II</i> oxidase (a) on a gold electrode modified with gold NPs and SAM thiols at pH 7 with 2.5 % PG (blue curve), NO inhibition of O <sub>2</sub> catalysis (pink curve) and NO release over time; b) Determination of the IC <sub>50</sub> of NO for the cyt <i>bd-II</i> oxidase. Conditions: air-saturated pH 7 phosphate buffer, scan rate 0.02V/s, rotation speed 1000 rpm. ....	139

Figure 5.5. Electrocatalysis of O <sub>2</sub> of the cyt <i>bd-I</i> oxidase (a, c) and <i>bd-II</i> (b, d) on a gold electrode modified with gold NPs and SAM thiols at pH 6 (a, b) and 8 (c, d) (blue curve), NO inhibition of O <sub>2</sub> catalysis (pink curve) and NO release within an hour. ....	140
Figure 5.6. Full UV-Vis spectra of <i>bd-II</i> oxidase in reduced (a) and oxidized (b) state upon addition of the 1:100 equivalent of NO to the sample at pH 7.....	141
Figure 5.7. The shift of the maximum of the heme d Fe <sup>+2</sup> - NO complex over one hour as a function of pH in 100mM phosphate buffer with 100 equivalent excess of NO to 5 μM cyt <i>bd-I</i> oxidase. ....	142
Figure 5.8. pH-dependent NO-binding and -release to the heme d in reduced state for <i>bd-I</i> a) pH 6.5, b) pH 7, c) pH 7.5, d) pH 8 and for <i>bd-II</i> at e) pH 6.5, f) pH 7, g) pH 7.5, h) pH 8; reduced protein (blue), complex heme d-NO (black), final state 60 min after binding NO (grey). ....	143
Figure 5.9. pH-dependent NO-binding to the heme <i>d</i> in oxidized state for <i>bd-I</i> a) pH 6.5, b) pH 7, c) pH 7.5, d) pH 8 and for <i>bd-II</i> at e) pH 6.5, f) pH 7, g) pH 7.5, h) pH 8; oxidized protein (red), complex heme d-NO (black), final state 60 min after the binding with NO (grey). ....	144
Figure 5.10. Titratable sidechains connect solvent channel with heme d cavity in <i>E. coli bd-I</i> (pdb code: 6RKO) (A) and <i>bd-II</i> (pdb code: 7OY2) (B). Water molecules are shown as small blue spheres. The substrate channel was probed with CAVER (shown as olive ( <i>bd-I</i> ) and blue ( <i>bd-II</i> ) spheres with diameters illustrated by sphere sizes). ....	146
Figure 5.11. UV-Vis dithionite reduced-oxidized spectra of cytochrome <i>bd-I</i> oxidase WT and mutants D58E, D58L.....	147
Figure 5.12. Oxidized-minus-reduced FTIR difference spectra of wild type cyt <i>bd-I</i> (black) and the D58E (red) and D58L (blue) variants.....	148
Figure 5.13. Duroquinol:oxygen oxidoreductase activity of cyt <i>bd-I</i> and <i>bd-II</i> wild type (black and red), the Asp58Glu (olive) and the Glu58Asp (blue) variants as a function of pH.....	149
Figure 5.14. Full UV-Vis spectra of the mutants D58E (a) and E58D (b) in reduced state upon addition of 1:100 equivalent of NO to the sample at pH 7.....	150
Figure 5.15. pH-dependent NO-binding and -release to the heme d in reduced state for D58E a) pH 6.5, b) pH 7, c) pH 7.5, d) pH 8 and for E58D e) pH 6.5, f) pH 7, g) pH 7.5, h) pH 8; reduced protein (blue), complex heme d-NO (black), final state 60 min after binding NO (grey). ....	151
Figure 6.1. Difference red-ox absorption spectra of cNOR WT and Variant without non-heme iron Fe <sub>B</sub> in phosphate buffer pH 7.5 (100 mM KPi, 100 mM KCl, 0.02% DDM) .....	156
Figure 6.2. Visible spectra of the wild type (a) and Fe <sub>B</sub> lacking variant cNOR (b) in the oxidized (red curves) and reduced (blue curves) in 100mM phosphate buffer pH 7.0, 100mM KCl, 0.02% DDM. ....	156
Figure 6.3. Ox-red FTIR difference spectra of the cNOR WT and Fe <sub>B</sub> less variant at pH 7.5 .....	157
Figure 6.4. High (a, b) and low frequency (c, d) RR spectra of the dry films of the cNOR (WT) and Fe <sub>B</sub> deficient variant (M) without Fe <sub>B</sub> at 457 nm and 541 nm laser excitation. ....	160
Figure 6.5. RR spectra of the cNOR WT dry films and solution in capillary after addition of NO (1:100). ....	162
Figure 6.6. Oxidative UV-Vis titration curves of cNOR WT (a, b) and Variant without non-heme iron Fe <sub>B</sub> (c, d) in buffer pH 7.5 (100 mM KPi, 100 mM KCl, 0.05% DDM).....	163
Figure 6.7. Multi-component analysis: Gaussian fitting of the 1 <sup>st</sup> derivative of the titration curves at 423 nm, 551 nm, 558 nm for WT (a, b, c) and Variant cNOR (d, e, f); black – 1 <sup>st</sup> derivative of the	



absorbance at certain wavelength, red – final fitted curve, green – separated contributions from the redox heme cofactors.....	164
Figure 6.8. Cyclic voltammograms of cNOR wild type and Fe <sub>B</sub> lacking variant immobilized on the glassy carbon electrode at pH 7.5, with a scan rate of 0.02 V/s. ....	166
Figure 6.9. Cyclic voltammograms of cNOR WT (red line), Fe <sub>B</sub> less variant (blue line) immobilized on the glassy carbon electrode in the presence of O <sub>2</sub> (a) and NO (b), black line shows the protein response without any substrate in the anaerobic atmosphere, experimental conditions: 0.02 V/s, 1000 rpm, pH 7.5 phosphate buffer. ....	168
Figure 6.10. Concentration dependent NO reduction on the glassy carbon electrode modified with cNOR WT (a) and Fe <sub>B</sub> less variant (d) at,0.02 V/s, 1000 rpm, pH 7.5. The reaction rate vs NO concentration Girsch and de Vries fit (b,e) and Michaelis-Menten fit (c,f). ....	169
Figure B.1. Kinetics of MAHMA NONOate decomposition in the phosphate buffer solutions and determination of the half-life by the following of the disappearance of the characteristic UV absorption band of NONOate at 267 nm a)-d).....	186
Figure B.2. The structures of the 20 common amino acids .....	190
Figure E.1. a) Oxidative titration of <i>bd</i> -I E445D variant in the range of +600/-200 mV vs. SHE, b) The differential absorbance of <i>bd</i> -I R448N at Soret band, 430 nm, plotted versus applied potential, c) Determination of the hemes <i>b</i> potential from differential UV/Vis spectra at 561 nm with modified Nernst equation, d) Determination of the heme <i>d</i> potential from differential UV/Vis spectra at 629 nm with modified Nernst equation. ....	191
Figure E.2. a) Example of the reductive titration of <i>bd</i> -I E445D variant in the range of +600/-400 mV vs. SHE, b) The differential absorbance of <i>bd</i> -I R448N at Soret band, 430 nm, plotted versus applied potential, c) Determination of the hemes <i>b</i> potential from differential UV/Vis spectra at 561 nm with modified Nernst equation, d) Determination of the heme <i>d</i> potential from differential UV/Vis spectra at 629 nm with modified Nernst equation.....	192

## List of schemes

---


Scheme 1.2 The three pathways of NO binding at the catalytic site of cNOR <sup>139</sup> .....	52
Scheme 1.3. Reaction pathway of NO with different cytochrome <i>bd</i> species <sup>155</sup> .....	57
Scheme 6.1. The production of the Fe <sub>B</sub> lacking variant of cNOR .....	155
Scheme A.1. The three electrode electrochemical cell for the cyclic voltammetry .....	173
Scheme A.2. Clark-type oxygen electrode .....	174
Scheme A.2. The thin-layer electrochemical cell .....	175
Scheme. A.4. The optical path in the UV/Vis spectrometer. ....	176
Scheme. A.5. The FTIR spectrometer Vertex 70 from Brucker Optics. ....	177
Scheme A.6. From Fourier Transform interferogram to the IR spectrum. ....	177
Scheme. A.7. The optical path in the Raman spectrometer. ....	178
Scheme B.1. The immobilization scheme of the cytochrome <i>bd</i> -I oxidase on the surface of the gold electrode (pdb file 6rko) .....	184

## List of tables

---

Table 1.1 The functions of the membrane protein complexes from the mitochondrial respiratory chain	39
Table 1.2. The structural features and electron pathways of the terminal oxidases. The active site cofactors are shown in black, ls/hs refer to low- and high-spin heme and 5c/6c -penta- and hexacoordinated Cu or Fe. 41	
Table 2.1. The developed techniques of protein attachment to the electrode.	71
Table 2.2. UV-vis characteristic bands of heme cofactors in reduced cytochromes from respiratory chain	83
Table 2.3. The principal contributions of the polypeptide backbone to the IR spectrum	88
Table 2.4. Secondary structure assignment from Amide I band	88
Table 2.5. The redox and spin-sensitive vibrational modes of hemes observed in Raman spectroscopy	90
Table 3.1. Half wave catalytic potential ( $E_{cat}$ ) obtained for the protein samples incubated with 2.5% phospholipids with different thiols mixtures. Standard error of measurements is 20 mV for $E_{cat}$ .	98
Table 3.2. Half wave catalytic potential ( $E_{cat}$ ), slope of the limiting current ( $\Delta i/\Delta E$ ) and variability of the limiting current value between two consecutive scans ( $\Delta i/i$ ), obtained for the proteins with different lipids. Standard errors of measurements (SEMs) are 20 mV for $E_{cat}$ , 0.003 A·mV <sup>-1</sup> for $\Delta i/\Delta E$ and 0.02 for $\Delta i/i$ . 99	
Table 3.3. Inhibition activity at a single concentration of 10 $\mu$ M with or without added quinone cytochrome <i>bd</i> oxidase of HQNO and synthetic aurachin D analogues.	104
Table 3.4. Half-inhibitory constants calculated for the compounds having the stronger inhibiting activity.	108
Table 4.1. FTIR differential spectra signals assignment of <i>bd</i> -I and <i>bd</i> -II from <i>E. coli</i>	116
Table 4.2. The redox potentials (vs SHE) of the heme cofactors from <i>bd</i> -II from <i>E. coli</i>	119
Table 4.3. The redox potentials of the cofactors of cytochrome <i>bd</i> oxidases from different organisms.	119
	33

Table 4.4. Redox potentials of the <i>bd-I</i> heme groups determined by UV-vis titration	130
Table 6.1. Tentative FTIR differential spectra signals assignment for the WT and variant of cNOR	158
Table 6.2. Frequencies of the RR of the studied cNOR from <i>P. denitrificans</i> observed in capillary compared to those given in literature for the cNOR in oxidized and reduced state at 414 nm excitation.	161
Table 6.3. Red-ox potentials (vs SHE) of the WT and Fe <sub>B</sub> lacking Variant of cNOR determined by potentiometric titration	165
Table 6.4. Redox potentials reported for nitric oxide reductase biosensors.	167
Table B.2. Oligonucleotides used in this work. Homologous areas are marked bolt.	180
Table B.3. The summarized conditions of the buffer exchange for the proteins probed in protein film voltammetry on gold or glassy carbon rotating electrodes.	182
Table B.4. Ratio of the absorbance of GNPs at the surface plasma resonance peak <i>A<sub>spr</sub></i> to the absorbance at the plateau of the peak at 450 nm <i>A<sub>450</sub></i> in dependence the particle diameter	183
Table B.5. Conditions of the redox-induced differential FTIR experiments.	186
Table B.6. Conditions of the RR measurements.	187
Table C.1. List of 19 mediators used in the differential redox-induced spectroscopy measurements. All mediators are low-weight redox active compounds.	189



# Chapter I

## Introduction: getting inside the protein world

---

- 1.1 Cell bioenergetics: oxidative phosphorylation
- 1.2 From electron transfer chain to respiration: functions of membrane complexes
- 1.3 Classification and structure of Complex IV
  - 1.3.1 Superfamily of heme-copper oxidases (HCO)
  - 1.3.2 The family of NOR oxidases
  - 1.3.3 Superfamily of *bd* oxidases: structural diversity and mechanism
- 1.4 State of art: role of nitric oxide in pathogen virulence
  - 1.4.1 Denitrification chain of bacteria
  - 1.4.2 Mechanism of NO binding with terminal oxidases
- 1.5 Inhibitors towards cytochrome *bd* oxidase for the perspective drug design
- 1.6 Aims of the project



## 1.1 Cell bioenergetics: oxidative phosphorylation

All living cells, eukaryotes and bacteria, depend on the ability to convert and store energy in order to maintain the essential functions such as growth, transport, signaling and respiration. The nutrition compounds taken from the environment like sugar, fatty acids and amino acids are oxidized by molecular oxygen and the energy released from these redox reactions is conserved in a form of adenosine 5'-triphosphate molecule (ATP). This process called the oxidative phosphorylation takes place in the aerobic respiratory chain located in the inner membrane of the mitochondria and in the plasma membrane of the bacteria<sup>19,20</sup>. The electron flow starts with catalytic oxidation of the low-potential redox donor NADH, then electrons are transferred over a series of metal cofactors bound to membrane proteins and finally they reduce the high-potential redox acceptor – molecular oxygen (Figure 1.1)<sup>21</sup>.

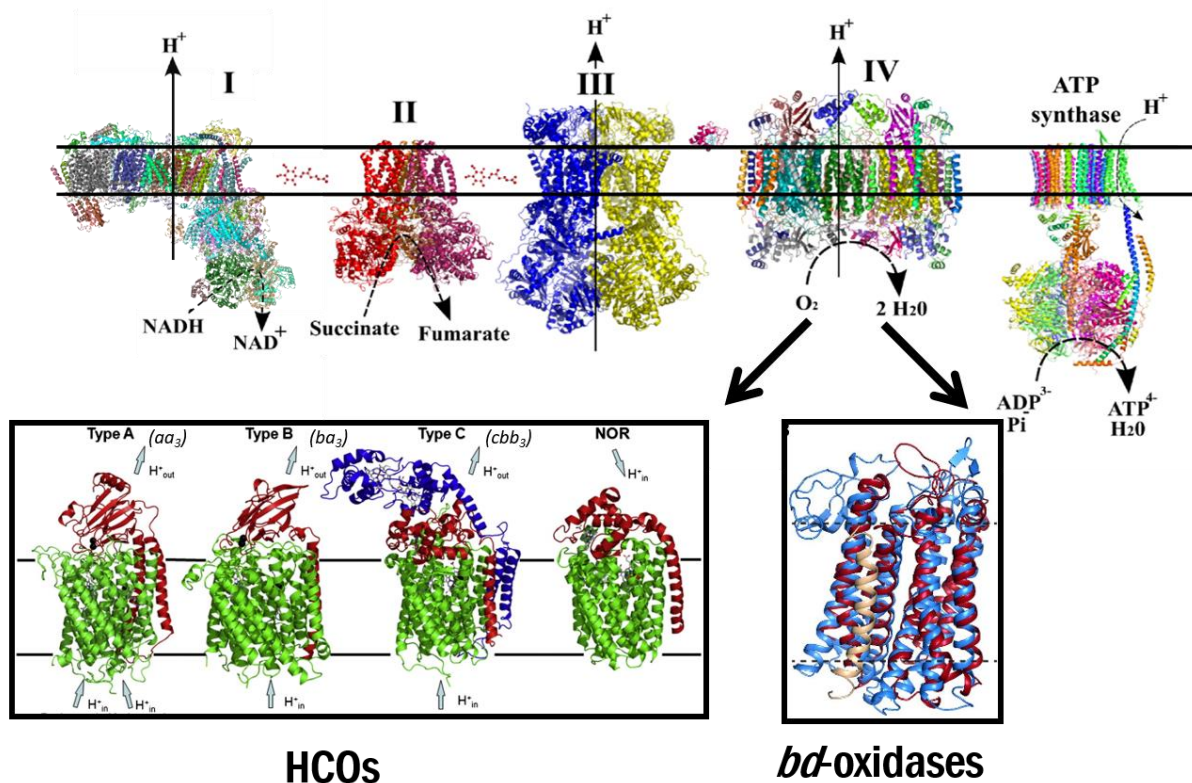


Figure 1.1. Schematic representation of the mitochondrial respiratory chain: Complex I (PDB: 4WZ7), Complex II (PDB: 2WDV), Complex III (PDB: 2A06), Complex IV (PDB: 3ASO) – heme-copper oxidases in mitochondria (HCOs) terminal acceptor in the electron transfer chain which reduces  $O_2$  to  $H_2O$ . Overall, a total of ten protons are translocated across the mitochondrial membrane per NADH oxidized (Proton flow is indicated by black arrows), and the electrochemical proton gradient is then used by the ATP synthase (PDB: 5LQY) to generate ATP<sup>22</sup>.

The energy of each step of the electron transfer generates a proton motive force ( $pmf$ )  $\Delta p$  from the negative side (n-side; matrix/cytoplasm) to the positive side (p-side;

intermembrane space/periplasm) of the membrane. The resulted electrochemical gradient  $\Delta\mu_H$  enables the synthesis of the energy carrier ATP by adenosine 5'-triphosphate synthase. The energy accumulation from the electrochemical gradient can be described as follows:

$$\Delta\mu_H = nF\Delta\varphi + RT\ln\left(\frac{[H^+]_p}{[H^+]_n}\right), \quad \text{Equation 1.1}$$

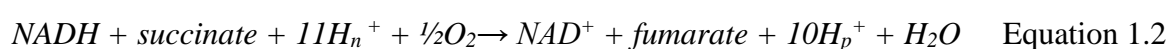
where  $F$  – Faraday's constant,  $\Delta\varphi$  – transmembrane potential difference,  $R$  – universal gas constant,  $T$  – temperature,  $[H^+]_{p/n}$  – the proton concentration in the more positive/negative side,  $n$  – charge of the proton.

This sequence of coupled reactions in the transmembrane protein complexes with the formation of a proton gradient was first proposed by Peter Mitchell in 1961<sup>23</sup>. As a result, from decomposition of a single molecule of glucose the energy obtained from chemical reaction is stored in 36 molecules of ATP.

It should be mentioned that the respiratory chain of bacteria and archaea can vary significantly from the one illustrated for eukaryotes in the Figure 1.1. It has a rich diversity, where sulfur or organic sulphoxides<sup>24</sup>, nitrogen oxides<sup>25</sup>, halogenated organic molecules<sup>26</sup> can be terminal acceptors of electrons instead of molecular oxygen. This factor contributes to the ability of prokaryotes to colonize many of Earth's most hostile microoxic and anoxic environments<sup>27</sup>.

## 1.2 From redox chain to respiration: function of membrane complexes

In mitochondrial respiratory chain (Figure 1.1) reduced NADH and succinate generated by the Krebs's cycle are oxidised by the membrane enzymes complex I and complex II, respectively. The released electrons are then shuttled to the membrane soluble quinone Q pool transforming them into quinols QH<sub>2</sub>. Each quinol carries two electrons and it is oxidized by the complex III, where one electron participates in the cytochrome c reduction and the other one is transferred to a quinone. Finally, cyt c delivers electrons to the complex IV, where the reduction of oxygen to water takes place. Complex I, III and IV are involved in the proton translocation across the membrane, resulting in the formation of the proton gradient required for the ATP synthesis at the complex V. Overall, the process can be summarized with the following equation:



The names and coupled catalytic reactions of the respiratory chain complexes are shown in the Table 1.1. Despite the popular representation of the respiratory chain as group of

separated functional enzymes, it was reported that many of them form larger assemblies called supercomplexes or respirasomes<sup>28–30</sup>.

Table 1.1 The functions of the membrane protein complexes from the mitochondrial respiratory chain

Name	Catalytic reaction	Pmf, H <sup>+</sup> /e 31
<b>Complex I</b> NADH:Quinone oxidoreductase <sup>32–36</sup>	$NADH + Q + 5H_n^+ \rightarrow NAD^+ + QH_2 + 4H_p^+$	2
<b>Complex II</b> Succinate:quinone oxidoreductase <sup>37–39</sup>	$Succinate + Q \rightarrow Fumarate + QH_2$	0
<b>Complex III</b> Quinol:cytochrome c oxidoreductase <sup>40–42</sup>	$2\text{cyt } c \text{ Fe}^{3+} + QH_2 + 2H_n^+ \rightarrow 2\text{cyt } c \text{ Fe}^{2+} + Q + 4H_n^+$	1
<b>Complex IV</b> Heme-copper oxidase superfamily <sup>43–46</sup>	$O_2 + 4\text{cyt } c \text{ Fe}^{2+} + (n+4) H_n^+ \rightarrow 2H_2O + 4\text{cyt } c \text{ Fe}^{3+} + nH_p^+$	2

In contrast to electron transport chains of eukaryotic mitochondria, bacteria have branched respiratory chains which enables them to survive in a wide variety of harsh environments, from acidic ponds and hot springs to anaerobic intestines of animals<sup>47–49</sup>. Many bacterial enzymes share common core architecture with the more complex eukaryotic counterparts, but alternative modular adaptations enable the bacterial enzymes to use a much broader set of electron donors and acceptors.

There are several differences between the respiratory chains of eukaryotes and procaryotes. First of all, bacteria cells use different routes of electron transfer depending on the growth conditions. Certain bacteria even can also switch between aerobic and anaerobic conditions (the facultative anaerobes), in which, for example, formate is oxidized by fumarate or nitrate instead of dioxygen<sup>50,51</sup>. Secondly, bacteria are able to use a range of primary dehydrogenases to deliver electrons such as NDH-1 and NDH-2 instead of mitochondrial complex I. The bacterial complex III can, in addition to ubiquinone ( $E_m = +90$  mV), also operate with low-potential quinones, such as menaquinone ( $E_m = -80$  mV). Thirdly, the architecture of the



cytochrome *c* as an electrons shuttle differs in bacteria: *P. denitrificans* uses a soluble cyt *c*, similar to that in mitochondria, but certain bacteria, such as *Bacillus subtilis*, use membrane-, lipid- and peptide-anchored cyt *c* modules<sup>52</sup>. Finally, there are many adaptations in the bacterial Complex IV. Some are related to the heme-copper oxidases (HCO) where Cu<sub>B</sub> has been replaced by an Fe<sub>B</sub> site that allows the *cbb*<sub>3</sub> oxidases to reduce NO to N<sub>2</sub>O, which is the main task of the NOR family<sup>53,54</sup>, while other are evolutionary not related to HCO and have a monoheme active site and do not pump protons, such as *bd* oxidases<sup>13,55,56</sup>.

Some bacteria like *Mycobacterium smegmatis* and *Flavobacterium johnsoniae* can similarly to eukaryotes organize their respiratory chain enzymes into higher-order supercomplexes, which are linked together by cardiolipin and modularly adapted subunits<sup>57–59</sup>. The understanding of the unique architecture of the bacterial respiratory chains will lead to future possibilities for drug design and open up new ways for treatment of infectious disease caused by the pathogenic bacteria.

### 1.3 Classification and structure of Complex IV

The Complex IV oxidases show a high degree of diversity in structure and habitat of colonization<sup>13,43,46</sup>. They vary in the type of the electron donor used (cyt *c* or quinols in some bacteria) and in the type of the heme cofactors. From the phylogenetic studies complex IV enzymes were classified into three superfamilies<sup>60</sup>: heme-copper oxidases (HCOs) including the cNOR and qNOR nitric oxide reductases, cytochrome *bd* oxidases and alternative oxidases. A subsequent division of the terminal oxidases into there superfamilies was based on the structural and phylogenic analysis of the proton uptake motive or the quinone binding site<sup>60–63</sup>. The structural characteristics of the terminal oxidases are summarized in the Table 1.2.

Table 1.2. The structural features and electron pathways of the terminal oxidases. The active site cofactors are shown in black, ls/hs refer to low- and high-spin heme and 5c/6c -penta- and hexacoordinated Cu or Fe.

Family		Name	Organism	Subunits (main+ auxiliary)	Electron donor	Electron pathway	Ref.	
HCOs	A-type	<i>aa</i> <sub>3</sub>	Beef heart	3+10	cyt <i>c</i>	cyt <i>c</i> → Cu <sub>A</sub> → heme <i>a</i> (ls6c, 2 His) → <b>heme a<sub>3</sub></b> (hs5c, His), <b>Cu<sub>B</sub></b> (3c, 3 His) → O <sub>2</sub>	64,65	
			<i>P. denitrificans</i>	3+1	cyt <i>c</i> <sub>552</sub> , cyt <i>c</i> <sub>550</sub>		66,67	
		<i>bo</i> <sub>3</sub>	<i>E. coli</i>	4	UQ-8	UQ-8 → heme <i>b</i> (ls6c, 2 His) → <b>heme o<sub>3</sub></b> (hs5c, His), <b>Cu<sub>B</sub></b> → O <sub>2</sub>	68,69	
	A <sub>2</sub>	<i>caa</i> <sub>3</sub>	<i>R. marinus</i>	2	4Fe-4S ferredoxins (HiPIP)	HiPIP → Cu <sub>A</sub> → heme <i>a</i> (ls6c, 2 His) → <b>heme a<sub>3</sub></b> (hs5c, His), <b>Cu<sub>B</sub></b> → O <sub>2</sub>	70	
	B-type	B <sub>1</sub>	<i>ba</i> <sub>3</sub>	<i>T. thermophilus</i>	2+1	cyt <i>c</i> <sub>552</sub>	cyt <i>c</i> → Cu <sub>A</sub> → heme <i>b</i> (ls6c, 2 His) → <b>heme a<sub>3</sub></b> (hs5c, 1 His), <b>Cu<sub>B</sub></b> → O <sub>2</sub>	71,72
		B <sub>3</sub>	<i>aa</i> <sub>3</sub>	<i>A. ambivalens</i>	2	CQ	CQ → heme <i>a</i> (ls6c, 2 His) → <b>heme a<sub>3</sub></b> (hs5c, His), <b>Cu<sub>B</sub></b> → O <sub>2</sub>	73,74
	C-type	<i>cbb</i> <sub>3</sub>	<i>P. stutzeri</i>	3+1	cyt <i>c</i> <sub>4</sub>	cyt <i>c</i> <sub>4</sub> → heme <i>c</i> (ls6c, 2 His) → heme <i>b</i> (ls6c, 2 His) → <b>heme b<sub>3</sub></b> (hs5c, His), <b>Fe<sub>B</sub></b> (3c, 3 His) → O <sub>2</sub>	75	
	NOR	cNOR	<i>P. denitrificans</i>	2	cyt <i>c</i> <sub>551</sub> , azurin	cyt <i>c</i> <sub>551</sub> → heme <i>c</i> (ls6c, His, Met) → heme <i>b</i> (ls6c, 2 His) → <b>heme b<sub>3</sub></b> (hs5c, His), <b>Fe<sub>B</sub></b> (4c, 3 His, 1 Glu) → NO	76,77	
	Bd	<i>bd</i> -I, <i>bd</i> -II	<i>E. coli</i>	2+2, 2+1	UQ	UQ → heme <i>b</i> <sub>558</sub> (ls6c, His, Met) → heme <i>b</i> <sub>595</sub> (ls5c, Glu) → <b>heme d</b> (hs5c, His) → O <sub>2</sub>	13,55,62,78	
		<i>bd</i>	<i>G. thermodenitrificans</i>	2+1	UQ, MK	UQ/MK → heme <i>b</i> <sub>558</sub> (ls6c, His, Met) → heme <i>b</i> <sub>595</sub> (ls6c, His, Glu) → <b>heme d</b> (hs5c, His) → O <sub>2</sub>		
<i>bd</i>		<i>M. tuberculosis</i>	2	MK	MK → heme <i>b</i> <sub>558</sub> (ls6c, His, Met) → heme <i>b</i> <sub>595</sub> (ls6c, Glu) → <b>heme d</b> (hs5c, His) → O <sub>2</sub>	79		

### 1.3.1 Superfamily of heme-copper oxidases (HCOs)

HCOs contain a high-spin heme which is ligated to one conserved histidine and in a close proximity ( $\sim 5\text{\AA}$ ) to a mononuclear copper site  $\text{Cu}_B$ . This superfamily includes diverse oxygen reductases and nitric oxide reductases (NOR) evolutionary related to HCOs. The earliest classification of heme-copper super family was proposed by Pereira et al.<sup>61</sup>, based on the division into the A-, B-, C-subfamilies depending on the proton channel pathways. Later, cNOR and qNOR were added to this classification<sup>60</sup>. A most recent classification was proposed Hemp and Gennis<sup>80</sup> and updated in 2022 by Murali et al.<sup>62</sup> on the basis of the phylogenetic analysis, structure of the active site and presence of conserved residues of the quinol-binding site. This resulted in the branched classification of 9 oxygen reductase subfamilies (A-, B-, C-, D-, E-, F-, G-, H-) and 6 NOR subfamilies (cNOR, qNOR, eNOR, nNOR, gNOR, sNOR). Here only the four most abundant groups will be briefly introduced (Fig.1.2).

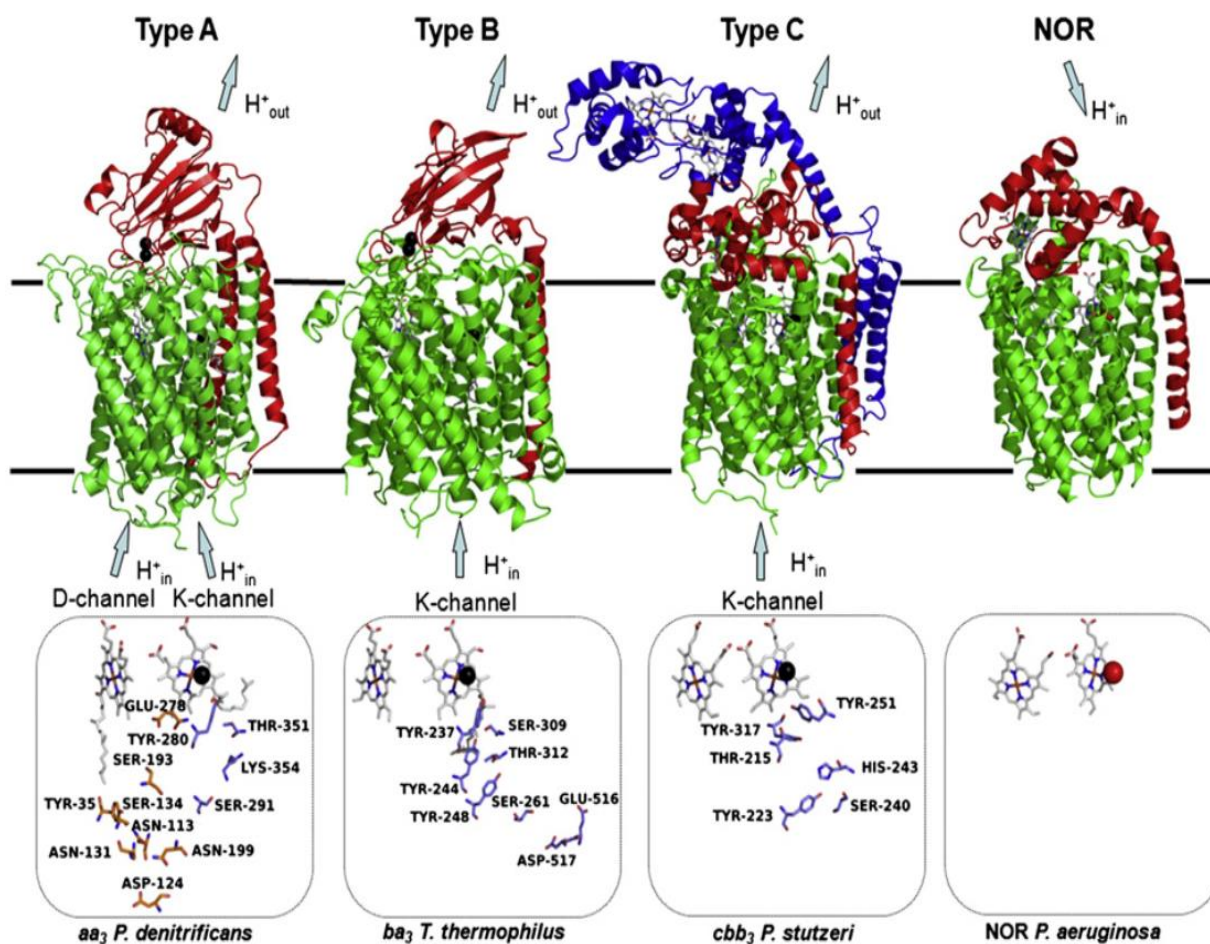


Figure 1.2. Structures of the A-, B-, and C-type HCOs and nitric oxide reductase containing main catalytic subunit (green) and auxiliary subunits (red and blue). The schematic representation of the proton channels for different types of HCOs: copper and iron ions are represented as black and red sphere, respectively, and hemes are shown as sticks (orange), reproduced from reference[60].

All members of the HCO superfamily share common characteristics:

- the main subunit I typically consists of 12 or more transmembrane helices containing six histidines needed for cofactor binding;
- the catalytic reaction occurs within subunit I at the binuclear active site composed a high-spin heme ligated by one conserved histidine and non-heme metal Cu or Fe;
- within the main subunit there is a low-spin heme ligated by two conserved histidines to transfer electrons from the electron donor cytochrome *c* or quinol.

*A-type oxidase.* Terminal oxidases of the A-type HCOs are well studied and present in many domains of life, eukaryotes and procaryotes. They are expressed at high levels of oxygen and therefore have a low affinity to oxygen ( $K_m$  in a  $\mu\text{M}$  level of concentrations) <sup>81</sup>. The proteins assigned to the A-type oxidases utilize two proton pathways, D and K, leading to the active site have been identified. They are named after the conserved key residues Asp124 and Lys354 (*P. denitrificans* numbering) at the entrance and seem to have different roles in the catalytic cycle. It was found that the D-pathway is involved into the transfer of chemical protons during the oxidative phase, stepwise reduction of oxygen to water, and proton pumping. The K-pathway is associated with the delivery of one or two chemical protons to the active site during the reductive phase, when the active site cofactors are re-reduced <sup>82</sup>.

Looking at the structures of the bovine enzyme <sup>64,83</sup>, *aa<sub>3</sub>* oxidase from *P. denitrificans* <sup>67</sup>, and cytochrome *bo<sub>3</sub>* from *E. coli* <sup>68</sup>, they all consist of at least two main subunits, that were shown to be essential to yield a functional proton pump <sup>82</sup>. In *aa<sub>3</sub>* oxidases the electrons are transferred through the Cu<sub>A</sub> center (subunit II) to the heme *a* and finally to the bimetallic active heme *a<sub>3</sub>*/Cu<sub>B</sub> (subunit I). In *bo<sub>3</sub>* oxidases all the redox cofactors are placed in the subunit I and the Cu<sub>A</sub> center is absent. Nevertheless, both types belong to the A<sub>1</sub> class, determined by the presence of the highly conserved glutamic acid residue at the end of the D-pathway. The *caa<sub>3</sub>* oxidase belongs to the A<sub>2</sub> class, that has a Tyr-Ser couple that is able to transfer protons at the end of D-channel.

*B-type oxidase.* The oxidases of the B-type are most common among archaea bacteria and they use either cytochrome *c* (B<sub>1</sub>, B<sub>2</sub>, B<sub>5</sub> subclass) or quinol as the electron donor (B<sub>3</sub>, B<sub>4</sub> subclass) <sup>63</sup>. These enzymes exhibit a higher affinity for O<sub>2</sub> ( $K_m$  at the nanomolar range) <sup>81</sup>, and they are often stable at high temperatures up to 80 °C and expressed under a low oxygen tension giving the respiratory flexibility for bacteria. The most well characterized representative of this class in the cytochrome *ba<sub>3</sub>* oxidase from *T. thermophilus* <sup>72</sup>. There are two main subunits,

where all cofactors reside. Likewise the A-type oxidases, the primary electron acceptor Cu<sub>A</sub> is situated in the subunit II, and then electrons are transferred to the low-spin heme *b* and finally to the binuclear center heme *a*<sub>3</sub>/Cu<sub>B</sub> in the subunit I. The B<sub>3</sub> subfamily oxidases like cytochrome *aa*<sub>3</sub> from *A. ambivalens* lacks the Cu<sub>A</sub> and heme *c* binding motive so it uses the quinol (caldariella quinol) and the electron donor, as well as B<sub>4</sub> subfamily from *Sulfolobus acidocaldarius*<sup>73, 63</sup>. Also, the B-type enzymes show a lower pumping stoichiometry (3 protons per O<sub>2</sub> molecule) and only one proton channel (the homologue of the K-proton channel).

*C-type oxidase.* Cytochrome *cbb*<sub>3</sub> oxidase, that are found in many bacterial organisms belong to the C-type family. They possess a very high affinity to O<sub>2</sub> (K<sub>m</sub> in nM range)<sup>84</sup>, so that allows many pathogenic bacteria to invade host organism under limited access to oxygen<sup>85</sup>. Interestingly, this type of oxidases also exhibits a NO reductase activity<sup>85</sup>. The structure of the most studied *cbb*<sub>3</sub> oxidase from *Pseudomonas stutzeri* is composed of four subunits: the catalytic CcoN subunit, the two cytochrome *c* subunits (CcoO and CcoP) involved in electron transfer, and the small CcoQ subunit with an unclear function. The electron chain starts at the cytochromes *c* and then electrons are transferred to the low-spin heme *b* and finally to the binuclear center heme *b*<sub>3</sub>/Cu<sub>B</sub>. As for the B-type oxidases, only one pseudo-K pathway is involved into proton pumping.

### 1.3.2 The family of NOR oxidases

The HCO superfamily also includes the nitric oxide reductases (NOR), of which the cNOR (cytochrome *c*-oxidizing) and qNOR (quinol-oxidizing) are the most well characterized. They are phylogenetically related to the C-family of O<sub>2</sub> reductases<sup>86</sup>. The most striking differences between HCOs and NORs is that in the latter Cu<sub>B</sub> is replaced by Fe<sub>B</sub> at the active site and that NORs do not pump protons. All NORs have at least two main subunits that resemble the CcoC and CcoN subunits of the C-type family (Fig. 1.3). Additionally, they contain Ca<sup>2+</sup> in the catalytic subunit that was suggested to participate in the correct positioning of the hemes for the electron transfer by coordination of Ca<sup>2+</sup> to the heme propionates<sup>87</sup>. It should be noted that as C-type oxidases show NO-reductase activity, NORs were reported to exhibit O<sub>2</sub>-reductase activity<sup>87</sup>.

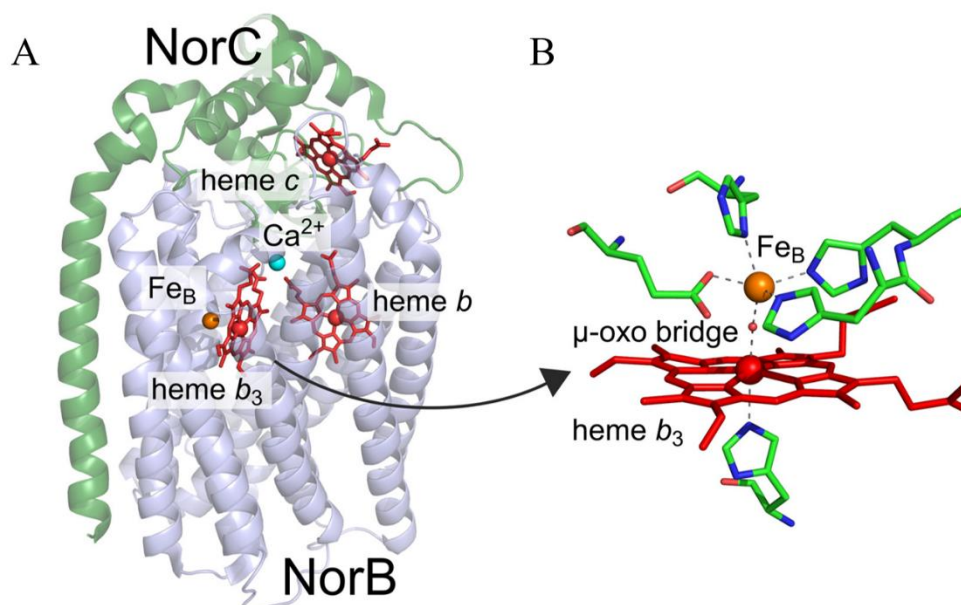
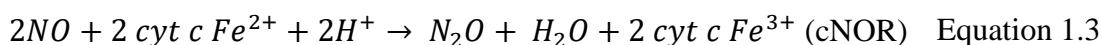


Figure 1.3. Crystal structure of cNOR (A) with the binuclear active site (B) from *P. aeruginosa* (PDB: 3OOR), composed of two subunits NorB (blue) and NorC (green) <sup>9</sup>.

The catalytic reduction of NO to N<sub>2</sub>O can be described as follows:



The isolated and well-characterized cNOR from *P. aeruginosa* includes the large NorB subunit of 12 transmembrane (TM) helices and the smaller NorC, which holds one TM and soluble domain in periplasm. The catalytic center housed in the NorB subunit is composed of the high-spin heme *b*<sub>3</sub> ligated by one His and the non-heme Fe<sub>B</sub> coordinated by three His and one Glu (Fig. 1.3B). There are evidences that the heme *b*<sub>3</sub> and non-heme Fe<sub>B</sub> are connected via a μ-oxo bridge within a 3.8 Å Fe-Fe distance <sup>87,88</sup>. Yet the exact mechanism of NO reduction at the bimetallic site and role of the non-heme Fe<sub>B</sub> in the catalytic cycle is still under debate <sup>7,89–91</sup>. The three possible mechanisms of the NO reaction in cNOR will be discussed in more details in the chapter 1.4.2. The electrons are transferred from the cyt *c* to the heme *c* (*E*<sub>m</sub> = 310 mV), then heme *b* (*E*<sub>m</sub> = 345 mV), and finally to the heme *b*<sub>3</sub> (*E*<sub>m</sub> = 60 mV) and non-heme Fe<sub>B</sub> (*E*<sub>m</sub> = 320 mV) <sup>89,92</sup>. The redox potential of the catalytic heme *b*<sub>3</sub> is much lower than the one of HCOs, so that it was suggested that this thermodynamic barrier is required in NORs to prevent formation of the Fe<sup>3+</sup>-NO species that could inhibit catalysis <sup>89</sup>.

The obvious structural similarities within the HCOs superfamily resulted in various evolution theories. The most probable scenario suggests that the A-type oxidases evolved the last because they include the most functionally sophisticated enzymes and expanded to all three

forms of life. It was proposed that NORs were present first followed by C-type oxidases, which in turn resulted in the B-type<sup>93</sup>.

### 1.3.3 Superfamily of cytochrome *bd* oxidases: structural diversity and mechanism

The family of cytochrome *bd* oxidases is not evolutionally related to the HCOs and to this date these enzymes were found only in the cells of prokaryotes. They catalyse reduction of molecular oxygen to water at the expense of the oxidation of specific quinols such as ubiquinol or menaquinol. Unlike HCOs, *bd* oxidases generate a proton motive force without pumping protons<sup>94</sup>: protons for oxygen reduction are taken up from cytoplasmic side of the membrane, while the protons generated from quinol oxidation are released to the periplasmic side. Missing proton pumping machinery decreases the energetic efficiency of the *bd* oxidases, however, their functionality is not limited by cellular bioenergetics. A large body of evidence confirms that *bd*-type oxidases are involved in the bacterial virulence, adaptability and antibiotics resistance. It was shown that these enzymes play role in the bacterial survival in adverse environmental conditions induced by nitric oxide<sup>95–98</sup>, ammonia<sup>99</sup>, nitrite<sup>100,101</sup>, sulfide<sup>102–106</sup>, and cyanide<sup>107,108</sup>. These enzymes are also involved in bacterial resistance against the harmful reactive oxygen and nitrogen species generated by the host in order to eliminate microbial agents<sup>109, 110</sup>. Cytochrome *bd* is able to decompose hydrogen peroxide<sup>107,111,112</sup> and peroxynitrite<sup>113</sup>. Furthermore, cytochrome *bd* contribute to the bacterial protection against antibiotic-induced stress<sup>114–116</sup>. Since the *bd* enzyme is not expressed by the mammal cells, it appears to be an attractive and promising therapeutic target for development of new generation antibiotics.

*Bd* oxidases have a very high affinity for oxygen<sup>12,14</sup> and their expression is often associated with microoxic conditions. Most *bd* oxidases are made up of two core subunits CydA and CydB and one or two auxiliary subunits (CydX, CydH), depending on the species. All catalytically active cofactors, the low-spin heme *b*<sub>558</sub> and two high-spin hemes *b*<sub>595</sub> and *d*, are located in the CydA subunit, including the hydrophilic quinol-binding site, Q-loop<sup>4,78,79,117, 3,118</sup>. By now, all structurally characterized *bd* oxidases turned out to use quinol as the electron donor. The quinol-binding domain is located in the hydrophilic loop region between the TM helices 6 and 7. The first classification the cytochrome *bd* oxidases was based on the length of the Q-loop, resulting in two subfamilies: L (long Q-loop) and S (short Q-loop)<sup>119</sup>. However, the recent phylogenomic study of *bd* oxidase superfamily performed by Murali et al<sup>62</sup> suggests that there are *bd*-type oxidases that lack the Q-binding motif and use cytochrome *c* as the donor of electrons. The new classification proposed by Murali identifies three families, qOR, OR-C

and OR-N, and several subfamilies within *bd* oxidases that include the four TM helices and at least two heme cofactors in the structure.

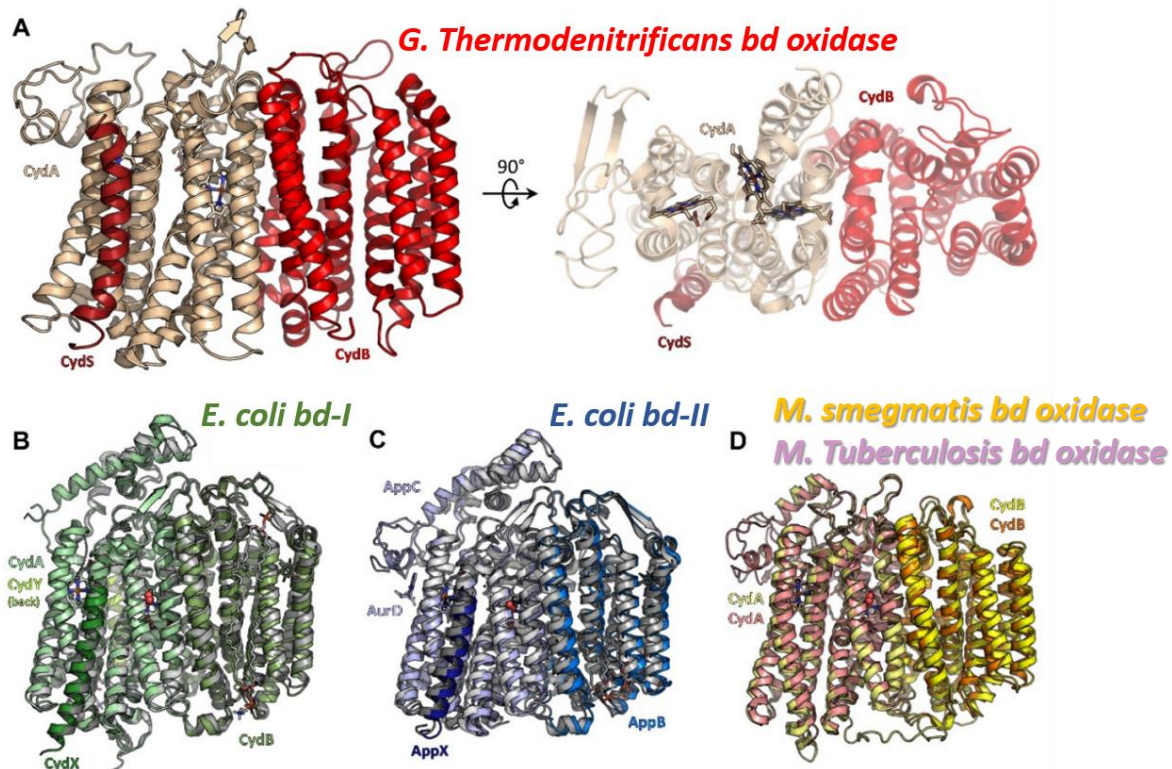


Figure 1.4. Structures of bacterial cytochrome *bd* oxidases: (A) *bd* oxidase of *G. thermodenitrificans* (pdb: 5DOQ) with subunit CydA (light beige), CydB (red), and CydS (dark red); (B) *E. coli* *bd-I* (pdb: 6RKO in green colours) with subunit CydA, CydB, CydX, and CydY; (C) *bd-II* oxidase from *E. coli* (pdb: 7OSE in blue colours, pdb: 7OY2 in grey tones) with subunit AppC (homologue to CydA), AppB (homologue to CydB), and AppX (homologous to CydS/X), 7OSE has been solved with the inhibitor aurachin D (AurD) bound to the Q-loop; (D) The mycobacterial *bd* oxidase (*M. smegmatis*, pdb: 7D5I, in yellow colours, *M. tuberculosis*, pdb: 7NKZ, in orange and salmon) with subunit CydA and CydB (reproduced from reference 56).

The first resolved structure of cyt *bd* was that of *Geobacillus thermodenitrificans* in 2016<sup>4</sup>. Intriguingly, after the release of the high-resolution cryo-EM structures of the *bd-I* (2019)<sup>3,118</sup> and *bd-II* (2021)<sup>78</sup> oxidases from *E. coli*, the heme cofactors have been found in an unexpected switched position. The recent release of two new structures of *bd* oxidases from *Mycobacterium smegmatis* and *Mycobacterium tuberculosis* (2021) revealed an even greater structural diversity in this enzyme family<sup>79,117</sup>.



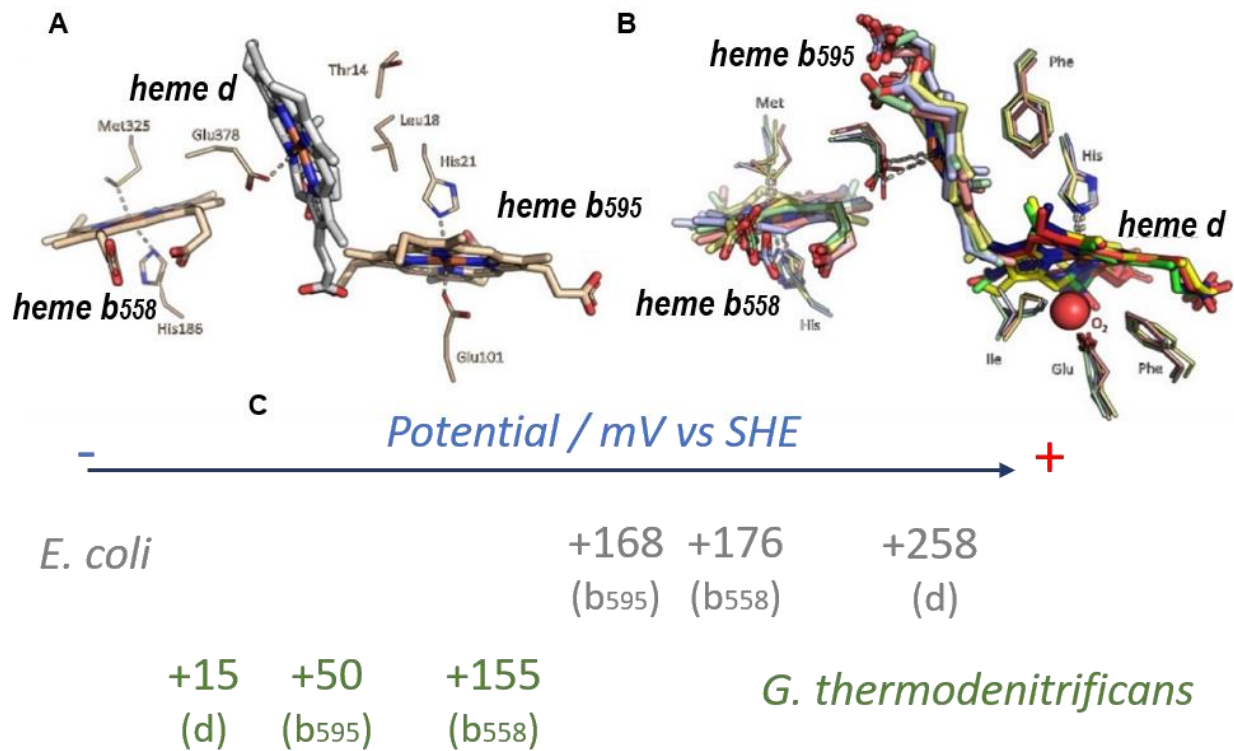


Figure 1. 5. (A) Triangular arrangement of the heme cofactors in *G. thermodenitrificans*: hemes *b*<sub>558</sub> and *b*<sub>595</sub> (light beige sticks), heme *d* (grey sticks). (B) The superposition of the active site in *E. coli* *bd*-I (green sticks), *E. coli* *bd*-II (blue sticks), *bd* from *M. smegmatis* (yellow sticks), and *bd* from *M. tuberculosis* (red sticks). Molecular oxygen shown in red spheres, reproduced from reference 56). (C) Redox potentials obtained from spectro-electrochemical titrations of *cyt bd* from *E. coli* and *G. thermodenitrificans* at pH 7 (vs SHE).

Despite the common architecture of the core subunits within cytochrome *bd* oxidase family, the heme cofactors triangular arrangement in the CydA subunits and, therefore, the catalytic mechanism varies. The low-spin heme *b*<sub>558</sub>, the cofactor that gets electrons from the quinol oxidation, is always placed closest to the Q-binding site and its axial ligands, His and Met are highly conserved, while the high-spin hemes *b*<sub>595</sub> and *d* location varies depending on the bacteria. In *G. thermodenitrificans* heme *b*<sub>595</sub> with axial ligands His21 and Glu101 residues, is placed in plane axis with *b*<sub>558</sub> and orthogonally to the heme *d* (Fig. 1.5A). Here the heme *d*, positioned closely to the protein-membrane interface is the active site with a suitable cavity formed by a Thr14 and a Leu18 residue for oxygen access from the membrane.

In the *E. coli* *bd*-I and *bd*-II oxidases and in mycobacterial *bds* the positions of heme *b*<sub>595</sub> and *d* are interchanged (Fig.1.5B). Heme *b*<sub>558</sub> is separated from the high-spin hemes by the totally conserved Trp441 (*E. coli* numbering) that may mediate electron transfer. The heme *b*<sub>595</sub> is located near the periplasmic side and it is ligated to Glu445. The heme *d* is located near the interface of CydB with the axial ligand His19, while on the opposite side of the heme the strong

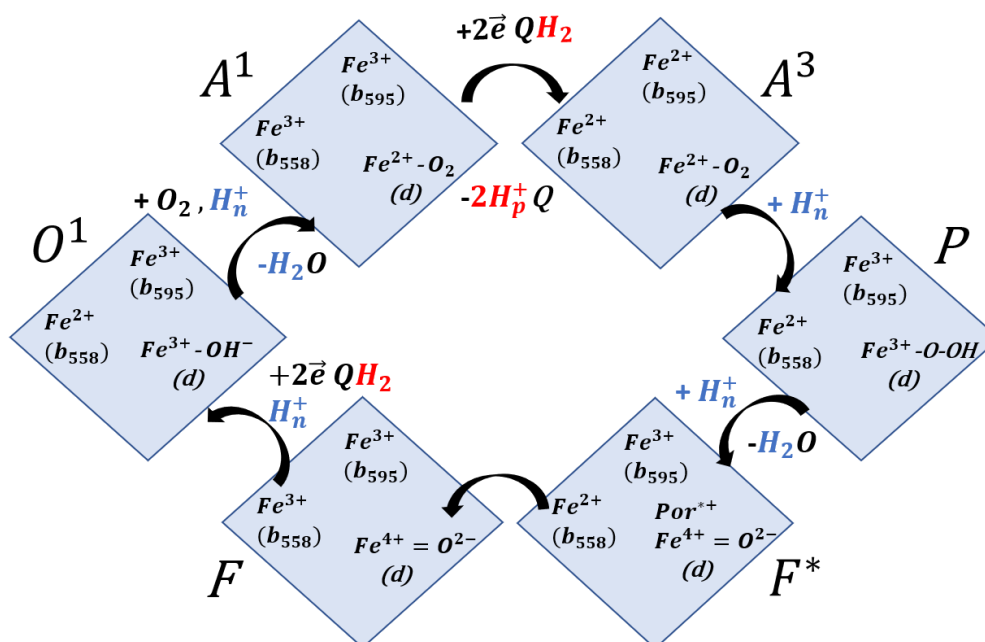
non-peptide density was assigned to oxygen. The voluminous cavity formed by hydrophobic isoleucine and phenylalanine residues close to heme *d* was found suitable for the binding of oxygen. The glutamate residue Glu99 which is located in coordinating distance to the central Fe atom completes the oxygen binding site. The exchanged position of the high-spin hemes in *bd* *G. thermodenitrificans* and *E. coli* are in line with the mid-point potentials determined by the redox titration (Fig. 1.5C) <sup>120</sup>. In *E. coli* heme *d* has the highest  $E_m$  value of all hemes (258 mV, pH 7, SHE), so that electrons flow from the quinol to heme *b*<sub>558</sub>, then to heme *b*<sub>595</sub> and finally to the *d*-heme center where oxygen is reduced. In *G. thermodenitrificans* a significantly lowest potential is observed (15 mV, pH 7, SHE), which would not allow an efficient electron transfer which might explain the low turnover rates <sup>121</sup>.

The quinol binding and oxidation occurs at the interface of hydrophilic Q-loop. The N-terminal part of this domain is highly flexible for the fast and transient binding of the quinol substrate. The only structure of a *bd* oxidase with a resolved Q-loop is from *E. coli* *bd*-II oxidase obtained with a bound Q-site inhibitor, Aurachin D <sup>78</sup>. Additionally, it can be used for the development of the inhibitors by addressing the protein surface features. It was shown that the Q-loop contains a conserved Glu and Lys residue that participate in the binding and oxidation of the quinol <sup>122, 123</sup>. In the structure of *E. coli* a bound ubiquinone-8 (for *bd*-I) and dimethylmenaquinone-8 (for *bd*-II) were found connecting the two main subunits <sup>78</sup>. In CydB/AppB subunit the bound quinone position corresponds to the heme groups in CydA/AppC. These large subunits have a similar structure, so that bound quinone probably is required to stabilize the integrity of the enzyme. Mycobacterial *bds* do not have bound quinone in subunit CydB, they utilize aromatic side chains instead to fill the equivalent positions of the heme groups.

The catalytic cycle of *bd*-I oxidase from *E. coli* is based on extensive studies of the reaction intermediates <sup>110,124,125,126</sup>, it is summarized in Scheme 1.1. The catalytic reaction would be next:



The catalytic reduction of molecular oxygen coupled with the 2 electrons donated from the quinol oxidation involves the intermediates termed O<sup>1</sup> (fully oxidized state), A<sup>1</sup> and A<sup>3</sup> (dioxygen bound state), P (peroxy state), F\*, F.



Scheme 1.1. The proposed catalytic cycle of the *bd-I* oxidase of *E. coli*, protons translocated to the positive and negative side of membrane are shown in red and blue, respectively.

During the O<sup>1</sup> → A<sup>1</sup> transition, one electron is transferred from heme b<sub>558</sub> to heme d, which binds O<sub>2</sub> in reduced state. Then, in the A<sup>1</sup> → A<sup>3</sup> transition, two electrons from a quinol molecule reduce heme b<sub>558</sub> and heme b<sub>595</sub>. A true transient peroxy complex of ferric heme d is formed during transition A<sup>3</sup> → P associated with oxidation of heme b<sub>595</sub>. In the next transition P → F\* the O–O bond cleavage occurs when the ferric heme d is further oxidized to the ferryl form with a porphyrin π-cation radical (Por<sup>•+</sup>). In the F\* → F transition, the radical is quenched by an electron from the ferrous heme b<sub>558</sub>. Finally, in the F → O<sup>1</sup> transition two electrons from a second quinol molecule reduce the ferryl heme d (to the ferric form) and heme b<sub>558</sub>. The P/F\* → F and F → O<sup>1</sup> were reported to be electrogenic<sup>94,127–129</sup>.

#### 1.4 The state of art: role of nitric oxide in pathogen virulence

Nitric oxide is a gas and a free radical which is known to have many important physiological roles. NO is one of the endogenous gaseous signaling molecules along with H<sub>2</sub>S and CO. Because of their small size and slight polarity, they can travel through aqueous and hydrophobic environments, and interact with diverse cellular targets. In biologic systems, NO is synthesised enzymatically from the amino acid L-arginine in a number of tissues using the three isoforms of nitric oxide synthase and it is the end product of different microbial metabolic pathways<sup>130</sup>. NO is recognised as a neurotransmitter and it is important in the endothelium-dependent regulation of blood flow and pressure<sup>131</sup>. Along with other free radicals, NO is also

important in the primary defence mechanisms of the host organism against attacks by microorganisms<sup>132</sup>. NO has a close interaction with iron-containing proteins and binds to the heme cofactors, which results in different protein modifications. This mechanism of NO binding with enzymes is even more evident in many inflammatory disorders and it can give information on the modes of action of the pathogen bacteria containing heme proteins<sup>131</sup>.

#### 1.4.1 Denitrification chain of bacteria

The transformation of the toxic NO into N<sub>2</sub>O is part of the Nitrogen cycle and it involves bacterial cells that can respire on nitrate and generate N<sub>2</sub> which is then released to atmosphere. In this bioenergetic process, the nitrate and nitrite and the gaseous N-oxides (NO and N<sub>2</sub>O) serve as a terminal acceptor of electrons instead of the molecular oxygen<sup>133</sup>. This is achieved by the denitrifying bacteria that express additional respiratory enzymes that replace some components of the mitochondrial respiratory chain. The overall denitrification of nitrate to molecular nitrogen is catalyzed by nitrate reductase (NAR), nitrite reductase (NIR), nitric oxide reductase (NOR) and nitrous oxide reductase (N<sub>2</sub>OR) (Fig. 1.6). The quinol pool is used as a source of electrons by NAR in the membrane, the NADH dehydrogenase and the cytochrome *bc*<sub>1</sub> are maintained as a complex I and complex III, respectively. Reduced water-soluble cytochrome *c* in the periplasm is the electron donor for NIR, NOR and N<sub>2</sub>OR. Nitrate and nitrite are shuttled over the membrane by the nitrate/nitrite antiporter (AP). The NO reduction to N<sub>2</sub>O catalyzed by NOR is a key process in the denitrification.

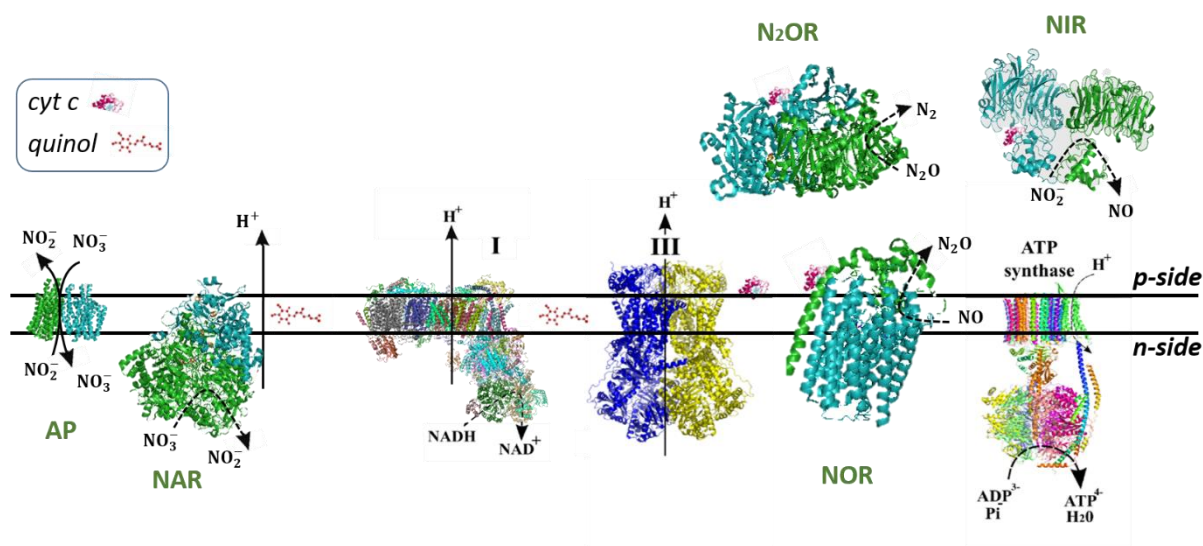


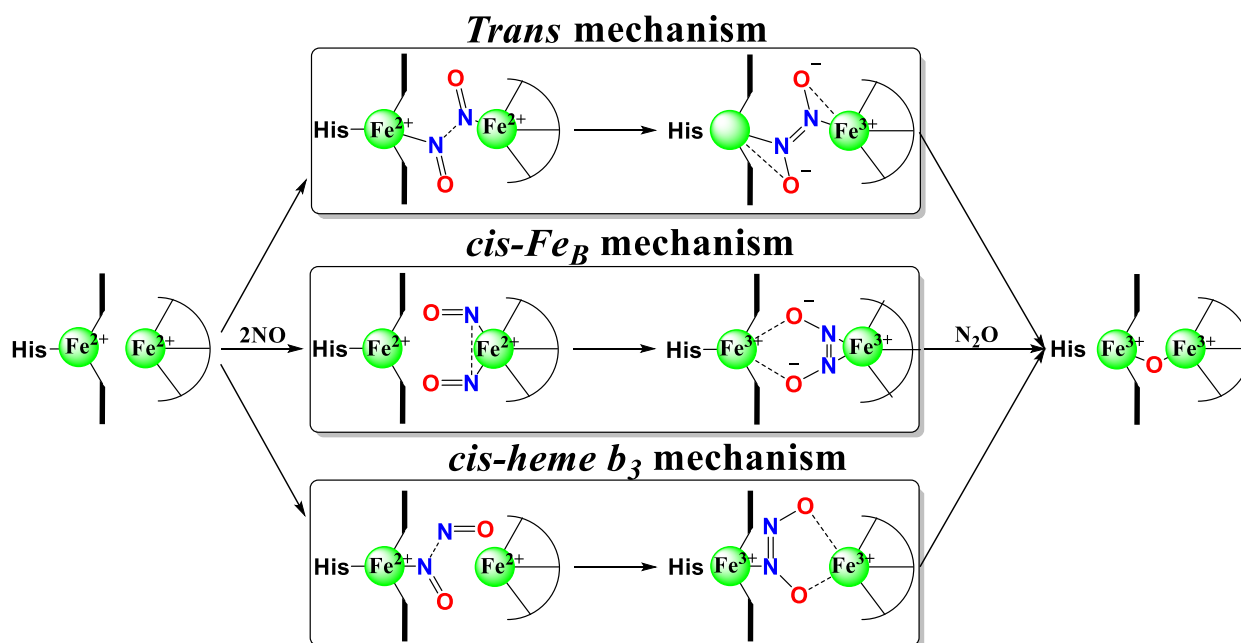
Figure 1.6. The denitrification chain in *Paracoccus denitrificans*. Denitrification-specific enzymes are in green and blue colors: AP (PDB: 4U4W), NAR (PDB: 1R27), NOR (PDB: 5GUW), N<sub>2</sub>OR (PDB: 1FWX), NIR (PDB: 1AOF) whereas enzymes also involved in aerobic respiration complex I (PDB: 4WZ7), complex III (PDB: 2A06) and ATP synthase (PDB: 5LQY) are shown in different colors.

### 1.4.2 Mechanism of NO binding with different oxidases

Recent biochemical studies highlighted the bioenergetic importance of NO as an electron acceptor in anaerobic environments. It is reported that not only NORs from respiratory chain of denitrifying bacteria but also some heme-copper oxidases and *bd* oxidases are able to bind nitric oxide<sup>134–137</sup>. The scope of NO functionality within respiratory enzymes has increased the awareness about the bacterial mechanisms to cope with NO in the pathogen–host interactions<sup>86</sup>.

#### *NO binding mechanism in cNOR*

Overall, the catalytic reduction of nitric oxide at the binuclear center of cNOR has four stages: the initial binding of two NO molecules to the diiron active site, the formation of an N–N bond yielding the hyponitrite intermediate, the cleavage of an N–O bond and the release of N<sub>2</sub>O. For the first two stages three possible mechanisms have been proposed (Scheme 1.2).



Scheme 1.2 The three pathways of NO binding at the catalytic site of cNOR<sup>138</sup>.

**The trans-mechanism** requires binding of two NO molecule to each cofactor, heme *b*<sub>3</sub> and Fe<sub>B</sub>, via the nitrogen atom to form an iron–nitrosyl dimer [{FeNO}]<sub>2</sub> intermediate<sup>86,139,140</sup>. The close proximity of the two metal–nitrosyl species promotes N–N bond formation either via an electrophilic attack by one nitrosyl at the nitrogen lone pair of the second nitrosyl, or via a radical coupling process, where the two nitrosyls combine to form a metal bound hyponitrite species (N<sub>2</sub>O<sub>2</sub><sup>2-</sup>). This model is supported by the rapid-freeze quench EPR experiments of the single turnover reactions in cNOR that allowed to trap a S = 1/2 low-spin heme {FeNO} and S

=3/2 non-heme {FeNO} species<sup>141</sup>. In the study with myoglobin favoring the trans-mechanism an engineered binuclear metal site similar to that in NOR a dinitrosyl intermediate was also characterized<sup>142</sup>. However, the computer calculations based on hybrid density functional theory contradict the trans-mechanism, showing that binding of a second NO molecule to Fe<sub>B</sub> would result in an intermediate too high in energy to be formed<sup>90</sup>.

**The cis:Fe<sub>B</sub> mechanism** suggests that both NO molecules form a cis-hyponitrite at the non-heme Fe<sub>B</sub> center<sup>143</sup>. It is similar to the finding of two NO molecules on the the Cu<sub>B</sub> cofactor of the *bo*<sub>3</sub> oxidase<sup>144</sup>. In this model the heme *b*<sub>3</sub> would be responsible only for the electron transfer and participation in the N–O bond cleavage in the next stages. It is strongly supported by the group of Thomson because of the very low redox potential observed for heme *b*<sub>3</sub> ( $E_m = 60$  mV) that was required to keep the cofactor oxidized while NO binds to Fe<sub>B</sub><sup>89</sup>. In addition, this mechanism does not involve the formation of {FeNO}<sub>3</sub> species, which were seen as a potential dead-end product<sup>89</sup>.

**The cis:heme *b*<sub>3</sub> mechanism** proposes that the heme *b*<sub>3</sub> binds a first molecule of NO resulting in {FeNO} species and then reacts with a second NO. The lone electron pair of the metal-bound nitrosyl is the target of an electrophilic attack by a free NO to generate a hyponitrite radical at the heme *b*<sub>3</sub>, supported by computational analysis<sup>145</sup>. The cis:heme *b*<sub>3</sub> mechanism has been suggested for the NO reductase activity in terminal oxidases where a heme {FeNO} species accumulates in pseudo-steady state conditions<sup>146</sup>. The calculated energy profile for a cis:heme *b*<sub>3</sub> mechanism shows that NO reduction and N<sub>2</sub>O formation are highly exergonic steps in cNOR catalysis and therefore re-reduction of the oxidized binuclear center must be endergonic, which is consistent with the low reduction potential of heme *b*<sub>3</sub> and means that the re-reduction phase is rate-limiting during turnover<sup>145</sup>.

Besides the catalytic reduction of the NO by NORs, a large body of evidence showed the substrate inhibition at NO concentrations higher than 10 μM, but the mechanism remains unclear<sup>17,54,147,148</sup>. It was proposed to occur most likely due to binding of NO to the ferric heme *b*<sub>3</sub><sup>147</sup>.

### ***NO binding to the HCO***

Some heme-copper oxidases show a NO reductase activity but much less efficient than NORs. Giuffrè et al. has shown that cytochromes *ba*<sub>3</sub> and *caa*<sub>3</sub> HCOs from *Thermus thermophilus* display a low but measurable NO reductase activity<sup>135</sup>. In this study a gas chromatography experiment with *ba*<sub>3</sub> oxidase in the anaerobic conditions detected N<sub>2</sub>O as the end product of

the NO decay. A NO reductase activity under reducing anaerobic conditions was reported for the purified mycobacterial *bcc-aa<sub>3</sub>* complex of up to 10  $\mu\text{M}$  of nitric oxide <sup>149</sup>. In the figure 1.7 NO-consuming activity is demonstrated for this complex by the fast drop in NO concentration after introduction of the enzyme at about 8  $\mu\text{M}$ . A similar activity was seen for the *bo<sub>3</sub>* oxidase from *E. coli* <sup>150</sup>, the *cbb<sub>3</sub>* oxidase from *P. stutzeri* <sup>134</sup> and *R. sphaeroides* <sup>53</sup>. As the *cbb<sub>3</sub>*-type oxidases share close phylogenetic relationship with NORs, it is not surprising that the cytochrome *cbb<sub>3</sub>* purified from *P. stutzeri* display a significant NO reductase activity ( $K_m = 12 \mu\text{M}$ ) <sup>134</sup> which, although considerably lower than that typical of NOR, is much higher than that of the *ba<sub>3</sub>*-type oxidase from *T. thermophilus*. It should be noted that mitochondrial bovine heart cytochrome c oxidase does not catalyze the anaerobic degradation of NO <sup>151</sup>. It can be seen that the NO reductase activity of the HCOs is not high, so it is not expected to contribute greatly to the defense mechanism against nitrosative stress.

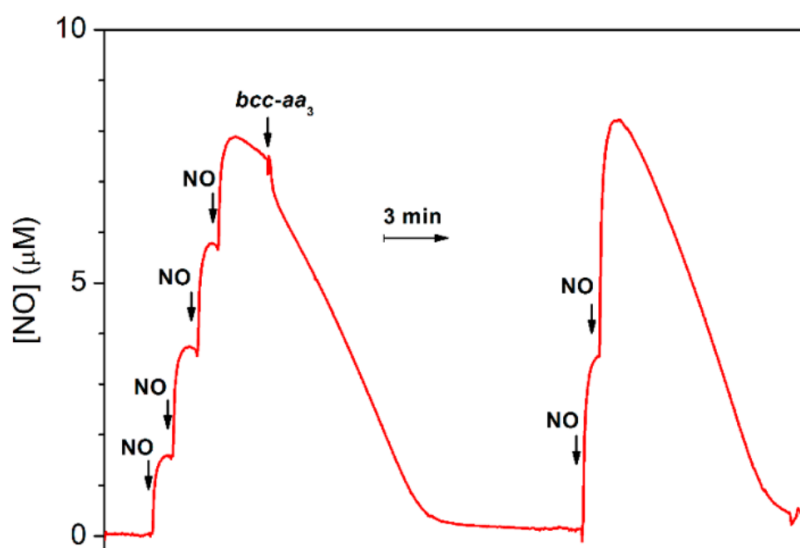


Figure 1.7. NO reductase activity of purified mycobacterial cytochrome *bcc-aa<sub>3</sub>* supercomplex. Four aliquots of 2.1  $\mu\text{M}$  NO (1.8  $\mu\text{L}$  of 1.8 mM NO each) were sequentially added to degassed buffer containing dithiothreitol (5 mM), MD menadione (0.26 mM) as the reducing system, and glucose (5 mM) and glucose oxidase (16 units/mL) to scavenge residual  $\text{O}_2$  in the 1.5-mL reaction chamber, where pre-reduced cytochrome *bcc-aa<sub>3</sub>* (200 nM) was added. Reproduced from reference <sup>149</sup>.

To this date, a few examples of the HCOs described above showed NO reductase activity in anaerobic conditions, while from extensive studies it was reported that with most oxidases NO acts as an inhibitor <sup>126,152</sup>. If the concentration of NO is low, in the nanomolar level, it reversibly inhibits enzyme oxygen reductase activity <sup>153</sup>, but at high micromolar concentrations, an irreversible increase of the  $K_m$  for oxygen is seen causing a damage to the enzyme <sup>154</sup>. At low reductive pressure (low turnover conditions) and high  $\text{O}_2$  tensions, the non-

competitive inhibition occurs. In this case NO reacts with enzyme species containing fully oxidized heme  $a_3/Cu_B$  or ferryl heme  $a_3$  leading to the nitrite-bound enzyme<sup>137,152,155,156</sup>. When the reductive pressure is high (high turnover conditions) and  $O_2$  tension is low, the  $O_2$  competitive inhibition prevails through the NO binding to the 2-electron reduced high-spin heme in the binuclear center resulting in production of the nitrosyl derivative of the enzyme<sup>153,157</sup>.

### ***NO binding to bd oxidases***

Unlike the HCOs, cytochrome *bd* oxidases do not show any measurable NO reductase activity under anaerobic conditions<sup>96</sup>. However, like most HCOs isolated *bd* oxidases from *E. coli* and *A. vinelandii* are rapidly and reversibly inhibited by nitric oxide with a half-inhibitory concentration ( $IC_{50}$ ) of about 100 nM at 70  $\mu M$   $O_2$ <sup>95</sup>. *E. coli* expresses cyt *bo*<sub>3</sub> heme-copper oxidase, and two cyt *bd* oxidase. A reversible inhibition was also demonstrated on the *E. coli* cells lacking cyt *bo*<sub>3</sub><sup>98,158</sup>. Interestingly, when one compares the profiles of the bovine cytochrome c oxidase and *bd* oxidase from *E. coli* activity recovery after the NO inhibition, it can be seen that *bd* recovers significantly faster (Fig. 1.8). The kinetics of oxygen consumption was measured for both enzymes upon addition of NO followed by the depletion of all unbound substrate by NO-scavenger oxyhemoglobin ( $HbO_2$ )<sup>159</sup>. It was also shown that *bd* oxidase deletion from a multi-drug resistant uropathogenic *E. coli*, impairs the survival of the bacteria in a mouse urinal tract and suggests that the *bd* oxidase-supported respiration under nitrosative stress is a key for host colonization at low  $O_2$  tensions<sup>160</sup>. The NO tolerance role of this unique enzyme also agrees with the expression of *bd* oxidase in *E. coli*<sup>161–163</sup>, *S. Typhimurium*<sup>164</sup>, *Staphylococcus aureus*<sup>165</sup>, *M. tuberculosis*<sup>166</sup>, and *Bacillus subtilis*<sup>167</sup> under NO stress. These evidences accumulate around the fact that the cytochrome *bd* expression could be part of a bacterial protection mechanism to evade the host immune attack.



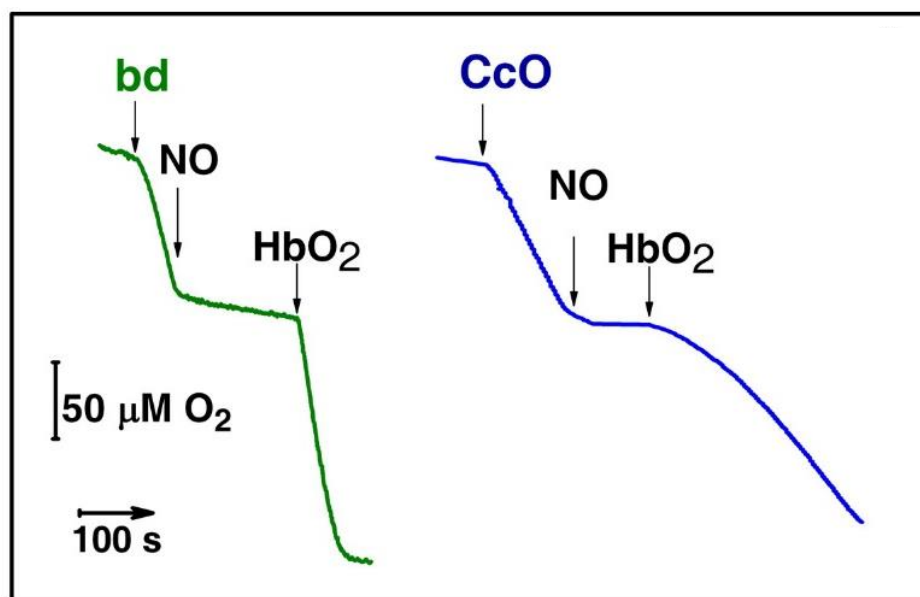
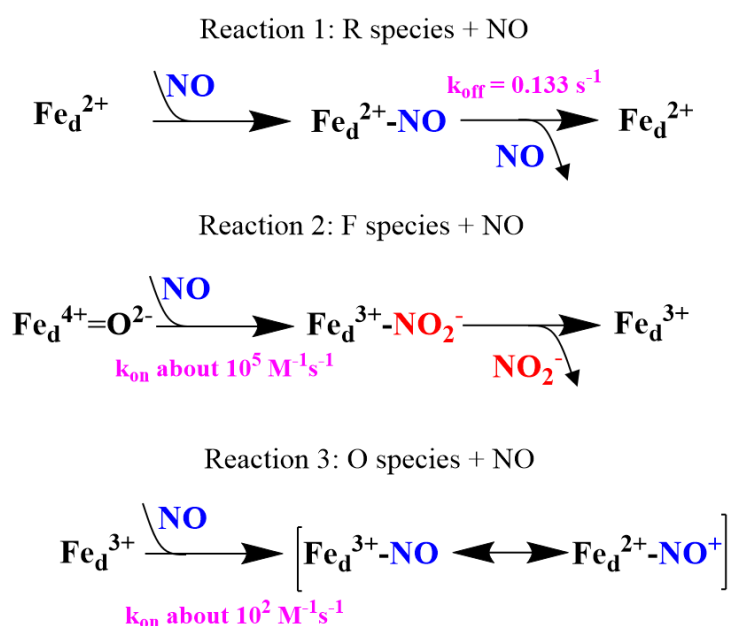


Figure 1.8. Oxygraphic traces showing NO inhibition of *E. coli* cytochrome *bd*-I and bovine CcO, and activity recovery after addition of oxy-haemoglobin (HbO<sub>2</sub>) to scavenge free NO, reproduced from reference <sup>159</sup>

In-depth understanding of the molecular mechanism of rapid activity recovery of *bd* oxidase after the NO inhibition will shed light on the role of these enzymes in the bacterial protection upon NO-induced stress. The extensive studies of Borisov group (<sup>95,96,149,159,168</sup>) point towards three possible pathways of NO binding to the high-spin heme *d* in the ferrous, ferryl, and ferric state (Scheme 1.3). In the case of the fully reduced heme *d* (R species) nitric oxide binds immediately and the rate of NO binding is expected to be ( $k_{on}$ ) at the same level as for the binding of O<sub>2</sub> to the fully reduced enzyme, i.e., in the range of  $10^8$  to  $10^9$  M<sup>-1</sup>·s<sup>-1</sup> <sup>169</sup>. As a result, the nitrosyl ferrous heme *d* Fe<sup>2+</sup>-NO adduct is formed (Scheme 1.3, reaction 1) which is confirmed by the shift of the Q-band from 630 to 641 nm in UV-Vis spectroscopy <sup>95,169</sup>. The experimental data showed that the rate of NO dissociation from ferrous heme ( $k_{off}$ ) in the purified fully reduced cyt *bd*-I of *E. coli* is unusually high,  $0.133$  s<sup>-1</sup> <sup>170</sup>, which is comparable with the value ( $0.163$  s<sup>-1</sup>) obtained for membrane preparations of *E. coli* mutant strain devoid of cytochrome *bo*<sub>3</sub> <sup>98</sup>. This  $k_{off}$  value is about 30 times higher as compared to one reported for NO dissociation from ferrous heme *a*<sub>3</sub> in the mitochondrial cytochrome *c* oxidase <sup>171</sup>. Furthermore, such a high NO dissociation rate explains the much faster cyt *bd* activity recovery than for bovine *aa*<sub>3</sub> oxidase after NO-inhibition (Fig. 1.8). NO binding to the active site heme in the ferryl state (F species) reported for *bd* oxidase of *A. vinelandii* is fast ( $\sim 10^5$  M<sup>-1</sup>·s<sup>-1</sup>) and it is proposed to form a nitrite adduct bound at the ferric heme *d* (Scheme 1.3, reaction 2) <sup>172</sup>. Again, this value is approximately 10 times faster than for the mitochondrial

cytochrome *c* oxidase ( $\sim 10^4 \text{ M}^{-1}\cdot\text{s}^{-1}$ )<sup>156,173</sup>. Then, nitrite is dissociated from the heme  $d^{3+}$ , however, the off rate for this process was not determined. A similar mechanism with the rapid NO transformation into  $\text{NO}_2^-$  by cytochrome *bd* was proposed for the F intermediate, which is highly populated in turnover<sup>124</sup>, and may also contribute to the mechanisms of bacterial resistance to NO. The NO binding to the ferric heme *d* (O species) undergoes with  $k_{\text{on}}$  of about  $\sim 10^2 \text{ M}^{-1}\cdot\text{s}^{-1}$  producing of a nitrosyl adduct,  $d^{3+}\text{-NO}$  or  $d^{2+}\text{-NO}^+$  (Scheme 1.3, reaction 3)<sup>168</sup>. This reaction is rather slow and, therefore, it does not have a significant contribution to reversible NO inhibition. Overall, cytochrome *bd* oxidase is responsible for the bacterial NO resistance due to extraordinary high NO off-rate and the ability to rapidly convert NO into  $\text{NO}_2^-$  in turnover.



Scheme 1.3. Reaction pathway of NO with different cytochrome *bd* species<sup>126</sup>.

## 1.5 Inhibitors towards cytochrome *bd* oxidase for the perspective drug design

Peculiar properties of cytochrome *bd* oxidases in the bacterial protection under oxidative and nitrosative stress together with their role in the drug-resistance make these enzymes an excellent target for the drug discovery. *Bd* oxidases were found in many pathogens including the *E. coli* and *M. tuberculosis* that cause numerous life-threatening diseases. Despite accumulated knowledge on the catalytic cycle of these enzymes, the resolved structures were only recently published for the *E. coli* (2019, 2021) and mycobacteria (2021), that nowadays allow to search for new inhibitors with novel modes of actions, as there are not many selective inhibitors proposed against *bd* oxidases in literature.

The aurachins, isoprenoid quinoline alkaloids extracted from the myxobacteria (*Stigmatella aurantiaca*), resemble the scaffold of the quinones that donate electrons to the cytochrome *bd* oxidases (UQ and MK). The study on the isolated quinol oxidases *bo*<sub>3</sub> and *bd* of *E. coli* by Meunier et al.<sup>174</sup> showed the potent inhibition properties of the Aurachin C and D towards the quinol oxidation site. Interestingly, 214 nM of Aurachin C inhibited activity of both terminal oxidases by 90%, while the presence of 400 nM Aurachin D selectively inhibits only *bd* oxidase by 93%. The group of T. Friedrich has determined the apparent IC<sub>50</sub> of Aurachins C and D for isolated *bd*-I and *bd*-II oxidases of *E. coli* by the measurement of the duroquinol:O<sub>2</sub> oxidoreductase activity on the Clark electrode: 12 and 35 nM for *bd*-I<sup>3</sup> and 7.1 and 11.1 nM for *bd*-II<sup>78</sup>.

The development of selective inhibitors towards *bd* oxidases on the basis of the Aurachins scaffold was reported by Miyoshi et al.<sup>175</sup>. This study showed that the inhibition properties of the Aurachin C can be improved by the introduction of the methyl group in 3<sup>rd</sup> position of the 2-N-decyl and 2-N-undecyl derivatives towards both *bo*<sub>3</sub> and *bd* enzymes that are structurally unrelated. This effect was proposed to be due to the local steric effect that favours the hydrophobic interaction at the quinol-binding site. An increase in the chain length of the 3-alkyl tail decreased the inhibitory potency only in cytochrome *bo*<sub>3</sub> that points at the binding pocket for the alkyl chain of cytochrome *bd* that is significantly larger than that of cytochrome *bo*<sub>3</sub>. Therefore, the modification of the Aurachin C derivatives allowed to extract information of the binding site properties of terminal oxidases. The recent work of the Radloff et al. showed the effect of the structural modification of the Aurachin D on the inhibition activity towards *bo*<sub>3</sub>, *bd*-I and *bd*-II oxidases from *E. coli*<sup>175</sup>. The Aurachin derivatives with long (decyl or longer) and short (butyl to octyl) alkyl substituents were tested to investigate the effect of the alkyl chain length on the inhibition potency. Here, the heptyl AurD-type derivatives were found to be the most potent inhibitors in the nanomolar range with high inhibitory selectivity for cytochrome *bd*-I. The hit-to-lead approach was used in our scientific group, based on the electrochemical sensor with immobilized cyt *bd*-I oxidase for the screening of a library of different families of the quinol-like scaffold: quinones, naphthoquinones, quinolones, coumarins and flavonoids<sup>176</sup>. Through the hit-to-lead optimization the inhibition efficiency of the Aurachin D derivatives and effect of the length of the isoprenyl chain were evaluated and detailed in the Chapter III of this thesis.

The strong evidence of the cytochrome *bd*-type menaquinol oxidase contribution to the drug resistance in mycobacteria spurred the development of the novel antibiotics<sup>177,178</sup>. *M.*

*tuberculosis* has a branched respiratory chain that makes this pathogen the second leading killer after Covid-19<sup>179</sup>. Under aerobic conditions, the *bcc-aa3* supercomplex ensure bacterial respiration, while under low oxygen levels, cytochrome *bd* serves as terminal oxidase. The promising drug Q203 (telacebec) against the mycobacterial respiratory enzymes, that is already at the stage of clinical trials, targets the cytochrome *bcc*<sup>180</sup>. However, this compound is not efficient towards the *bd* oxidase that provides the alternative respiration route for the pathogenic mycobacteria, so that the search for selective inhibitor towards *bd* oxidase from *M. tuberculosis* for the combination with Q203 is a great challenge.

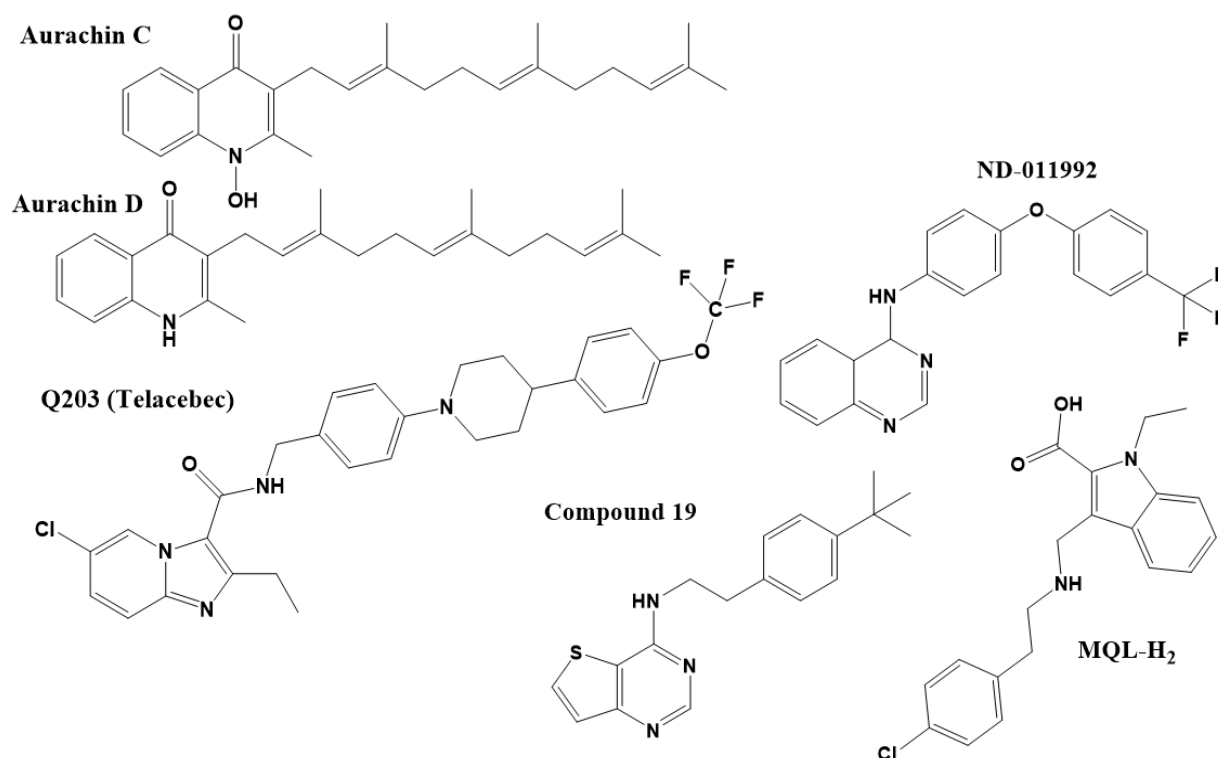


Figure 1.9. Structures of the potent inhibitors of the cytochrome *bd* oxidase activity.

The Aurachin D has also a strong effect on the *bd* oxidases from mycobacteria with  $IC_{50}$  of around 400 nM in inverted vesicles of *M. smegmatis*<sup>181</sup>. However, when applied alone it does not inhibit growth of mycobacteria, giving the minimal inhibitory concentrations (MICs) of more than 85  $\mu$ M and 100  $\mu$ M for the *M. smegmatis* and *M. tuberculosis*, respectively<sup>181,182</sup>. It was shown that the combination of Q203 with Aurachin D gives synergistic effect on the inhibition: the growth of *M. tuberculosis* is significantly reduced and MIC for Q203 decreases from 10 nM to 1.25 nM<sup>182</sup>. Another example of the combinatory effective inhibitor of the mycobacteria respiration and ATP synthesis was presented by Lee et al.<sup>183</sup>, where the small molecule ND-011992 together with Q203 was an effective tool against

replication and antibiotic tolerance of *M. tuberculosis* in-vitro. Although ND-011992 is ineffective on its own, this drug combination increased efficacy in a mouse model of tuberculosis infection. By the in-silico screening the novel inhibitor MQL-H<sub>2</sub> was identified that targets the menaquinol loop region and inhibits ATP synthesis in *M. smegmatis* inverted membrane vesicles with IC<sub>50</sub> of 34 μM<sup>184</sup>. A new class of potent inhibitors towards mycobacterial *bd* oxidase was discovered by Hopfner et al<sup>185</sup>. The presented thieno[3,2-d]pyrimidin-4-amines showed an IC<sub>50</sub> from 6 to 54 μM, as determined from the ATP depletion tested against *M. tuberculosis* strains in the presence of Q203. None of the compounds inhibit the ATP synthesis alone, that confirms that they inhibit specifically the *bd*-type oxidases. Among all the compounds tested, the compound 19 showed the highest inhibitory activity in the assay. All these findings are very promising for the development of new effective inhibitors of the *bd* oxidase, a unique bacterial respiratory enzyme.

## 1.6 Aims of the project

This PhD project is devoted to the study of the cytochrome *bd* oxidases reactivity with small molecules such as oxygen and nitric oxide and in the related enzymatic systems. There are several aims that will be covered in scope of this work:

**1. The optimization of the electrochemical assay based on *bd*-I oxidase from *E. coli* immobilized on the 3D gold nanoparticle electrode for the inhibition study.**

The previously developed bioelectrochemical sensor needs to be tuned to the nature of the studied enzyme by protein film voltammetry. It is adapted for the inhibition screening of Aurachin D derivatives for the discovery of new effective inhibitor hits that can serve as useful templates for further derivatization of compounds with potent antibiotic effect. The results have a global value to provide helpful data for the identification of new antibiotics with new modes of action.

**2. Comparison of the catalytic reaction of homologues *bd*-I and *bd*-II oxidases**

*E. coli* expresses two *bd*-type oxidases to ensure the respiration of pathogenic bacteria in the microoxic environments. The catalytic reduction of O<sub>2</sub> for *bd*-I and *bd*-II isoforms is studied by the spectroscopic and electrochemical methods in the relation with enzymes' structural differences. The role of the high spin heme *b*<sub>595</sub> in the catalytic cycle is also investigated through the characterization of the generated E455D and R448N variants of cytochrome *bd*-I oxidase.

**3. The nitric oxide reactivity of the cytochrome *bd* oxidases**

The role of the *bd* oxidases for the bacterial defense strategies under NO-induced stress is not clear. For this goal, the NO binding mechanism of *bd*-I and *bd*-II oxidases and mutated variants of these enzymes is compared. On the basis of a bioelectrochemical sensor, the inhibitory effect of nitric oxide on the enzyme electrocatalysis with oxygen is evaluated. The NO binding and release is investigated as a function of pH.

**4. The role of the Fe<sub>B</sub> in the catalytic mechanism of cNOR from *Paracoccus denitrificans***

There are three proposed catalytic pathways of the reduction of NO at the active site of cNOR composed of the high-spin heme *b*<sub>3</sub> and non-heme Fe<sub>B</sub>, however, the role of latter is still under debate. In order to understand better the role of Fe<sub>B</sub>, we have done a comparative study of the wild type and Fe<sub>B</sub> lacking variant reactivity with O<sub>2</sub> and NO





# Chapter II

## Techniques of analysis

---

### 2.1 Direct electrochemistry

- 2.1.1 The protein film voltammetry
- 2.1.2 Theories behind electron kinetics in proteins
- 2.1.3 Electron transfer mechanism of immobilized enzymes
- 2.1.4 Immobilization and signal enhancement strategies
- 2.1.5 Steady-state electrochemistry

### 2.2 Inhibition of protein activity as method of characterization

### 2.3 UV-Vis spectroscopy

- 2.3.1 Absorption spectroscopy for proteins
- 2.3.2 UV-Vis potentiometric titration

### 2.4 Infrared spectroscopy

- 2.4.1 IR spectroscopy of proteins: Amide I and Amide II region
- 2.4.2 FTIR differential spectroscopy coupled to electrochemistry

### 2.5 Raman spectroscopy of heme proteins





## 2.1 Direct electrochemistry

The voltammetry of adsorbed proteins started its development from 1970s when the direct electron transfer to enzymes was reported<sup>186,187,188</sup>. The catalytic properties and mechanism of the enzymatic reaction is largely studied by the electrochemical methods. The protein immobilized on the surface of the electrode can be used as a biosensor for direct electrochemistry. This gives many advantages as compared to other sensors such as a small quantity of sample used, short time of response, variation of the experimental conditions and several types of detection (amperometry, potentiometry, cyclic voltammetry, conductometry). However, there are requirements that should be maintained in order to obtain a good catalytic response of immobilized enzyme. Firstly, the protein films on the electrode surface should be sufficiently stable over the duration of the experiment. Secondly, an effective kinetics of interfacial electron transfer from the electrode surface to the active site of the enzyme should be provided. An extensive description of the redox mechanisms studied over the past years gives in idea of the reduction potentials in biological systems (Fig.2.1).

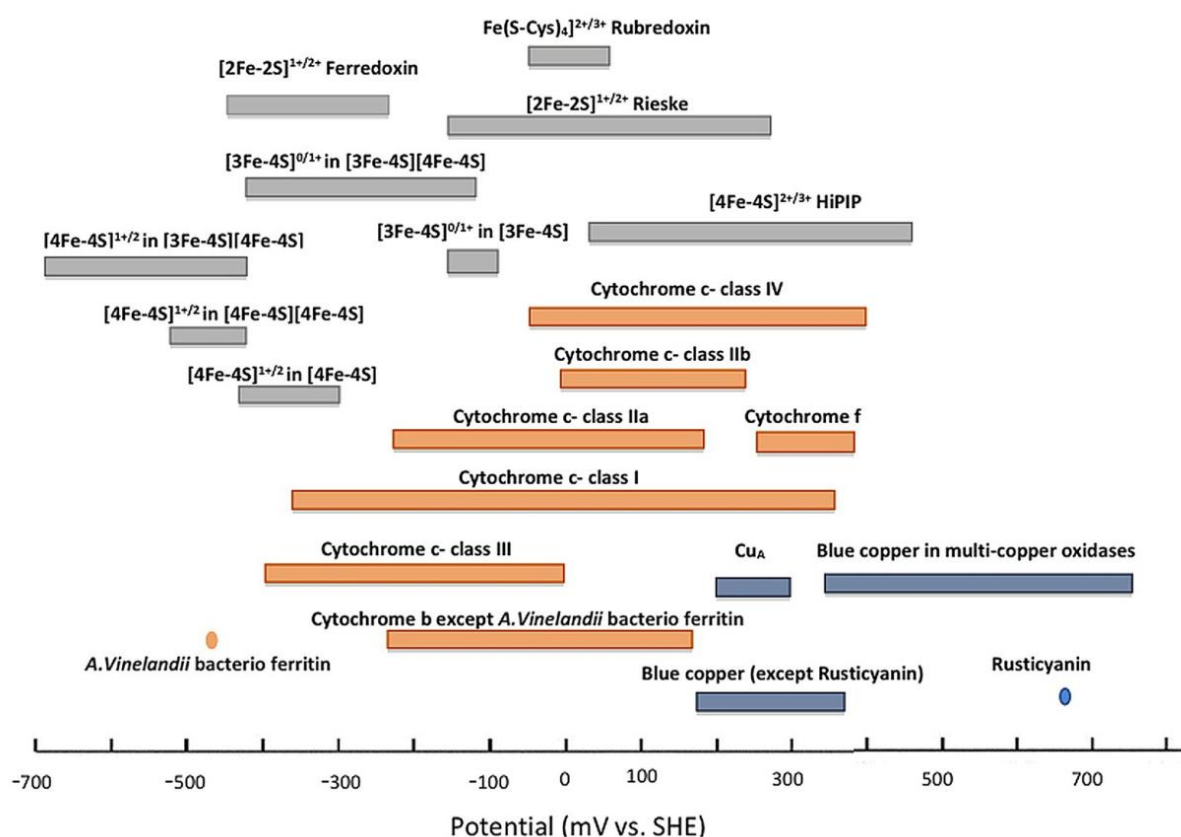


Figure 2.1. The biological redox scale at pH 7 (Reproduced from reference<sup>189</sup>).

The direct electrochemistry method has many advantages compared to protein voltammetry in solution:

- the redox state of the adsorbed protein is controlled better through the electrode potential compared with the species influenced by diffusion in solution;
- the sample economy, usually a few pmol needed for series of experiments;
- waveform gives information on reversibility, homogeneity (a Nernstian half-height width  $83/n$  mV at  $0^\circ\text{C}$ ) and coupled catalytic reactions;
- screening under varying conditions (pH, T, concentration of substrate or inhibitors) and by changing scan rate it is possible to study slow and fast catalytic reactions.

### 2.1.1 The protein film voltammetry

The protein film voltammetry (PFV) is the method of dynamic electrochemistry which means that experiments are carried out under non-equilibrium conditions: the applied potential differs from the equilibrium potential. In this case system is forced to move back to equilibrium by taking (giving) electrons from (to) the electrode. As a result, this reduction (oxidation) recorded as a current which proportional to the rate of the reaction (the amount of electric charge passing the electrode per unit time). When the redox active protein is adsorbed on the electrode surface, the diffusion does not have influence on the electrochemical system.

In PFV, the measured current is the sum of a Faradaic current  $i_f$  (which reveals the redox transformations of molecules that come sufficiently close to the electrode) and a capacitive current  $i_c$ , which does not involve the interfacial passage of electrons,

$$i = i_f + i_c = \frac{dQ_f}{dt} + \frac{dQ_c}{dt} = \frac{dQ_f}{dt} + C \cdot \frac{dE}{dt} \quad \text{Equation 2.1}$$

where  $C$  is the capacitance of the electrical double layer on electrode, which proportional to the electrode surface.

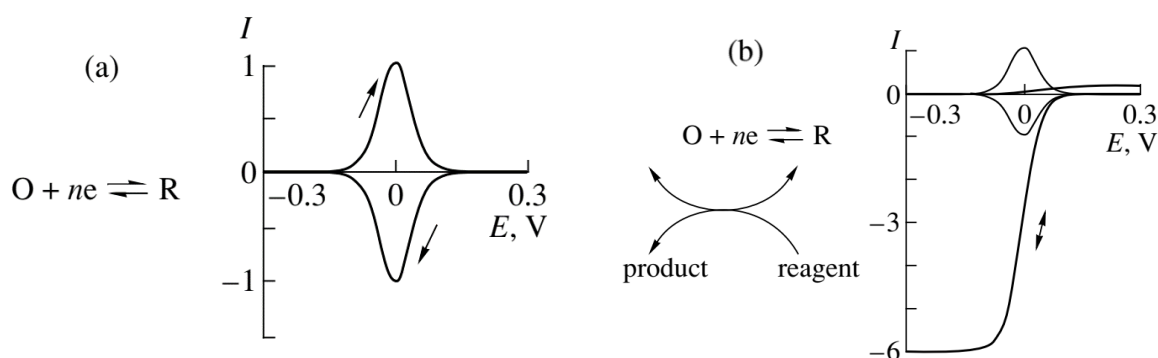


Figure 2.2. a) Cyclic voltammetry for the adsorbed redox couple, displaying reversible electron transfer; b) electron transfer coupled to catalytic reaction in the presence of the substrate (stationary electrochemistry) Reproduced from reference <sup>190</sup>.

The ideal form of the voltammogram when the redox protein is adsorbed on the electrode is shown on the Fig.2.2 (a), when the symmetrical oxidation and reduction peaks centered at the reduction potential  $E^\circ$ ,  $E^\circ = E_{p,c} = E_{p,a}$ .

Integration of the reduction/oxidation peak area allows to evaluate the coverage of the adsorbed redox active protein on the electrode surface  $\Gamma$ :

$$\Gamma = \frac{Q_f}{nAF} \quad \text{Equation 2.2}$$

where,  $Q_f$  is the charge passing for the redox couple for transferring  $n$  electrons,  $F$  is the Faraday constant, and  $A$  is the electrode surface.

The apparent electron transfer rate constant can be determined from the plots of the peak separation values dependent on the scan rates  $\nu$ , known as trumpet plots.

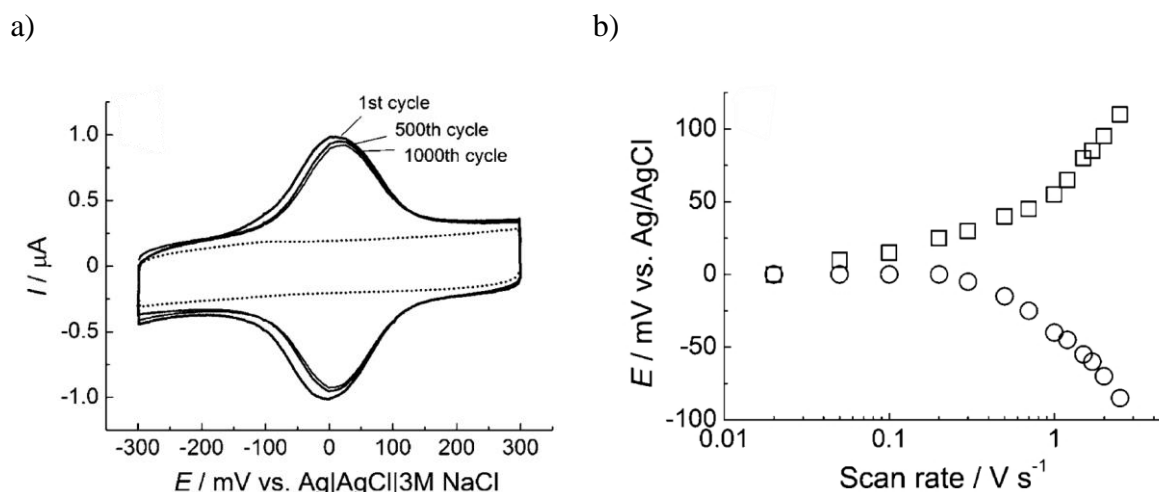


Figure 2.3. a) Cyclic voltammograms of cytochrome *c* at pH 7.0 with a scan rate of  $100 \text{ mVs}^{-1}$ ; b) Trumpet plots, cathodic (circle) and anodic (square) potentials were determined from voltammograms at each scan rate Reproduced from reference <sup>191</sup>.

Using the Laviron method <sup>192</sup>, the transfer coefficient  $\alpha$  and the rate constant of the electrochemical reaction  $k_{ET}$  can be deduced from the experimental plots of the peak potentials ( $E_a$  or  $E_c$ ) as a function of the sweep rate  $\nu$  [ $\text{V/s}$ ]. Upon increase of the  $\nu$  the difference between the peak potentials increases, so that from variations of  $E_a$  and  $E_c$  as a function of  $\log(\nu)$  the intersection gives  $\nu_a$  and  $\nu_c$  which leads to the  $k_{ET}$ :

$$k_{ET} = \frac{\alpha n F \nu_c}{RT} = (1 - \alpha) \frac{n F \nu_a}{RT} \quad \text{Equation 2.3}$$

The transfer coefficient  $\alpha$  can be determined from the width of the peak or from the expression:

$$\log\left(\frac{\nu_a}{\nu_c}\right) = \log\left(\frac{\alpha}{1-\alpha}\right) \quad \text{Equation 2.4}$$

There are several aspects that should be taken into account during electrochemical experiments:

- Availability of redox center (catalytic site, cofactor)
- The efficient distance to maintain electron transfer
- Immobilization of the protein in reactive conformation on the surface

The proteins that can be studied by PFV should contain a surface-exposed redox active center (e.g. cytochrome c peroxidase) or buried inside the matrix center that connected through the chain of redox cofactors (e.g. hydrogenase in Fig. 2.4) to ensure the direct electron transfer. To support electric connection with electrode it is enough having one of the cofactors for electron exchange. However, it is important to maintain the distance of 14 Å or less between electron transfer structures in the enzyme<sup>193, 194</sup>.

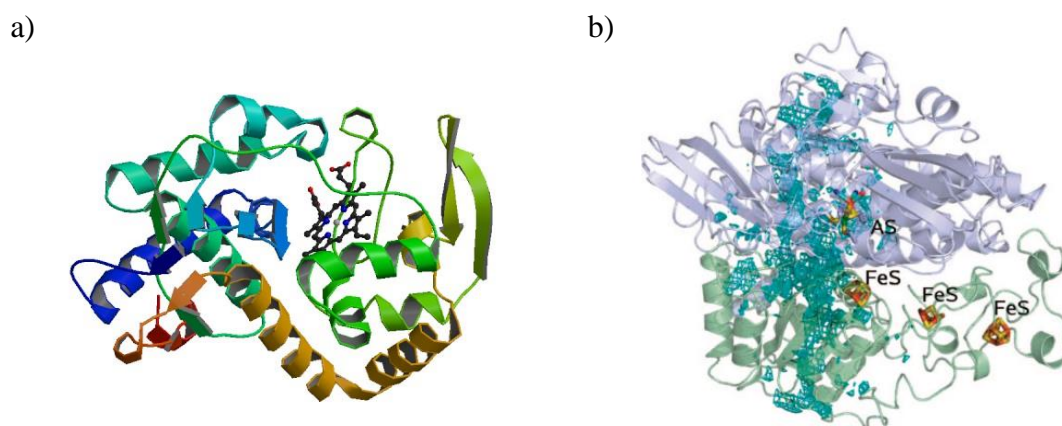


Figure 2.4. Models of the structure a) cytochrome c peroxidase<sup>195</sup> and b) *D. fructosovorans* NiFe hydrogenase, showing the two proteins assembled in the heterodimer (light blue and green), the buried active site (AS), the three lined-up iron-sulfur (FeS) clusters used for transferring electrons. Reproduced from<sup>196</sup>.

Moreover, the way protein is oriented on the surface can be tailored by different immobilization techniques<sup>191, 197</sup>. For electrochemical studies, it is essential to make sure that a native conformation is retained<sup>198, 199</sup>. To prove that the enzyme adsorbed on the electrode is not denatured, the catalytic activity upon substrate at reasonable rate and in adequate potential scale should be checked. However, some proteins in denatured state can show the residual catalytic signal because of the redox cofactors, so that the combination of the spectroscopic techniques (FTIR, UV-Vis) with electrochemical approach can be used to check the preservation of the enzyme secondary structure. To summarize, the requirements for successful PFV method are to develop a protein immobilization procedure with homogenous orientation towards electrode, which allows the direct electron transfer and keeps the protein in a functional conformation.

## 2.1.2 Theories behind electron kinetics in proteins

*Marcus theory.* For the simple redox reaction (Eq.2.5) in solution (the homogeneous electron transfer), the values for the two rate constants depend on the potentials of D (donor) and A (acceptor) and other parameters.



Due to classical Marcus theory<sup>200</sup> this process requires the formation of a transient complex, in which the kinetics of the electron transfer can be described by an equation:

$$k_{ET} = C \cdot \exp\left[-\frac{(\Delta G^\circ + \lambda)^2}{4\lambda RT}\right] \quad \text{Equation 2.6}$$

where  $\Delta G^\circ$  is the standard free energy of the reaction,  $\lambda$  is the reorganization energy, which reflect outer and inner sphere nuclear rearrangement that accompanies charge transfer,  $C = \sqrt{\frac{4\pi^3}{h^2\lambda RT}} H_{AB}^2$  – the expression of the preexponential factor, which depends on strength of the electronic coupling between the acceptor and the donor.

It shows that the kinetics of electron transfer depends on two parameters,  $\Delta G^\circ$  and  $\lambda$ . The main consequence from the classical theory is that biological electron flow over long distances with a relatively small release of free energy is possible because the protein fold creates a suitable balance between free energy of reaction and the reorganization energy. For the interfacial electron transfer the redox reaction flows according to:



Due to *the Butler Volmer theory*, the rate constant of a one electron transfer step depends on the overpotential applied  $\eta = E - E^\circ$ , where  $E^\circ$  is the reduction potential of the molecule and  $E$  is an electrode potential, and the charge transfer coefficient  $\alpha$ :

$$k_{ox} = k_0 \exp^{((1-\alpha)\eta F/RT)}, k_{red} = k_0 \exp^{(-\alpha\eta F/RT)} \quad \text{Equation 2.8}$$

With the increase of the electrode potential, the rates of oxidation (reduction) exponentially increase (decrease). The factor  $k_0$  depends on the coupling between the electrode and the redox molecules, so that the greater  $k_0$  is, the faster the electron exchange happens. In this expression

it is assumed that the concentrations at the electrode are equal to the concentrations in the bulk electrolyte, so that the mass transfer rate is much greater than the reaction rate.

*Electron tunnelling.* The theory developed by Moser and colleagues evaluates the effective distances for the intramolecular electron transfer<sup>193</sup>. It shows that the electron tunnelling decreases exponentially as the distance between covalently bridged redox centres through the insulating barrier increases, proportional to  $e^{-\beta R}$ :

$$\log_{10} k_{ET} = 15 - 0.6R - 3.1(\Delta G + \lambda)^2/\lambda \quad \text{Equation 2.9}$$

where  $R$  is the edge-to-edge distance and  $\beta$  is the parameter proportional to the square root of the barrier height, the coefficients 0.6 and 3.1 reflect  $\beta = 1.4\text{\AA}^{-1}$ .

The thorough analysis of the proteins with known atomic structure, whose function involves electron transfer, revealed that electrons can travel up to 14 Å between redox centres through the protein medium. Moreover, the transfer over longer distances always involves employing a chain of cofactors.

### 2.1.3 Electron transfer mechanism of immobilized enzymes

In protein voltammetry there are two possible ways to transfer electrons, either directly or mediated<sup>201</sup>. The direct electron transfer (DET) happens when the redox enzymes possess the tightly bound cofactors in the active site which can exchange electrons directly with the electrode. Success relies on the minimal distance between electrode and enzymes redox centers, which are sufficiently exposed towards electrode with favorable orientation.

#### Direct Electron Transfer (DET)    Mediated Electron Transfer (MET)

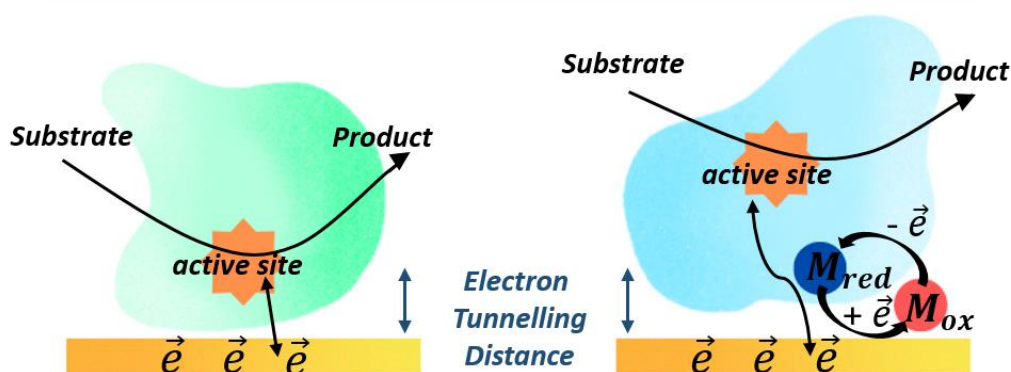


Figure 2.5. Direct and mediated electron transfer in protein voltammetry.




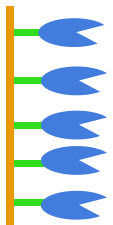
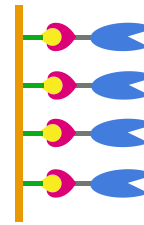
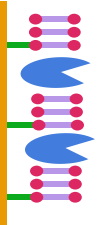

For some bioelectrochemical systems it is hard to immobilize enzyme close enough to electrode for DET, so that the mediated electron transfer (MET) facilitates redox reaction<sup>202</sup>. In this case electron exchange goes through the mediator, typically low molecular weight redox

active molecule. These agents deliver electrons from the electrode surface to the enzyme active center fast and with reversible kinetics. Moreover, the perfect mediator should have stable oxidized and reduced forms and exhibit regeneration under low overpotential and being pH independent. If the mediator and protein are added in solution (homogeneous mediation), it is necessary to include a separating membrane between anode and cathode to prevent short-circuiting and cross reactions. Heterogeneous mediation occurs when the mediator is added to the solution for reaching an immobilized enzyme or when the mediator is already incorporated with enzyme on electrode surface.

#### 2.1.4 Immobilization and signal enhancement strategies

A variety of techniques were developed to address the major challenges in protein immobilization such as maintenance of enzyme activity, stability to changing conditions, enzyme life-time, accessible orientation of the active center on the electrode surface<sup>199</sup>. The methods of immobilization can be classified by obtained orientation of the protein on the surface or by type of sorption interactions (physio- and chemisorption).

Table 2.1. The developed techniques of protein attachment to the electrode.

Non-oriented immobilization			Well-oriented immobilization			
						
<b>Physical adsorption</b>	<b>Entrapment</b>	<b>Cross-linking</b>	<b>Covalent binding</b>	<b>Bioaffinity</b>	<b>Tethered bilayer</b>	<b>SAM</b>

#### Non-oriented immobilization

*Physical sorption.* The most common and easily adapted method is the adsorption of the enzyme on the electrode. The bonding is based on unspecific weak interactions, such as electrostatic or hydrophobic forces. This technique is only suitable for a limited range of either small and soluble redox proteins or those with hydrophobic domains. However, this technique has many problems such as the enzyme desorption especially from metal surfaces, different uncontrolled orientation, denaturation and reactivity deprivation.

Glassy carbon electrodes<sup>203</sup> or pyrolytic graphite electrodes<sup>190</sup> are suitable for this purpose. By changing electrode surface pretreatment, the variation of the surface carbonyl or hydroxyl groups, changing O/C ratio, could be obtained for stronger protein bonding.



Although, the major obstacles are that proteins absorbed in various direction towards electrode and the nature of interactions with different groups on surface is unclear.

*Entrapment.* Proteins can be physically incorporated into the matrix of conducting polymers<sup>204</sup> or hydrogels<sup>205</sup>. It is a sustainable method to reach a high stability and long life-time of the protein film, as well as an efficient DET because of small distances to electrode surface. Apart from these merits, entrapped enzymes often lose sensitivity and represent heterogeneous orientation.

*Cross-linking.* Another well-known technique is immobilization of proteins via cross-linking bifunctional molecules (glutaraldehyde, hexamethylenediamine) or other functionally inert protein such as bovine serum albumin<sup>206</sup>. This approach increases the stability due to strong chemical binding between proteins but the distortion of enzyme reactive conformation and inactivation are the drawbacks of the method.

### Well-oriented immobilization

*Covalent attachment.* Covalent coupling is the specific chemical method of immobilization in which protein is bound to the surface through its functional groups and the linker molecule on the electrode surface. This technique is known for enzyme stability and well-defined orientation but has a problem of lower activity after immobilization. There are different approaches depending on the nature of the linkers:

- Au<sub>electrode</sub>-S-Cys: the proteins with given cysteine, thiolate and the disulfide groups that are not involved in catalytic reaction can be successfully attached to the gold surface through direct chemisorption<sup>197, 207</sup>. In this case an efficient DET and well orientation can be achieved but the denaturation is a problem.
- Cu-, Ni-chelating agents: immobilization of histidine-tagged protein using to a copper-<sup>208</sup> or nickel-chelating complex attached to an electrode surface<sup>209</sup>. Via the coordination of the nitrogen from the imidazole side chains the His-tag the strong protein attachment with controlled orientation is achieved.
- "Wiring" linkers: functionalized nanostructures or wiring molecules (pyrroloquinoline quinone PQQ) provide connection between redox cofactor and electrode allowing an interfacial and intramolecular electron transfer<sup>210, 211</sup>.

*Bioaffinity.* This strategy employs specific tight interaction between affinity pairs such as lectin-sugar, antigen-antibody, and biotin-avidin<sup>212</sup>. There are two possible approaches to attach protein to the electrode surface either through precoupled affinity ligand/target enzyme complex or via a molecule with affinity to the surface which conjugates to enzyme. The bonded

protein maintains catalytic activity and homogeneous orientation, exhibits better stability against denaturation. However, this technique is applicable only for the enzymes with available specific groups (histidine, biotin).

*Tethered bilayer.* For this method, electrode modified by confined tethered bilayer lipid membranes which are made up of specially designed self-assembled phospholipids and small alkanethiol molecule <sup>213</sup>. Because of different chain length they form nanoscale phase-separated domains on the gold surface, so that proteins can be embedded into bilayer regions. This technique has been successfully applied to study membrane proteins <sup>214</sup>, but the direct electron transfer can be impaired.

*Self-assembled monolayers (SAM).* The electrode surface can be modified by covalently attached alkanethiols or silanes that form a tight self-assembled monolayer (SAM). This layer is formed by a bifunctional molecule  $X-(CH_2)_n-Y$ , where X is a substituent that anchors the molecule on the surface, and Y is a functional group that interacts with the protein. This technique is very common and exhibits many advantages:

- Protein stability and orientation is controlled by the nature (polar/nonpolar) and charge of the head-group of the linker. It is reported that cytochrome *c* is successfully immobilized on negatively charged SAM <sup>191</sup>, while cytochrome *aa<sub>3</sub>* oxidase prefers the neutral surfaces <sup>215</sup>.
- The direct electron transfer is adjusted by the length of the linker.
- SAM shield protein from direct contact with electrode, so that the native conformation is preserved.
- The attached protein is also protecting the thiolated SAM layer from the desorption.

Further, there are some limitations of this method such as instability under extreme conditions and high oxidative potentials, relatively short life-time of the immobilized film, and the defects in monolayer might cause protein desorption.

### Signal enhancement

In order to increase sensitivity of electrical sensors and biosensing enzyme-based devices different signal amplification protocols were developed. The recent advances in nanotechnology offer broad opportunities to benefit from the unique chemical and physical properties of nanoparticles by varying their size, composition and shape.

The use of nanomaterials can improve the immobilization of biomolecules and enhance electron transfer between electrode surfaces and proteins. The coupling of conducting polymer

nanowires, carbon nanotubes, oxide and metal nanoparticles dramatically enhances the intensity of the analytical signal. For example, carbon nanotubes increase the electrochemical reactivity of biomolecules and promote the electron-transfer reactions of proteins due to their remarkable electrical, mechanical and structural properties<sup>216</sup>. The metal nanomaterials have large specific surface area and high surface free energy, so they can adsorb proteins strongly, which is useful for immobilization in biosensor constructions<sup>217</sup>.

Among the wide variety of nanomaterials gold nanoparticles (GNPs) are extremely suitable for the development of more sensitive electrical biosensors because of their physical and chemical properties<sup>218, 219, 191</sup>. The application of GNPs in sensing devices has many advantages:

- an ease of preparation;
- the high affinity to thiols for many immobilization approaches;
- their excellent conductivity leads to the enhancement of the electron transfer between redox centers in proteins and electrode surface;
- unique catalytic properties can be used for the decrease of the overpotentials in many electrochemical reactions<sup>220, 221</sup>;
- large surface area makes possible to increase quantity of adsorbed enzymes, which in return amplify the detected signal.

### 2.1.5 Steady-state electrochemistry

After adding the substrate in solution to the adsorbed protein, the shape of the voltammogram changes because the current response depends on diffusion of the substrate to the electrode surface Fig.2.1b. Thus, the mass transport of substrate should be controlled in order to minimize the influence of migration, diffusion and convection moves.

Migration is easily reduced through the use of electrolyte in high concentration compared to the substrate, so it is statistically more probable that the electrolyte will migrate to the electrode surface for charge balance. Diffusion occurs from a movement across concentration gradient from the areas of high to areas of low concentration. The molecules in solution move by convection when the mechanical forces (vibration, stirring) are influential. The frequently used system with rotating electrode introduces a controlled convective movement of the solution which increases the efficiency of the transport of redox species, avoiding depletion near the electrode during reaction. In this case the steady current-potential response obtained because of the stable thickness of the diffusion layer, and current reaches the limit value  $i_{lim}$  under these conditions. However, electrons are no longer confined to the

adsorbed protein film, the balance occurs between electrochemical and catalytic redox transformation of the active sites, so that it is important to measure the catalytic turnover number of the enzyme.

The Levich equation shows that the limiting current depends on the concentration of electroactive species  $C$  and the square root of the electrode rotation rate  $\omega$ :

$$i_{lim} = 0.620nFAv_s^{-1/6}D^{2/3}C\omega^{1/2} \quad \text{Equation 2.10}$$

where  $v_s$  is the kinematic viscosity of the solution [ $\text{cm}^2/\text{s}$ ],  $D$  is the substrate diffusion coefficient [ $\text{cm}^2/\text{s}$ ].

The graph in the coordinates of  $\frac{1}{i_{lim}} = f\left(\frac{1}{\sqrt{\omega}}\right)$  is called a Koutecky-Levich plot (Fig.2.7). From this relation, the equation (2.5) distinguishes catalytic current from measured  $i_{lim}$  :

$$\frac{1}{i_{lim}} = \frac{1}{i_k} + \frac{1}{0.62nFAv_s^{-1/6}D^{2/3}C\omega^{1/2}} \quad \text{Equation 2.11}$$

By the extrapolation of  $i_{lim}$  value at the infinite rotation rate, the mass transport is no longer rate limiting, and the obtained value reveals the catalytic efficiency of the enzyme, so  $k_{cat}$  can be calculated:

$$\frac{1}{i_k} = \frac{C+k_M}{nFA\Gamma C k_{cat}} \quad \text{Equation 2.12}$$

where  $C$  is the concentration of substrate,  $k_M$  is the Michaelis-Menten constant, and  $A, \Gamma$  are taken from integration of the reduction peak without substrate<sup>196</sup>. Thus, the turnover rate should be determined under conditions when interfacial electron transfer and mass transport in solution do not confine the current.

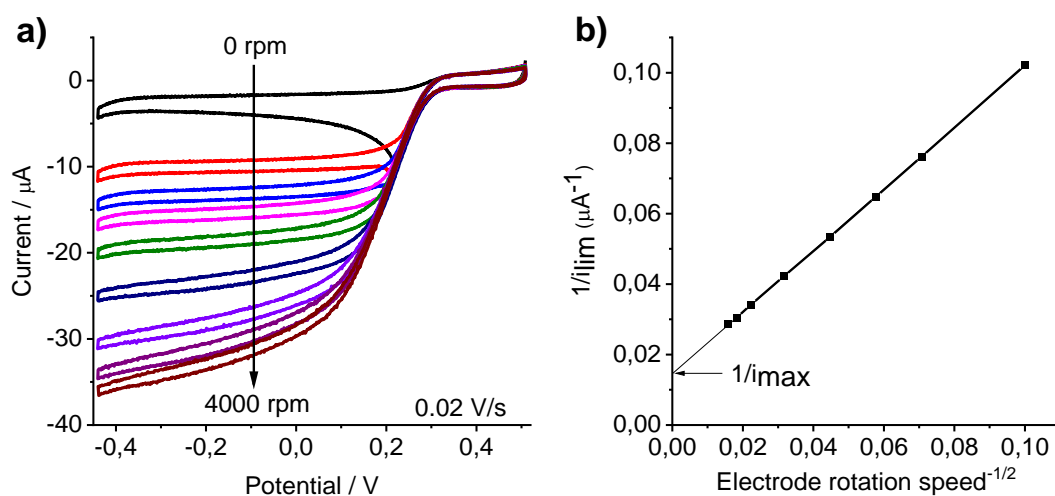


Figure 2.7. a) Catalytic current measured for cytochrome  $ba_3$  adsorbed at a rotating gold nanoparticles electrode as a function of rotation speed ; b) Koutecky-Levich plot showing small but nonzero intercept at infinite rotation rate, allowing one to estimate  $k_{cat}$ . Reproduced from reference<sup>222</sup>.

## 2.2 Inhibition of protein activity as method of characterization

The mechanism of the ligand binding to the enzyme can be investigated through extensive inhibition assays. The effect of the different small molecules on the enzyme activity gives information about the nature of the binding pocket and helps to develop strategies for drug discovery. The reaction between the enzyme  $E$  with a single substrate  $S$  leading to the formation of product  $P$  through the enzyme-substrate complex  $ES$  is presented by the classical Michaelis-Menten model of enzyme kinetics<sup>223</sup>:



$$v_0 = k_2 \frac{[E]_0[S]}{K_m + [S]} = \frac{v_{max}[S]}{K_m + [S]}, \text{ where } K_m = \frac{k_{-1} + k_2}{k_1} \quad \text{Equation 2.14}$$

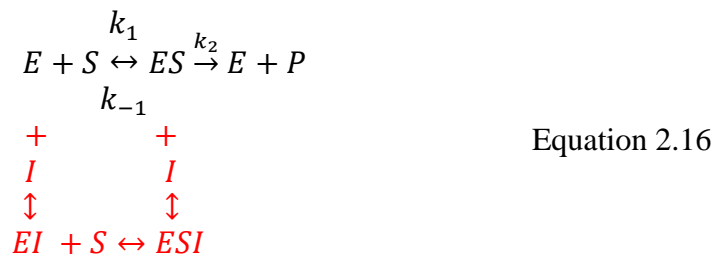
In this model,  $v_{max}$  refers to the maximum rate achieved by the system, which happens at the saturating substrate concentration  $[S]$  for a particular enzyme concentration  $[E]_0$ . The  $K_m$  is equal to substrate concentration when half of enzyme active sites are bound to the substrate and the reaction rate becomes half of  $v_{max}$ . If the  $k_2 \ll k_{-1}$ , the  $K_m$  is equal to the substrate dissociation constant  $K_S$ . The lower  $K_m$  is, the highest the affinity of the enzyme for the substrate. The  $v_{max}$  and  $K_m$  values of the enzyme can be easily measured from the slope and intercept of the double reciprocal plot transformed from the Michaelis-Menten equation, called the Lineweaver-Burk plot<sup>224, 225</sup>:

$$\frac{1}{v_0} = \frac{K_m}{v_{max}} \cdot \frac{1}{[S]} + \frac{1}{v_{max}} \quad \text{Equation 2.15}$$

However, the majority of enzymatic reactions have multiple substrates and products, even the bi-substrate reactions account for about 60% of the known enzymatic reactions. Michaelis-Menten model can be successfully used for more complex reactions by evaluating a turnover number  $k_{cat}$  that shows the quantity of substrate molecules utilised by protein to produce product per unit of time.

When the inhibitor  $I$  is added to the enzyme, its activity is either reduced for a certain time and then restored (reversible inhibition) or the enzyme activity is blocked permanently (irreversible inhibition). The molecules of inhibitor can bind either to the enzyme  $E$  in

competition with the substrate  $S$  (competitive inhibition), or to the enzyme-substrate complex  $ES$  (uncompetitive inhibition). If both modes are applicable the model is called mixed inhibition<sup>226,227</sup> (Eq.2.16).



In competitive inhibition the  $EI$  complex is formed, so substrate molecule cannot bind to the active site. The kinetics equation is modified by a factor  $\alpha$  and apparent Michaelis constant is expressed through the inhibition constant as follows:

$$K_m^{app.} = K_m \alpha = K_m \left( 1 + \frac{[I]}{K_I} \right), \text{ where } K_I = \frac{[E][I]}{[EI]} \qquad \text{Equation 2.17}$$

The factor  $\alpha$  is a function of the inhibitor concentration and it is related to the affinity for the enzyme, it cannot be less than 1 ( $\alpha=1$  when no inhibitor added). If different molecules are screened, the strongest inhibitor is the one with higher  $\alpha$  factor and, therefore, with lower  $K_I$ . In the competitive inhibition, only apparent constant  $K_m^{app.}$  changes, the  $v_{max}$  remains unchanged by the presence of the inhibitor. The effect of the competitive inhibitor can be diminished by the increase of the substrate concentration. In the *uncompetitive* inhibition, the inhibitor binds only to the  $ES$  complex, it does not bind to the free enzyme. This type of inhibitor affects the substrate affinity apparent constant  $K_m^{app.}$  and the reaction rate is decreased by factor  $\alpha'$  (apparent rate:  $v_{max}^{app.} = v_{max}/\alpha'$ ). The  $v_{max}/K_m$  is unchanged, the effect of a uncompetitive inhibitor can only be partially overcome by high concentrations of the substrate. The *mixed* inhibitor has a higher affinity either for the free enzyme or enzyme-substrate complex. The presence of a mixed inhibitor usually affects both  $v_{max}$  and  $K_m$ . Due to the inhibition factors  $\alpha$  and  $\alpha'$  the mixed inhibitors are effective both at low and at high concentrations. All three above-mentioned examples refer to the reversible inhibition.

In irreversible inhibition, the inhibitor (inactivator) permanently inactivates the enzyme by the formation of a covalent bond with the active site. The main purpose of this inhibitor is to remove enzyme from the reaction. In the kinetics of an irreversible inhibitor the inactivator reduces the concentration of functional enzyme at all substrate concentrations. When the dissociation constant of the  $EI$ -complex is so low that the reversible inhibition resembles irreversible, it is called *tight-binding inhibitor*<sup>228–230</sup>.

The inhibition can be evaluated by the half-inhibition concentration  $IC_{50}$  that represents the concentration at which a substance exerts half of its maximal inhibitory effect. It is the most common parameter in the drug discovery analysis, sometimes in pharmaceutical assay the  $IC_{90}$  is used. The change in  $IC_{50}$  for the competitive inhibition is mathematically described by the Cheng–Prusoff relationship<sup>231</sup>:

$$IC_{50} = \left(1 + \frac{[S]}{K_m}\right) K_I \quad \text{Equation 2.18}$$

For the classical inhibitors the inhibition constant greatly exceeds the concentration of enzyme ( $K_I \gg [E]_0$ ). In case of the tight-binding inhibitors, the affinity of compounds is so high that the apparent value of dissociation constant for the  $EI$  complex  $K_I^{app}$  is equal to or less than the total concentration of the enzyme used in the assay ( $K_I \ll [E]_0$ ).<sup>229,232</sup> As a result, the concentration of free inhibitor is far below the total concentration in the reaction mixture. Therefore, the classical steady state Michaelis-Menten kinetics based on equilibrium assumptions cannot be used. To get  $K_I^{app}$  values the Morrison quadratic equation can be employed for the dose-response curves, here  $K_I^{app}$  does not depend on  $[E]$ :

$$v = v_0 \left(1 - \frac{([E] + [I] + K_I^{app}) - \sqrt{([E] + [I] + K_I^{app})^2 - 4[E][I]}}{2[E]}\right) \quad \text{Equation 2.19}$$

where  $v_0$  is a control rate at  $[I] = 0$ ,  $v$  – initial reaction rate,  $[I]$  – total inhibitor concentration,  $[E]$  – active enzyme concentration,  $K_I^{app}$  – apparent inhibition constant.

This equation gives a great advantage for the inhibition assays performed using the electrochemical sensors. When the protein is immobilized on the surface of the electrode, the concentration of the electroactive protein can be fixed or used as a parameter in the Morrison equation followed by the fitting of the inhibition activity as a function of the inhibitor concentration.

The linear form of the Morrison approach was presented by Henderson models<sup>233</sup>, which intend to reveal the tight-binding inhibition. Henderson equation includes plotting of fractional velocity (velocity with inhibitor divided by velocity without inhibitor  $\frac{v_I}{v_0}$ ) as a function of inhibitor concentration  $[I]$  or the plot of a parameter  $\frac{[I]}{1 - \frac{v_I}{v_0}}$  as a function of  $\frac{v_0}{v_I}$  that should be linear in case of a tight-binding inhibitor.

The Henderson equation can also be presented for different modes of inhibition:

$$\frac{[I]}{1 - \frac{v_I}{v_0}} = [E] + K_I^{app} \cdot \frac{v_0}{v_I}; \quad K_I^{app} = K_I \left( 1 + \frac{[S]}{K_m} \right) - \text{competitive}$$

$$\frac{[I]}{1 - \frac{v_I}{v_0}} = [E] + K_I^{app} \cdot \frac{v_0}{v_I}; \quad K_I^{app} = K_I \left( 1 + \frac{K_m}{[S]} \right) - \text{uncompetitive} \quad \text{Equation 2.20}$$

$$\frac{[I]}{1 - \frac{v_I}{v_0}} = [E] + K_I^{app} \cdot \frac{v_0}{v_I}; \quad K_I^{app} = \left( \frac{[S] + K_m}{\alpha K_I + \frac{K_m}{K_I}} \right) - \text{mixed}$$

The information on the mechanism of inhibition can be extracted from these plots where the tight-binding inhibitions takes place (Fig. 2.8). When the concentration of enzyme is fixed, Henderson plots are built at increasing concentration of the substrate. The slopes of the curves increase in case of the competitive inhibition and decrease in uncompetitive inhibition.

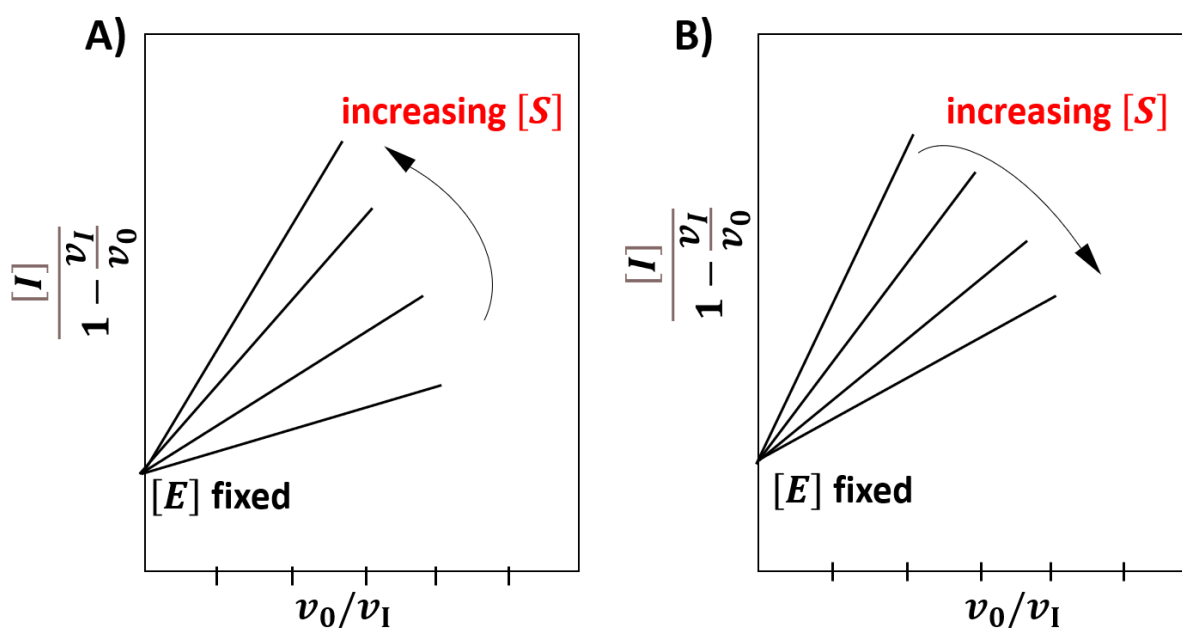


Figure 2.8. The model Henderson plots at different concentration of substrate for competitive (A) and uncompetitive (B) inhibition.

For drug design the aim is to find the perfect, "suicide" inhibitor, that will have a very high affinity to the active site and undergo irreversible inhibition. The good start in the screening approach is to begin with the compound that resemble the natural substrate and develop the lead molecules in the respect to the structure–activity relationships of the binding site.



## 2.3 UV-Vis spectroscopy

Spectroscopic methods are based on the interaction of the matter with the electromagnetic radiation (light). The energy of this radiation can be presented as a function of the wavelength or the frequency of the electromagnetic wave:

$$E = h\nu = h\frac{c}{\lambda} \quad \text{Equation 2.21}$$

where  $c$  - speed of light,  $h$  – Planck's constant. The electromagnetic spectrum covers a continuous range of wavelengths from radio waves at the low-frequency to  $\gamma$ -rays at the high-frequency, Fig. 2.9a.

The interaction of matter with the electromagnetic radiation can be understood as the change in the state of the sample after absorption of light. The energy levels for all physical processes at the atomic and molecular levels are quantized, thus if there are no available energy levels which match the quantum energy of the incident radiation, then the sample will be transparent to that radiation, and it will pass through. The quantum interpretation of the photon absorption by the molecule and interactions is illustrated in Jablonski diagram (Fig. 2.9b). The photon absorption provokes transitions from the lower energy state  $E_1$  to the one with the higher energy  $E_2$ . The difference between these states  $\Delta E$  is equal to the required electromagnetic radiation  $h\nu$ , which is proportional to its frequency (Hz), for convenience represented in wavenumber  $\text{cm}^{-1}$  ( $\nu, \text{cm}^{-1} = 10^7/\lambda, \text{nm}$ ). In general, the spectroscopic techniques are classified by the range of the incident light (X-ray spectroscopy, infrared spectroscopy), by the type of interaction between light and matter (absorption, scattering) or by the studied species (molecular and atomic spectroscopy). In this thesis mainly two spectroscopic methods were employed: UV-visible and infrared spectroscopies. These techniques are powerful tools to investigate interactions in the biological systems and to reveal the reaction mechanism of proteins with different substrates.

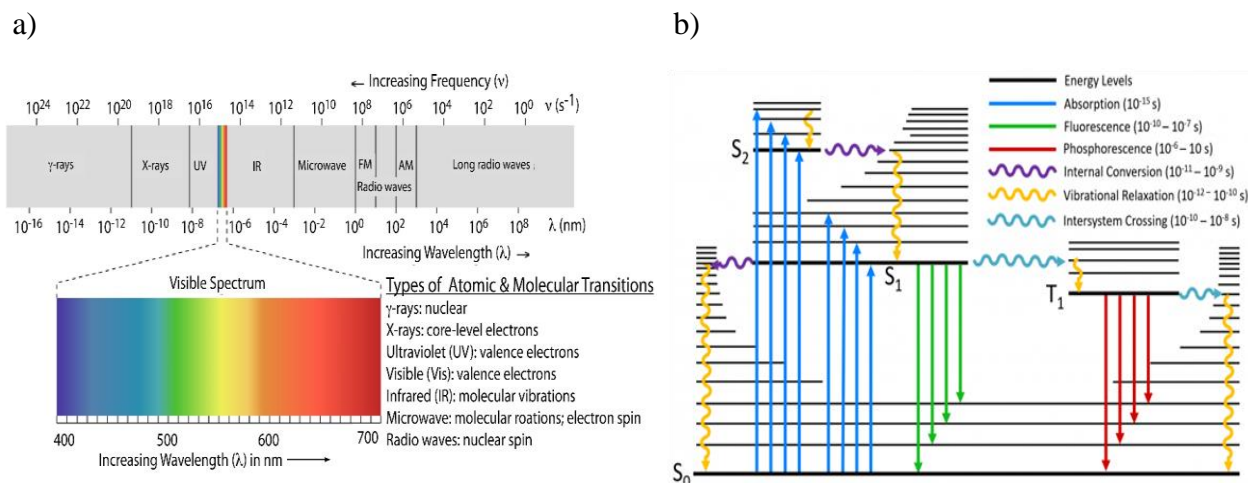


Figure 2.9. a) The electromagnetic spectrum showing the boundaries between different regions and the type of atomic or molecular transition responsible for the change in energy; b) Jablonski diagram of the possible transitions that can occur after a molecule has been photoexcited, reproduced from <sup>234</sup>.

The principles of the UV-Vis spectroscopy are based on the measurement of the absorbed  $A$  or transmitted light  $T$  of ultraviolet (200–400 nm) or visible (400–800 nm) range by chemical compounds which results in the production of distinct spectra. In this region transitions of valence electrons within atoms and molecules from the ground to excited state are involved. In organic molecules the superposition of the electronic transitions from bonding or nonbonding orbitals to empty antibonding orbitals:  $\sigma \rightarrow \sigma^*$ ,  $\pi \rightarrow \pi^*$ ,  $n \rightarrow \pi^*$ ,  $n \rightarrow \sigma^*$ , except ones between  $\pi$  and  $\sigma$  orbitals that are excluded by symmetry, are depicted in a UV-vis spectrum <sup>235</sup>. Whereas in metal complexes, other types of transitions exist, such as  $d \rightarrow d$ , metal-to-ligand and ligand-to-metal charge transfers.

The Bouguer-Lambert-Beer law states that for a constant path length  $l$ , the intensity of the incident light passing through the absorbing medium diminishes exponentially with concentration, therefore the absorbance is proportional to concentration of the sample:

$$A = \lg\left(\frac{I_0}{I}\right) = -\lg\left(\frac{I}{I_0}\right) = -\log T = \epsilon lc \quad \text{Equation 2.22}$$

where  $I_0$  and  $I$  are the intensities of the incident and transmitted light respectively,  $\epsilon$  – molar extinction coefficient,  $l$  – path length of the sample in  $cm$ ,  $c$  – molar concentration of the sample.

The extinction coefficient  $\epsilon$  is influenced by the nature of the absorbing species and is dependent on the wavelength. In biochemistry, the extinction coefficient of a proteins at 280 nm depends almost exclusively on the number of aromatic residues, particularly tryptophan, and can be predicted from the sequence of amino acids <sup>236</sup>.

### 2.3.1 UV-vis spectroscopy for proteins

In proteins, there are three different internal chromophores, functional groups that are responsible for the electronic absorption bands:

- the peptide bond linking the amino acids absorbs weakly around 220 nm;
- the aromatic amino acids phenylalanine, tyrosine, tryptophan, and histidine (a disulphide bond) contribute with bands in the range of 230– 300 nm;
- protein cofactors, such as chlorophyll, flavin, and heme.

The last group gives strong absorbance in the visible region of the spectrum that bear a metal ions and and groups with extended  $\pi$ -electron systems. The intense bands here produced by the  $\pi \rightarrow \pi^*$  transitions in the conjugated system and metal-to-ligand charge transfer transitions in coordination complexes<sup>237</sup>. These electronic transitions are sensitive to the environment of the surrounding protein scaffold and red-ox states, so that the alterations in the UV-Vis spectrum reveal the possible structural and conformational changes.

In particular, heme cofactors are coordination complexes that consist of an iron ion coordinated to a porphyrin acting as a tetradentate ligand, and to one or two axial ligands. They are good chromophores with spectrum highly dependent on the spin and redox state of the central iron cation (Fig. 2.10) and type of heme (Fig. 2.11 and Table 2.2).

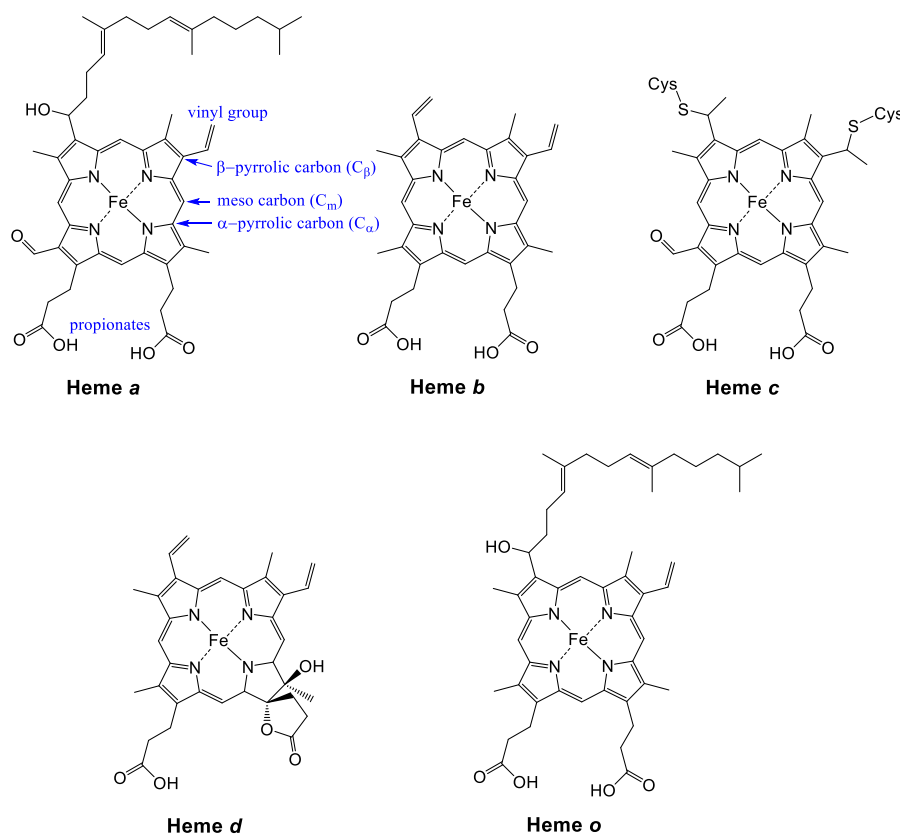


Figure 2.10. Structures of the hemes found in enzymes of the respiratory chain.

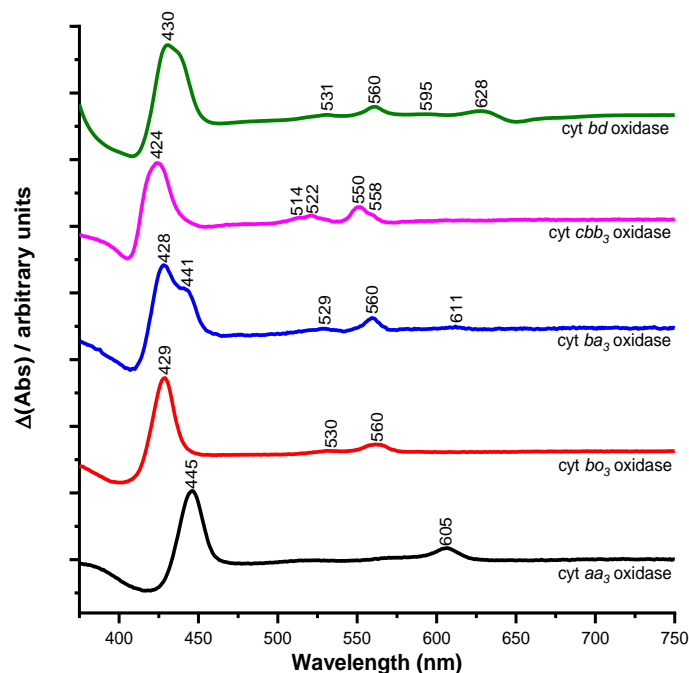


Figure 2.11. Differential red-ox spectra of the UV/Visible spectra of cytochrome  $aa_3$  oxidase from *P. denitrificans*, cytochrome  $bo_3$  oxidase from *E. coli*, cytochrome  $ba_3$  oxidase from *T. thermophilus*, cytochrome  $cbb_3$  oxidase from *P. stutzeri*, and cytochrome  $bd$ -I oxidase from *E. coli*. Reproduced from reference <sup>222</sup>.

Hemoproteins exhibit three characteristic bands in the visible region, namely the Soret band or ( $\gamma$ -band) in the range of 400–450 nm and Q-bands:  $\beta$ -bands (500–560 nm), and  $\alpha$ -bands (540–630 nm).

Table 2.2. UV-vis characteristic bands of heme cofactors in reduced cytochromes from respiratory chain <sup>222</sup>.

Type of heme	Soret band, nm	$\beta$ -band, nm	$\alpha$ -band, nm
Heme <i>a</i>	442-445		604-611
Heme <i>b</i>	426-430, 439	528-532, 561	555-566, 595
Heme <i>c</i>	415-418	515-520	547-552
Heme <i>o</i>	426		555
Heme <i>d</i>	430		620-630

The spectrum of hemoproteins is highly sensitive to the red-ox state of the central iron cation so that the combining of an applied controlled potential with the UV-Vis technique makes up a powerful tool for the study of red-ox events within the catalytic cycle of these enzymes.

## 2.3.2 UV-Vis potentiometric titration

Potentiometric titration consists in the UV-Vis spectra of the analyte confined in an electrochemical cell as a function of the potential. The applied method allows to differentiate the contribution of the multiple red-ox active cofactors and determine their mid-point potential. All the titration experiment in this work were performed in the custom-made thin-layer electrochemical cell <sup>11</sup> (see description in Annex A.3).

In this experiment potentiometric titration can be performed in reductive or oxidative titration, giving information on the reversibility and stability of the red-ox transitions. The measurements start from the fully reduced/oxidized state of the studied protein, and then the series of the UV-vis spectra are recorded as a function of a slowly changing potential in the range of +500/-500 mV vs Ag/AgCl. The step of the potential shift is 50 mV in the regions far from the red-ox transition and 25mV in the redox transition region, Fig. 2.12a. The system is equilibrated after each change of potential so it can take up to 20 hours for the proteins with a few redox cofactors. This experiment is done under constant temperature control.

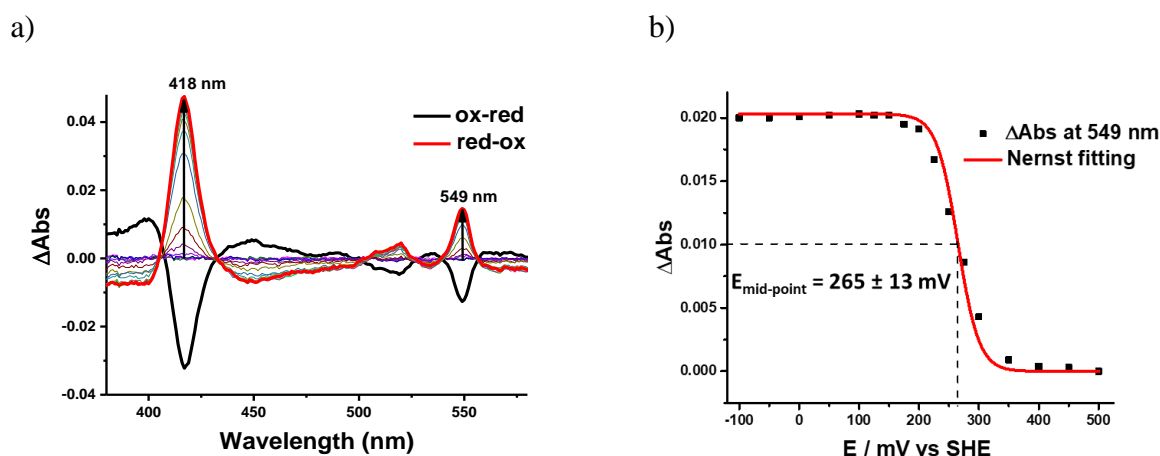


Figure 2.12. a) Differential red-ox spectra of the UV-Vis potentiometric titration of cis-trans isomerase from *Pseudomonas aeruginosa*; b) Fitting with modified Nernst equation for determination of the mid-point potential of the red-ox active cofactors of the protein.

The data analysis includes plotting of the changes of differential absorption at particular wavelength versus applied potential and fitting with a modified Nernst equation:

$$y = y_0 + \frac{A}{1 + \exp\left(\frac{n \cdot F \cdot (x - E)}{1000 \cdot R \cdot T}\right)} \quad \text{Equation 2.23}$$

where  $y_0$  – baseline,  $x$  – applied potential,  $A$  – maximal differential absorption/amplitude in the redox state before oxidative/reductive titration,  $n$  – number of electrons,  $R$  – universal gas

constant,  $8.314 \text{ J/K}\cdot\text{mol}$ ,  $T$  – temperature (in K) during experiment,  $F$  – Faraday constant,  $96480 \text{ C/mol}$ ,  $E$  – mid-point potential.

This equation can be derived from the original Nernst equation:

$$E = E_{1/2} + \frac{RT}{nF} \ln \frac{[Ox]}{[Red]} \quad \text{Equation 2.24}$$

With application of the Bouguer-Lambert-Beer law activities can be replaced by the absorption values. The differential absorption obtained from the measurements can be expressed through total absorptions of reduced/oxidized form and total absorption of partly reduced/oxidized system:  $\Delta A = A - A_{red} \Rightarrow A_{ox} - A = A_{ox} - A_{red} - \Delta A$ , and as a result the differential absorption is expressed as a function of potential equation:

$$\Delta A = \frac{A_{ox} - A_{red}}{1 + \exp\left(-\frac{nF}{RT}(E - E_{1/2})\right)} \quad \text{Equation 2.25}$$

This method can be applied to different proteins with red-ox active cofactors to calculate the mid-point potential with an error of about 20 mV. The precision of the determination depends on the number of the cofactors and their relative potential separation.

## 2.4 Infrared spectroscopy

The absorption of infrared light (IR) with wavelength in the range from 1 to 1000  $\mu\text{m}$  excites the vibrational and rotational transitions of molecules. This light has longer wavelength as compared to the UV-Vis light and smaller frequency, so that its energy is not enough to excite the transition of electrons. Under IR radiation, the typical vibrational transition happens from the ground state ( $v = 0$ ) to the first excited state ( $v = 1$ ), however, the transitions to the second vibrational state or beyond called overtones are possible but they have much lower intensities.

The Infrared spectrum is usually presented as a function of the wavenumbers ( $\text{cm}^{-1}$ ), the infrared spectral region is subdivided into three main parts:

- the near-infrared (NIR):  $12500 - 4000 \text{ cm}^{-1}$ ;
- the middle-infrared (MIR):  $4000 - 400 \text{ cm}^{-1}$ ;
- the far-infrared (FIR):  $400 - 10 \text{ cm}^{-1}$ .

Simple diatomic molecule has only one bond that can stretch. This model can be presented as balls connected with a weightless spring. The mass of each ball ( $m_1$  and  $m_2$ ) is proportional to its atomic mass, and the spring stretched proportionally to the chemical forces

that bond these atoms. If the periodic oscillation follows the Hooke's law, the stretching vibration is expressed using the equation for the simple harmonic oscillation:

$$\nu = \frac{1}{2\pi} \sqrt{\frac{k}{M}}, M = \frac{m_1 \cdot m_2}{m_1 + m_2}, \quad \text{Equation 2.26}$$

where  $k$  is the force constant of the bond. Therefore, the frequency of the stretching is a function of the atomic mass and rigidity of the bond (strength of the vibrating bond)<sup>238</sup>. This dependency is used in experiments with isotope labeling such as H<sub>2</sub>O/D<sub>2</sub>O exchange experiment. The vibrational frequency increases with increasing polarity of the bond which itself influenced by the intra- and intermolecular effects.

In polyatomic molecules, the atoms have three degrees of freedom in three directions, so the molecule with  $N$  atoms has  $3N$  degrees of freedom. For linear molecules, two degrees of freedom describe rotation and three degrees describe translation, so the remaining  $3N-5$  are the number of fundamental vibrations, for non-linear molecules this number is  $3N-6$ . In general, vibrations can be divided into two main categories: stretching (symmetric  $\nu_s$  and asymmetric  $\nu_{as}$ ) and bending (in-plane bending – scissoring  $\delta$  and rocking  $\gamma_r$ , out of plane bending – wagging  $\gamma_w$  and twisting  $\gamma_t$ ). All the above vibrational modes are typically observed in the mid-IR region (Fig. 2.13), except stretching modes in metal-ligand complexes that occur in far-IR. Absorption bands associated with the stretching and bending vibrations in molecules typically occur in the range of 500–4000  $\text{cm}^{-1}$ .

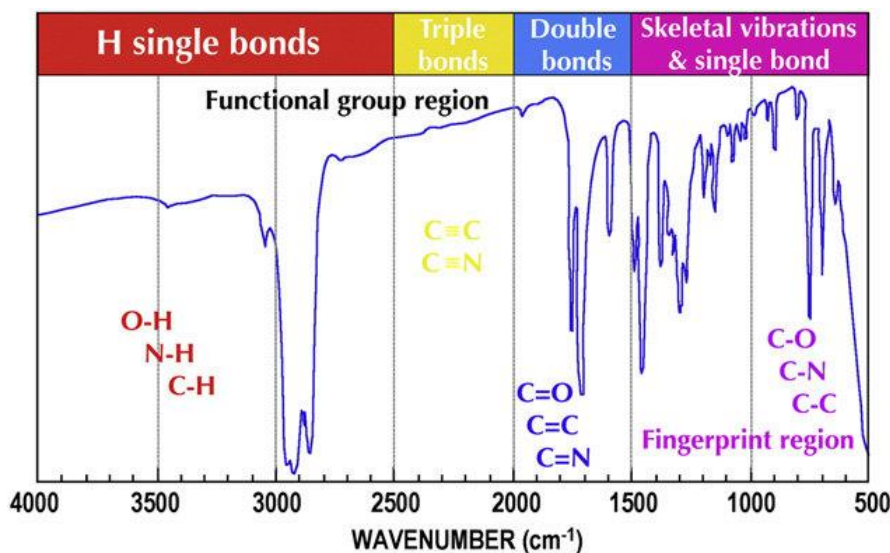


Figure 2.13. A typical mid-IR transmission spectrum showing in a schematic way typical absorptions lines associated to vibrational modes of molecules. Reproduced from reference<sup>239</sup>.

Infrared spectroscopy is a powerful method for the structure assignment of small organic molecules. In the complex protein structure, IR method has found many applications

for studying the architecture of the polypeptide scaffold, investigating the conformational changes of the vibrating groups and elucidating molecular mechanism of the enzymatic reactions.

#### 2.4.1 Infrared spectroscopy of proteins: Amide I and Amide II region

The chemical structure of a protein is very complex, it includes the main polypeptide chain, side chain residues and the prosthetic groups or cofactors bonded to the scaffold, so the IR absorption spectrum consist of overlapping bands of all the bonds vibration contributions (Fig. 2.14). The characteristic regions in the protein spectrum that are coming mainly from the vibrational modes of the protein backbone are listed in Table 2.3. While Amide I and Amide II bands are present in every protein spectrum, the vibration bands from the side chain residues of amino acids provide the unique signature for each protein. The catalytically important residues play a key role in the elucidating the molecular mechanism as they are sensitive to the protonation events and environment changes<sup>240</sup>.

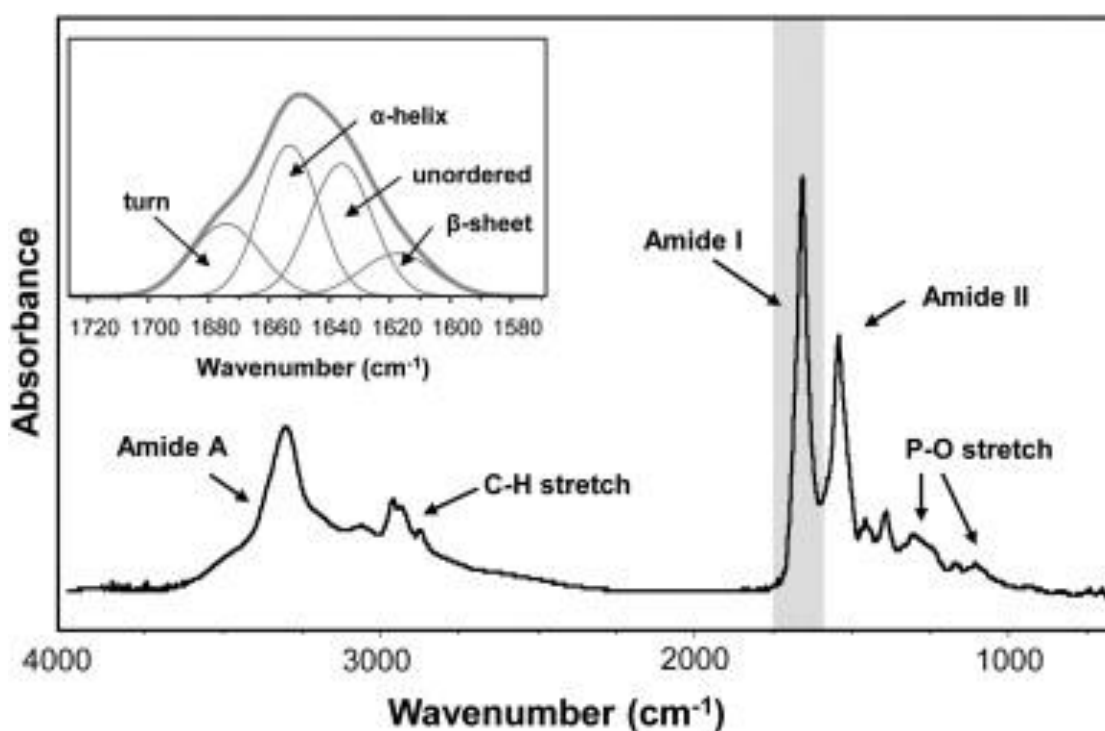


Figure 2.14. A typical FTIR spectrum of a protein in phosphate buffer showing the Amide I and Amide II bands at  $\sim 1650\text{ cm}^{-1}$  and  $\sim 1540\text{ cm}^{-1}$ , respectively. (Inset) Expanded view of the Amide I band, which can be deconvoluted into its secondary structure components. Reproduced from reference<sup>241</sup>.



Table 2.3. The principal contributions of the polypeptide backbone to the IR spectrum <sup>240</sup>.

Region	Frequency, $\text{cm}^{-1}$	Vibrational mode
Amide A	3310-3270	$\nu(\text{N-H})$
Amide B	3100-3030	$\nu(\text{N-H})$ resonant with Amide II overtone
Amide I	1610-1695	$\nu(\text{C=O})$ 70%, $\nu(\text{C-N})$ , $\delta(\text{CCN})$ , $\delta(\text{N-H})$
Amide II	1480-1575	$\nu(\text{C-N})$ , $\delta(\text{N-H})$ (60%), $\delta(\text{C=O})$ , $\nu(\text{C-C})$ , $\nu(\text{C-N})$ (40%)
Amide III	1220-1320	$\nu(\text{C-N})$ , $\delta(\text{C=O})$ , $\nu(\text{C-C})$ , $\delta(\text{N-H})$ ,

In proteins, amide I band depends on the polypeptide backbone structure but not on the nature of the side chain. Nevertheless, amide I deconvolution reveals the secondary structure of protein which makes IR spectroscopy a valuable technique for investigation of protein structure and different processes such as folding, unfolding, and aggregation.

Table 2.4. Secondary structure assignment from Amide I band <sup>240</sup>.

Conformation	Band position (in $\text{H}_2\text{O}$ ), $\text{cm}^{-1}$	Band position (in $\text{D}_2\text{O}$ ), $\text{cm}^{-1}$
$\alpha$ -helix	1654	1652
$\beta$ -sheet	1633	1630
$\beta$ -sheet	1684	1679
Turns	1672	1671
Disordered	1654	1645

Despite all the benefits, IR spectra of proteins can be hard to attribute because of the overlapping contributions from different compounds (lipids, surfactants, buffer) and water vibrational modes in solution. These hurdles can be overcome by using deuterated solvents, isotope labelling, site-directed mutagenesis, and working with difference spectra of the protein reaction.

#### 2.4.2 FTIR differential spectroscopy coupled to electrochemistry

For the red-ox active enzymes IR spectra of the reduced and oxidized state look very similar, so differential spectroscopy is a good method to highlight the changes. In the same electrochemical cell (*see description in Annex A.3*) as for the UV-vis potentiometric titration, the protein reaction can be probed by applying a potential step and recording the IR spectrum before and after the change<sup>11</sup>. As a result, obtained difference spectrum reveals only the fingerprint of the conformational changes that has occurred avoiding the contribution from the solvent or humidity, Fig. 2.15.

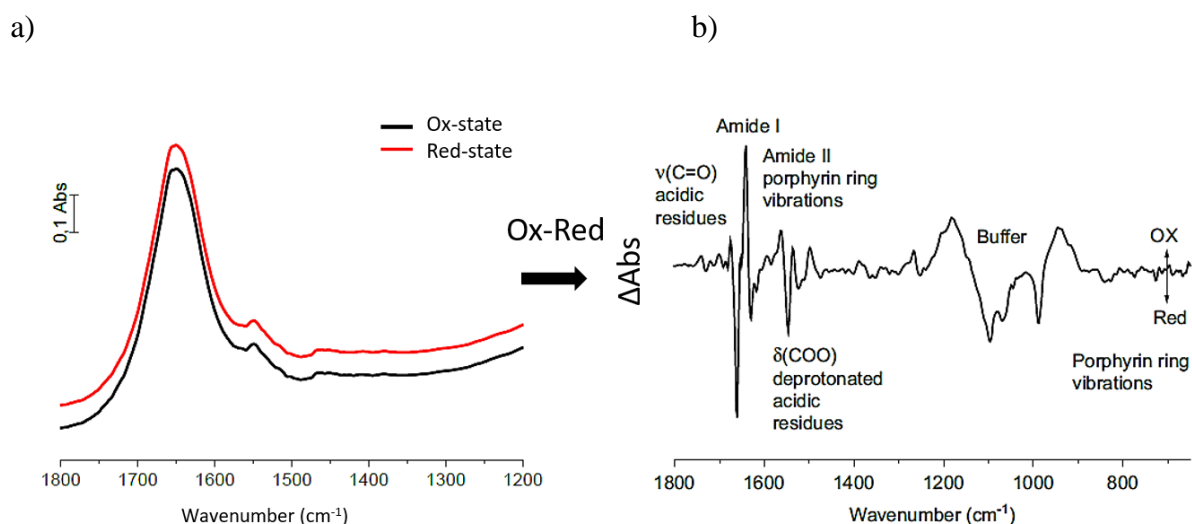


Figure 2.15. Schematic representation of the spectra of the oxidized and reduced forms (a) and redox-induced difference spectrum of the cytochrome *c* oxidase from *P. denitrificans* for the full potential step from -0.5 to 0.5 V vs. a Ag/AgCl reference electrode (b). Reproduced from reference <sup>242</sup>.

This technique is particularly useful for the proteins with several red-ox cofactors such that involved in the photosynthesis or respiration. If the mid-point potential of the cofactor is known, the red-ox induced difference IR spectroscopy in the thin-layer electrochemical cell allows a step-by-step potential control, so the study of the intermediates of the red-ox reactions is possible. From the technical point, it is important to keep the absolute absorbance of the most intense Amide I band lower than 1 to avoid the saturation and the correct subtraction of the solvent contribution. Additionally, difference spectra have much lower intensity thus the accumulation of the several cycles is needed (usually 60-80) to obtain an acceptable signal-to-noise ratio. Previous studies from the literature can help to attribute the bands <sup>240,243,244</sup>.

## 2.5 Raman spectroscopy of heme proteins

The Resonance Raman spectroscopy scattering is based on the light scattered inelastically from a sample. It is a powerful technique for the investigation of the metalloproteins because the RR spectra are rich in information about the environment, redox and spin state of the metal-containing cofactors such as hemes and iron sulfur clusters <sup>245,246</sup>. Additionally, the Resonance Raman is not influenced by the water comparing with IR spectroscopy. There are several characteristic contributions in the Raman spectra of the redox heme cofactors attributed to the skeletal modes, see Table 2.5. The nomenclature of the modes is proposed by Spiro et al <sup>246-248</sup>. The position and intensity of the RR signature reflect the changes in the environment of cofactors linked to the electron transfer or substrate binding, so that the reactions of the hemes can be monitored by Raman spectroscopy. Additionally,


vibrational modes of ligands bound to the hemes may be assigned by isotopic labeling, and therefore, their properties and structural changes can be studied.

Table 2.5. The redox and spin-sensitive vibrational modes of hemes observed in Raman spectroscopy

Mode	Wavenumber, $\text{cm}^{-1}$	Attribution <sup>249-252</sup>
$\nu_{10}$	1640-1620	$\nu(\text{C}_\alpha\text{C}_m), \nu(\text{C}_\beta\text{C}_\beta), \nu(\text{C}_\alpha\text{C}_\beta)$
$\nu_2$	1570-1600	$\nu(\text{C}_\beta\text{C}_\beta), \nu(\text{C}_\alpha\text{C}_m)$
$\nu_3$	1510-1470	$\nu(\text{NC}_\alpha), \nu(\text{C}_\alpha\text{C}_\beta), \nu(\text{C}_\alpha\text{C}_\beta)$
$\nu_4$	1370-1350	$\nu(\text{C}_\alpha\text{C}_\beta), \nu(\text{C}_\alpha\text{C}_m), \nu(\text{C}_\beta\text{C}_\beta)$

\*for the  $C_\alpha$ ,  $C_\beta$ , and  $C_m$  refer to the Fig. 2.10

Besides the benefits of the Resonance Raman spectroscopy for the protein study, the major drawback is that the Raman scattering generally is weak comparing to the IR. However, the sensitivity can be improved by adsorbing protein species on nanostructured metal surface giving the signal enhancement by the electric field, known as surface-enhanced Resonance Raman spectroscopy SERRS. It noteworthy that Resonance Raman technique is reserved to the study of the cofactors that absorb light in UV-Vis and NIR spectrum and not fluorescent.



# Chapter III

## Cytochrome *bd*-I oxidase of *E. coli* inhibition assay with Aurachins

---

### 3.1 Electrochemical sensor for protein inhibition study

3.1.1 Morphological study of the electrode modified with gold nanoparticles by scanning electron microscopy SEM

3.1.2 The choice of the thiols and lipids for cytochrome *bd*-I oxidase immobilization

### 3.2 Inhibition screening of cytochrome *bd*-I oxidase with Aurachin D derivatives

3.2.1 Activity screening by the electrochemical sensor with immobilized *bd*-I oxidase

3.2.2 Fast inhibition screening of Aurachin D synthetic analogues

3.2.3 Effect of the ubiquinol on the inhibition assay

3.2.4 Concentration dependent study to determine half-inhibitory constant of the lead compounds

### 3.3 Conclusions



It is estimated that about 80% of modern targets of the pharmaceuticals are the membrane proteins<sup>253</sup>. They are encountered for the multiple essential functions of any living cell, such as transport, signalling and respiration. Cytochrome *bd* oxidases is a unique family of membrane proteins found only in the respiratory chain of prokaryotes, including several pathogens such as *Escherichia coli*, *Mycobacterium tuberculosis*, *Salmonella* and *Klebsiella pneumoniae* which cause a number of life-threatening diseases. It is believed that *bd* oxidases also play a crucial role in bacteria protection against oxidative and nitrosative stress<sup>5,254,255</sup>, as well as in their virulence, adaptability and resistance to antibiotics<sup>177,182,256</sup>. Thanks to its exclusive properties, the enzyme is a potential target for the development of next-generation antimicrobial agents<sup>56</sup>.

In this chapter the electrochemical assay was used for the inhibition screening of a quinol-like library of small molecules against cytochrome *bd* oxidase. This work aims at identifying effective inhibitor hits that can serve as useful templates for further derivatization of compounds with potent antibiotic effect. These studies will provide helpful data for the development of new antibiotics with the new modes of action.

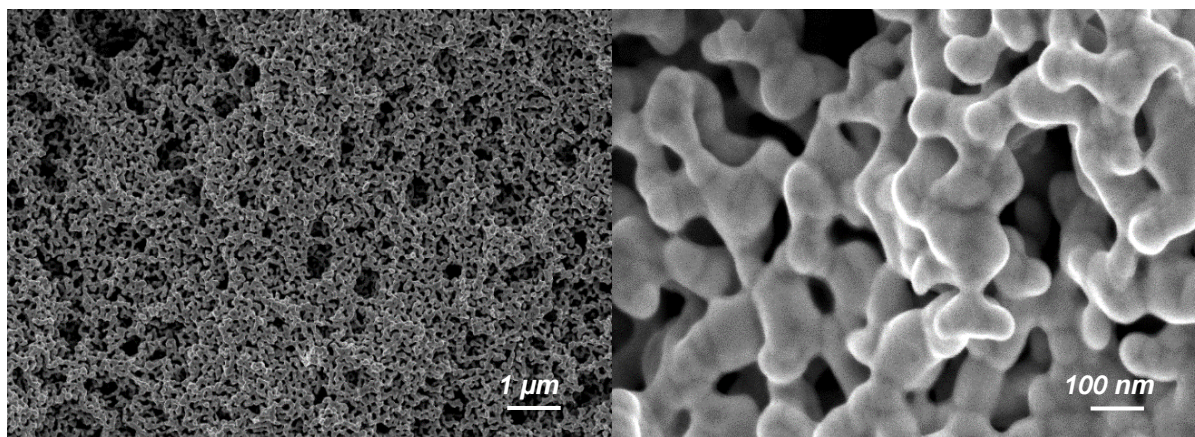
### 3.1 Electrochemical sensor for cytochrome protein inhibition study

Due to their hydrophobic nature, membrane proteins are more difficult to handle than soluble ones. Previously, in our research group, the technique of enzyme immobilization on 3D gold nanoparticles electrodes modified with self-assembled monolayer of thiols was developed<sup>10,56,257</sup>. This method can be customized to small proteins ranging from cytochrome *c* to various heme copper oxidases *aa<sub>3</sub>*, *ba<sub>3</sub>*, *bo<sub>3</sub>*, and *cbb<sub>3</sub>* in the respiratory chain. The optimization and preparation of the bioelectrochemical sensor for the effective immobilization of the cytochrome *bd*-I oxidase film on rotating gold electrode will be discussed in this chapter. The method of immobilization consists of three steps and it was optimized to last less than three hours<sup>10</sup> (see in *Annex B.3.4*).

#### 3.1.1 Morphological study of the electrode modified with gold nanoparticles by scanning electron microscopy SEM

The morphology of the rotating gold electrode after the modification with gold nanoparticles was characterized by SEM in the Institute Physical and Chemistry Materials of Strasbourg (IPCMS-UMR 7504). The electrode surface after the single addition of 7  $\mu$ L of 15 nm gold nanoparticles concentrated solution is shown in Figure 3.1 at 1  $\mu$ m and 100 nm

magnification. The formation of a highly porous structure which consists of interconnected ligaments of 25 to 100 nm in width, which form uniformly distributed pores that are 40-80 nm



in diameter is observed.

Figure 3.1. SEM images of the electrode surface after single deposition of the gold nanoparticles at  $1\mu\text{M}$  (a) and evaluation of the of ligaments size at 100 nm scale (b).

Following the surface investigation, electrochemical characterization of the modified electrode was performed in 0.1 M  $\text{H}_2\text{SO}_4$ . Results of the cyclic voltammetry experiment with nanostructured electrode showed the significant increase in the surface area (Fig. 3.2). By integrating the reduction peak of gold oxide monolayer at +1.1 V vs SHE, assuming the charge to be  $390\ \mu\text{C}\cdot\text{cm}^{-2}$ <sup>258</sup>, the calculations showed that the electrochemically active surface area of modified with nanoparticles electrode was approximately 8 times larger compared with a bare gold electrode, from 0.13 to  $1.1\ \text{cm}^2 \pm 5\%$ .

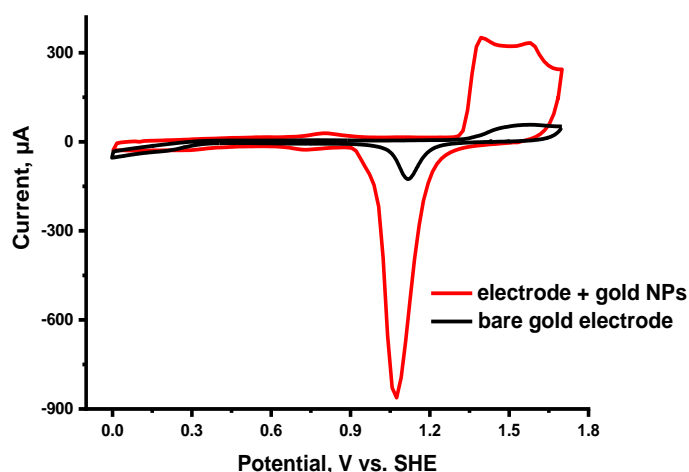


Figure 3.2. Cyclic voltammograms of a modified NPs electrode (red curve) and a flat gold electrode (black curve) with the same geometric area in 0.1 M  $\text{H}_2\text{SO}_4$  solution at scan rate of  $0.1\ \text{V}\cdot\text{s}^{-1}$ .

SEM technique was used to estimate the influence of the next step of biosensor modification on the surface morphology. The surface rugosity from the side views after the overnight deposition of a self-assembled layer of neutral (1:1 mixture of 1-hexanthiol and 6-mercaptohexan-1-ol) and negatively charged thiols (equimolar mixture of 1-hexanthiol, 6-mercaptohexan-1-ol, mercaptohexanoic acid) are shown on Figure 3.3. It is seen that both mixtures of thiols do not disrupt the pore morphology and have similar crater-like 3D nanostructure profile.

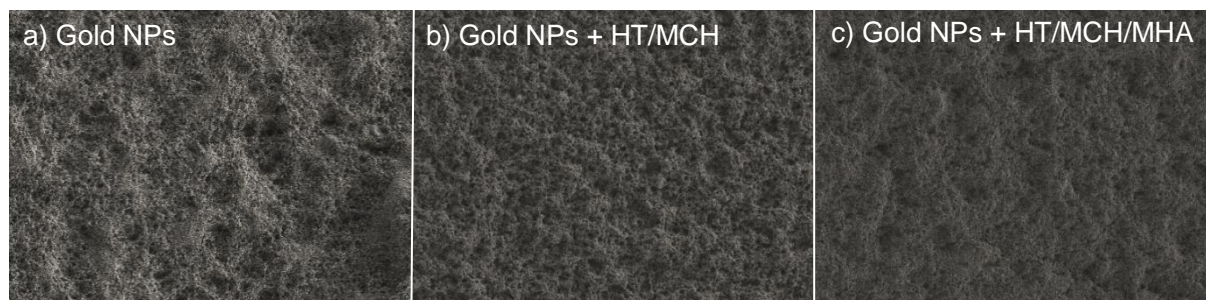


Figure 3.3. The evaluation of rugosity at  $10\mu\text{m}$  scale of 3D gold nanoparticle electrode (a) and electrodes after overnight incubation with neutral thiols (b) and negatively charged thiols (c).

It is important to verify the stability of the porous gold nanostructure after the incubation in thiol solution in the real time scale for the fast preparation of the electrochemical sensor. The modified electrodes were tested after one-hour incubation in ethanol solution of thiols. It is known the physisorption and the Au-S bond formation of the 90% thiols attached takes less than 10 min. It is followed by the slow stage of the correction of the conformational defects for the next 7 hours<sup>259</sup> to form the well-organized rigid SAM. Here the one-hour incubation time is a good compromise for obtaining the flexible SAM coverage for the protein immobilization and the stable signal of the sensor<sup>260,261</sup>. The top views at the 200 nm scale shows the high porosity of the surface with an average size of the pores from 30 to 80 nm in diameter. Although the presence of mercaptohexanoic acid in the SAM structure seems to form more densely packed porous surface, it does not perturb the 3D gold nanoparticles organization on the electrode.



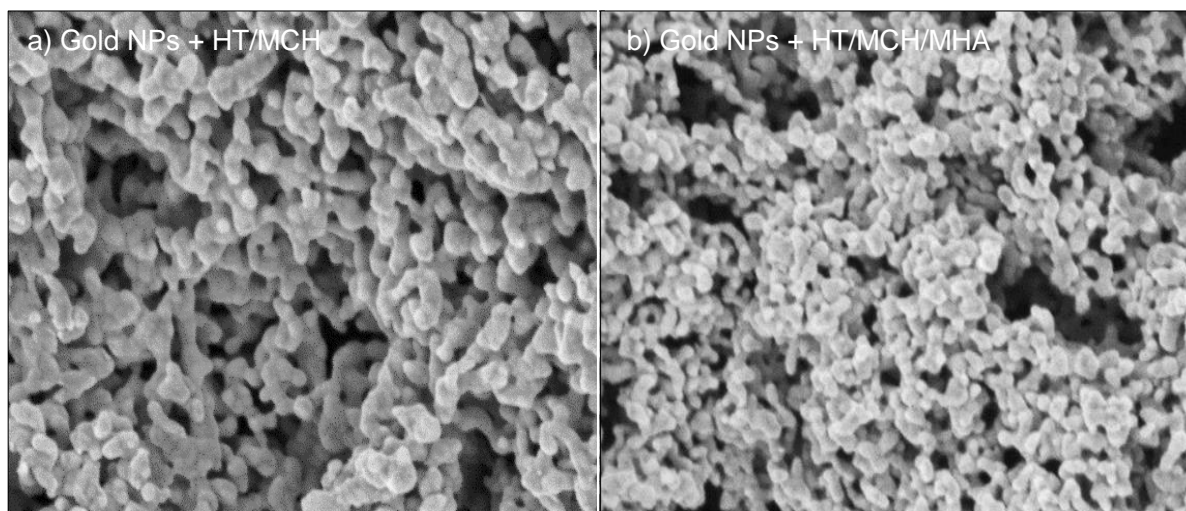


Figure 3.4. Evaluation of porosity at the 200 nm scale of 3D gold nanoparticle electrode after 1h incubation with neutral thiols (a) and negatively charged thiols (b).

In conclusion, all modified electrodes, with and without thiols layer show the formation of a highly porous surface after deposition of the gold nanoparticles. The rugosity at 10 $\mu$ m scale is not changed after formation of the thiols SAM and the thiols layer does not perturb the 3D porous nanostructure on the electrode. However, the organic layer covering gold nanoparticles is hardly visible, and the differences between neutral and negatively charged SAMs of thiols cannot be distinguished.

### 3.1.2 The choice of the thiols and lipids for cytochrome *bd*-I oxidase immobilization

The nature and charge of the thiols SAM have a direct impact on the stability of the protein film on the electrode surface and electrocatalytic properties<sup>261,262</sup>. It is crucial to choose the suitable match of the thiol mixture with the protein surface for obtaining stable cytochrome *bd* oxidase films on the modified gold electrode. To preserve the catalytic properties of the studied enzyme on the electrode surface the presence of lipids is essential. More generally, interactions between lipids and protein are crucial for the structural integrity of membrane enzymes and can directly influence the redox potential of the hemes<sup>263–265</sup>.

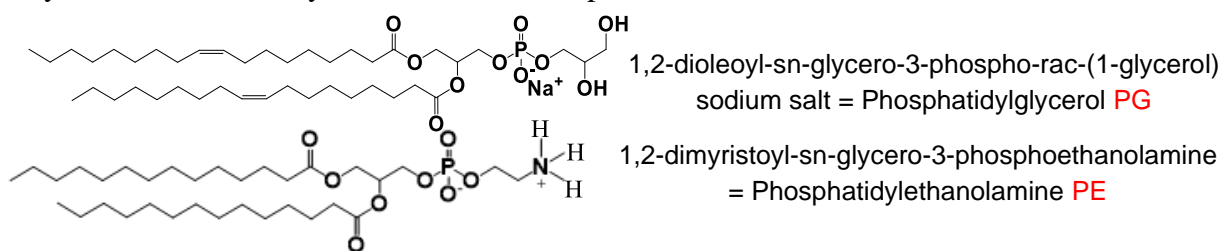


Figure 3.5. Structure of the lipids probed for the protein film stability examination.

The samples of cytochrome *bd*-I oxidase were immobilized on both neutral and negatively charged SAMs composed of an equimolar mixture of polar and non-polar thiols (1:1 HT and MCH) and the same mixture with addition of mercaptopropionic acid (MPA), mercaptohexanoic acid (MHA), mercaptoundecanoic acid (MUA), respectively (Fig.3.6). The studied enzyme was previously incubated with the 2.5% zwitter ionic lipid phosphatidyl ethanolamine PE or 2.5% negatively charged phosphatidyl glycerol PG, phospholipids that are naturally present in high amount in *E. coli* membranes<sup>13,55</sup> (Fig.3.5).

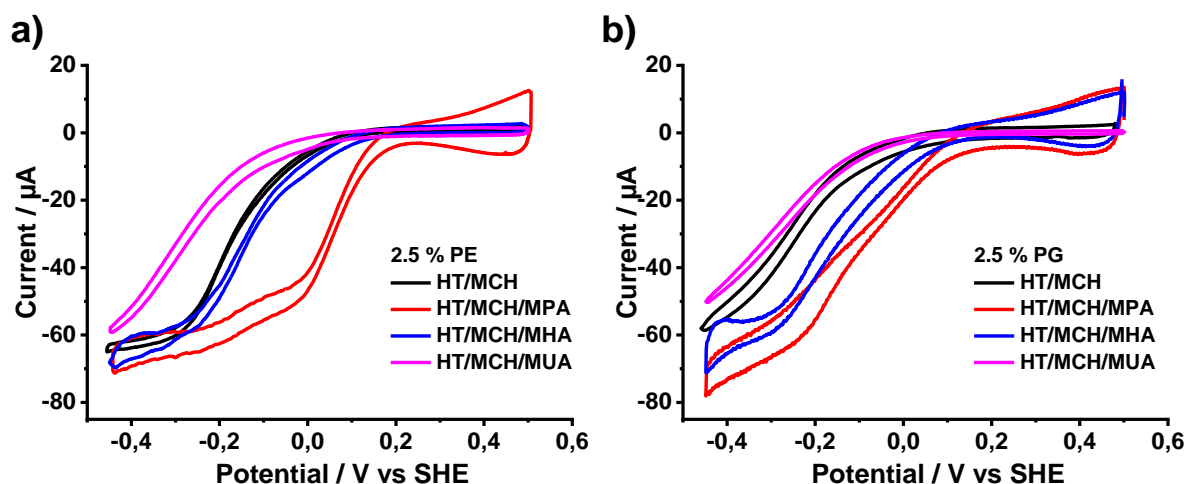


Figure 3.6. Voltammograms obtained for cytochrome *bd* oxidase with added 2.5% PE (a) and 2.5% PG (b) on gold NPs modified with HT/MCH (1/1) (black trace), HT/MCH/MPA (1/1/1) (red trace), HT/MCH/MHA (1/1/1) (blue trace) and HT/MCH/MUA (1/1/1) (pink trace).

For both *bd*-I samples incubated with PE and PG, the longer the chain of the negatively charged thiols the more negative the half-wave potential of the catalytic curve  $E_{\text{cat}}$  was obtained (see Table 3.1). The mixture with MUA showed the lowest  $E_{\text{cat}}$  and catalytic current in the two tested series. It was explained by Nikolaev et al.<sup>261</sup> that the longer distance between the electrode surface and protein redox cofactors due to the longer chain of the thiol linker decreases the interfacial electron transfer and thus the reaction occurs at higher overpotential. Even though thiols mixture with MPA led to the highest  $E_{\text{cat}}$ , this mixture is not suitable for the electrochemical sensor. The mixture of thiols with MHA that had the similar  $E_{\text{cat}}$  in the presence of the PE and PG, -147 mV and -151 mV, respectively. Looking at the shape of the curves, a true plateau is only obtained with 2.5% PE and HT/MCH thiols. For all the other conditions tested, the voltammograms does not reach a plateau. Therefore, for the sensor the conditions 2.5% PE and HT/MCH thiols were selected.

Table 3.1. Half wave catalytic potential ( $E_{cat}$ ) obtained for the protein samples incubated with 2.5% phospholipids with different thiols mixtures. Standard error of measurements is 20 mV for  $E_{cat}$ .

<i>bd</i> -I sample incubated with 2.5% PE	$E_{cat}$ / mV vs SHE	<i>bd</i> -I sample incubated with 2.5% PG	$E_{cat}$ / mV vs SHE
<i>HT/MCH</i>	-168	<i>HT/MCH</i>	-223
<i>HT/MCH/MPA</i>	+57	<i>HT/MCH/MPA</i>	-138
<i>HT/MCH/MHA</i>	-147	<i>HT/MCH/MHA</i>	-151
<i>HT/MCH/MUA</i>	-284	<i>HT/MCH/MUA</i>	-276

The influence of lipids on the cytochrome *bd*-I oxidase film stability was tested via cyclic voltammetry after the overnight incubation of the protein solution with 2.5 % PE, 2.5 % PG or a mixture of both 1.25% PE/1.25 % PG on a neutral SAM. It should be noted that *bd* oxidases purification conditions (amount and type of detergent used, salt content) influence the residual lipid content in the batch, therefore, the protein immobilization conditions should be tuned for each new protein preparation. For the protein batch used, a suitable protein stability and higher catalytic current were observed for the films on gold nanoparticles modified with a mixture of neutral thiols HT and MCH so for the examination of the lipid effect this SAM modification was chosen. Figure 3.7 presents the resulting voltammograms, where noticeably, the highest catalytic current and the best stability were reached with zwitterionic PE.

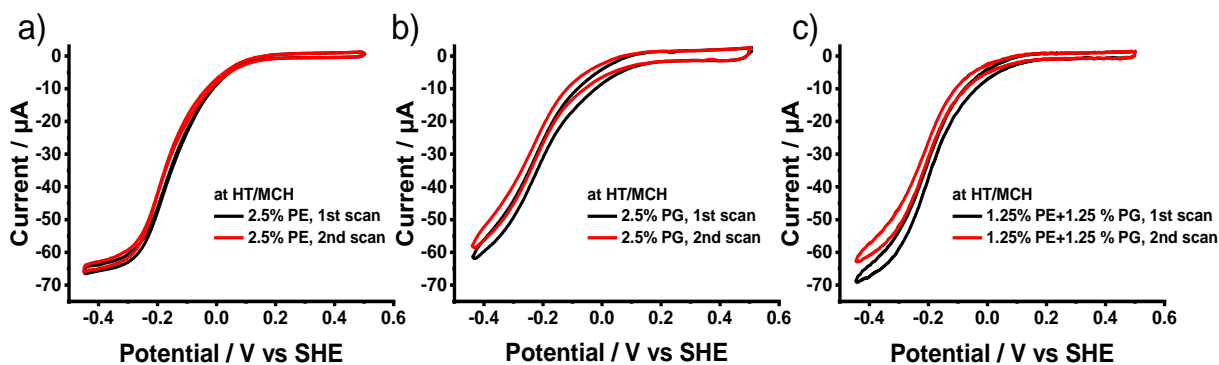


Figure 3.7. Two consecutive voltammograms obtained for cytochrome *bd* oxidase modified with HT/MCH SAM and with 2.5% PE (a), 2.5% PG (b) and with 1.25% PE + 1.25% PG (c) incubated with protein solution.

Previously it was shown that there is a mutual influence of the lipid and electrode surface charge: with delipidated *bd* oxidase sample the best electrocatalytic responses were obtained on neutral gold surface when negatively-charged PG was used and on charged gold surface when zwitterionic PE was used<sup>261</sup>. Here, the stability was evaluated from the decrease of the catalytic current  $\Delta i/i$  after two voltammograms of 10 min interval in the region of the limiting current. The kinetic efficiency of the oxygen reaction was estimated from the half

wave potential  $E_{cat}$  of the sigmoidal curve. Additionally, the slope  $\Delta i/\Delta E$  in the region of the limiting current gives information on the favorable orientation of the protein for the interfacial electron transfer<sup>266</sup>. The obtained results of the examined parameters are summarized in the Table 3.2.

Table 3.2. Half wave catalytic potential ( $E_{cat}$ ), slope of the limiting current ( $\Delta i/\Delta E$ ) and variability of the limiting current value between two consecutive scans ( $\Delta i/i$ ), obtained for the proteins with different lipids. Standard errors of measurements (SEMs) are 20 mV for  $E_{cat}$ , 0.003 A·mV<sup>-1</sup> for  $\Delta i/\Delta E$  and 0.02 for  $\Delta i/i$ .

Sample	$E_{cat}$ / mV	$\Delta i/i$ , %	$\Delta i/\Delta E$ / $\mu\text{A}\cdot\text{mV}^{-1}$
2.5% PE	-172	1.21	0.046
2.5% PG	-242	5.48	0.102
1.25% PE + 1.25% PG	-204	8.98	0.072

In summary, the protein sample incubated with 2.5% PE showed the best catalytic response of the prepared electrodes with a signal loss of less than 2 % after each scan. Interestingly, for this sample  $E_{cat}$  was also higher but the values for the other two lipid combinations were very close. The stability of the protein film drastically decreased when the mixture of the PE and PG phospholipids was used, it may be caused by the presence in the sample of one of the lipid types in great amount after the preparation. It might be suggested that for the stability and proper catalytic function a certain equilibrium of the PE and PG lipids in the protein film is required. For this batch, 2.5% PE added to *bd-I* oxidase solution also showed the highest level of the homogeneity in protein orientation for a favorable electron transfer.

The above determined parameters were adapted for the stable and fast response of the immobilized cytochrome *bd-I* oxidase on the 3D gold nanostructured electrode modified by thiolated SAM. Thus, the contribution of 2.5% of the zwitterionic phospholipids to the protein attached on neutral gold surface (1:1 HT and MCH) assured the stability of the electrochemical sensor for a primary screening of a library of small molecules for the identification of inhibitors against this respiratory chain enzyme.

## 3.2 Inhibition screening of cytochrome *bd*-I oxidase with Aurachin D derivatives

Cytochrome *bd* oxidase is one of the enzymes in bacterial cells that ensure reduction of molecular oxygen to water upon the diverse environmental conditions and oxidative stress<sup>159</sup>. The main catalytic reaction happens after the oxidation of the hydrophobic quinols, ubiquinol UQ and menaquinol MQ in *Escherichia coli*. All redox cofactors, namely heme *d*, heme *b*<sub>558</sub> and heme *b*<sub>595</sub>, are located in CydA subunit that also contains a hydrophilic loop, the Q-loop, involved in quinone binding and contribute to the structural integrity of the entire enzyme complex<sup>122,267,268</sup>.

By selective inhibition of the quinol-binding site of terminal oxidase, the electron transfer chain is disrupted and oxygen reduction is blocked causing respiration deficiency for the pathogenic bacteria. In the literature, only few selective inhibitors were discovered against cytochrome *bd*-I oxidase, such as the isoprenoid quinolone alkaloids aurachins C and D<sup>15,174,269</sup>, some prenylphenols isolated from fungi<sup>270</sup>, the indole derivative MQL-H2<sup>184</sup>, and a very recently reported antimicrobial peptide MccJ25<sup>271</sup>. Among the above listed, Aurachin D shows a high inhibitory activity against cytochrome *bd*-I oxidase from *E. coli*, but not against the cytochrome *bo*<sub>3</sub> oxidase, which belongs to the heme copper oxidase family of enzymes found in mammalian cells. Previously, in our research group an electrochemical sensor was used to identify inhibitors of the protein in a focused library of 34 compounds which belong to the families of quinones, naphthoquinones, phenols, quinolones, coumarins and flavonoids<sup>260</sup>. Now, the developed electrochemical assay based on the immobilization of the cytochrome *bd*-I oxidase on electrodes modified with gold nanoparticles was employed for the testing of the inhibitory potency of more complex compounds than the primary hits. The aim of this study was to determine the most potent inhibitor against cytochrome *bd*-I oxidase out of synthetic derivatives of Aurachin D.

### 3.2.1 Activity screening by the electrochemical sensor with immobilized *bd*-I oxidase

The typical sigmoidal-shaped voltammograms (black curves, Figure 3.8) proves the reduction of molecular oxygen at the electrode catalyzed by the immobilized proteins. In control experiments with electrode in the absence of protein they are not observed. There are three possible responses upon testing molecules with ubiquinone-like scaffold against the cytochrome *bd*-I oxidase.

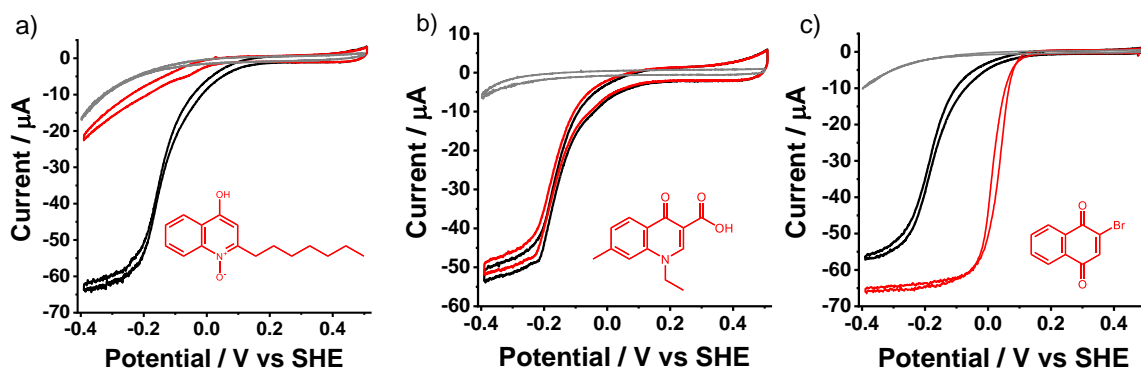


Figure 3.8. Cyclic voltammograms of the cytochrome bd-I oxidase oxygen reduction (black curves) alone and after addition of the 50  $\mu\text{M}$  HQNO a), nalidixic acid b), and 2-bromo-1,4 naphthoquinone c) (red curves), grey curves represent control voltammograms before protein immobilization.

In figure 3.8a, it is shown that after addition of 50  $\mu\text{M}$  of 2-Heptyl-4-hydroxyquinoline-N-oxide (HQNO), a non-selective inhibitor of quinol-binding site<sup>15</sup>, the voltammogram turns back to background levels, so most of the immobilized proteins have lost their activity. However, the addition of the same concentration of nalidixic acid, an antibiotic which is known to inhibit the transcription and replication of DNA in gram-negative bacteria<sup>255</sup>, has no effect on the voltammograms (Figure 3.8b) and thus it has no inhibition activity against cytochrome bd oxidase. The 2-bromo-1,4-naphthoquinone, the bromide derivative of the menaquinone, shows a rather unexpected activating effect on the immobilized proteins (Figure 3.8c). It leads to both an increase in the catalytic current and a shift of the catalytic potential from -0.15 V to 0.03 V. Thus, the reduction of  $\text{O}_2$  at the electrode requires less overpotential and occurs with a higher turnover.

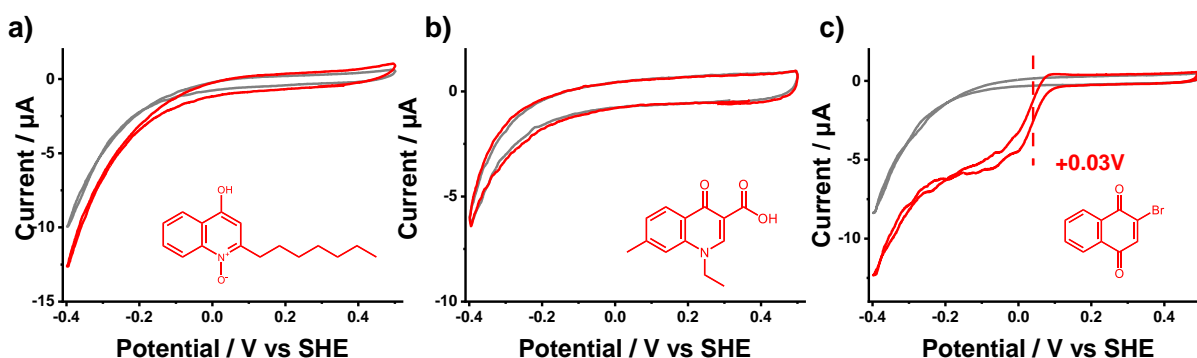


Figure 3.9. Control cyclic voltammograms in the absence of protein (grey curves) and effect of the added 50  $\mu\text{M}$  HQNO a), nalidixic acid b), and 2-bromo-1,4 naphthoquinone c) (red curves).

It is noted that in the control experiment on the electrode without immobilized protein HQNO and nalidixic acid did not show any redox signals in the tested range of potentials, Figure 3.9a, b. In contrast, in Figure 3.9c, the 2-bromo-1,4-naphthoquinone showed a reduction

signal at +0.03 V, which is in the same range of potentials where the reduction of O<sub>2</sub> by the protein occurs in the presence of this molecule. The naphthoquinone thus probably acts as a redox mediator, making the electron transfer between the electrode and the immobilized proteins more efficient. It can be explained by the proximity of 2-bromo-1,4-naphthoquinone reduction potential to the midpoint potentials of protein hemes: +0.17, +0.18 (hemes *b*) and +0.26 V (heme *d*) at pH 7<sup>14</sup>, so it is able to transfer its electrons to the enzyme redox cofactors. Another explanation can be linked to the fact that cytochrome *bd*-I oxidase from *E. coli* can accommodate both 1,4-benzoquinone derivatives (ubiquinone) and 1,4-naphthoquinone derivatives (menaquinone) substrates as electron donors with redox potentials of +0.11 V and -0.08 V at pH 7 respectively<sup>272,273</sup>, while the 2-bromo-1,4-naphthoquinone also exhibits a reduction potential in this range (+ 0.03 V).

This electrochemical assay allows us to identify inhibitors of cytochrome *bd*-I oxidase that compete with the ubiquinone substrate at the “Q-loop” and block the transfer of electrons to the active site. On this basis, the inhibitory potency of synthetic derivatives of the well-known selective inhibitor of quinol-binding site Aurachin D was evaluated in a fast-screening procedure at 10 μM concentration.

### 3.2.2 Inhibition screening of Aurachin D synthetic analogues

Previously, the inhibitory potency of a different compounds that are structurally related to the quinol substrate was evaluated at a 10 μM concentration against *bd*-I oxidase immobilized on gold electrode. As a result, the hit scaffolds were chosen to be promising for the next modification<sup>260</sup>. The quinolones substituted by alkyl or iodine substituents in position C-2 and C-3 showed an inhibitory effect better than 10%. In contrast, the quinolones with no substituent or polar substituents such as hydroxy, carboxylic acids or esters showed no or little inhibition towards cytochrome *bd*-I oxidase, which strongly suggests that the quinone binding pocket contains hydrophobic residues.

In order to increase the inhibitory efficiency of the initial hit fragments a series of more complex natural product-based quinolones were synthesized by our collaborators from Saarland University using the Conrad-Limpach cyclization<sup>260</sup>. The present compounds are the synthetic analogues of the quinolone alkaloid Aurachin D which resembles the ubiquinol scaffold, the detailed scheme of the synthesis of AD-4 molecules is showed in ref<sup>260</sup>. Among this library all compounds have a methyl group in C-2 position and differ by substituent in C-3 position, isoprenoid chain of various length and halogen or methyl group, Figure 3.10.

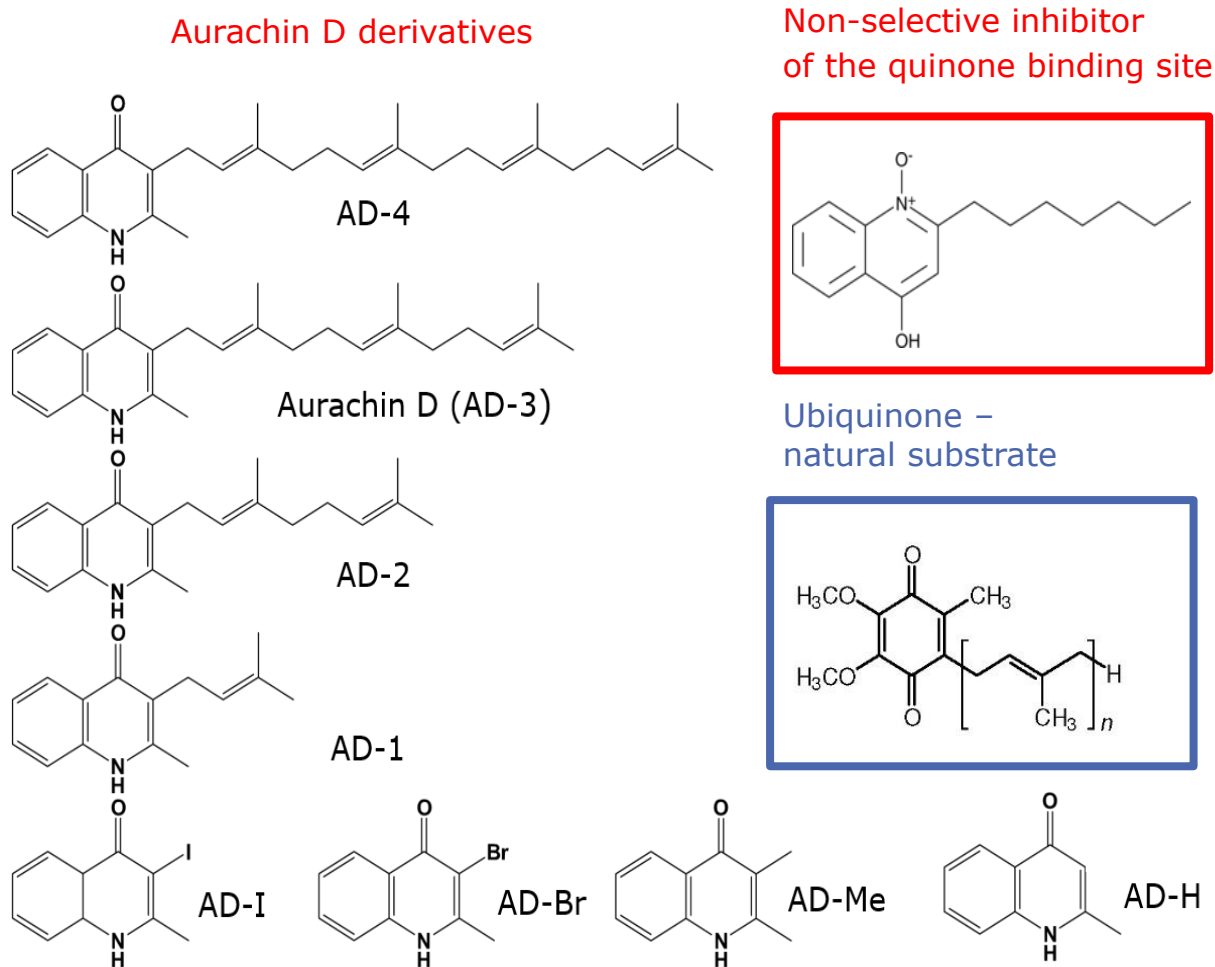


Figure 3.10. Structures of the Aurachin D analogues tested in the inhibition study towards *bd-I* oxidase immobilized on gold electrode.

The inhibition efficiency at 10  $\mu\text{M}$  concentration was determined from the decrease of the maximum current value at -0.4 V (Figure 3.11). Before every inhibition test three subsequent voltammograms with 10 min interval were recorded to verify the proper stability of the enzyme immobilized on the electrode. A decrease in the catalytic current of more than 5% was considered as unacceptable to carry on the experiment. A freshly prepared electrode was used for each inhibitor, and the measurements were repeated with three different electrodes in order to report the mean values and standard deviations. The inhibition activity of the proposed compounds was compared with the non-selective inhibitor of the quinol-binding site HQNO. Additionally, the protein solutions were incubated 24 hours before the immobilization without and with 3 and 12 equivalent excesses of quinone in order to test whether the inhibition



is competitive or not. The results of the inhibitory activity at a single addition of 10  $\mu\text{M}$  with or without added ubiquinone substrate are summarized in the Table 3.3.

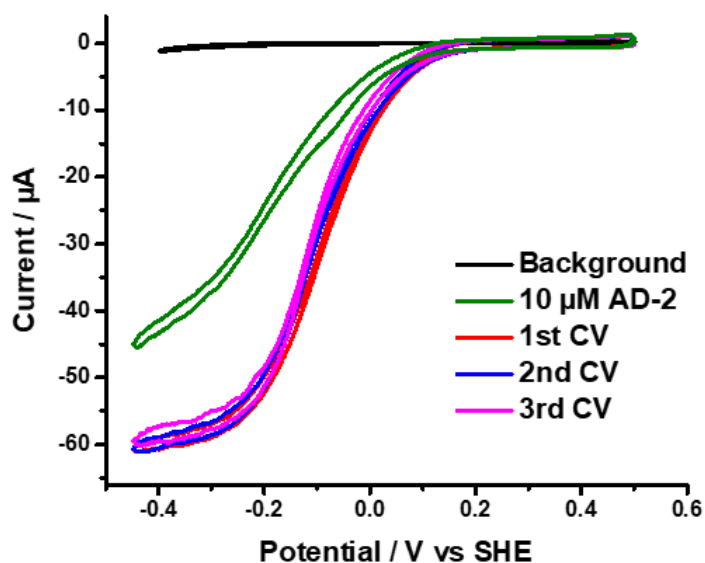


Figure 3.11 Inhibition of *bd-I* oxidase activity upon introducing 10  $\mu\text{M}$  AD-2 solution in DMSO (green curve) after verifying the stability of the electrode signal by 3 subsequent CVs (red, blue and pink curve), the control CV without added protein is showed in black.

The results of the fast inhibition screening indicate that the inhibition effectiveness decreases as follows:



Table 3.3. Inhibition activity at a single concentration of 10  $\mu\text{M}$  with or without added quinone cytochrome *bd* oxidase of HQNO and synthetic aurachin D analogues.

Compound	Inhibition at 10 $\mu\text{M}$ (%)		
	without added UQ <sub>1</sub>	with 3 eq UQ <sub>1</sub>	with 12 eq UQ <sub>1</sub>
HQNO	21 $\pm$ 3.1	24 $\pm$ 3.4	27 $\pm$ 4.4
AD-1	16 $\pm$ 1.1	17 $\pm$ 2.4	19 $\pm$ 1.1
AD-2	37 $\pm$ 1.8	23 $\pm$ 3.8	15 $\pm$ 0.7
AD-3	27 $\pm$ 1.2	19 $\pm$ 3.9	10 $\pm$ 0.1
AD-4	6 $\pm$ 2.3	7 $\pm$ 1.5	-
AD-H	1 $\pm$ 0.7	3 $\pm$ 0.9	-
AD-I	11 $\pm$ 0.4	6 $\pm$ 0.6	-
AD-Br	6 $\pm$ 0.9	10 $\pm$ 4.4	-
AD-Me	5 $\pm$ 3.1	2 $\pm$ 1.3	-

It was shown that the quinolones without a substituent and substituted by alkyl or halogen in C-3 position exhibit less than 15 % of inhibition against cytochrome *bd-I* oxidase,

only AD-I exhibits activity of more than 10 %. Meanwhile, the length of isoprenyl chain in this position plays a crucial role in the inhibition activity, however, it does not grow proportionally to the increasing hydrophobicity (Fig. 3.12). In the series of AD-1 to AD-4, an increase of inhibitory activity is observed here from one to two isoprene repetitive units followed by a rapid decrease for the molecules with longer isoprenoid chain. Noteworthy, these data are not influenced by the limited solubility of the most lipophilic compounds AD-3 and AD-4 in the buffer solution, as it was probed for all compounds on model solutions by UV measurements at 10  $\mu$ M concentration level.

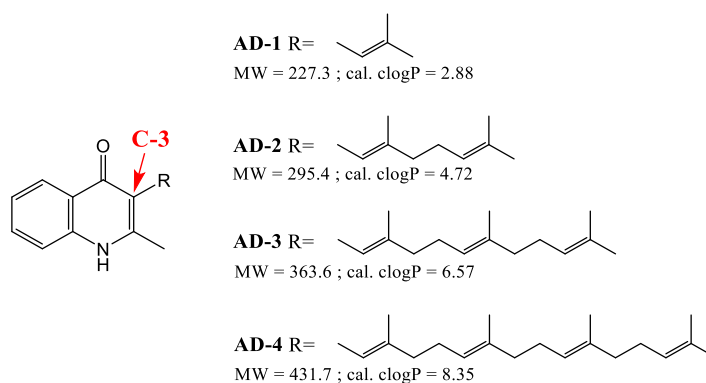


Figure 3.12 Log *P* values calculated for the series compounds varied in the length of isoprenyl chain in C-3 position.

The highest activity is observed for the AD-2 compound, that seems to be the most efficient inhibitor in this series. It may be explained by the shape of the quinol binding site of the protein, that is not able to accommodate molecules with too bulky substituents. Interestingly, the activity of AD-2 was higher than the values for a well-known inhibitor Aurachin D (AD-3) within all ranges of ubiquinol excess. However, it is known that cytochrome *bd*-I oxidase binds physiological substrate ubiquinol with eight isoprene repetitive units thus steric effects alone cannot explain the influence of chain length observed here. It might be explained by the specific interaction with the flexible N-terminal domain of the Q-loop rather than the stickiness of the molecules alone.

Additionally, an interesting correlation between the inhibitor potency and the amount of added ubiquinone was spotted. The inhibition efficiency of AD-2 and AD-3, the most active compounds, significantly decreases with the increased quantity of the quinone incubated with the protein solution. Meanwhile, for the less active molecules, AD-1 and AD-4, no strong effect of quinone is observed. This suggests that Aurachin D and synthetic derivative AD-2 compete with the natural substrate of the enzyme for the quinol-binding site.

## 3.2.3 Effect of the ubiquinol on the inhibition assay

Following the interesting features in the effect of added ubiquinone on the activity of the tested Aurachins, additional data analysis was performed to confirm the fact of the competitive inhibition. From the concentration dependent experiment for the lead compound from the 10  $\mu\text{M}$  fast screening AD-2 (Fig. 3.13a) the Henderson model for the tight-binding inhibitors with one binding site per protein was employed<sup>233</sup>.

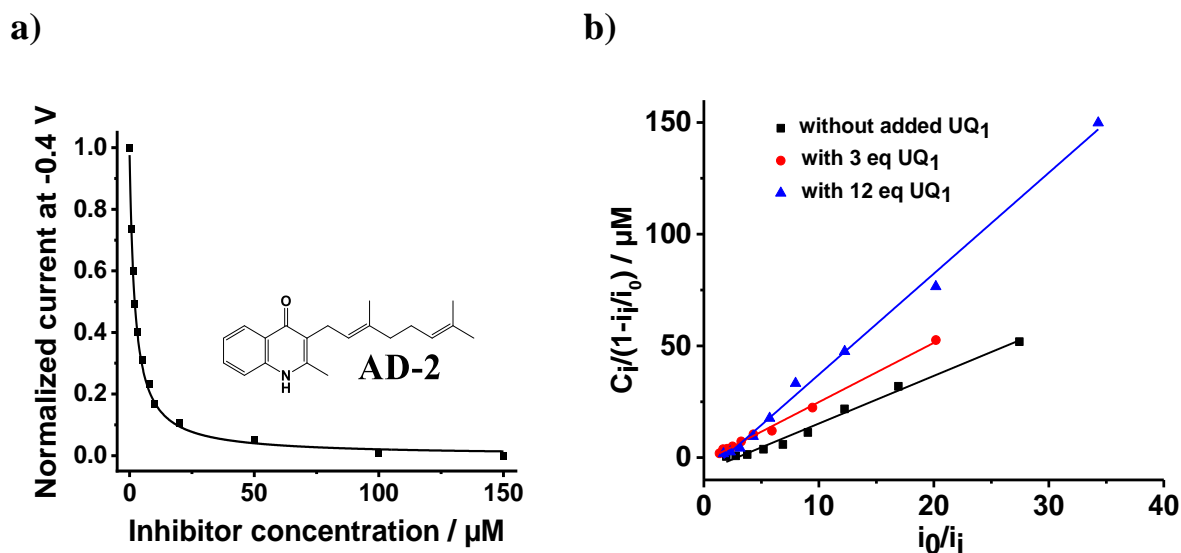


Figure 3.13. a) Concentration dependent inhibition of the *bd-I* oxidase immobilized on gold 3D electrode by AD-2; b) Henderson plots obtained for the AD-2 at different amount of ubiquinol in protein sample.

As a result, the plots of the quantity  $C_i/(1 - i/i_0)$  as a function of  $i_0/i$  at various amounts of added ubiquinone substrate were obtained, Fig.3.13b. In this expression,  $C_i$  is the concentration of inhibitor,  $i$  the residual catalytic current at -0.4 V and  $i_0$  the catalytic current in absence of inhibitor. Here the slope of the Henderson plot clearly increases with the concentration of the substrate (UQ<sub>1</sub>) from 2.13  $\mu\text{M}$  without ubiquinol added to 2.65 and 4.52  $\mu\text{M}$  at 3 equivalents and 12 equivalents ubiquinol excess respectively. This is again proving that Aurachin D derivative with two isoprenoid units act as a competitive inhibitor of the *E. coli* *bd-I* oxidase.

## 3.2.4 Concentration dependent study to determine half-inhibitory constant of the lead compounds

For the series of molecules with different length of isoprenyl side chain, a concentration-response analysis was carried out (Fig. 3.14a). Several aliquots of the inhibitor stock solution in DMSO were added to the 20 mL buffer solution and voltammograms were recorded with 10 min interval. By plotting the decrease of the catalytic current at -0.4V as a

function of the inhibitor concentration, the half-inhibitory concentration  $IC_{50}$  were determined using the optimized electrochemical sensor.

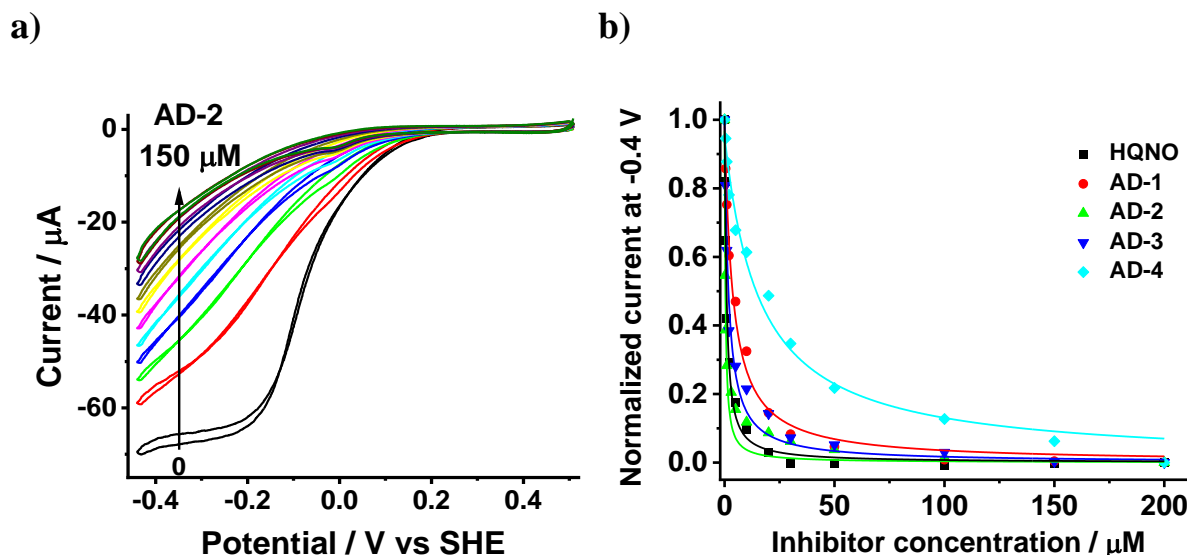


Figure 3.14. a) Inhibition effect of the AD-2 on the activity of *bd*-I oxidase immobilized on the nanostructured electrode; b) Plot of the normalized current at  $-0.4V$  versus the concentration of Aurachin D derivatives and HQNO. Conditions: air-saturated pH 7 phosphate buffer, scan rate  $0.02V/s$ , rotation speed  $1000\text{ rpm}$ .

Calculated  $IC_{50}$  constants were compared with those of non-selective inhibitor of the quinol-binding site HQNO, Table 3.4. It is noted that the electrochemically determined values were found in the micromolar range, what is higher than the values determined in solution due to the immobilization of the enzyme. For instance, in literature the  $IC_{50}$  reported for Aurachin D towards cytochrome *bd* oxidase from *E. coli* are in nanomolar level<sup>15,174</sup>. Here without added ubiquinol to the protein sample we obtained half-inhibitory concentration of  $2.2\mu M$  for AD-3. It can be explained by the orientation of the quinol-binding site on the electrode surface in the way that access to it is limited. It would be interesting to compare  $IC_{50}$  values determined in the assay with proteins in dispersed membranes<sup>174</sup>. These measurements with immobilized protein within a lipid bilayer membrane on the surface of the electrode might promote the interaction between lipophilic molecules and the membrane proteins and could improve the sensibility of the present assay.

Table 3.4. Half-inhibitory constants calculated for the compounds having the stronger inhibiting activity.

Compound	IC <sub>50</sub> / $\mu$ M		
	without added UQ <sub>1</sub>	with 3 eq UQ <sub>1</sub>	with 12 eq UQ <sub>1</sub>
<b>HQNO</b>	1.1 $\pm$ 0.2	2.3 $\pm$ 0.3	2.5 $\pm$ 0.5
<b>AD-1</b>	3.8 $\pm$ 0.1	7.6 $\pm$ 0.3	2.7 $\pm$ 0.3
<b>AD-2</b>	1.1 $\pm$ 0.7	1.7 $\pm$ 0.4	0.9 $\pm$ 0.2
<b>AD-3</b>	2.2 $\pm$ 0.5	3.3 $\pm$ 0.8	3.9 $\pm$ 0.6
<b>AD-4</b>	14.4 $\pm$ 0.5	15.8 $\pm$ 0.9	-

The obtained results exhibit a similar tendency in the activity determined at 10  $\mu$ M concentration: the inhibitor potency grows as follow: *AD-4* < *AD-3* < *AD-2*  $\approx$  *HQNO* > *AD-1*. The lowest IC<sub>50</sub> belong again to the *AD-2* compound and this value is close to the *HQNO*, meanwhile, the least active inhibitor is *AD-4* that confirms the suggestion that quinolones with too big substituent are not preferred by the quinol-binding site of *E. coli* oxidase. In this experiment, there is no clear correlation between the activity of the tested molecules and amount of quinol. It can be seen that all these compounds show effective inhibition of the protein activity at much lower concentration than were determined at the fast-screening procedure at 10  $\mu$ M level where 50 % inhibition was not reached (see Table 3.3). Literature suggests that titration-based approaches are more reliable for the inhibition studies, whereas the traditional screening method at a single concentration can more easily generate false positives and false negatives responses<sup>274</sup>.


### 3.3 Conclusions

Based on the study, the optimal conditions for the cytochrome *bd*-I oxidase film non-covalent attachment were established for the bioelectrochemical sensor. The role of gold nanoparticles in the immobilization protocol was elucidated by a morphological study. It is proved that the electrode modified with a single portion of 15 nm gold nanoparticles solution exhibits a highly porous structure formation with an eight-fold increase of the electrochemically active surface area for protein immobilization. At the step of the thiolated SAM formation, it was shown that thiols do not perturb the nanoporous structure of the electrode. However, the organic SAM covering gold nanoparticles is hard to characterize by SEM technique as it is complicated to highlight the difference between SAMs varying in nature and charge.

Taking into account the residual amount of phospholipids after each purification of the enzyme and cooperative effect of thiols and lipids on the surface<sup>261</sup>, the electrode modification protocol was tuned to this batch of cytochrome *bd-I* oxidase. Unfortunately, to know the exact amount of each phospholipid in the protein sample the classical methods of quantification like LC-MS and IR spectroscopy is too sample costly, so here we suggest two steps for protocol adjusting. Firstly, the choice of optimal thiols for electrode surface modification was based on the higher catalytic signal and lower over potential that corresponded here to the mixture of the non-charged thiols, 1-hexanthiol and 6-mercaptohexan-1-ol. Secondly, the best stability and level of homogeneity in the protein catalytic evaluation, where the best compromise was obtained for the 2.5% zwitterionic lipid PE, but not PG as it was reported for the delipidated batch before<sup>261</sup>. It might be linked to the unbalanced residual amount of the certain type of phospholipid after the purification of protein, thus the steps described in this work can be helpful for the fast tuning of the immobilization protocol for different proteins.

As shown in this chapter, an electrochemical sensor was successfully used for the fast screening of the library of the inhibitors against cytochrome *bd-I* oxidase. To determine the lead inhibitor out of the synthetic derivatives of the natural alkaloid Aurachin D, a fast screening at a 10  $\mu\text{M}$  concentration and dose-dependent analysis were carried out. The quinolones with alkyl and iodine substituents in C-2 and C-3 were identified as potent inhibitors with an activity higher than 10 %, suggesting the presence of the hydrophobic residues in the quinone binding pocket. This study showed that the length of isoprenoid chain plays crucial role on inhibition in synthesized derivatives of Aurachin D. There was no reported influence of the inhibition activity on the increase of the alkyl chains with 8 to 12 carbons for quinolone derivatives before<sup>174</sup>. The highest inhibition activity was observed for the compound AD-2 with isoprene units, but not Aurachin D (AD-3), as previously shown in literature<sup>15</sup>. In the concentration-dependent study, the lowest  $\text{IC}_{50}$  at 1.1  $\mu\text{M}$  was also found for AD-2 molecule revealing that quinol-binding site prefer quinolones with long lipophilic substituent at C-3 position, but not too bulky as AD-4. Additionally, the most active compounds AD-2 and AD-3 act as competitive inhibitors having their inhibition potency decreased with the increase of the natural substrate ubiquinol in the protein sample. All these findings pave the way for future development of new antimicrobial drugs against pathogenic bacteria containing cytochrome *bd-I* oxidase.





# Chapter IV

## Insight in reactivity of *E. coli* *bd* oxidases with molecular oxygen

---

### 4.1 Characterization of *bd*-I and *bd*-II oxidases from *E. coli*

4.1.1 UV-Vis and FTIR spectroscopic characterization of homologue *bd* oxidases

4.1.2 Potentiometric titration of cytochrome *bd*-II oxidase

4.1.3 Protein film voltammetry of *bd*-I and *bd*-II oxidases

### 4.2 The influence of mutations Glu445 and Arg448 on cyt *bd*-I oxidase catalytic properties

4.2.1 Spectral characterization of E445D and R448N variants

4.2.2 Oxygen electrocatalytic reaction and NO reactivity of the variants of cyt *bd*-I oxidase

4.2.3 UV-Vis redox titration of the E445D and R448N variants

### 4.3 Conclusions





The enzymatic reduction of oxygen is one of the most important metabolic processes in life. Family of cytochrome *bd* oxidases fulfill this role in bioenergetics by catalyzing the reduction of the molecular oxygen at the heme *d* coupled with the oxidation of the quinol at the Q-binding site<sup>4,119</sup>. This enzyme was found only in the prokaryotic cells<sup>2</sup> and it was shown to contribute to the bacterial survival during the oxidative stress and help pathogens to adapt for adverse environment. In-depth understanding of the enzyme mechanism is required to elucidate the role of the *bd* oxidases in bacterial virulence and adaptation.

In this chapter the catalytic reduction of O<sub>2</sub> for two isoforms of cytochrome (cyt) *bd* oxidase from *E. coli*, *bd-I* and *bd-II* are discussed. The spectroscopic and electrochemical properties will be compared for both enzymes in the relation with the structural differences<sup>55,78</sup>. For better understanding of the role of the high spin heme *b*<sub>595</sub>, which was initially believed to be the part of a di-heme catalytic center<sup>12,275,276</sup>, site-directed mutation of the E445 residue, the confirmed ligand of this heme<sup>13,55</sup>, was done. The generated E455D and R448N variants of cyt *bd-I* has been investigated by means of UV-Vis and FTIR spectroscopies. The effect of the mutation on the redox properties of the hemes and on the catalytic oxygen reduction was studied.

#### 4.1 Characterization of *bd-I* and *bd-II* oxidases from *E. coli*

In order to compare the cytochrome *bd-I* and *bd-II* oxidase catalytic reaction with O<sub>2</sub> the spectroscopic and electrochemical characterization was done. The recently available structures of these highly comparable in structure oxidases gave an insight on the small but visible differences in the gas channel that might influence the reactivity and binding with the small gaseous molecules<sup>78</sup> (Fig.4.1). The UV-Vis and redox induced infrared differential spectroscopic technique were employed for the characterization of the *bd-I* and *bd-II* environment of the heme cofactors and the direct electrochemical approach was used to study the catalytic oxygen reduction reaction.

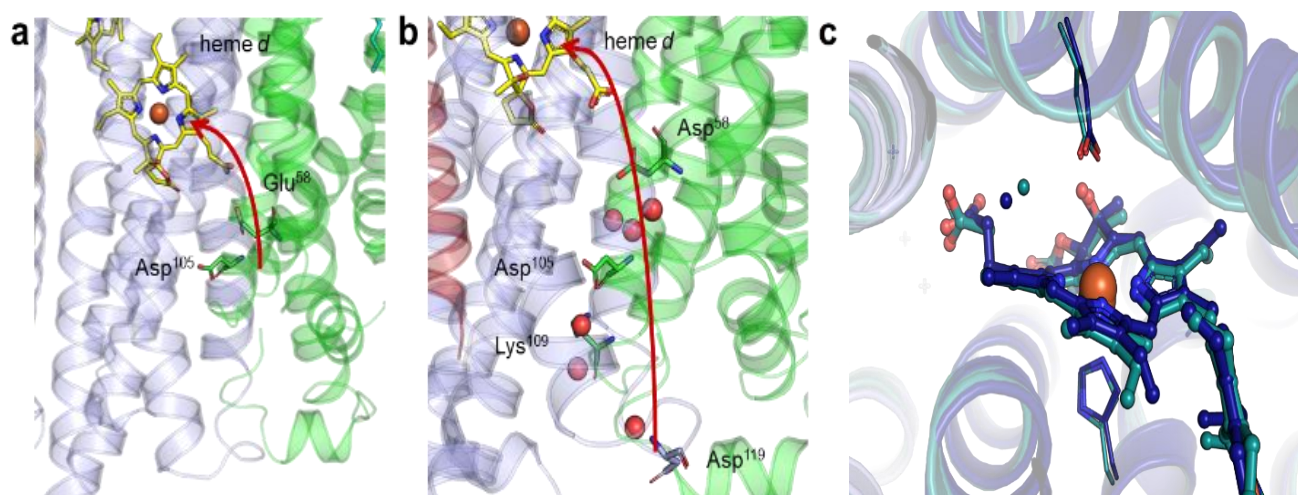


Figure 4.1. Differences in the proton channel of homologues *bd* oxidases: a) shows the short channel in *bd-II* (pdb code: 7OY2) that begins at the end of the large, hydrophilic cavity, b) the longer proton pathway along a series of titratable amino acid residues in *bd-I* (pdb code: 6RKO)<sup>78</sup>; c) comparison of the active sites of *bd-I* and *bd-II* oxidases from *E. coli*. Subunit *cydA* is shown in blue, *cydB* in green, the proton pathways are indicated by red arrows that connect titratable residues.

#### 4.1.1 UV-Vis and FTIR spectroscopic characterization of homologues *bd* oxidases

The differential red-ox spectrum of the *cyt bd-II* resembles the one from *bd-I* from *E. coli* (Fig.4.2). Both show almost the same position of the  $\alpha$ -band of hemes *b* at 562 nm, 595 nm and of the  $\alpha$ -band of heme *d* at 629 nm.

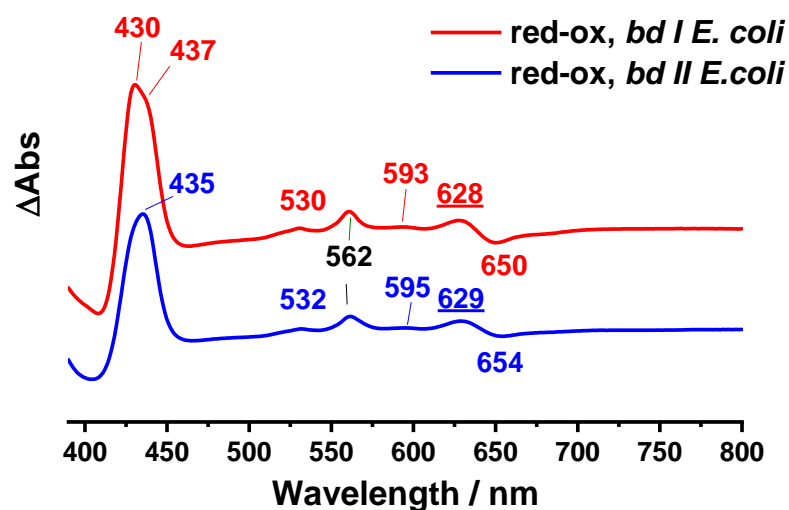


Figure 4.2. Dithionite-reduced minus air-oxidized difference UV-Vis spectra of the *bd-I* (red) and *bd-II* (blue) oxidase

Also, there is a slight shift of the  $\beta$ -band to 532 nm as compared to the *bd-I* oxidase. The main spectral difference is the shift of the Soret band from 430 to 435 for *cyt bd-II*,

additionally the *bd*-I oxidase has a shoulder at 437 that is less pronounced. Overall, the spectral analysis point to a similar environment of the heme *d* for *bd*-I and *bd*-II.

The red-ox induced FTIR difference spectra were recorded at 13°C and pH7 in the thin-layer electrochemical cell (*see description in Annex A.3*). This technique allows to follow the changes in IR spectrum linked to the protonation/deprotonation events and conformational movements that occur during the electron transfer reaction<sup>240, 277</sup>.

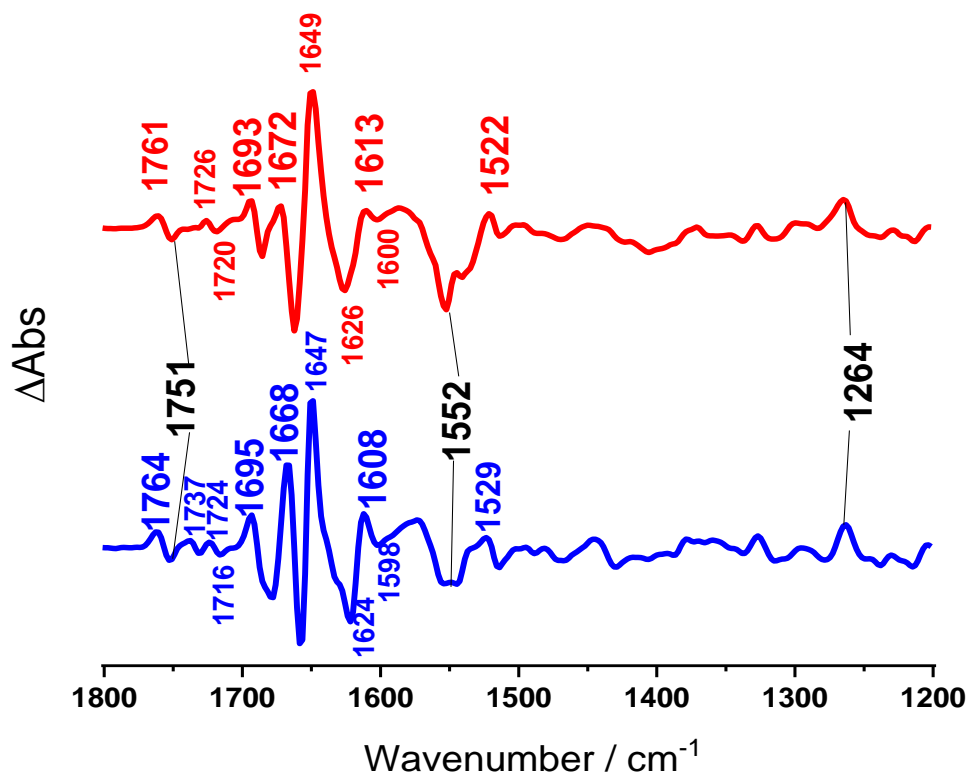


Figure 4.3. Ox-red induced FTIR difference spectra of the *bd*-I (red) and *bd*-II (blue) oxidase from *E. coli*.

The spectral profile of both *bd* oxidases look very similar with some minor differences in the wavenumbers of the the signals in the amide I and amide II regions (Fig. 4.3). The positive bands and negative bands correspond to the oxidized and reduced state respectively. A suggested assignment of the FTIR signals is given in the Table 4.1.

In the spectral region from 1700 to 1680  $\text{cm}^{-1}$ , bands at 1695 and 1682  $\text{cm}^{-1}$  correspond to the protonated heme propionates. The region above 1710  $\text{cm}^{-1}$  includes the contribution of C=O vibrations of the Asp and Glu aminoacids with and without H-bonding (in hydrophobic environment)<sup>272</sup>. The vibrational signal assignment relies on the similarity of the sequence of two *bd* oxidases, here the analogy signals may be attributed to the corresponding conserved residues in cyt *bd*-II oxidase. The signals at 1761/1751  $\text{cm}^{-1}$  and 1764/1751  $\text{cm}^{-1}$  seen in difference spectra for cyt *bd*-I and *bd*-II, respectively, were previously attributed to the Glu99A

(numbers refer to *Escherichia coli* cyt *bd-I*)<sup>278</sup>. The positive bands, at 1737 cm<sup>-1</sup> for *bd-II* and 1724/1716 cm<sup>-1</sup> were detected, they were attributed to the acidic residue Glu in the H-bonding based on the mutation Glu107A showed for *bd-I* oxidase<sup>278</sup>.

Table 4.1. FTIR differential spectra signals assignment of *bd-I* and *bd-II* from *E. coli*

Band position, cm <sup>-1</sup>		Group assignment <sup>272,277,278</sup>
<i>E. coli bd II</i>	<i>E. coli bd I</i>	
<b>1264</b>	1264	vibrations of C-O bond in C-OCH <sub>3</sub> side chain of UQ
<b>1327</b>	1327	δ(CH), ν <sub>s</sub> (COO <sup>-</sup> )
<b>1529</b>	1522	ν(C=N) and δ(C=C) of backbone, ν(C=C) of porphyrin ring, δ <sub>as</sub> (COO <sup>-</sup> ) of Asp or Glu
<b>-1552</b>	-1552	ν(C=N) and δ(C=C) of backbone, ν(C=C) of porphyrin ring, δ <sub>as</sub> (COO <sup>-</sup> ) of Asp or Glu
<b>-1624</b>	-1626	oxidized UQ
<b>1647</b>	1649	ν(C=O) backbone, individual amino acids, oxidized UQ
<b>-1658</b>	-1662	ν(C=O) backbone, individual amino acids, oxidized UQ
<b>1668</b>	1672	ν(C=O) backbone, individual amino acids
<b>-1682</b>	-1685	ν(C=O) of heme propionates
<b>1695</b>	1693	
<b>-1724</b>	-1720	ν(C=O) of Asp or Glu with H-bonding
<b>1716</b>	1726	
<b>1737</b>		ν(C=O) of Asp or Glu with H-bonding
<b>-1751</b>	-1751	ν(C=O) of Asp or Glu without H-bonding (in hydrophobic environment); heme <i>d</i>
<b>1764</b>	1761	

In the amide I region (1690-1620 cm<sup>-1</sup>), bands at 1668, 1658 and 1647 cm<sup>-1</sup> in cyt *bd-II* oxidase spectrum corresponded to the C=O vibrations of the polypeptide backbone and individual aminoacids. For the amide II region (1570-1520 cm<sup>-1</sup>), bands at 1552 and 1529 cm<sup>-1</sup> showed the contributions of the CN stretching, NH bending vibrations of the polypeptide backbone and the C=C vibrations of the porphyrin ring of the heme cofactors. The -COO<sup>-</sup> groups of the deprotonated acid residues of Asp or Glu may also contribute to the 1552 cm<sup>-1</sup>

band. The small shifts in the amide I and amide II regions for cyt *bd*-II oxidase revealed only small differences in the organization of the polypeptide backbone for this enzyme.

In both protein samples the presence of ubiquinone UQ was evident from the band at  $1264\text{ cm}^{-1}$  corresponding to C-O bond vibrations in O-CH<sub>3</sub> group and by the bands at  $1608\text{ cm}^{-1}$  and  $1647\text{ cm}^{-1}$  that can be attributed to the  $\nu(\text{C}=\text{C})$  and  $\nu(\text{C}=\text{O})$  vibrations of the oxidized UQ<sup>277</sup>. In conclusion, both enzymes showed a similar profile in their difference IR spectra with a small shift in the wavenumbers in the region in amide I and amide II band pointing at a comparable environment of the hemes. However, clear differences were seen in the band of the acidic residues suggesting some alterations in the structure of cyt *bd*-II oxidase.

#### 4.1.2 Potentiometric titration of cytochrome *bd*-II oxidase

In order to determine the potentials of the heme groups in cytochrome *bd*-II oxidase a potentiometric titration in the same electrochemical cell was performed. This approach allows to follow stepwise the alterations in the UV-Vis spectrum of the enzyme upon changing the potential. The typical titration experiment for the cytochrome *bd*-II oxidase in the reductive direction from +700 mV to -300 mV vs SHE is shown in the Fig. 4.4. It was possible to distinguish the contribution of the heme *d* at 629 nm, however, the heme *d* was not titrated at the significantly high potential in contrast to the cyt *bd*-I oxidase. It was observed in at +350 mV vs SHE (red curve, Fig.4.4b) compared with the full ox-minus-red spectrum of the cyt *bd*-II oxidase (black curve, Fig. 4.4b).

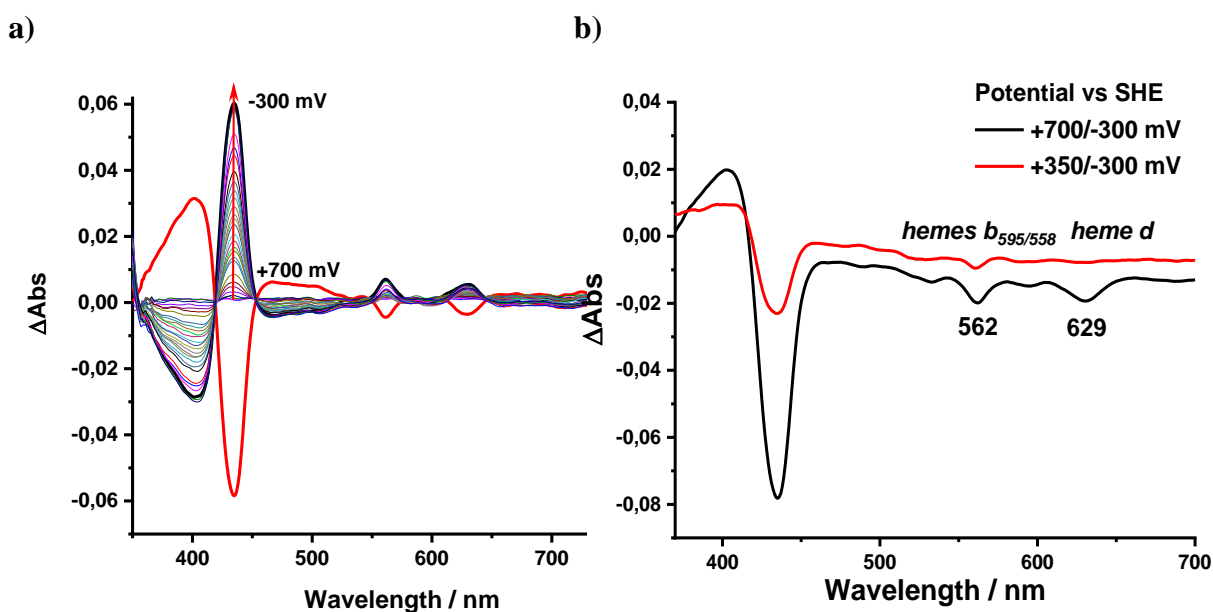


Figure 4.4. a) Example of the reductive titration of *bd*-II in the range of +700/-300 mV vs SHE; b) The differential spectra at +350 mV vs. SHE compared with full red-ox spectra.

The redox potential of hemes *b* was obtained from the fit of the oxidative and reductive titration curves in the Soret band and 562 nm region. An averaged value of +256 mV was determined for the two hemes *b*. Unfortunately, it was not possible to distinguish values for each heme *b*<sub>595</sub> and *b*<sub>558</sub> because the difference between them is less than 100 mV (Fig. 4.5). The redox potential of the heme *d* cofactor was found at +432 mV vs SHE from the Nernst fit of the Soret band and 629 nm  $\alpha$ -band titration curves. For the cytochromes *bd*-I and *bd*-II oxidases from *E. coli* the potential of the heme *d* is higher by almost 200 mV than the hemes *b*, which suggests that electrons are spontaneously from the hemes *b* to the heme *d* active site.

The experimental mid-point potentials values obtained from the potentiometric titration in the oxidative and reductive directions are summarized in the Table 4.2. All the potentials in the study are referenced vs SHE.

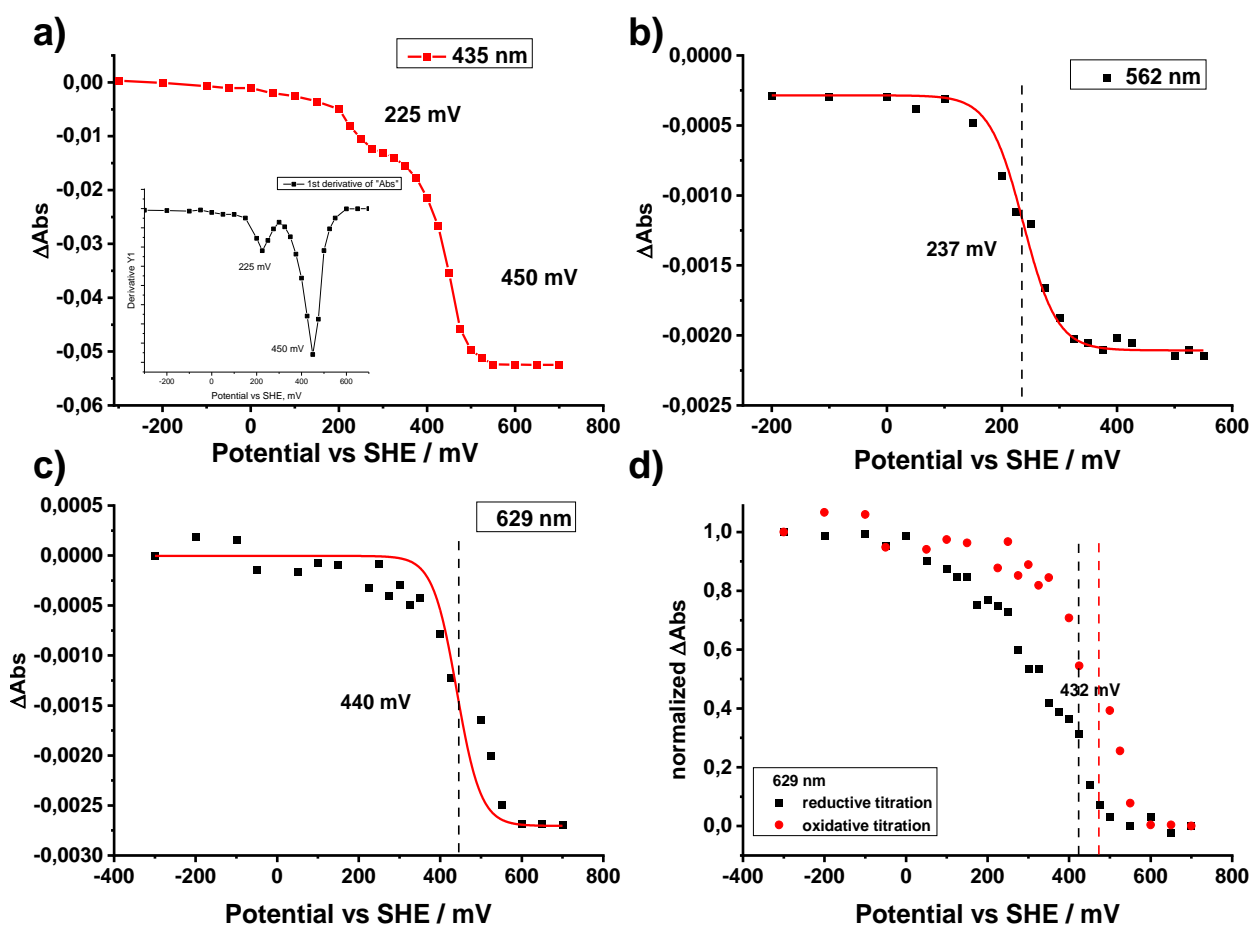


Figure 4.5. a) The evolution of the absorbance of *bd*-II in Soret band (435 nm) versus applied potential; b) Determination of the hemes *b* potential from differential UV/Vis spectra at 562 nm; c) Determination of the heme *d* potential from differential UV/Vis spectra at 629 nm; d) The reductive and oxidative titration for the determination of the redox potential of the heme *d*.

The potentiometric titration was done in two directions to reveal the information on the presence of additional kinetic processes or cooperativity in one redox direction. In the case of *cyt bd-II* oxidase, the experiments showed that hysteresis between the potentials measured during oxidative and reductive titrations was less than 40 mV, that suggests a good reversibility.

Table 4.2. The redox potentials (vs SHE) of the heme cofactors from *bd-II* from *E. coli*, the standard error is 20 mV.

Titration experiment	<i>heme b<sub>595</sub>, b<sub>558</sub></i>	<i>heme d</i>
pH 7, oxidative titration	+237 mV	+440 mV
pH 7, reductive titration	+275 mV	+425 mV
pH 7, red-ox potential	<b>+256 mV</b>	<b>+432 mV</b>

The obtained potentials for the *cyt bd-II* oxidase were compared with the values from other species in the Table 4.3. The most striking observation here was the extremely high potential of the heme *d* for the cytochrome *bd-II* oxidase throughout the values for different bacteria, which was almost 200 mV higher than one found for *bd-I* from the same bacterial origin<sup>14, 222</sup>. The higher potential for the heme *d* in the cytochrome *bd-II* oxidase was suggested to have an influence on the activity of the protein. It was reported that the duroquinol:dioxygen oxidoreductase activity was 2.5-fold slower for *cyt bd-II* oxidase as compared to the *bd-I* type<sup>78</sup>.

Table 4.3. The redox potentials of the cofactors of cytochrome *bd* oxidases from different organisms.

<i>E. coli</i>	pH 7 <i>bd-II</i>	<b>+432 (d)</b>	<b>+237 (b<sub>1</sub>, b<sub>2</sub>)</b>	this study
	pH 7 <i>bd-I</i>	+258 (d)	+ 168 (b <sub>595</sub> ) +176 (b <sub>558</sub> )	14
<i>A. vinelandii</i>	pH 7	+310 (d)	+251 (b <sub>595</sub> ) +166 (b <sub>558</sub> )	14
<i>G. thermodenitrificans</i>	pH 7	+155 (b), +50 (b), +15 (d)		3,13
	pH 6 in the presence of CN <sup>-</sup>	+174 (b), +59 (b), -43 (d)		

Giving the significant gap of almost 200 mV in the redox potentials between hemes *b* and the heme *d* and slower activity for the cytochrome *bd-II* oxidase, the investigation of the catalytic reduction of oxygen was probed on the 3D gold nanoparticles electrodes modified with the SAM thiols previously described in the Chapter III.



4.1.3 Protein film voltammetry of *bd*-I and *bd*-II oxidases

Residual phospholipids in the membrane protein sample after the purification process plays a crucial role on its reactivity<sup>261,264,279</sup>. The influence of the phospholipids that naturally present in high amount in *E. coli* membranes<sup>3,13</sup> on the electrocatalysis of *bd*-I oxidase in PFV was shown in the Chapter III. The optimal catalytic response and stability of the enzyme film in PFV on the gold electrode was reached after addition of 2.5% PE. Giving the similarity in sequence with cyt *bd*-II oxidase up to 60%, this enzyme was incubated overnight with 2.5% PE, 2.5% PG, and a mixture of both phospholipids. The protein sample was deposited on the surface and left for two hours at 4°C on the 3D gold nanoparticle electrode modified with a mixture of neutral thiols as described in Chapter III. The corresponding cyclic voltammograms of the cyt *bd*-II oxidases are shown in Fig. 4.6.

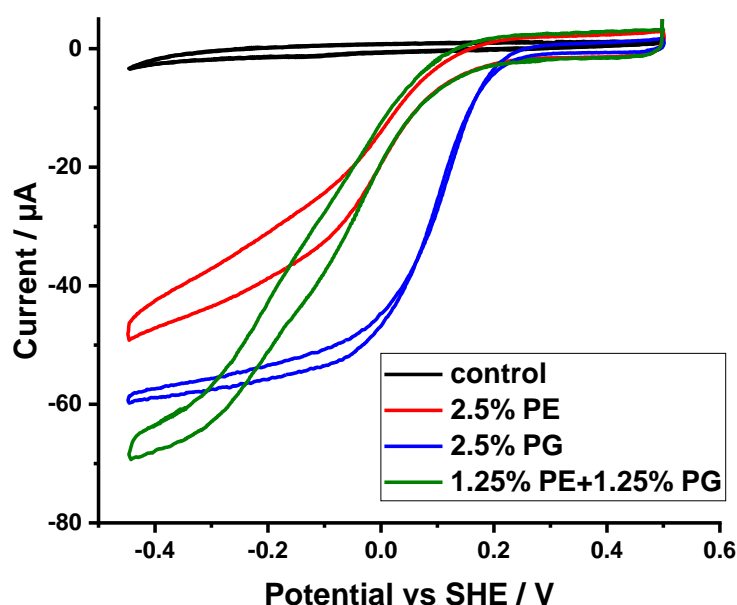


Figure 4.6. Voltammograms obtained for cytochrome *bd*-II oxidases incubated with 2.5% PE (red curve), 2.5% PG (blue curve) and the mixture of 1.25% PE and 1.25% PG (green curve) on gold NPs modified with HT/MCH thiols. Experimental conditions: air-saturated pH 7 phosphate buffer, scan rate 0.02V/s, rotation speed 1000 rpm.

It is noticeable that the lowest half-wave potential of the catalytic curve was seen when PG lipid was added, with an upshift of up to 100 mV as compared to the PE or mixture of lipids. A sigmoidal shape of the voltammogram similar to the wild type *bd*-I oxidase for the catalytic reduction of oxygen is also seen for the protein sample co-immobilized with negatively charged lipids. For the PE and mixture of lipids in the enzyme sample, a more complicated voltammograms is observed for the catalytic curve, which may be related to the ability of the *bd*-II oxidase to form dimers, previously reported from the mass-spectrometry

experiments<sup>78</sup>. In this case, the shape of the curve can also point towards the protein immobilization in different orientations on the electrode.

In the figure 4.7 the cyclic voltammograms of the cytochrome *bd*-I and *bd*-II oxidases obtained with different lipids were compared. In the electrochemical experiments, the onset potential of the catalytic reduction of oxygen for cyt *bd*-II oxidase is at least 200 mV higher than for *bd*-I oxidase with any type of lipids added.

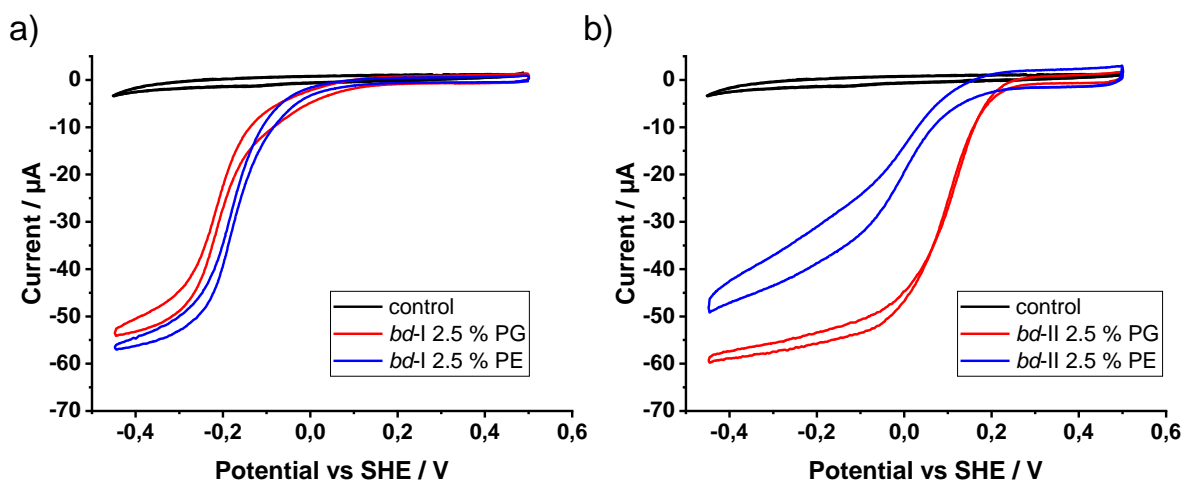


Figure 4.7. Voltammograms obtained for cytochrome *bd*-I (a) and *bd*-II (b) oxidases incubated with 2.5% PE and 2.5% PG respectively on gold NPs modified with HT/MCH thiols. Experimental conditions: air-saturated pH 7 phosphate buffer, scan rate 0.02V/s, rotation speed 1000 rpm.

The cytochrome *bd*-II sample required negatively charged lipids for a good compromise between catalytic response, lowest mid-point potential and acceptable stability of the protein film on the electrode surface. For cyt *bd*-I oxidase the addition of PG gives a sigmoidal curve with high catalytic current, but the stability of the signal upon successive scans is lower (Chapter III). So, the best electrocatalytic activity on gold nanoparticles modified with 1:1 mixture of thiols (HT/MCH) was obtained when adding 2.5% PE for cyt *bd*-I and 2.5% PG for cyt *bd*-II. The need for the different lipid type of the homologue *bd* oxidases of the same bacterial origin to ensure the optimal catalytic properties may be explained by different residual amount of lipids in the sample after the purification<sup>261</sup>.

The electrocatalysis of oxygen was probed as a function of pH for these enzymes. Both isoforms exhibit their highest catalytic in the pH-range from 6 to 7. The catalytic response of the immobilized *bd*-I oxidase decreased at pH 7.5 by 35% and at pH 8 by almost 50%. For the cytochrome *bd*-II oxidase, the loss in the catalytic current over pH 7 was only 20%. So, the influence of pH on the electrocatalytic activity is lower for *bd*-II than *bd*-I oxidase. It was interesting to compare the pH dependent activities of these isolated enzymes in solution.

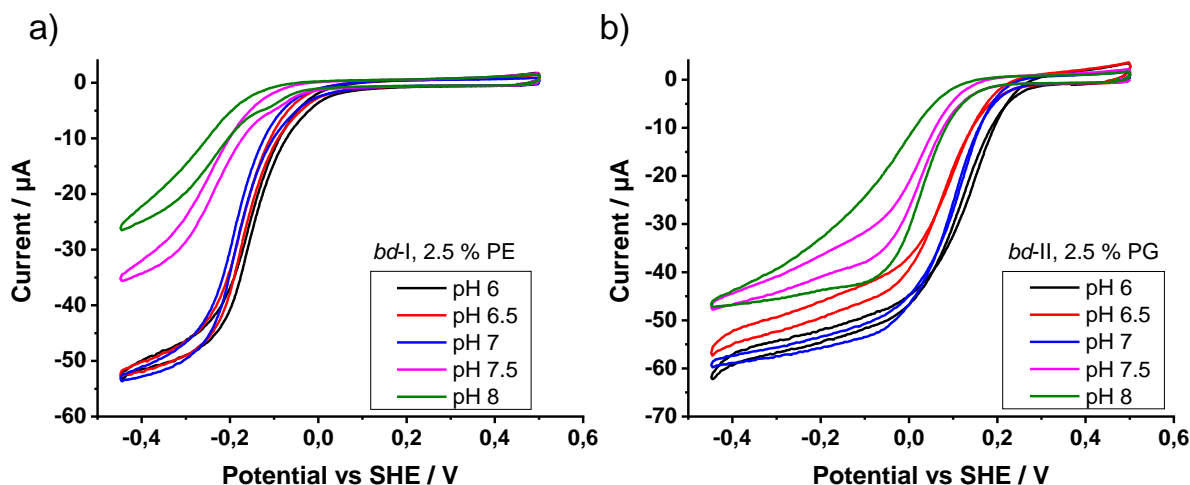


Figure 4.8. The pH-dependent oxygen catalysis of cytochrome *bd-I* (a) and *bd-II* (b) oxidases incubated with 2.5% PE and 2.5% PG, respectively, on gold NPs modified with HT/MCH thiols. Experimental conditions: air-saturated pH 7 phosphate buffer, scan rate 0.02V/s, rotation speed 1000 rpm.

The duroquinol: oxygen oxidoreductase activities in solution as a function of pH were measured using a Clark electrode by Jan Kägi from the group of Prof. T. Friedrich (Freiburg University), Fig. 4.9. The activity of *bd-I* oxidase increases with pH, while the activity of *bd-II* oxidase reaches a peak at a pH of 7.0. The superposition of the activity curves is in line with measurements for the *bd* oxidase performed by the group of Prof. R.B. Gennis in the bacterial membrane where both isoforms were present<sup>280</sup>. In the electrochemical assay the pH tendency is significantly different for the cytochrome *bd-I* oxidase probably due to a decreased stability of the protein film at pH 7.5 and 8 that gives a lower catalytic response.

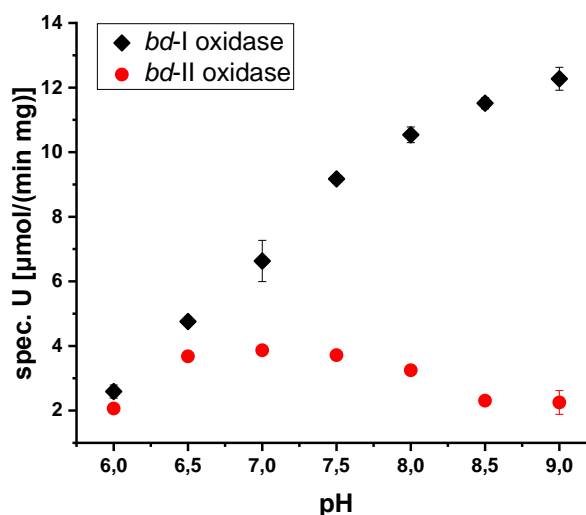


Figure 4.9. Duroquinol: oxygen oxidoreductase activities of cyt *bd-I* (black) and *bd-II* (red) as a function of pH measured with a Clark electrode (Freiburg University).

Overall, both *bd* oxidases from *E. coli* were successfully immobilized on the gold electrode. The electrochemical study showed an influence of the lipids on the electrocatalytic properties; however, this may be related to the purification protocol and the residual amount of the phospholipids in the sample. Interestingly, the onset potential of the catalytic reduction of oxygen for cyt *bd*-II oxidase was almost least 200 mV higher than for *bd*-I oxidase, which may be explained by the significant shift of the mid-point potential of the heme *d*, 258 mV for *bd*-I and 432 mV for *bd*-II, as determined by the potentiometric titration. Moreover, it was shown that the pH influences differently the O<sub>2</sub> reduction activity of the cyt *bd*-I and *bd*-II oxidases.

## 4.2 The influence of the Glu445 and Arg448 residues on cyt *bd*-I oxidase catalytic properties

The Glu445 residue is a ligand of the heme *b*<sub>595</sub>, that was proposed to be part of a di-heme active site before the structures of the *bd* oxidases were resolved<sup>13,55</sup>. Here Glu445 was exchanged by site-directed mutagenesis to Asp maintaining the acidic functional group at this position and Arg448, a conserved residue in hydrogen bonding distance to Glu445 was exchanged to Asn (Fig. 4.10). The effect of the mutations on the catalytic properties of the cytochrome *bd*-I oxidase was studied by electrochemical methods. The obtained variants were active in the membranes and still exhibited a turnover of  $41 \pm 2$  % and  $20 \pm 4$  % for E445D and the R448N, respectively. The oxidoreductase activity measurements were performed by T. Gerasimova from the group of Prof. T. Friedrich (Freiburg University) in bacterial membranes using a Clark-type electrode<sup>267</sup>.

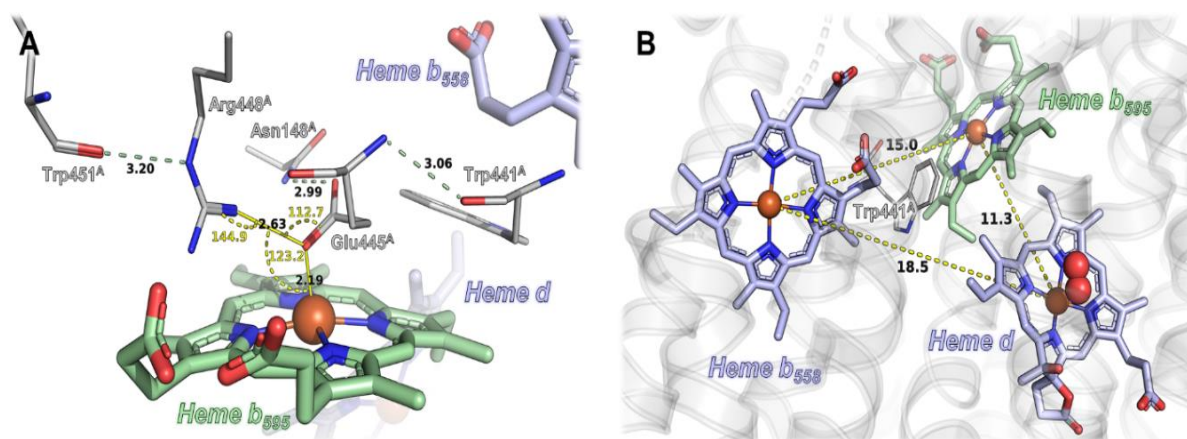


Figure 4.10. Active site of cytochrome *bd*-I oxidase of *E. coli*. (A) Coordination geometry of Glu445<sup>A</sup> and Arg448<sup>A</sup> at heme *b*<sub>595</sub> in subunit *CydA*, Hydrogen bond angles (°) and distances (Å) are indicated. (B) Heme arrangement in *CydA* with Fe-Fe distances between the hemes given in Å. Trp441<sup>A</sup> serving as electron shuttle between hemes *b*<sub>558</sub> and *b*<sub>595</sub> is additionally shown. A dioxygen molecule is coordinated by the active site heme *d*.

## 4.2.1 Spectral characterization of E445D and R448N variants

The UV-Vis and FTIR spectroscopies were used to confirm the structural integrity of the obtained variants of cyt *bd*-I oxidase. From the UV-vis difference spectra (dithionite-reduced minus air-oxidized) of the E445D and R448N variants the presence of all three heme cofactors was confirmed (Fig. 4.11).

In contrast to the E445A mutation reported before <sup>127</sup>, the E445D variant was fully reduced by dithionite. Only a small shift of band the characteristic for the *d* heme from 628 to 629 nm was observed. Furthermore, the shape of the Soret signal has changed and the maximum shifted from 430 to 429 nm in the variants. The shoulder of this band also shifted from 437 nm to 440 nm in both variants. This can be explained by the mutation of the residues in the proximity of the heme *b*<sub>595</sub>, that was reported to have a contribution in the Soret band at 440 nm <sup>281</sup>.

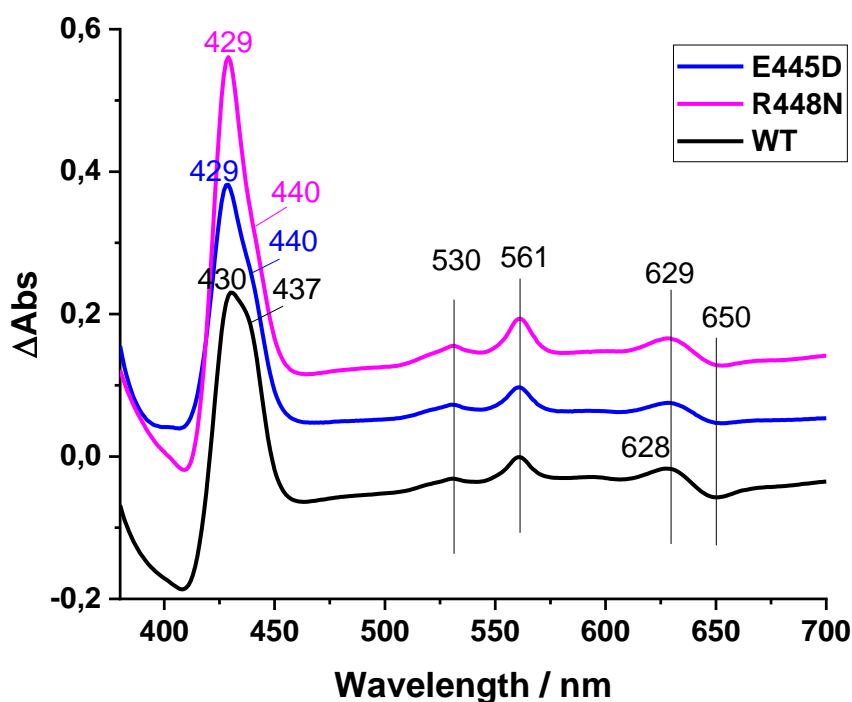


Figure 4.11. Dithionite-reduced minus air-oxidized UV-vis difference spectra of cyt *bd*-I oxidase (black) and the E445D (blue) and R448N (pink) variants.

The ox-red induced difference FTIR spectra of E445D and R448N variants are shown in Figure 4.12. The spectral profile of the variants is compared to the wild type one. In the amide I region (1690-1620  $\text{cm}^{-1}$ ), bands at 1670, 1660 and 1647  $\text{cm}^{-1}$ , that correspond to the C=O vibrations of the polypeptide backbone and individual aminoacids, as well as ubiquinone UQ, the natural substrate of Q-binding site. In both variants the signals of the UQ were detected at 1647 (C=O), 1612 (C=C) and 1263/1265 ( $-\text{COCH}_3$ )  $\text{cm}^{-1}$ . However, in the R448N variant

an additional signal at  $1294\text{ cm}^{-1}$  was seen that corresponds to vibrations of the C-O bond in the methoxy group of the menaquinone. These two quinones (ubiquinone and menaquinone) were previously detected in less active mutants of *cyt bd-I*<sup>278, 282</sup>.

In the spectral region of the amide II band ( $1570\text{-}1520\text{ cm}^{-1}$ ), where the signals of the  $\nu(\text{C}=\text{N})$  and  $\delta(\text{C}=\text{C})$  of the polypeptide backbone as well as the  $\delta_{\text{as}}(\text{COO}^-)$  of acidic residues contribute, two variants showed significant differences in the spectra. For the E445D enzyme the negative band at  $1554\text{ cm}^{-1}$  and positive band at  $1524\text{ cm}^{-1}$  were upshifted as compared to the wild type, that points at the small changes in the structure that may be due to the replacement of the Glu to Asp at the proximity to the heme  $b_{595}$ . Additionally, the pair of signals at  $1761/1751\text{ cm}^{-1}$ , typical for  $(-\text{COOH})$  vibrations of the acidic residues<sup>243,283</sup>, are only slightly shifted because the acidic residue probably remains coordinated to heme  $b_{595}$ .

In R448N variant, there major alterations observed in this region of the amide II. The band of the cytochrome *bd-I* oxidase at  $1552\text{ cm}^{-1}$  is upshifted in the variant spectra, while the signal at  $1522\text{ cm}^{-1}$  was strongly altered. Additionally, for the R448N variant the signals of acidic residues at  $1761/1751\text{ cm}^{-1}$  seen in the wild type moved up to 7 wavenumbers. All these findings could be explained by the strong influence of the mutation of Arg448 to asparagine residue, that is in hydrogen bonding distance from Glu445 acidic residue.

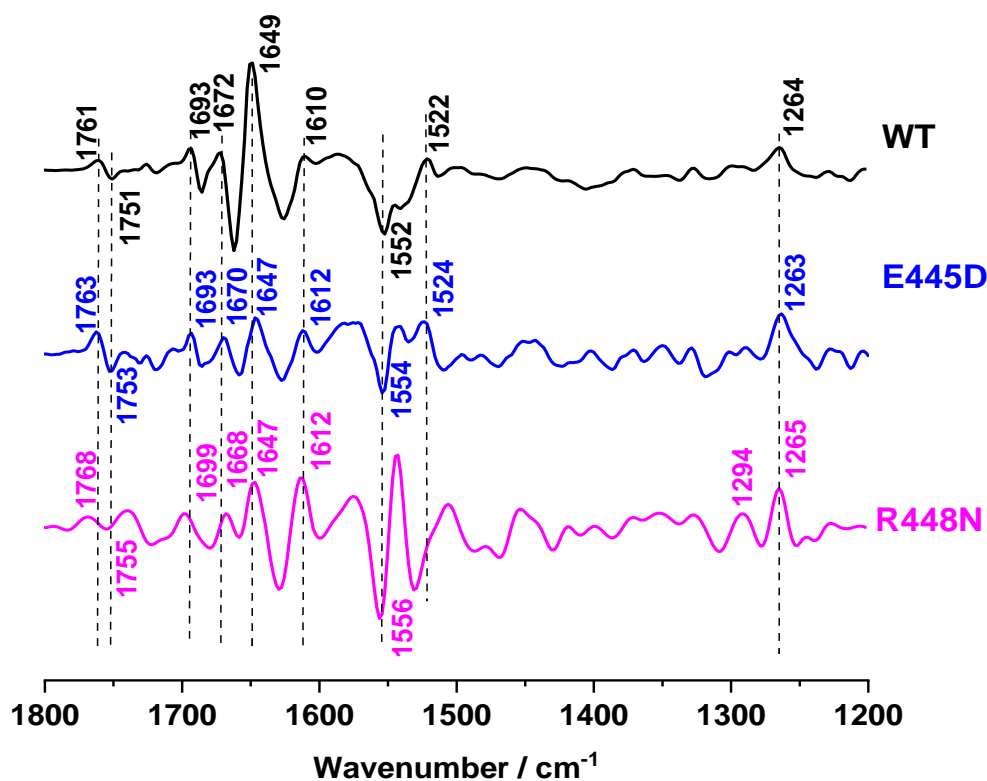


Figure 4.12. FTIR ox-red differential spectra of WT *cyt bd-I* oxidase and mutants E445D, R448N (+500/-500 mV vs Ag/AgCl).

#### 4.2.2 Oxygen electrocatalytic reaction and NO reactivity of the variants of cytochrome *bd*-I oxidase

The E445D and R448N variants were successfully immobilized on the gold nanoparticles electrode for electrocatalytic studies. The voltammograms of both variants (Fig. 4.13, blue and pink lines) were strongly altered, both in shape and magnitude as compared to the wild type enzyme. For the R448N variant, in particular, a limiting current was not reached in the potential range studied here. The shape of the CV can give information on the kinetics of the substrate catalysis<sup>196</sup>, a catalysis that is less efficient in the case of the mutants shown here.

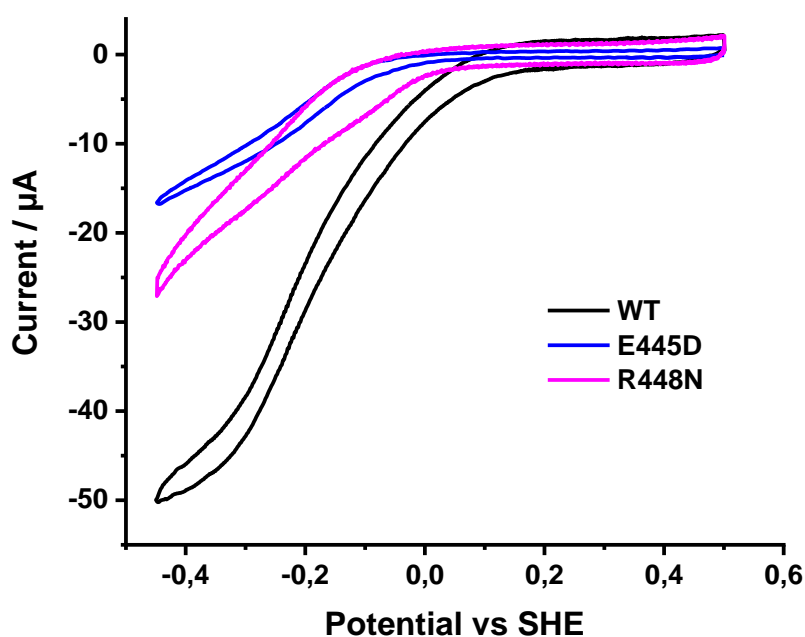


Figure 4.13. Voltammograms of the *cyt bd*-I wild type (black) and the E445D (blue) and R448N (pink) variants in air-saturated pH 7 phosphate buffer; scan rate: 0.02V/s, rotation speed: 1000 rpm.

It was reported that binding of nitric oxide to the *d*-heme of *cyt bd* leads to inhibition of the enzyme, but the oxygen reductase activity of the enzyme is quickly and fully recovered upon NO depletion<sup>95, 96</sup>. The effect of nitric oxide on E445D and R448N variants was also probed by PFV. An aliquot of NO-releasing compound (MAHMA NONOate) was added to the buffer solution at pH 7 and the cyclic voltammograms were recorded every 10 min over one-hour experiment. In the case of the wild type *cyt bd*-I, upon addition of 50 μM NO the electrocatalytic activity in presence of O<sub>2</sub> was completely lost but was recovered by almost 60% after 20 min (Fig. 4.14a). The NO binding and release experiments clearly confirmed that it was oxygen reduction, which was measured in this assay. A similar behavior was observed

at pH 7 for the *bd*-I oxidase variants, so that the electrocatalytic studies confirmed the ability of these mutants to react with oxygen and to bind and release NO.

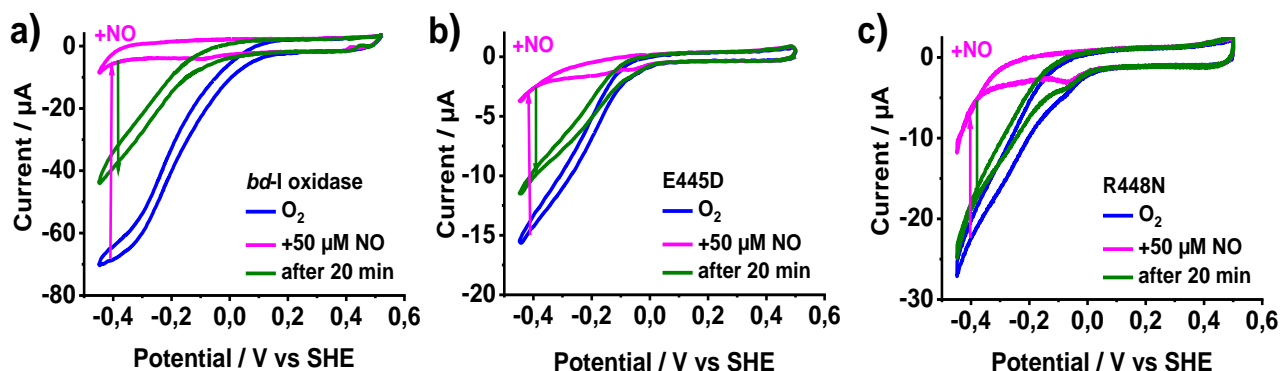
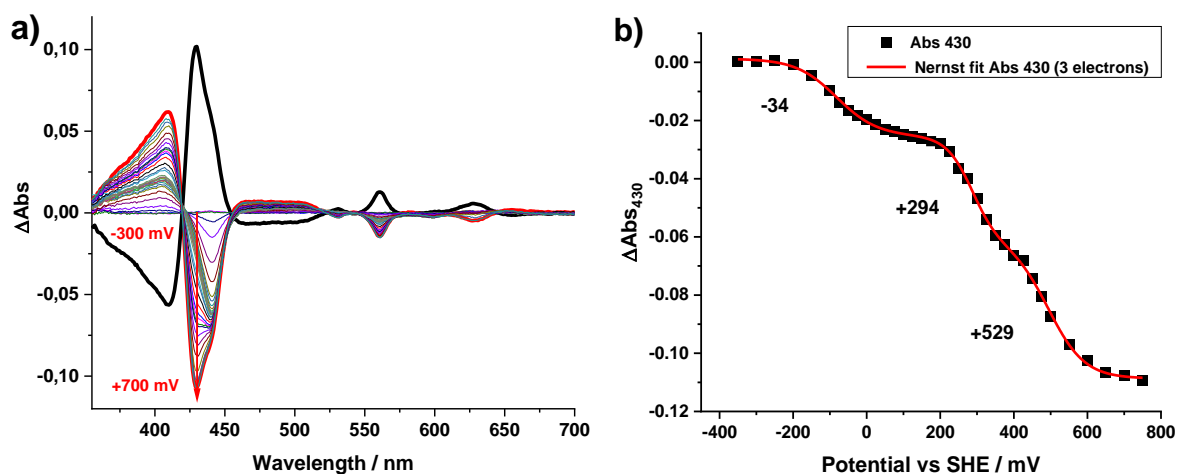


Figure 4.14. The effect of NO inhibition on the electrocatalytic  $O_2$  reduction of the wild type *bd*-I oxidase (a), E445D (b) and R448N (c) variants on a gold electrode modified with gold NPs and SAM thiols at pH 7 with 2.5 % PE. Conditions: air-saturated pH 7 phosphate buffer, scan rate 0.02V/s, rotation speed 1000 rpm.

#### 4.2.3 UV-Vis redox titration of the E445D and R448N variants

In order to determine if the differences in the voltammograms of the electrocatalytic oxygen reduction of the R448N and E445D enzymes could be due to alterations in the redox potentials of the hemes, the potentiometric titrations were carried out for the variants. The UV-Vis redox titration was performed in the electrochemical cell for both variants in oxidative and reductive direction in the range of -0.3 to 0.7 V vs SHE. The redox state of the heme *d* was monitored at 629 nm, whereas that of the hemes *b* at the  $\alpha$ -band at 561 nm as well as at the Soret band at 430 nm. Examples of titration curves and Nernst fit for the calculation of the midpoint potential of the heme cofactors in R448N variant are shown in the Fig. 4.15 and 4.16. The titration curves for the variant E445D are shown in the Appendix E.1.





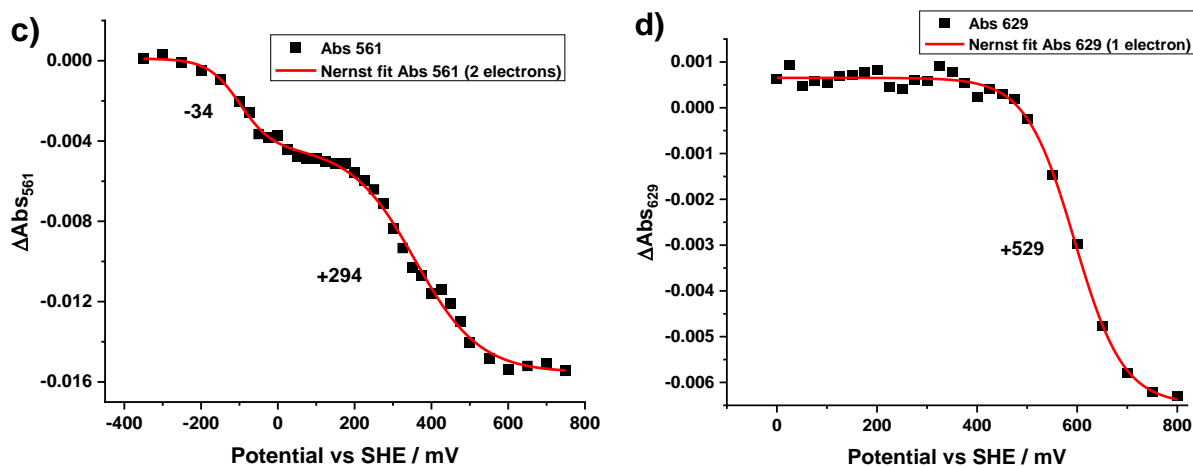
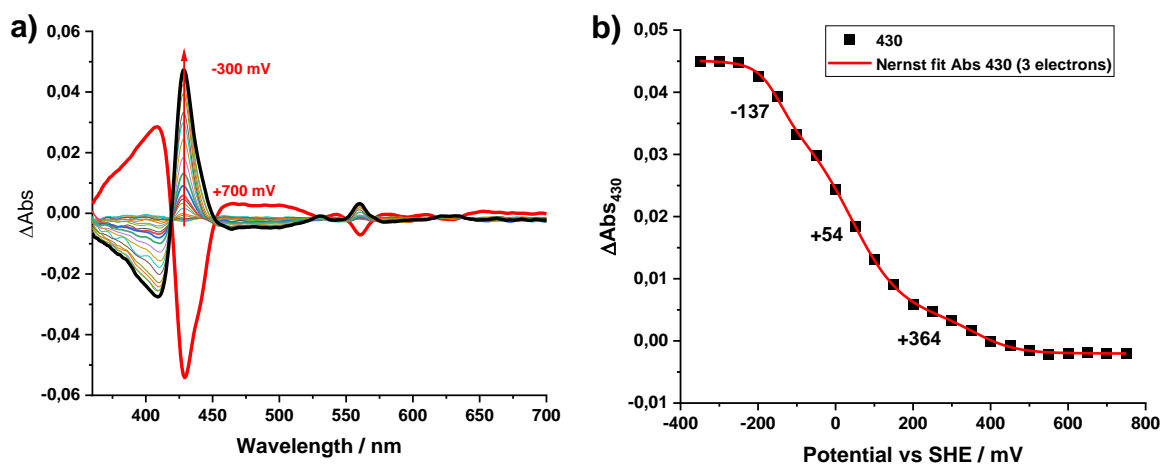


Figure 4.15. a) Oxidative titration of *bd-I R448N* variant in the range of +700/-300 mV vs. SHE, b) The differential absorbance of *bd-I R448N* at Soret band, 430 nm, plotted versus applied potential, c) Determination of the hemes *b* potential from differential UV/Vis spectra at 561 nm with modified Nernst equation, d) Determination of the heme *d* potential from differential UV/Vis spectra at 629 nm with modified Nernst equation.

A significant difference in the potential values determined by oxidative and reductive titrations was observed for the active site heme *d*. In case of the oxidative titration, the mid-point potential was found over 500 mV, when the respective potential transition was detected after 20 hours of the experiment. When the titration was carried out in the reductive direction, the band of heme *d* at 629 nm was the first to appear and mid-point potential was determined at +364 mV, so the difference was about 200 mV. This can be related to the strong effect of the Arg448 residue on the electron transfer from the heme *b*<sub>595</sub> to the heme *d*. Both hemes *b* have been suggested to show a slightly different absorption in the Soret region: 430 for heme *b*<sub>558</sub> and 440 nm for heme *b*<sub>595</sub>, respectively<sup>281</sup>. However, due to the very close absorption and the close redox potential the two redox transitions of the hemes are not well distinguishable.



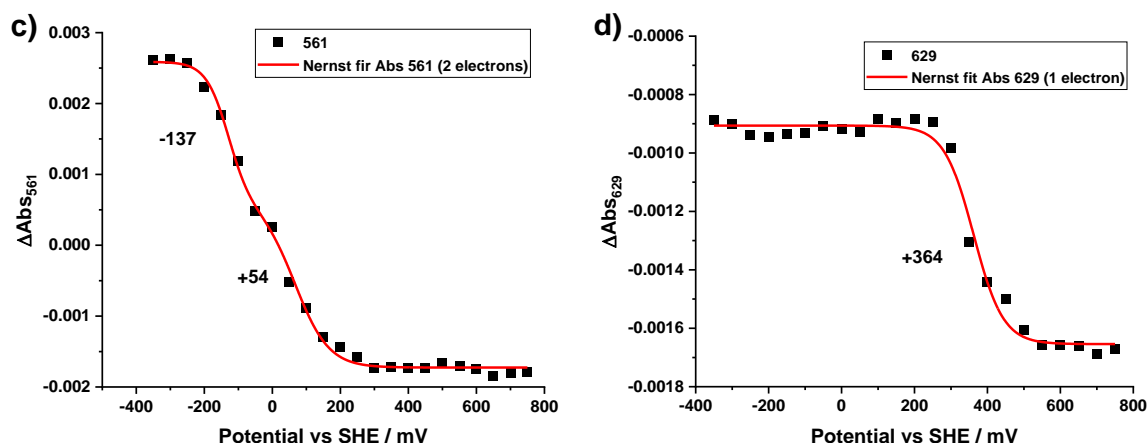


Figure 4.16. a) Example of the reductive titration of *bd-I R448N* variant in the range of +700/-300 mV vs. SHE, b) The differential absorbance of *bd-I R448N* at Soret band, 430 nm, plotted versus applied potential, c) Determination of the hemes *b* potential from differential UV/Vis spectra at 561 nm with modified Nernst equation, d) Determination of the heme *d* potential from differential UV/Vis spectra at 629 nm with modified Nernst equation.

In the figure 4.17 the normalized titration curves in the Soret region, where all three heme groups contribute, are plotted for the R448N variant. The titration in the oxidative direction was slowed down as the system required more time for equilibration that led to the higher potentials obtained for all the hemes. The large hysteresis also points towards the slow electron transition so it may require an overpotential in both directions which can be result of the introduced mutation.

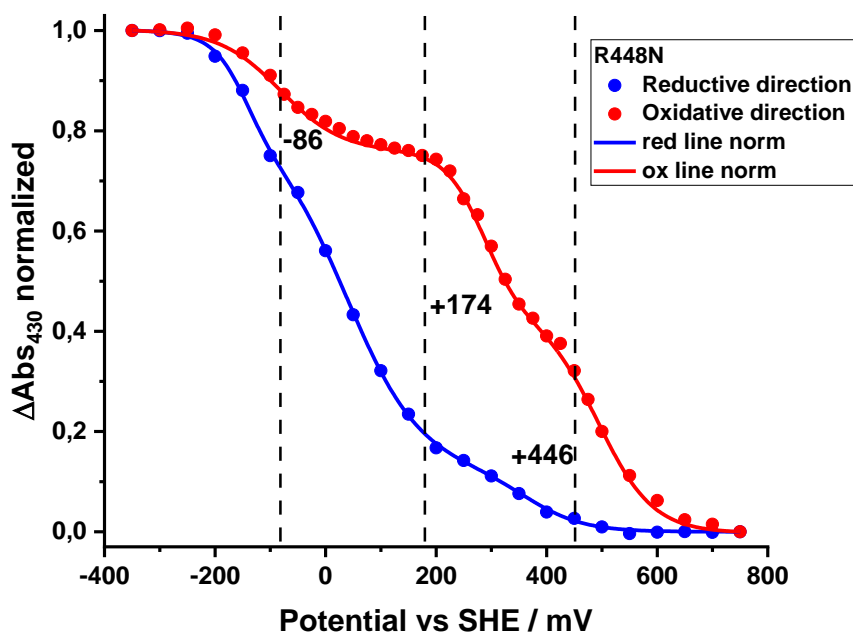


Figure 4.17. Summarized potentiometric titrations of *bd-I R448N* in reductive (blue) and oxidative (red) directions.

In case of the E445D variant the hysteresis between titrations was less than 20 mV, which is in the range of the standard error of the method. This showed that the replacement of Glu to Asp acidic residue does not drastically perturb the kinetics of the catalytic reaction, giving a good reversibility of redox reaction and absence of the coupling reactions during electron transfer. The average values of the potentials of the variants obtained from titrations in oxidative and reductive directions are given in the Table 4.4 as compared and compared with those of the wild type enzyme <sup>14, 222</sup>.

Table 4.4. Redox potentials of the *bd-I* heme groups determined by UV-vis titration; the standard error of the measurement is 20 mV.

Samples of <i>bd-I</i> oxidase	Potential vs SHE, mV		
	<i>heme b</i> ( <i>b</i> <sub>558</sub> )*	<i>heme b</i> ( <i>b</i> <sub>595</sub> )*	<i>heme d</i>
WT	176	168	258
E445D	124	276	310
R448N	174	-86	446

\* the assignment to the respective *b*-heme is tentative and for wild type based on reference <sup>14</sup>.

In the E445D variant, the redox potential of heme *b*<sub>595</sub> was up-shifted by 100 mV and that of heme *d* by 50 mV. In the R448N variant, the heme *b*<sub>595</sub> redox potential was down-shifted by 254 mV and that of heme *d* was up-shifted by 188 mV. This large shift of the redox potentials is not surprising when taking into account that the R448 residue is in hydrogen bonding interaction with the E445 ligand of the heme *b*<sub>595</sub>. Previous studies have shown that secondary interactions, such as hydrogen bonds involving the heme axial ligands, significantly influence the redox potential values of hemes <sup>284–288</sup>. The strong shifts in the redox potentials of the R448N variant probably perturb the electron transfer, and could explain the slower equilibration of the enzyme during titration experiment.


Overall, both E445D and R448N variants are still able to catalyze the oxygen reduction and bind NO in electrochemical studies. However, the catalytic current of the variants was significantly lower than for the wild type *bd-I* oxidase, which could also be due to alterations in the electron transfer chain of the enzyme. Giving the fact that E445D and R448N variants still showed significant turnover in bacterial membranes, these results demonstrates that heme *b*<sub>595</sub> is not contributing to oxygen reduction, which is in line with the structural data.

### 4.3 Conclusions

The two homologues cytochrome *bd*-I and *bd*-II oxidases from *E. coli* exhibited a highly comparable catalytic behavior. Also, the UV-Vis and red-ox induced FTIR differential spectroscopies showed a highly comparable absorbance profile for these enzymes that confirms that the environment of the redox active heme groups is similar in the two enzymes. However, the vibrational signals of the protonated acidic residues in the infrared spectrum of the cytochrome *bd*-II oxidase are shifted in comparison with the *bd*-I, that could contribute to the changes in the protonation/deprotonation states which itself can result in the alterations in the catalytic properties. This observation was in line with the results of protein film voltammetry experiments where the influence of pH was different for the two enzymes. For this assay *bd* oxidases were successfully immobilized on the gold nanoparticles electrode modified with SAM in optimized conditions. Additionally, the half-wave potential of the cytochrome *bd*-II oxidase was found at least 200 mV higher than for *bd*-I oxidase that was probably due to the upshifted potential of the active site where oxygen reduction occurs. This suggestion was supported with the results of the potentiometric titration where the mid-point potential of heme *d* was 432 mV cyt *bd*-II, which is 170 mV higher than for *bd*-I, respectively <sup>78</sup>.

The mechanism of the oxygen reduction was discussed for the E445D and R448N variants of the cytochrome *bd*-I oxidase in order to investigate the role of the heme *b*<sub>595</sub> in the catalytic cycle of the enzyme. It was shown that both variants are partially functional towards the oxygen reduction and nitric oxide binding and release, and they follow the same behavior of NO reversible inhibition with time as seen for the wild type enzyme. However, the catalytic current for E445D and R448N is much lower than for cytochrome *bd*-I oxidase and the shape of the catalytic curve was strongly altered as well. All these findings point towards a perturbed reactivity of these mutants with molecular oxygen. The slow equilibration of the reaction and high hysteresis within potentiometric titration in oxidative and reductive titrations was seen for the R448N variant which could be explained by a less favorable electron transfer caused by the introduced mutation, and as a result a significant shift in the mid-point potentials of the heme cofactors. In the E445D variant the potential of the heme *b*<sub>595</sub> was affected the most which is in the agreement with the structural data, confirming that Glu445 is the ligand of this heme <sup>13,55</sup>. Nevertheless, even with a large gap in the potentials of the heme *b*<sub>595</sub> and *d*, these mutants were able to catalyze oxygen reduction probed with a Clark electrode in solution and on the gold electrode surface in PFV setup. The results in the chapter proved that heme *b*<sub>595</sub> is not

contributing to oxygen reduction. This is in line with the structural data, that demonstrates that oxygen reduction occurs only at the heme *d*, as heme *b*<sub>595</sub> is too far to form a di-heme site<sup>13,55</sup>.



# Chapter V

## Reactivity of *bd* oxidases with nitric oxide

---

### 5.1 Nitric oxide binding to the cytochrome *bd*-I oxidase from *E. coli*

5.1.1 The oxygen electrocatalysis inhibition of cytochrome *bd*-I oxidase by nitric oxide

5.1.2 UV-Vis spectroscopy of the cytochrome *bd*-I oxidase in the presence of NO

### 5.2 Characterization of NO-binding to the homologues *bd* oxidases from *E. coli*

5.2.1 Electrocatalytic inhibition of cytochrome *bd*-II activity by NO

5.2.2 Following the spectral signature of the NO binding reaction for *bd*-II oxidase

5.2.3 pH-dependent kinetics of NO release in reduced and oxidized states

### 5.3 The role of Asp58 and Glu58 in *bd*-I and *bd*-II oxidases for NO-binding

5.3.1 The spectral characterization of the Asp58Glu and Asp58Leu cytochrome *bd*-I variants

5.3.2 NO binding of the mutated D58E and E58D *bd*-I and *bd*-II oxidases

### 5.4 Conclusions



The catalytic reduction of O<sub>2</sub> takes place at the high spin *d*-type heme in all *cyt bd* oxidases that is also the binding site for small uncharged signalling molecules such as CO, H<sub>2</sub>S and NO. In case of nitric oxide, it is produced by the host in biologic systems as a defence mechanism against invading microbial pathogens. Therefore, in order to promote virulence, the infectious bacteria have developed mechanisms that enable bacterial respiration under nitrosative stress. In particular, it was demonstrated that *bd* oxidases enhance the bacterial survival in *E. coli* under oxidative and nitrosative stress<sup>95,98,159</sup>. Consistently, a protective role of the *bd* oxidases agrees with the expression of this enzyme in *Salmonella Typhimurium*<sup>164</sup>, *Staphylococcus aureus*<sup>165</sup>, and *Mycobacterium tuberculosis*<sup>166</sup> in response to NO. Therefore, the understanding of the NO binding with cytochrome *bd* oxidase will help to evaluate the relevance of this reaction for microbial pathogenicity.

In the present chapter the cytochrome *bd*-I and *bd*-II oxidases reactivity with nitric oxide is discussed. *E. coli* contains two highly comparable cytochrome *bd* oxidases<sup>6,78</sup>, *bd*-I and *bd*-II. Despite the high similarity in sequence and structure, there are differences in accessibility of the active site through the gas channel that may cause the differences in binding to the small gaseous molecules. Here, the NO binding mechanism of *bd*-II and mutated variants of these enzymes was compared. On the basis of a bioelectrochemical sensor optimized for the inhibition assay in Chapter III, the inhibitory effect of nitric oxide on the enzyme electrocatalysis with oxygen was evaluated for the homologues *bd* enzymes<sup>260</sup>. The UV-Vis spectroscopic characterization of the NO binding and release is investigated as a function of pH. The findings of this chapter will provide helpful information on the role of the two *bd* oxidases for the bacterial defense strategies under NO-induced stress.

## 5.1 Nitric oxide binding to the cytochrome *bd*-I oxidase from *E. coli*

### 5.1.1 The oxygen electrocatalysis inhibition of cytochrome *bd*-I oxidase by nitric oxide

The response of the electrochemical sensor based on the *bd*-I oxidase immobilized on the surface of gold nanoparticles modified with thiol SAM on a single addition of 50 μM nitric oxide was monitored over an hour, Fig. 5.1a. The nitric oxide was added as an aliquot of 10 mM NaOH solution of NO-releasing compound MAHMA NONOate that decomposes at physiological pH giving two equivalents of NO (Scheme 5.1). It is noted that the release of the NO from the MAHMA NONOate is pH dependent. NO is released immediately at pH 7, while at pH 8 the release is slower. The mechanism and kinetics of the pH-depending MAHMA NONOate decomposition is described in *Annex B.5.1*.



The electrocatalytic O<sub>2</sub> reduction by cytochrome (cyt) *bd*-I oxidase was confirmed by the observation of a voltammogram sigmoidal shape with a maximum of the catalytic current at -0.4 V vs SHE. For each electrode the three subsequent voltammograms were recorded in oxygenated phosphate buffer pH 7 to ensure the stability of the enzyme film on the electrode.

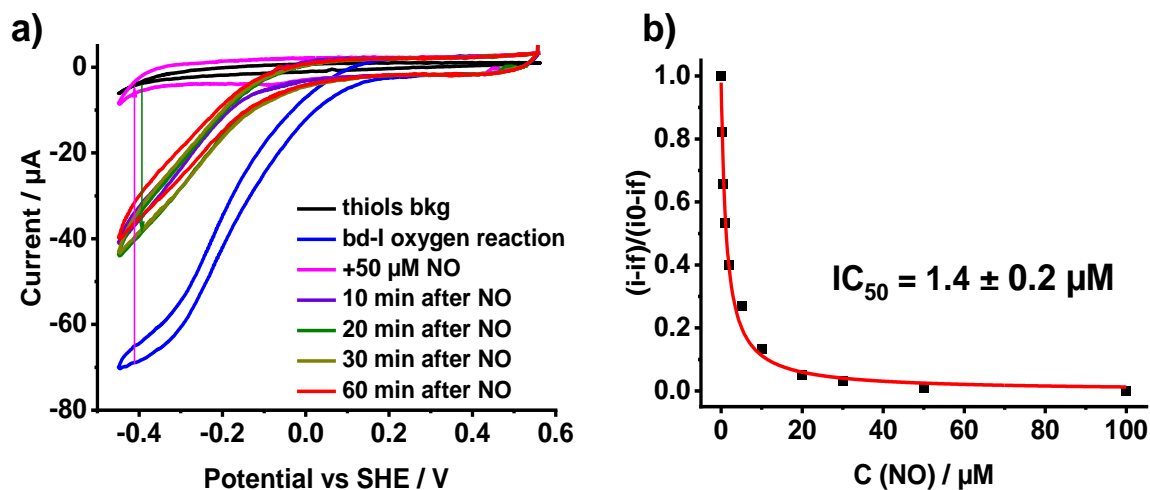


Figure 5.1 a) Electrocatalytic reduction of O<sub>2</sub> by the cyt *bd*-I oxidase (a) on a gold electrode modified with gold NPs and SAM thiols at pH 7 with 2.5 % PE (blue curve), NO inhibition of O<sub>2</sub> catalysis (pink curve) and NO release over time; b) Determination of the IC<sub>50</sub> of NO for the cyt *bd*-I oxidase. Conditions: air-saturated pH 7 phosphate buffer, scan rate 0.02V/s, rotation speed 1000 rpm.

It was observed that protein catalytic activity towards oxygen is fully inhibited by NO as the corresponding cyclic voltammogram (pink curve) reached the background level seen for electrodes in the absence of protein. However, after 10 min the activity of the *bd*-I oxidase towards O<sub>2</sub> was restored to around 52 %, whereas, in 20 min after addition of NO activity already reached 60 %, in the next 40 min no changes were further seen for the activity of cyt *bd*-I oxidase. This experiment was repeated three times on freshly prepared bioelectrochemical sensors giving the mean value of activity restoration of  $65 \pm 7$  % at a single dose of 50  $\mu\text{M}$  NO. The reversibility of the NO inhibition of the cytochrome *bd*-I oxidase activity from *E. coli* was previously reported by Giuffrè et al.<sup>159</sup>. It was shown that after the binding and scavenging of all free NO by oxyhemoglobin (HbO<sub>2</sub>), cyt *bd*-I oxidase showed a rapid recovery of the inhibited enzymatic O<sub>2</sub> activity. This unusually fast dissociation of NO from *bd*-type oxidases leading to prompt restoration of respiration proposed to be related to the bacterial protection mechanism. The interesting finding in our electrochemical experiment is that the protein activity is not restored completely. It can be explained by some protein that remaining reinhibited of NO that stays in solution. This small activity loss might also be caused by the desorption of protein from the electrode surface after a several scans.

The half-inhibitory concentration was determined from the NO dose-dependent experiment and averaged over three measurements. The value of 1.4  $\mu\text{M}$  in phosphate buffer pH 7 with concentration of dissolved oxygen of about 220  $\mu\text{M}$  is higher than that determined in solution ( $\text{IC}_{50}$  100nM NO at 70  $\mu\text{M}$   $\text{O}_2$ ) by Borisov et al <sup>170</sup>. In the study of M. Mason et al <sup>98</sup>, the NO inhibition of the *E. coli* cells respiration was probed in the *bo3*-lacking membranes, giving the  $\text{IC}_{50}$  of 218 nM at oxygen concentration of 160  $\mu\text{M}$ . In the literature, it was shown that NO acts as a competitive inhibitor for *bd* oxidases as  $\text{IC}_{50}$  values decreased upon the decrease of the oxygen concentration. It is also noted that an electrochemically determined  $\text{IC}_{50}$  value is often shifted in comparison to values obtained in solution <sup>98,260</sup> due to the immobilization of the enzyme, but they are suitable for the comparison of different enzymes studied in the same conditions.

### 5.1.2 UV-Vis spectroscopy of the cytochrome *bd*-I oxidase in the presence of NO

The NO binding to the cytochrome *bd*-I oxidase in dithionite-reduced and air-oxidized states was probed by the UV-Vis spectroscopy. The experiment was performed in the glass cuvette upon addition of NO in 100 equivalent excesses to the protein. The 5  $\mu\text{M}$  protein sample was reduced by the addition of a few grains of sodium dithionite. Noticeably, in both redox states the Q-bands of the two hemes *b*, namely 531, 560 nm (red) and 530 nm (ox), are left intact by the presence of nitric oxide (Fig. 5.2). On the contrary, the band attributed to the heme *d* at 630 nm is upshifted to 641 nm in reduced state and the band at 647 nm in oxidized state is downshifted to 638 nm. Hardly noticeable changes in the shape of the Soret band are seen probably due to the alterations of the heme *d*.

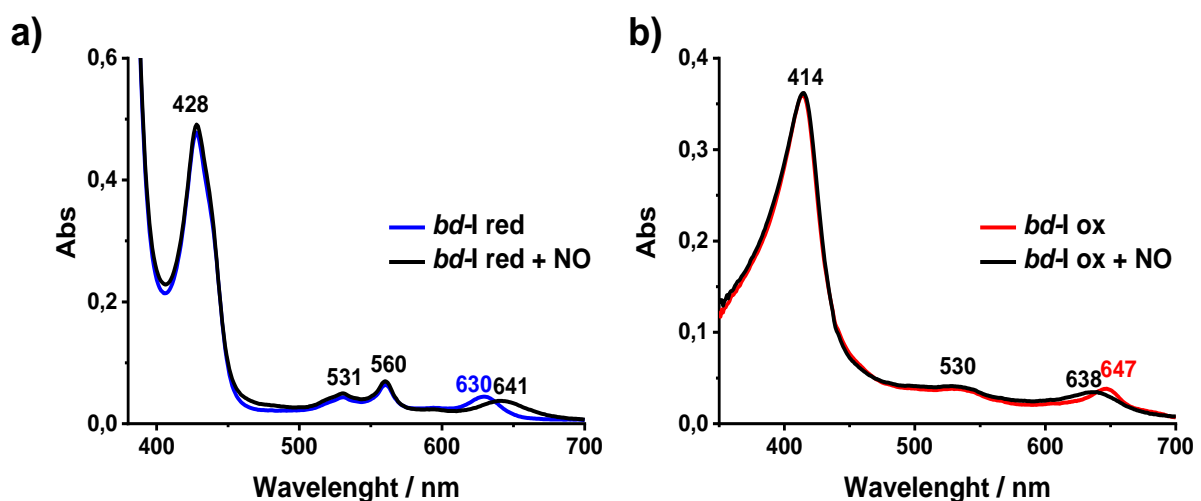


Figure 5.2. UV-Vis spectra of the *bd*-I in reduced (a) and oxidized (b) state upon addition of 1:100 equivalent of NO to the sample at pH 7.

The changes observed here upon NO binding are in agreement with those reported in literature<sup>95,169,289</sup>. These findings are in line with the fact that NO substrate is in competition with oxygen at the active site composed of the heme *d*, forming the heme *d* Fe<sup>2+</sup>-NO nitrosyl-adduct in reduced state. Together with the electrocatalytic reversibility of NO inhibition, these results point at the NO reaction with the cytochrome *bd* oxidases as one of the key protective mechanisms of *E. coli* against nitrosative stress.

## 5.2 Characterization of NO-binding to the homologues *bd* oxidases from *E. coli*

*E. coli* contains two homologues cytochrome *bd* oxidases, *bd*-I and *bd*-II, with highly comparable structures and highly similar sequence of 60%<sup>6,78</sup>.

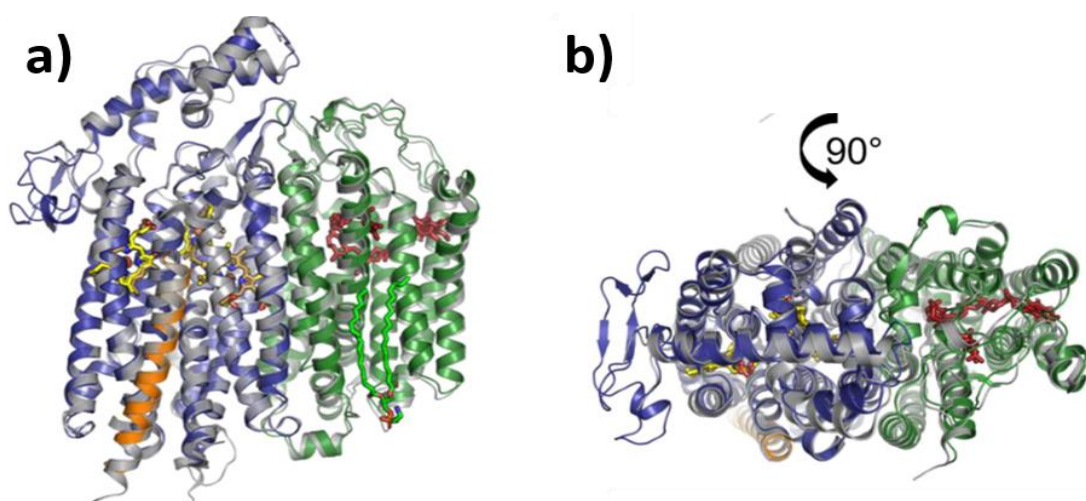


Figure 5.3. Superposition of *bd*-II with *bd*-I structures from *E. coli* (a) and top view (b)<sup>78</sup>. The homologous subunits of *E. coli* *bd*-I are all shown in gray, the heme groups are shown in yellow and ubiquinone-8 in red.

However, there are differences in accessibility of the catalytic center through the gas channel that can modulate difference in NO reactivity. Here, the focus is on the comparison of the NO binding mechanism of *bd*-I and *bd*-II oxidases.

### 5.2.1 Electrocatalytic inhibition of cytochrome *bd*-II activity by NO

The effect of nitric oxide on electrocatalytic O<sub>2</sub> reduction was also studied for the cytochrome *bd*-II oxidase. It worth mentioning that stable protein films on the 3D gold nanoparticles electrodes modified with thiol SAM were obtained only after addition of 2.5% PG phospholipids to the *bd*-II sample previously washed twice in phosphate buffer pH 7 to decrease the amount of the detergent.

First difference seen is that the onset of catalysis is 100 mV higher for the *bd*-II than for the cyt *bd*-I oxidase, pointing at the lower overpotential required and thus, it may be related

to the higher affinity of *bd*-II towards oxygen. Secondly, there are two visible contributions in the catalytic curve at  $-0.002\text{V}$  and  $-0.226\text{V}$  half-wave potentials which is not typical for *bd*-I oxidase. This character of the voltammogram is probably linked to the ability of cyt *bd*-II to exist in the form of monomers and dimers showed by mass photometry<sup>78</sup>. Thirdly, the reversible NO inhibition of the protein activity is characteristic for both homologues oxidases at pH 7. Upon NO addition cyt *bd*-II oxidase immediately loses its electrocatalytic signal due to the inactivation of the enzymes, likewise *bd*-I isoform. Within 20 min after introduction of  $50\ \mu\text{M}$  NO the recovery of catalytic activity reached 74 %, and the  $\text{IC}_{50}$  of  $1.3\ \mu\text{M}$  was determined for this enzyme.

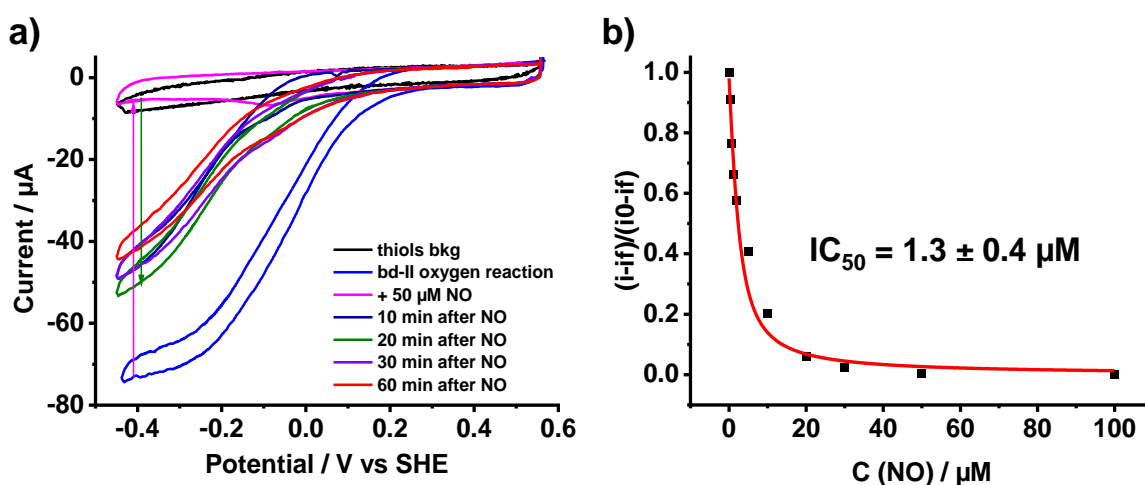


Figure 5.4. a) Electrocatalytic  $\text{O}_2$  reduction by cyt *bd*-II oxidase (a) on a gold electrode modified with gold NPs and SAM thiols at pH 7 with 2.5 % PG (blue curve), NO inhibition of  $\text{O}_2$  catalysis (pink curve) and NO release over time; b) Determination of the  $\text{IC}_{50}$  of NO for the cyt *bd*-II oxidase. Conditions: air-saturated pH 7 phosphate buffer, scan rate  $0.02\text{V/s}$ , rotation speed 1000 rpm.

We then looked at the effect of pH on the NO inhibition activity for both enzymes. For this purpose, the electrocatalytic study with immobilized proteins on gold nanoparticles electrodes was performed in phosphate buffers of pH 6 and 8. The prompt inhibition of the enzyme activity was also seen at pH 6 for both oxidases, however, at pH 8 it took up to 10 minutes to reach the full inhibition (Fig. 5.5). Additionally, it was seen that at pH 8 after NO binding to the protein, the catalytic activity was not restored for over an hour suggesting that nitric oxide acted as a potent inhibitor of cytochrome *bd* oxidases at alkaline pH. Interestingly, the self-crossing shape of the curve was seen only at pH 6 in direction of oxidation for the voltammograms recorded immediately after NO addition. It can be due to coupled process such as protonation event (e. g., of the heme ligand, amino acid).

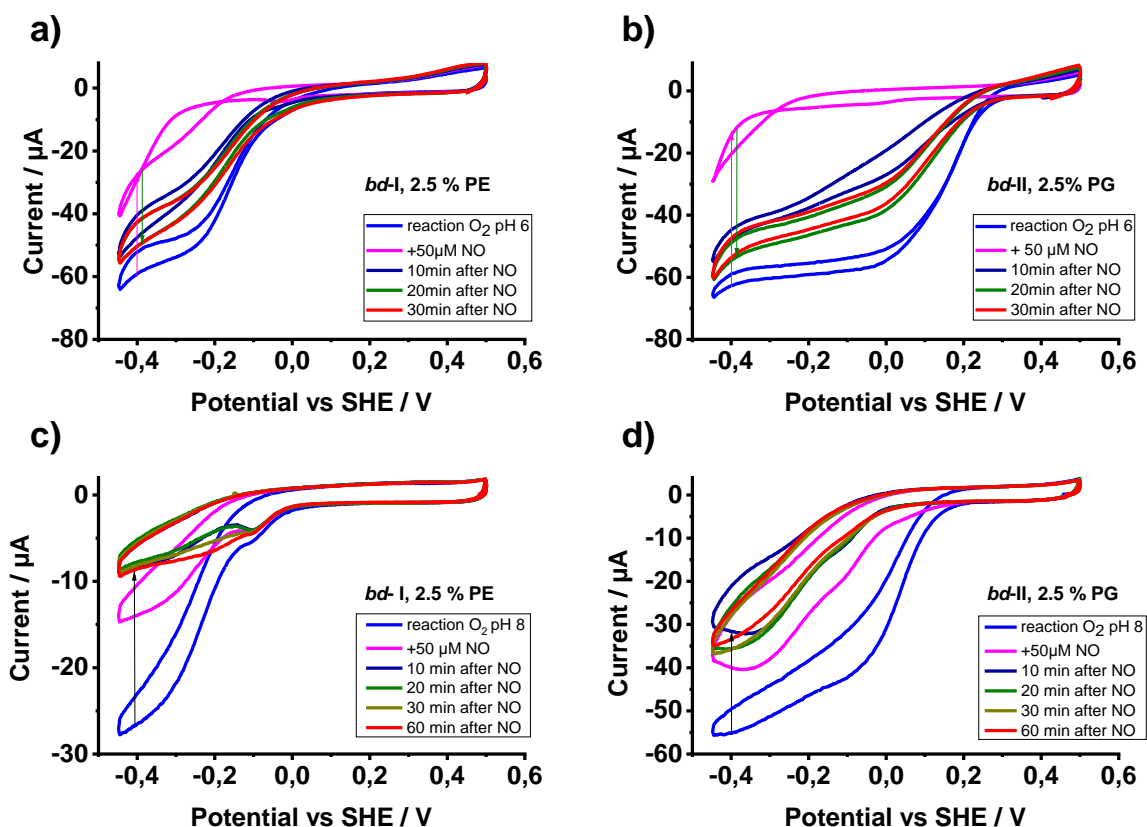


Figure 5.5. Electrocatalysis of  $O_2$  of the cyt *bd-I* oxidase (a, c) and *bd-II* (b, d) on a gold electrode modified with gold NPs and SAM thiols at pH 6 (a, b) and 8 (c, d) (blue curve), NO inhibition of  $O_2$  catalysis (pink curve) and NO release within an hour.

### 5.2.2 Following the spectral signature of the NO binding reaction for *bd-II* oxidase

Similarly to *bd-I*, when NO was added to the cyt *bd-II* oxidase only changes in the bands of the heme *d* were seen. The bathochromic shift from 630 to 641 nm in reduced form and hypochromic shift from 649 to 638 nm in oxidized state were similar for those seen for cyt *bd-I* oxidase. Again, the position of the Q-bands attributed to heme  $b_{558}$  and  $b_{595}$  was not affected by nitric oxide. The only difference was the maximum and shape of the Soret band, which was typical for the *bd-II* isoform<sup>78</sup>.

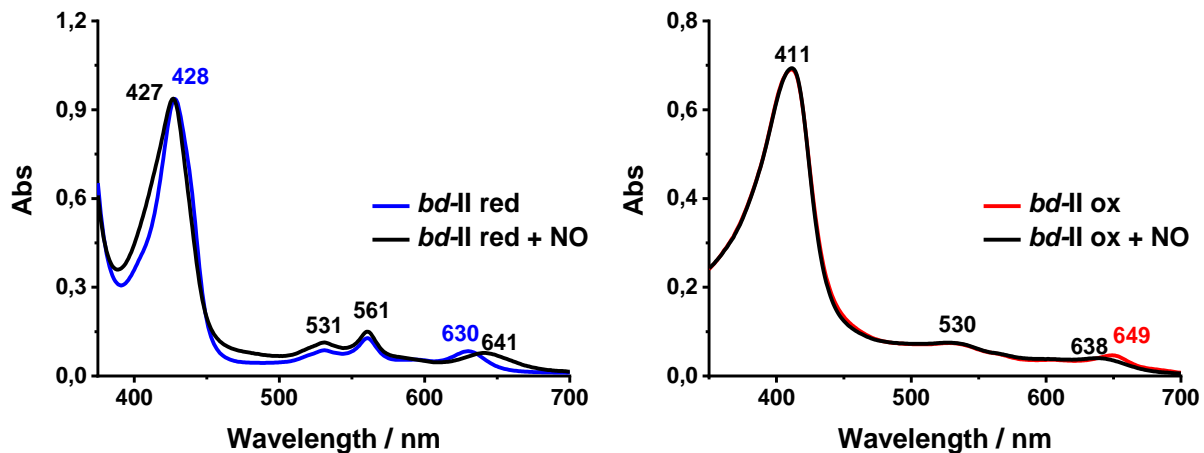


Figure 5.6. Full UV-Vis spectra of *bd-II* oxidase in reduced (a) and oxidized (b) state upon addition of the 1:100 equivalent of NO to the sample at pH 7.

### 5.2.3 pH-dependent kinetics of NO release in reduced and oxidized states

UV-Vis spectroscopy was also employed to follow the NO-binding and release from the active site of cytochrome *bd-I* and *bd-II* as a function of pH. The reduced state binds and releases NO leading to the suggestion that *cyt bd* protects *E. coli* against NO inhibition. To the best of our knowledge, all kinetic studies of this reaction were performed at pH 7, suggesting the molecular mechanism of NO binding for this enzyme in ferrous, one-electron reduced (mixed valence, MV), ferryl and ferric state of the heme *d*<sup>95,168,170,290</sup>. From the absorbance spectra of *bd* oxidases, the formation of the heme *d* Fe<sup>2+</sup>-NO complex leads to a shift of the signal at 630 nm to 641 nm and its release to the appropriate backshift (heme *d* Fe<sup>2+</sup>-O<sub>2</sub>). Therefore, the release of NO and substitution back by O<sub>2</sub>, allows us to follow the transition of the maximum of the heme *d* band as a function of pH (Fig. 5.7). The hypsochromic shift of the band with maximum at 641 nm was monitored after a single introduction of 500 μM NO to the reduced protein, from NO-releasing compound MAHMA NONOate for an hour. Visible spectra were recorded every minute. The binding kinetics in our experiments were thus also governed by the NO formation from NONOate and does not necessarily reflect an intrinsic property of the enzyme, even if the same pH was applied for both enzymes.

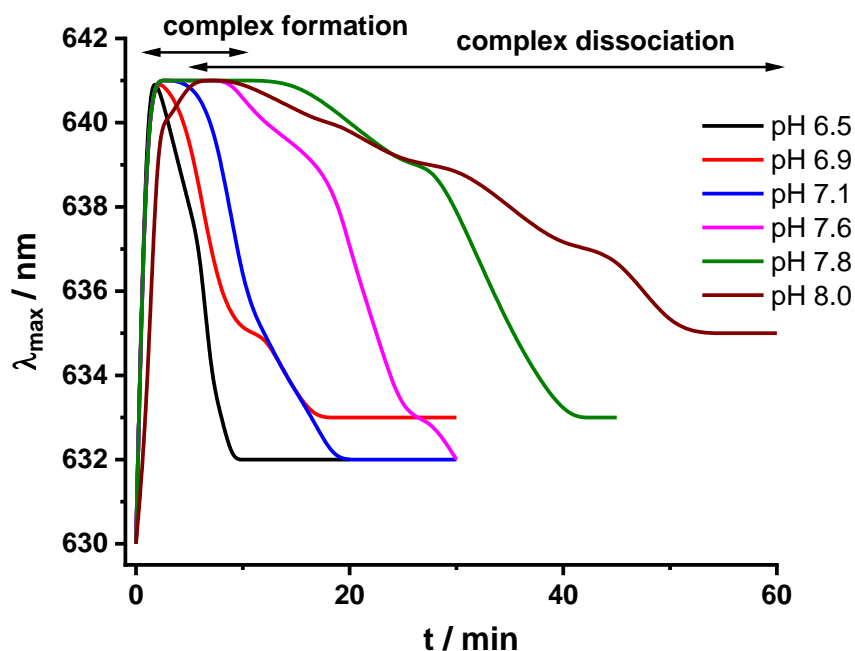


Figure 5.7. The shift of the maximum of the heme *d*  $Fe^{2+}$ -NO complex over one hour as a function of pH in 100mM phosphate buffer with 100 equivalent excess of NO to 5  $\mu$ M cyt *bd*-I oxidase.

It can be seen that at all pH values the heme *d*-NO complex was formed immediately with 641 nm maximum, except at pH 8 where this value was reached only after 5 minutes of ongoing reaction. The release of NO from heme *d* is 10 times slower at higher pH, up to 50 minutes, while it takes 5-10 min at pH 6.5 and 7. To investigate the mechanism of this process in details the pH dependent NO release from the active site was investigated for the two homologues cytochrome *bd* oxidases, *bd*-I and *bd*-II by UV/vis spectroscopy.

The Figures 5.8 shows the series of UV/vis spectra obtained for both cyt *bd* oxidases in the reduced and oxidized state after NO addition in phosphate buffers of pH values from 6.5 to 8 in the spectral region characteristic for the heme *d*. The NO release (backshift to 632 nm) was seen from both enzymes between pH 6.5 and 7.5. Overall, NO was faster released from *bd*-II at more acidic pH values than from *bd*-I. At pH 7.5 NO is released with similar rates from both enzymes, while at pH 8 it was hardly released from *bd*-I, while it was still bound to cyt *bd*-II even after one hour. Thus, NO is an effective inhibitor at pH 8.

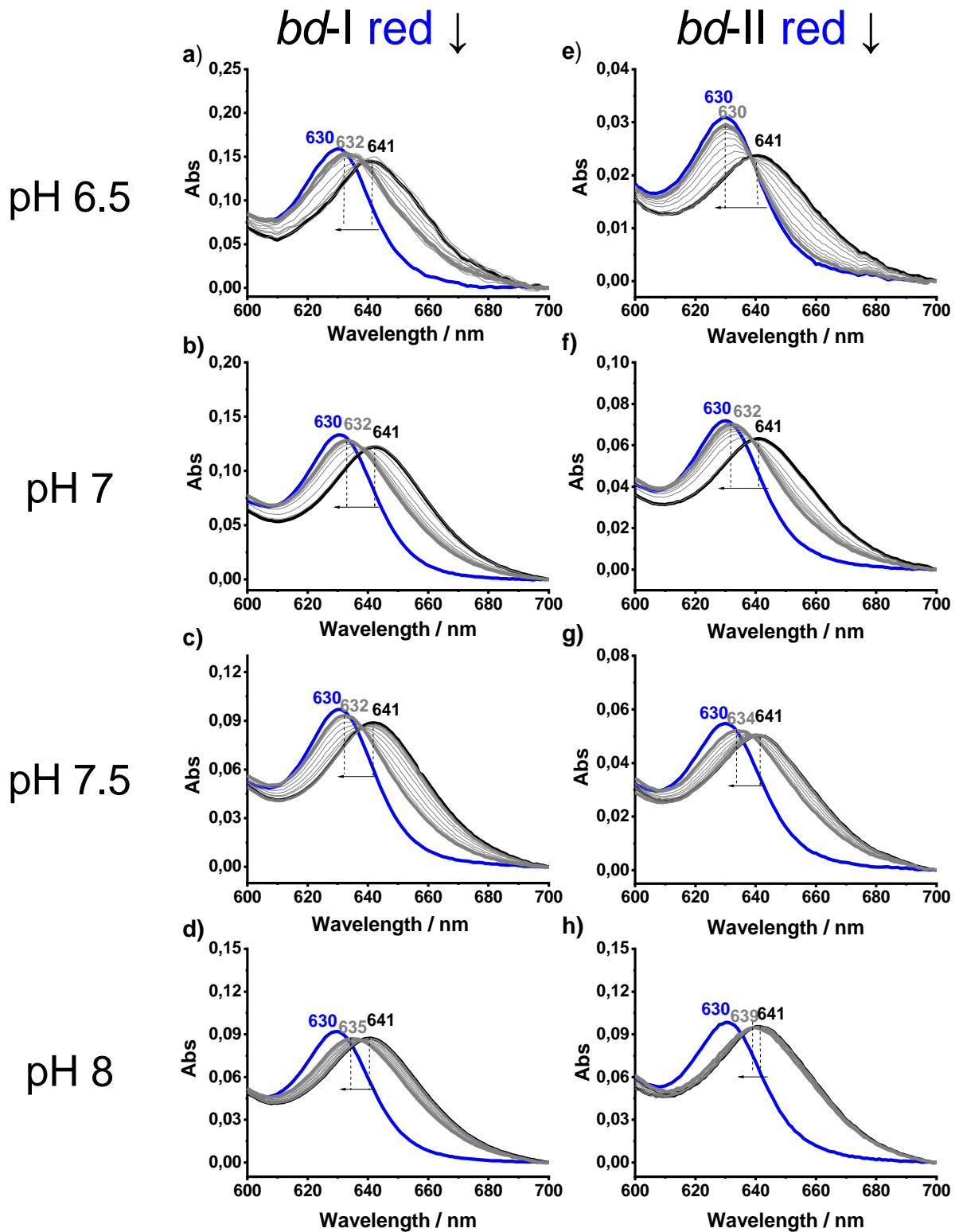


Figure 5.8. pH-dependent NO-binding and -release to the heme *d* in reduced state for *bd-I* a) pH 6.5, b) pH 7, c) pH 7.5, d) pH 8 and for *bd-II* at e) pH 6.5, f) pH 7, g) pH 7.5, h) pH 8; reduced protein (blue), complex heme *d*-NO (black), final state 60 min after binding NO (grey).



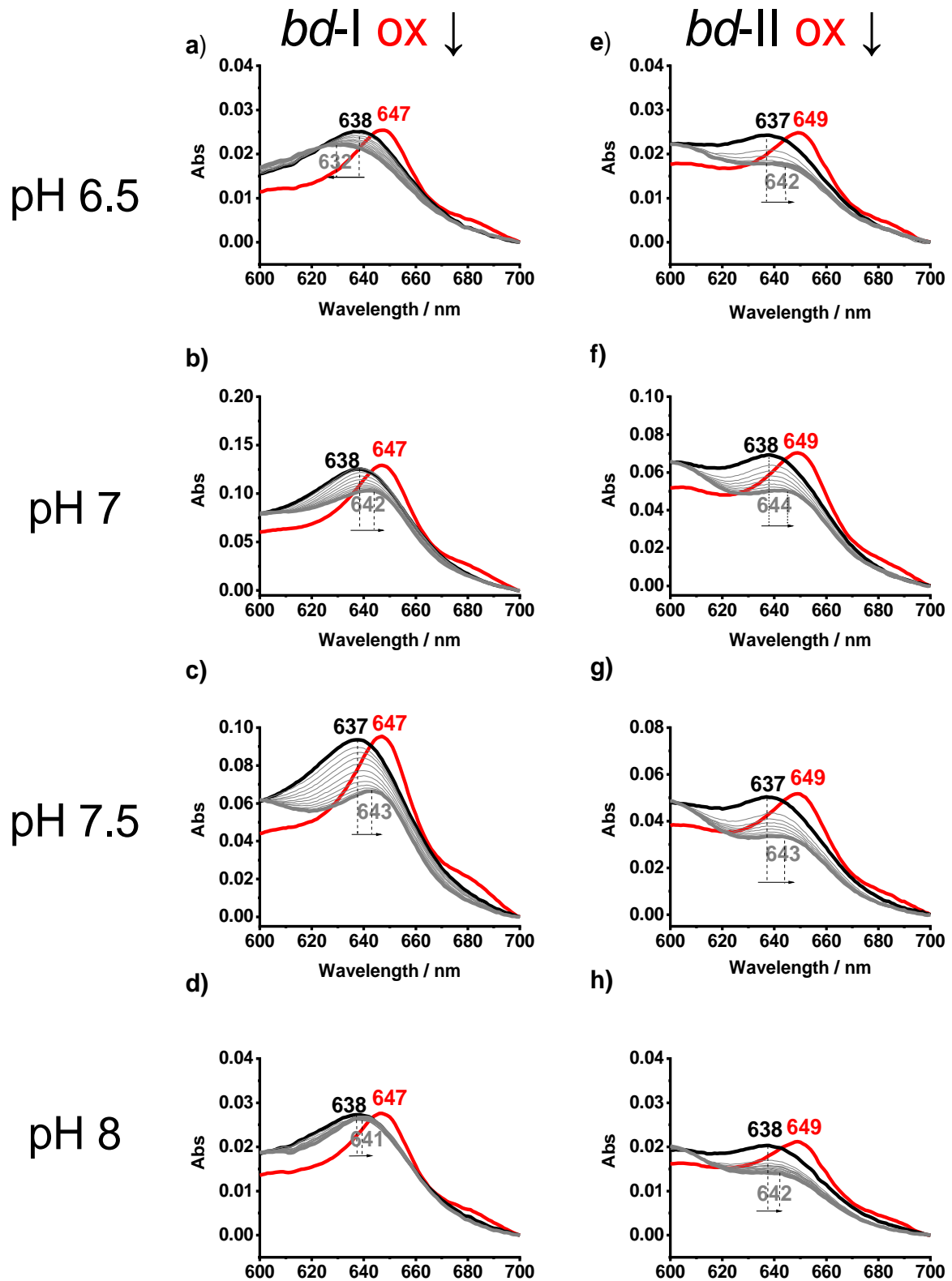


Figure 5.9. pH-dependent NO-binding to the heme *d* in oxidized state for *bd-I* a) pH 6.5, b) pH 7, c) pH 7.5, d) pH 8 and for *bd-II* at e) pH 6.5, f) pH 7, g) pH 7.5, h) pH 8; oxidized protein (red), complex heme *d*-NO (black), final state 60 min after the binding with NO (grey).

Figure 5.9 depicts the series of the visible spectra obtained after addition of NO to the *bd*-I and *bd*-II oxidase samples in the oxidized form at different pH values. The characteristic shift from 649 to 637 nm signifies the binding of NO to the heme *d*. The spectral changes seen in an hour experiment suggest that heme *d* cannot fully recover from the nitric oxide binding and therefore a new state is formed. It was proposed by Borisov et al that the ferric enzyme binds NO at heme *d* yielding a nitrosyl adduct ( $d^{3+}\text{-NO}$  or  $d^{2+}\text{-NO}^+$ ) with characteristic optical features (an absorption increase at 639 nm) <sup>168</sup>. Interestingly, for *bd*-I oxidase at pH 6.5 the reverse evolution is seen as compared to *bd*-II oxidase: the peak of the heme  $d^{3+}\text{-NO}$  complex is moving in opposite direction from 637 to 632 nm rather than reaching the original state before addition of nitric oxide, thus a different state of the NO complex may be obtained.

In summary, in order to identify differences between *E. coli* *bd*-I and *bd*-II oxidases reactivity with NO, the UV/vis spectra and electrocatalytic properties of both enzymes as a function of pH were compared. The unusually high NO dissociation rate is part of the role of the *bd* oxidases as a defense factor of the *E. coli* bacterium <sup>159</sup>. It was shown that the reversible inhibition of oxygen catalysis by nitric oxide at pH 7 is similar for both *bd* oxidases. The determined half-inhibitory concentration of 1.3  $\mu\text{M}$  for *bd*-II oxidase and about 70 % recovery of the enzyme activity after single addition of 50  $\mu\text{M}$  NO is highly comparable with values obtained for the cyt *bd*-I oxidase by protein film voltammetry. The pH dependence of NO release from the reduced active site differed between the two oxidases as monitored by UV-Vis spectroscopy. It was shown that NO release is slower at higher pH for both isoforms, and at pH 8 NO is not released over two hours from cyt *bd*-II oxidase, and is thus a potent inhibitor. In oxidized state, the direct pH dependency of the NO reactivity with *bd* oxidases from *E. coli* was not observed. However, when comparing the oxidized form of *bd I/bd II* at pH 6 and reduced *bd I/II* at pH 8 the release of NO is clearly different, as well as the spectral signatures changes.

### 5.3 The role of Asp58 and Glu58 in *bd*-I and *bd*-II oxidases for NO-binding

The analysis of the recently published cryo EM structures of cytochrome *bd*-I and *bd*-II reveal that there are major differences in the solvent channel towards the active site <sup>3,6,13,78</sup>. It appears that the gating residues Asp58 of *bd*-I and Glu58 of *bd*-II in CydB subunit connecting the solvent channel with the active site heme *d* may represent the turnstiles of proton supply for O<sub>2</sub> reduction. Figure 5.10 shows these different channels and importantly the differences of the pKa values for the residues 58 that is located in both enzymes in a very hydrophobic environment. The calculated pKa with PropKa program (*see in Annex C.3*) give 8.71 for Asp

58 and 10.97 for Glu58 in *bd-I* and *bd-II*, respectively. The difference is thus more than 2pK units, these calculations were done by D. Wohlwend from the group of Prof. T. Friedrich (Freiburg University). However, calculating the electrostatic surface potential by Advanced Poisson-Boltzmann Solver (APBS) around this position indicated that Asp58 is presumably protonated at neutral pH due to its hydrophobic environment that favors the protonated carboxyl group over the de-protonated carboxylate. Therefore, to specifically investigate the contribution of position 58 to NO binding, the cyt *bd-I* variant Asp58Glu and the cyt *bd-II* Glu58Asp variant were generated and then NO reactivity was characterized.

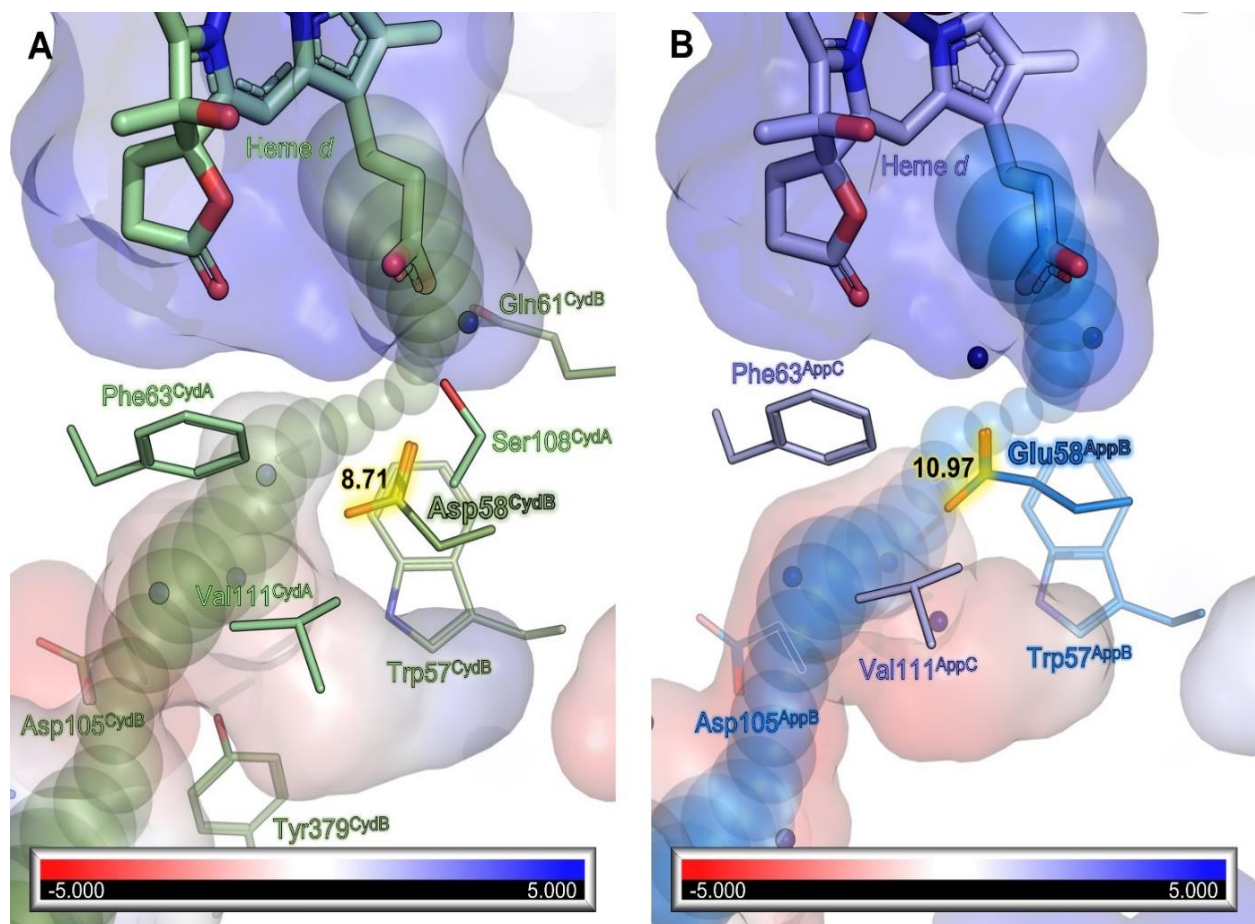


Figure 5.10. Titratable sidechains connect solvent channel with heme *d* cavity in *E. coli* *bd-I* (pdb code: 6RKO) (A) and *bd-II* (pdb code: 7OY2) (B). Water molecules are shown as small blue spheres. The substrate channel was probed with CAVER (shown as olive (*bd-I*) and blue (*bd-II*) spheres with diameters illustrated by sphere sizes).

### 5.3.1 The spectral characterization of the Asp58Glu and Asp58Leu cytochrome *bd-I* variants

To elucidate a possible function of Asp58 in CydB subunit of cytochrome *bd-I* oxidase, it was individually exchanged to a glutamate (D58E) and leucine (D58L) residue by site directed mutagenesis. Firstly, the structural integrity of the obtained *bd-I* variants was

confirmed by UV-Vis spectroscopy (Fig. 5.11). In all differential dithionite-reduced minus air-oxidized spectra the signature of all three heme cofactors is seen. The small alterations in the shape of the Soret band in comparison with the wild type point at the slight change in the environment of the hemes modulated by the introduced mutations.

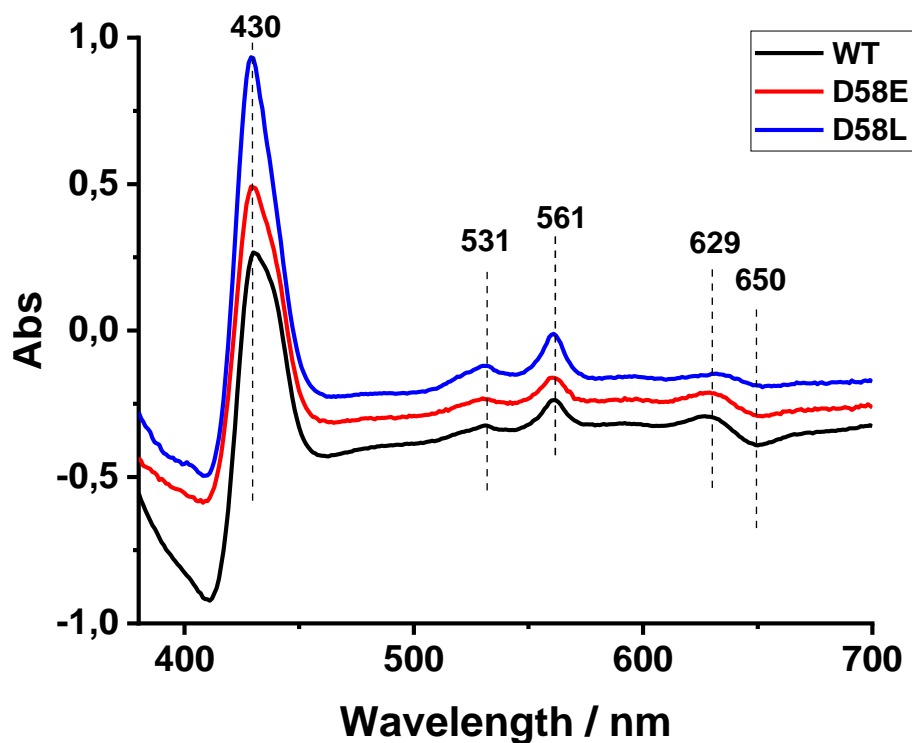


Figure 5.11. UV-Vis dithionite reduced-oxidized spectra of cytochrome *bd*-I oxidase WT and mutants D58E, D58L.

Secondly, FTIR spectroscopy in the thin-layer electrochemical cell was employed to evaluate the changes due to the mutation of the Asp58. The (oxidized-minus-reduced) redox induced FTIR difference spectra of cyt *bd*-I and its variants are shown in Fig. 5.12.

The wild-type FTIR spectrum of cyt *bd*-I and *bd*-II was described in Chapter III, where the characteristic signals for ubiquinone were seen in all spectra at 1649 (C=O), 1612 (C=C) and 1265  $\text{cm}^{-1}$  (-COCH<sub>3</sub>) (Fig. 5.12). Interestingly, the spectra of the D58L variant also contained signals of menaquinone, for example at 1293  $\text{cm}^{-1}$ , whereas, both quinones were previously detected in less active mutants of cyt *bd*-I<sup>282</sup>. Another change in the signature was detected at about 1672  $\text{cm}^{-1}$ , where protonated heme propionates contribute<sup>291</sup>. Such a shift points to changes in the hydrogen bonding to the heme *d* propionate's (-C=O) groups and may be explained by its close proximity of 3.8 Å to Asp58.

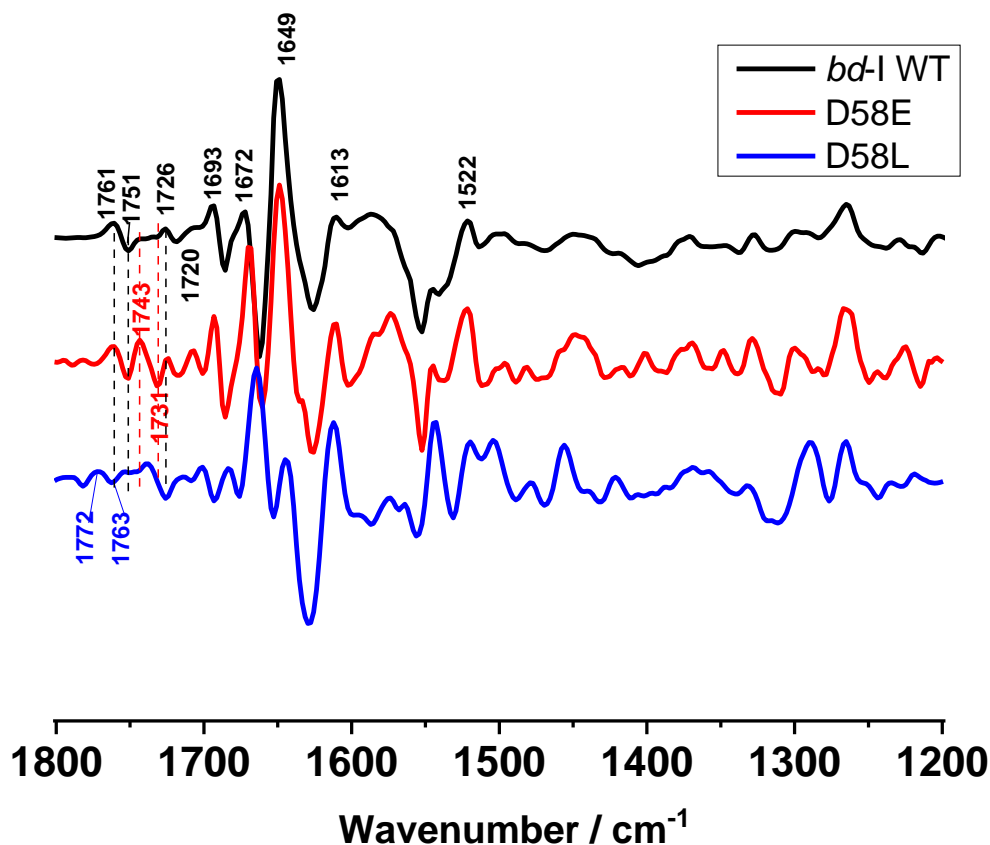


Figure 5.12. Oxidized-minus-reduced FTIR difference spectra of wild type *cyt bd-I* (black) and the D58E (red) and D58L (blue) variants.

In the spectra of mutants, the most prominent changes are seen in the region from 1700 to 1800  $\text{cm}^{-1}$  where the vibrational modes of the protonated acidic residues are expected<sup>240</sup>. The bands at 1726  $\text{cm}^{-1}$  and at 1761/1751  $\text{cm}^{-1}$  were clearly detectable in the spectra of wild type and the D58E variant but absent in the leucine variant. The positive signal at 1726  $\text{cm}^{-1}$  was previously assigned to Glu107Ala, and 1761/1751  $\text{cm}^{-1}$  to Glu99Ala<sup>278</sup>. However, it is worth mentioning that mutations at unequivocal position led to a strong perturbation of the signals of bound hemes and might lead to an unequal assignment.

For the D58E variant the new band at 1741/1731  $\text{cm}^{-1}$  appeared probably as a result of the introduced mutation, giving a high pKa calculated for this residue which must be protonated in the hydrophobic environment at pH 7. In addition, characteristic signals for (-COOH) vibrations at 1590-1520  $\text{cm}^{-1}$  are displaced that may originally correspond to the deprotonated Asp58 and now reflect contributions from Glu58. In the case of D58L, all above mentioned vibrational modes for the wild type and D58E in the region of protonated acids are not detected.

The significant alterations in the redox induced FTIR data upon the exchange of the Asp58 residue are in line with activity measurements<sup>292</sup> performed by J.Kagi from the group

of Prof. T. Friedrich (Freiburg University). The results of the duroquinol:oxygen oxidoreductase activity as a function of pH demonstrated that the D58L variant exhibited nearly no activity, while D58E variant showed a significantly increased activity especially at alkaline pH. All these findings confirm the importance of the acidic residue in 58<sup>th</sup> position for the catalysis. It is suggested that the Asp58 of subunit CydB from *E. coli* cyt *bd*-I oxidase is a part of a proton pathway transferring protons from the cytoplasm to the active site in subunit CydA for oxygen reduction<sup>292</sup>. Taking into account the competition of the nitric oxide with oxygen at the heme *d*, at the next step we focused on the investigation the influence of the acidic residue at 58<sup>th</sup> position in cyt *bd*-I and *bd*-II on the NO inhibition activity.

### 5.3.2 NO binding of the mutated D58E and E58D *bd*-I and *bd*-II oxidases

The mutants of the Asp to Glu (D58E) and Glu to Asp (E58D) of the cytochromes *bd*-I and *bd*-II were kindly prepared by group of Prof. T.Friedrich. Both mutations did not alter the UV/vis spectra of the preparations. The duroquinol:oxygen oxidoreductase activity of the obtained variant was also measured by our collaborators, elucidating the importance of these residue for the pH dependent catalytic activity.

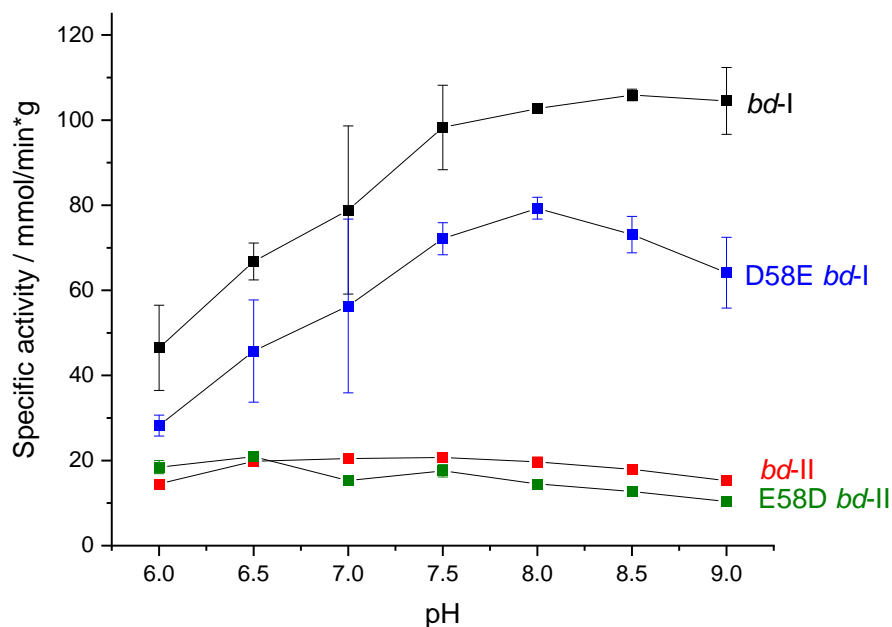


Figure 5.13. Duroquinol:oxygen oxidoreductase activity of cyt *bd*-I and *bd*-II wild type (black and red), the Asp58Glu (olive) and the Glu58Asp (blue) variants as a function of pH.

For the wild type, the activity of cyt *bd*-I raised continuously from pH 7 to pH 9, while activity of cyt *bd*-II showed a broad maximum between 6.5 and 7.5. This pH dependence is in

agreement with data reported for both enzymes in the bacterial membrane<sup>280</sup>. The activity pattern was similar for the mutated enzymes with the replacement of acidic residue in 58<sup>th</sup> position (Fig. 5.13). However, the D58E variant had rather unexpectedly high absolute values comparing to the parental cytochrome *bd*-I oxidase.

The visible spectra of the reduced forms of D58E (Fig. 5.14a) and E58D (Fig. 5.14b) mutants were recorded upon addition of nitric oxide. Again, it is seen that only heme *d* binds the substrate resulting in the bathochromic shift from 630 to 641 nm accompanied by the small changes in the Soret band, likewise the wild type enzymes.

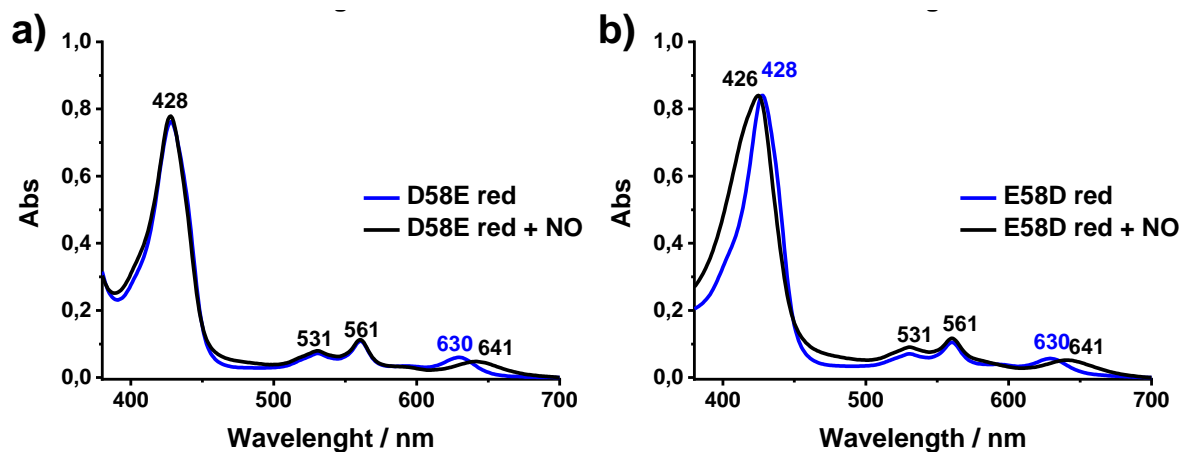


Figure 5.14. Full UV-Vis spectra of the mutants D58E (a) and E58D (b) in reduced state upon addition of 1:100 equivalent of NO to the sample at pH 7.

In the next step, the pH dependent NO binding and release was investigated for both variants in the same conditions as the wild type. The series of the visible spectra of the D58E and E58D cytochrome *bd* oxidases in reduced state between pH 6.5 and 8 are shown in the Fig. 5.15. In contrast with the wild type, over all the pH studied range the NO was only partly released from the enzyme as indicated by a small back shift to 636/638 nm. For both variants, no signal shift was seen in all at alkaline solution for over an hour. It can be concluded that in these mutants NO remained mostly bound to the active site, heme *d*. Whether the small 3-4 nm shift of the signal reflects a different mechanistic state or just a small change in the structure needs to be probed in further experiments.

The spectral results obtained for the cytochrome *bd*-I and *bd*-II oxidase with mutated 58<sup>th</sup> position in the CytB subunit gave an important information about the role of this acidic residue for the oxygen and NO binding. Strong changes were observed in the activity profiles and the FTIR difference spectra of the D58E, D58L variants of *E. coli* cyt *bd*-I. While the oxidoreductase activity gave the similar profile in the pH dependent activity for both mutants as compared to the wild type, the character of the NO release from the active site has

significantly changed. These alterations might be modulated by conformational changes within the proton channel of the mutated variants and, therefore, changes in the ability to reverse the binding of molecular oxygen at the heme *d*.

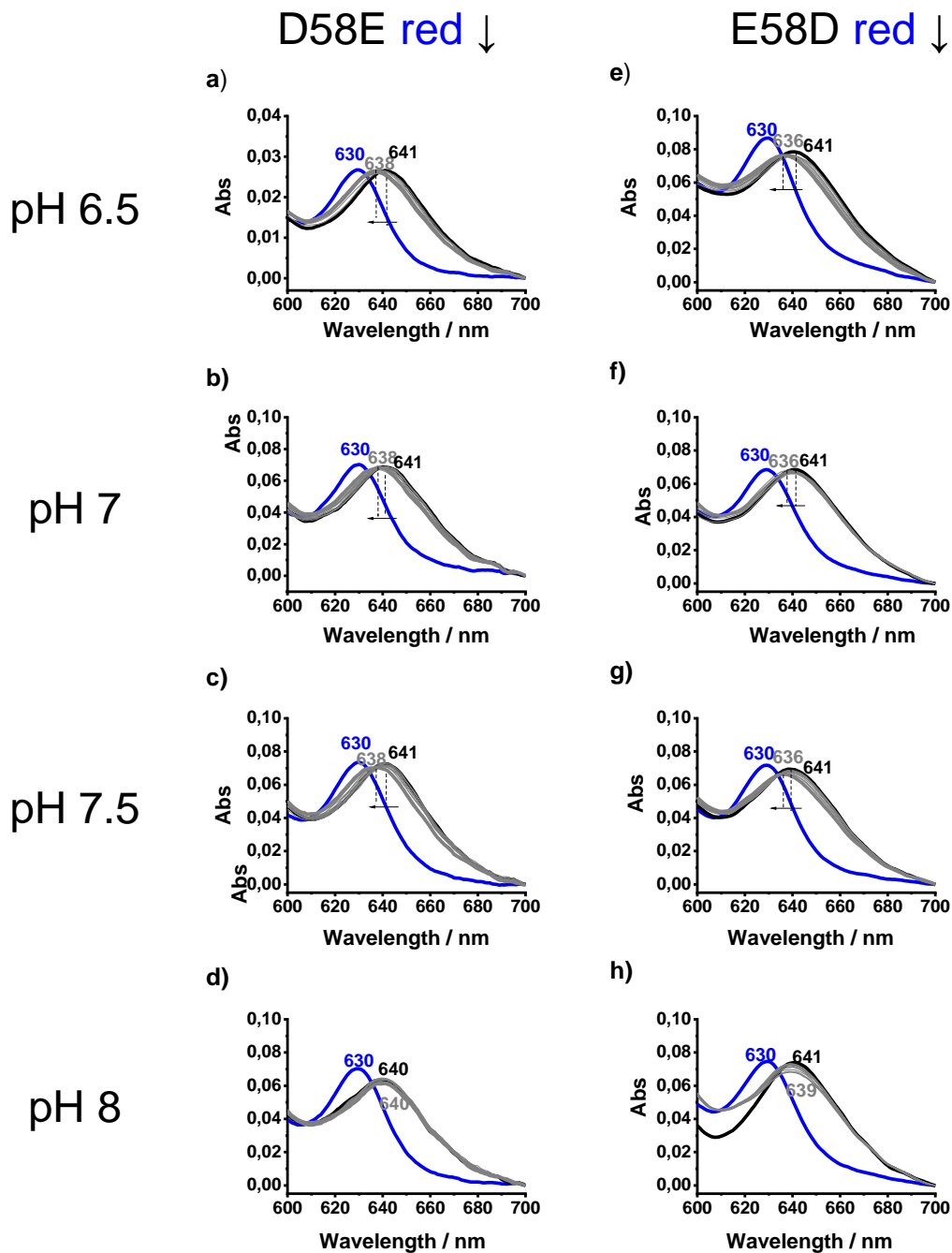


Figure 5.15. pH-dependent NO-binding and -release to the heme *d* in reduced state for D58E a) pH 6.5, b) pH 7, c) pH 7.5, d) pH 8 and for E58D e) pH 6.5, f) pH 7, g) pH 7.5, h) pH 8; reduced protein (blue), complex heme *d*-NO (black), final state 60 min after binding NO (grey).




## 5.4 Conclusions

From the experiments discussed in this chapter, we can conclude that nitric oxide reactivity in reduced and oxidized state of *bd* oxidases from *E. coli* is solely related to the binding at the high-spin heme *d*. The NO release from the cytochrome *bd*-I and *bd*-II oxidase was investigated in the broad range of physiological pH from 6 to 8 by electrochemical and spectroscopic methods. When NO is added, it competes with molecular oxygen at the active site and immediately inhibits the oxidoreductase activity at pH 7 as proved by protein film voltammetry. However, the NO inhibition is reversed over time, up to 70 % recovery for proteins immobilized on the gold nanoparticles electrodes modified with thiol SAM. This tendency is true for the solutions up to pH 7.5. At pH 8, however, the NO is acting as a potent inhibitor. This is in line with the UV-Vis experiments, where upon increase of the pH in protein solutions *bd*-I oxidase NO release is slowed down, whereas *cyt bd*-II is not able to release NO from the heme *d* at alkaline pH.

Finally, the NO reactivity was investigated in the variants of the *cyt bd*-I and *bd*-II oxidases with the exchange of the Asp→Glu and Glu→Asp, respectively, at 58<sup>th</sup> position in CydB subunit. The release of NO from the active site was altered in both mutants, thus these residues might play a crucial role in bacterial protection against nitrosative stress.

Overall, these findings contribute to the knowledge of the NO reaction mechanism of the unique prokaryotic enzyme *bd* oxidase, giving valuable insight into the pH dependent character of the NO release from the active site. The results mentioned above suggest that the acidic residue at 58<sup>th</sup> position in subunit CydB participate in the proton transport to the active site. Before, only residues of CydA were considered to explain the reactivity of *cyt bd* oxidases. Further investigations of the role of Asp58 in *cyt bd*-I oxidase and Glu58 in *cyt bd*-II oxidase for the catalytic mechanism of enzyme reactions with gaseous substrates will be done. Additionally, these results will open new perspectives on the understanding the role of these enzymes in the high tolerance of *E. coli* to nitrosative stress and enhanced pathogenicity.



# Chapter VI

## Spectroelectrochemical characterization of cNOR from *Paracoccus denitrificans* and the Fe<sub>B</sub> lacking variant

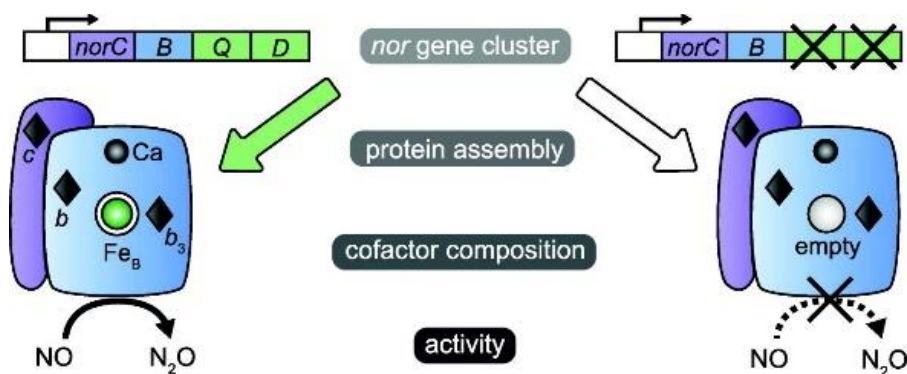
---

- 6.1 Spectral characterization of cNOR WT and Fe<sub>B</sub> depleted enzyme
  - 6.1.1 UV-Vis spectroscopy of cNOR in the thin-layer electrochemical cell
  - 6.1.2 FTIR difference spectroscopy of WT and Variant
  - 6.1.3 Raman spectroscopy of cNOR WT and Fe<sub>B</sub> deficient enzyme films and solution
- 6.2 Electrochemical study of cNOR WT and Fe<sub>B</sub> lacking enzyme
  - 6.2.1 Potentiometric titration of cNOR WT and Fe<sub>B</sub> lacking enzyme
  - 6.2.2 Probing electrocatalytic activity of cNOR on carbon electrodes
- 6.3 Conclusions



The cytochrome c-dependent NO reductase (cNOR) is involved in the important step of the anaerobic respiration of denitrifying bacteria. It ensures the catalytic reduction of toxic nitric oxide to nitrous oxide, however, there are some questions remaining on the reaction mechanism. In the literature there are three proposed catalytic pathways of the two-electron reduction of NO at the active site composed of the heme *b*<sub>3</sub> and Fe<sub>B</sub>, but the role of the Fe<sub>B</sub> center is still under debate<sup>54,7,89,90</sup>.

This chapter aims to understand the role of the non-heme iron redox center in the catalytic cycle of cNOR from *Paracoccus denitrificans*. The structural characterization of the wild type (WT) and Fe<sub>B</sub> lacking variant by difference infrared and UV-Vis spectroscopy, Resonance Raman spectroscopy is shown. The Fe<sub>B</sub> less enzyme was obtained by deleting the accessory chaperons NorQ and NorD in the gene which resulted in the absence of the non-heme iron center<sup>9</sup>. In this part, the mid-point potentials of the heme cofactors were determined, and the electrocatalytic study of O<sub>2</sub> and NO reaction was probed by protein film voltammetry on a glassy carbon electrode.



Scheme 6.1. The production of the Fe<sub>B</sub> lacking variant of cNOR, reproduced from<sup>9</sup>.

## 6.1 Spectral characterization of cNOR WT and Fe<sub>B</sub> depleted enzyme

The wild type cNOR and the Fe<sub>B</sub> deficient variant were characterized by spectral techniques coupled to electrochemistry. The difference spectroscopic (UV-vis and IR) experiments were performed in the thin-layer electrochemical cell designed for study of the structural changes of enzymes in response to the change in the redox state of their cofactors.

### 6.1.1 UV-Vis spectroscopy of cNOR in the thin-layer electrochemical cell

The structural characterization by UV-vis redox difference spectroscopy of the wild type and Fe<sub>B</sub> lacking variant was performed in electrochemical cell. The differential spectra of the electrochemically reduced at -0.4 V minus oxidized at the +0.7 V vs SHE are shown in Fig. 6.1. All three heme cofactors of the wild type enzyme, namely low-spin *heme c*, *heme b* and

high-spin *heme b*<sub>3</sub>, contribute to the signature Soret band at 422 nm and Q-bands at 522 and 551 nm with a shoulder at 558 nm; these peaks are characteristic of the reduced form of cNOR in solution<sup>293</sup>. The difference spectrum of the Fe<sub>B</sub> lacking variant showed an identical profile, confirming the presence of all the heme cofactors and their similar environment as well as the intact structural integrity of the protein.

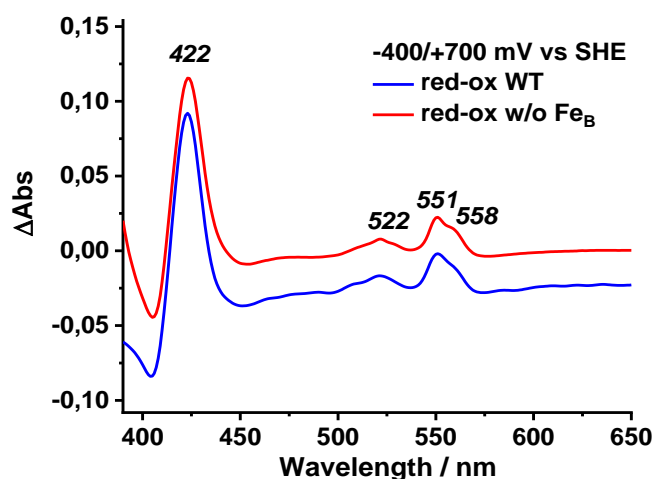


Figure 6.1. Difference red-ox absorption spectra of cNOR WT and Variant without non-heme iron Fe<sub>B</sub> in phosphate buffer pH 7.5 (100 mM KPi, 100 mM KCl, 0.02% DDM)

The UV-Vis spectra of the chemically reduced enzyme, by addition of a few grains of dithionite, and oxidized one, by addition of the ferricyanide, enzyme showed overall the same profile as in the electrochemical cell except some differences in the Q-bands. In the fig. 6.2 the reduced and oxidized spectra of the wild type and Fe<sub>B</sub> lacking variant in the range from 450 to 650 nm are presented.

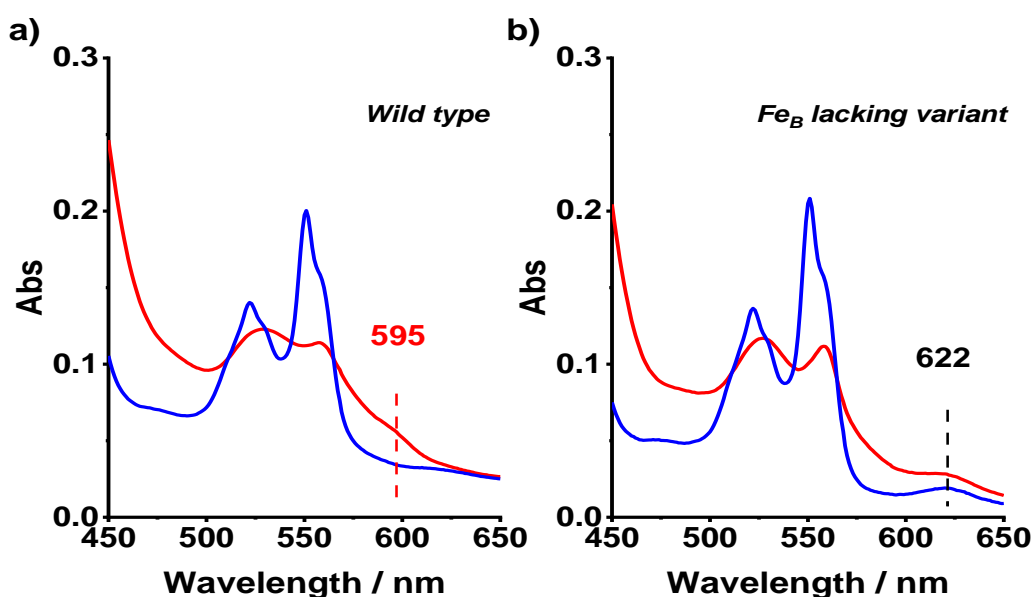


Figure 6.2. Visible spectra of the wild type (a) and Fe<sub>B</sub> lacking variant cNOR (b) in the oxidized (red curves) and reduced (blue curves) in 100mM phosphate buffer pH 7.0, 100mM KCl, 0.02% DDM.

For the wild type cNOR a small charge transfer (CT) band at 595 nm is seen, which is due to the contribution of the high-spin heme *b*<sub>3</sub> in oxidized state. This band disappears upon the reduction of the wild type enzyme, while it is completely absent for the cNOR without Fe<sub>B</sub>. It was reported that this band has variations in intensity and position around 600 nm<sup>9, 92,139,140,294</sup>, and in some cNOR enzymes is barely visible or not detected at all<sup>295,296</sup>. It is also suggested that the presence of the CT band in the cNOR strongly depends on the preparation and purification protocol<sup>54</sup>. Noticeably, in the red-ox differential spectra recorded in the electrochemical cell for both cNOR samples the CT band was not observed, probably due to very low intensity and a thin optical path of few μm in the cell. Another interesting finding, is the peak at 622 nm found for the Fe<sub>B</sub> lacking variant that did not disappear even in the reduced state, however, the origin of this band is unclear.

### 6.1.2 FTIR difference spectroscopy of WT and Variant

Differential red-ox induced infrared spectroscopy was used to reveal changes in the protonation state of individual amino acids, secondary structure and environment of cofactors during the electron transfer to the protein. This experiment was conducted at 5°C and pH 7.5 in the same thin-layer electrochemical cell. The oxidized-minus-reduced FTIR difference spectrum of WT was compared with Fe<sub>B</sub> lacking variant (Fig. 6.3).

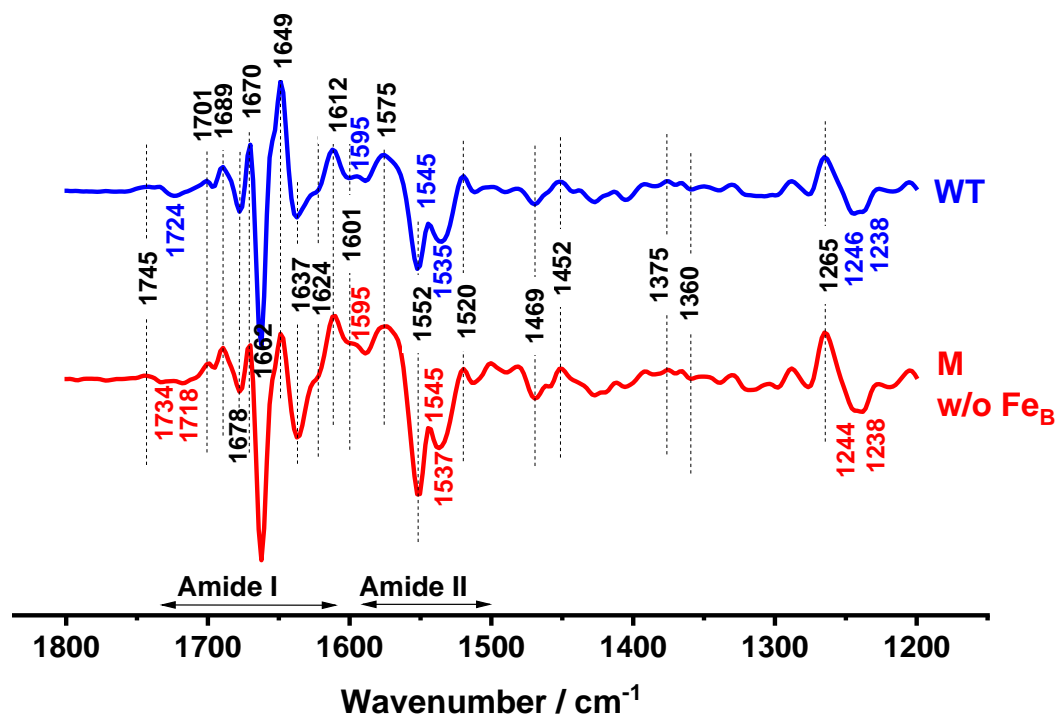


Figure 6.3. Ox-red FTIR difference spectra of the cNOR WT and Fe<sub>B</sub> less variant at pH 7.5

FTIR difference spectra reflect changes in the polypeptide backbone in the amide I (1620–1680 cm<sup>-1</sup>) and amide II (1560–1540 cm<sup>-1</sup>) regions caused by the redox transition of the enzyme's cofactors. The positive bands and negative bands correspond to the oxidized and reduced state respectively; a suggested assignment of the signals is given in Table 6.1.

Table 6.1. Tentative FTIR differential spectra signals assignment for the WT and variant of cNOR

Band position, cm <sup>-1</sup>		Group assignment <sup>243,291,297,298</sup>
WT	Variant	
1745	1745	ν(COOH) of Asp or Glu
-1724	-1734, -1718	
1689, 1701	1689, 1701	ν(C=O) of heme propionates, Arg ν <sub>as</sub> (CN <sub>3</sub> H <sub>5</sub> <sup>+</sup> )
-1678	-1678	
-1662	-1662	Amide I ν(C=O) backbone, individual amino acids, Arg ν <sub>as</sub> (CN <sub>3</sub> H <sub>5</sub> <sup>+</sup> ), Gln ν(C=O), Arg ν <sub>s</sub> (CN <sub>3</sub> H <sub>5</sub> <sup>+</sup> )
1649	1649	
-1637	-1637	
-1624	-1624	
-1601	-1601	ν <sub>37</sub> (C <sub>a</sub> C <sub>m</sub> ) of porphyrin ring, Tyr-OH ν(CC)
1595	1595	
1575	1575	Amide II, ν(C=N) and δ(C=C) of backbone, δ <sub>as</sub> (COO <sup>-</sup> ) of Asp or Glu
-1552	-1552	
1545	1545	ν <sub>38</sub> (C <sub>b</sub> C <sub>b</sub> ) of porphyrin ring
-1535	-1537	δ <sub>as</sub> (COO <sup>-</sup> ) heme propionates, ν <sub>38</sub> (C <sub>b</sub> =C <sub>b</sub> ) of porphyrin ring
1520	1520	Tyr-O <sup>-</sup> ν(C=C), δ (CH)
1375	1375	ν <sub>41</sub> (C <sub>a</sub> N) of porphyrin ring, δ <sub>s</sub> (COO <sup>-</sup> ) heme propionates
-1360	-1360	
1265	1265	δ <sub>42</sub> (C <sub>m</sub> H) of porphyrin ring, ν <sub>s</sub> (COO <sup>-</sup> )
-1246	-1244	Trp δ(CH) ν(CC), Asp/Glu ν(CO) Tyr-OH ν(CO), ν(CC)
-1238	-1238	Tyr-OH ν(C=O), ν(CC)

In the spectral region above 1710 cm<sup>-1</sup> are expected the contribution of the C=O vibrations of the Asp and Glu aminoacids. Bands at 1689 and 1678 cm<sup>-1</sup> correspond to the protonated heme propionates<sup>92</sup>. In the amide I region (1680-1620 cm<sup>-1</sup>), bands at 1662, 1649, 1637 with shoulder at 1624 cm<sup>-1</sup> correspond to the C=O vibrations of the polypeptide backbone and individual aminoacids.

For the amide II region (1570-1520 cm<sup>-1</sup>), bands at 1575, 1552, 1535, and 1537 cm<sup>-1</sup> show the contributions of the CN stretching, NH bending vibrations of the polypeptide backbone and the C=C vibrations of the porphyrin ring of the heme cofactors. The signals at 1535cm<sup>-1</sup> (WT) and 1537 (Variant) can also be assigned to the asymmetric vibrations of the heme propionates. The -COO<sup>-</sup> groups of the deprotonated acid residues of Asp or Glu also may also contribute to the 1552 cm<sup>-1</sup> band. The bands at 1520 cm<sup>-1</sup> together with 1246, 1238 cm<sup>-1</sup> for WT and 1244, 1238 cm<sup>-1</sup> for Variant, are originating from the vibrational modes of Tyr residues.

There are several characteristic signals observed for both protein samples for the porphyrin ring vibration modes suggesting the similar environment of the hemes:  $\nu_{37}(\text{C}_a\text{C}_m)$  at -1601 and 1595 cm<sup>-1</sup>,  $\nu_{38}(\text{C}_b\text{C}_b)$  at 1545 and negative peaks 1535 (WT) and 1537 (Variant) cm<sup>-1</sup>,  $\nu_{41}(\text{C}_a\text{N})$  at 1375 and 1360 cm<sup>-1</sup>, and  $\delta_{42}(\text{C}_m\text{H})$  at 1265 cm<sup>-1</sup><sup>297</sup>.

Overall, the ox-red FTIR difference spectrum of the Fe<sub>B</sub> lacking variant of cNOR shows a comparable profile, pointing at the similarity of secondary structure of the enzyme. There are few differences: in the region of protonated/deprotonated Asp and Glu, a negative peak at 1724 cm<sup>-1</sup> is observed for WT and -1734, -1718 cm<sup>-1</sup> for Fe<sub>B</sub> lacking variant; an upshifted positive signal for WT at -1246 cm<sup>-1</sup> (region of the vibrational mode of Tyr residues) that also can be attributed to the little differences in C=O vibrations of the Asp and Glu acidic residues. The differences in the FTIR spectra might also come from the preparation of the cNOR without Fe<sub>B</sub> since the absence of the chaperones NorQ and NorD could promote the conformations changes. Without the solved microscopic structure of the modified enzyme we do not know for sure if lacking Fe<sub>B</sub> is the only difference between these two preparations.

### 6.1.3 Raman spectroscopy of cNOR WT and Fe<sub>B</sub> deficient enzyme films and solution

The Resonance Raman (RR) technique is a powerful tool to determine the spin and coordination state of the iron atom of hemoproteins. RR spectroscopy has been applied to broadly explore the heme environment of the wild type cNOR and its variant lacking non-heme iron center. High and low frequency RR spectra of the dry films were recorded at 457 and 514 nm excitation. The signature of all hemes, *c* and *b*-type low-spin hemes and high-spin heme *b*<sub>3</sub>,



is seen in the 1200-1700 cm<sup>-1</sup> range, Fig. 6.4 *a,b*. There are several informative porphyrin modes in the high-frequency range:  $\nu_4$  that gives information on the redox state and  $\nu_2$ ,  $\nu_3$ ,  $\nu_{10}$  that gives information on the ligation state such as penta- or hexacoordination of the metal center, 5C or 6C respectively<sup>148,299</sup>.

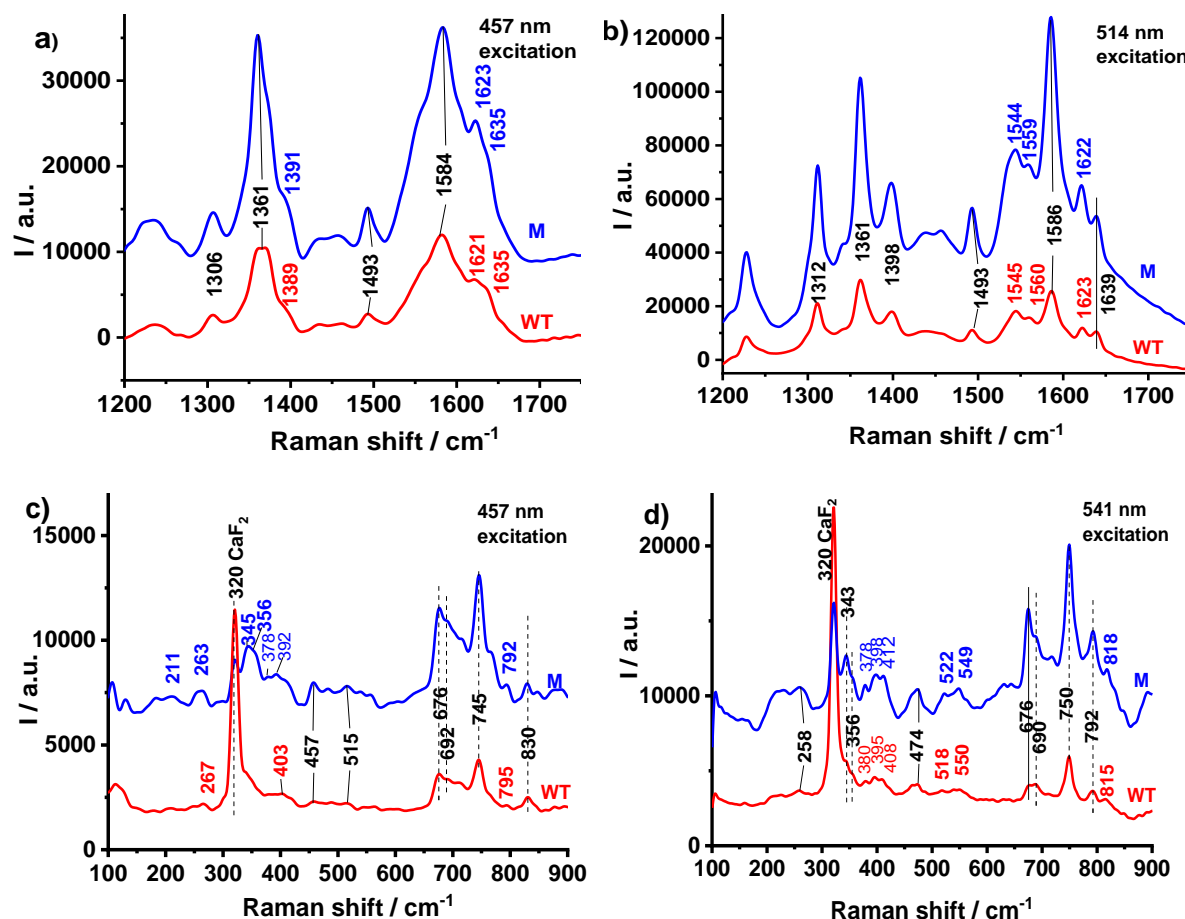


Figure 6.4. High (*a, b*) and low frequency (*c, d*) RR spectra of the dry films of the cNOR (WT) and Fe<sub>B</sub> deficient variant (*M*) without Fe<sub>B</sub> at 457 nm and 541 nm laser excitation.

A first noticeable point is that the Raman scattering spectra have better resolution at 514 nm excitation for both samples. Secondly, the most remarkable feature for WT cNOR and the variant is the presence of the Fe<sup>2+</sup> porphyrin marker band at 1361 cm<sup>-1</sup> and a complete absence of the Fe<sup>3+</sup> band at 1373 cm<sup>-1</sup> ( $\nu_4$ ), meaning that all hemes are in reduced state. Even though, the RR spectra were recorded with a minimal laser power and exposure time of less than a few seconds laser-induced photoreduction probably happened to both proteins in our experimental conditions. Low temperature RR techniques is required to obtain the oxidized state spectra in this experiment. The 5C/HS characteristic modes are observed for the WT and variant cNOR heme *b*<sub>3</sub> at 1559 and 1560 cm<sup>-1</sup> ( $\nu_2$ ) respectively. The porphyrin modes at

1584/1586 cm<sup>-1</sup> ( $\nu_2$ ) belong to the heme *b*, while the 1591 ( $\nu_2$ ) for heme *c* is not resolved. The  $\nu_{10}$  vibrational mode for the heme *b*<sub>3</sub> at 1606 cm<sup>-1</sup> is missing, however, two bands at 1622 cm<sup>-1</sup> and 1639 cm<sup>-1</sup> are seen for both cNOR at 514 nm excitation, suggesting a splitting of  $\nu_{10}$  band. These two bands are known to indicate the partial oxidation of the low-spin hemes *c* and *b* and therefore, a mixture of heme *b*<sup>3+/2+</sup> species and hemes *c*<sup>3+/2+</sup> species<sup>299</sup>. The porphyrin marker band for both proteins at 1493 cm<sup>-1</sup> can be attributed to  $\nu_3$  mode of 6C/LS reduced heme *b* and heme *c*. The bands at 1623 (WT) and 1622 cm<sup>-1</sup> (Fe<sub>B</sub> lacking variant) can also include the contribution of vinyl stretching  $\nu_{c=c}$ <sup>148</sup>.

In the low frequency RR spectra, in addition to vibrations of the porphyrin macrocycles, Fe-ligands motions are included. In the range 200-900 cm<sup>-1</sup> the most interesting are two oxygen-sensitive modes  $\nu_{as}(\text{Fe-O-Fe})$  at 815 and 833 cm<sup>-1</sup> of the heme/nonheme diiron center<sup>92,299</sup>. These bands have been attributed in the oxidized state of cNOR to the open and closed conformations of the catalytic cycle. Here, the 830 cm<sup>-1</sup> band is observed for both proteins at 457 nm excitation, while the 815 and 818 cm<sup>-1</sup> ones are seen at 514 nm excitation for the WT and mutated cNOR respectively. The reason why we observe these bands separately could be due to the presence of only small fraction of oxidized hemes, not giving a clear outlook on the interaction of oxygen with heme *b*<sub>3</sub> and non-heme Fe<sub>B</sub>.

Table 6.2. Frequencies of the RR of the studied cNOR from *P. denitrificans* observed in capillary compared to those given in literature for the cNOR in oxidized and reduced state at 414 nm excitation.

Mode	This study				From reference [298]			
	Oxidized		Reduced		Oxidized		Reduced	
	5C/HS	6C/LS	5C/HS	6C/LS	5C/HS	6C/LS	5C/HS	6C/LS
$\nu_2$	–	<b>1584,</b> <b>1586</b>	<b>1559,</b> <b>1560</b>	<b>1584,</b> <b>1586</b>	<b>1578</b>	<b>1584</b>	<b>1560</b>	<b>1584/1591</b>
$\nu_3$	–	–	–	<b>1493</b>	<b>1492</b>	<b>1505</b>	<b>1472</b>	<b>1494</b>
$\nu_4$	–	–	<b>1361</b>	<b>1361</b>	<b>1373</b>	<b>1373</b>	<b>1362</b>	<b>1362</b>
$\nu_{10}$	–	<b>1639</b>			<b>1630</b>	<b>1639</b>	<b>1606</b>	

\*5C/HS five-coordinated high-spin heme *b*<sub>3</sub>, 6C/LS six-coordinated low-spin heme *b* and heme *c*

Raman spectroscopy was also used also to monitor the reaction of the WT and Variant of cNOR with nitric oxide at pH 7.6, experiment was carried on in the glass capillary. A 100-equivalent excess of NO-releasing compound (MAHMA NONOate) was added to the 10  $\mu\text{M}$  cNOR solution (1:100 / cNOR: NO), and after 2 minutes the RR spectra were recorded at 514 nm laser excitation (Fig.6.5).

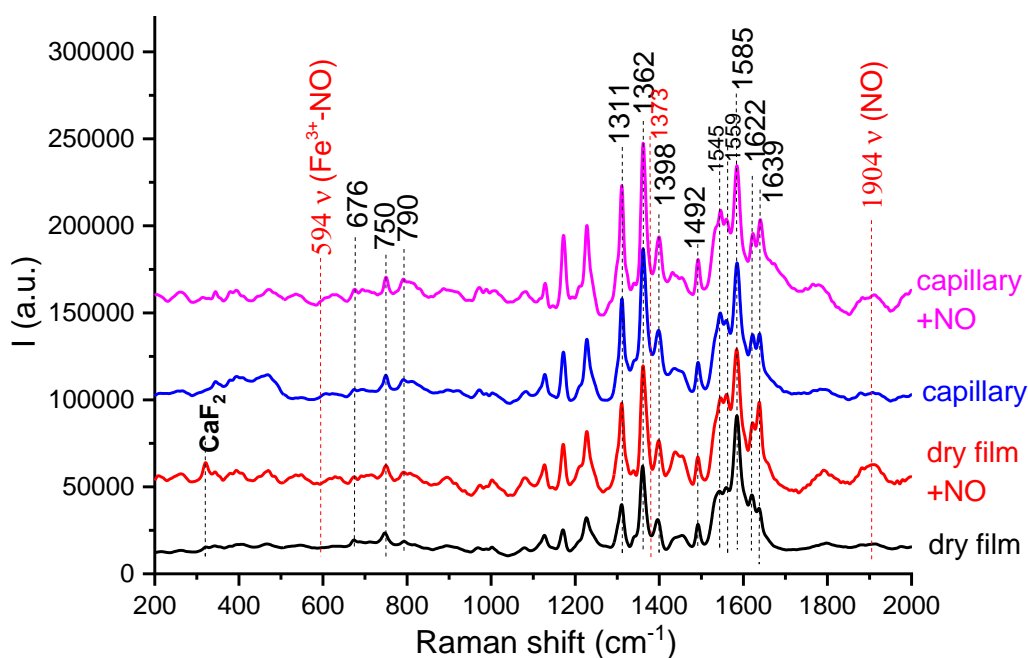


Figure 6.5. RR spectra of the cNOR WT dry films and solution in capillary after addition of NO (1:100).

Interestingly, for the WT and variant without Fe<sub>B</sub> we did not observe the two characteristic modes of the ferric-NO complex:  $\nu(\text{Fe}^{3+}\text{-NO})$  stretching frequency expected at  $594\text{ cm}^{-1}$  and,  $\nu(\text{NO})$  at  $1904\text{ cm}^{-1}$ . These bands indicate the presence of the catalytic intermediate in the NO reduction cycle<sup>88,148</sup>. Again, this can be the consequence of the photo reduction, as confirmed by the absence of the  $1373\text{ cm}^{-1}$  band of the ferric species, and photo-induced dissociation of NO from the protein complex.

Despite the high similarity of the RR spectra before and after addition of NO to the wild type cNOR sample, there are small but clear changes in porphyrin signature. Upon addition of NO a change in the relative intensities of the bands at  $1622$  and  $1639\text{ cm}^{-1}$  is seen. In particular, the more pronounced  $1639\text{ cm}^{-1}$  band may indicate a change of the ferrous species into the ferric hexacoordinated hemes upon addition of NO.

Overall, the RR spectroscopy confirmed the structural integrity of the studied cNOR samples and the characteristic signature of all the hemes in reduced state in the high-frequency range were observed. It is recommended to perform also this experiment with laser excitation in the range of  $413\text{-}440\text{ nm}$ , which corresponds to the Soret absorption region of the porphyrins. In the range of  $200\text{-}900\text{ cm}^{-1}$  we could not observe the characteristic heme *b*<sub>3</sub> Fe-O-Fe<sub>B</sub> band discussed in the literature. In this case, the low-temperature technique at  $110\text{ K}$  in a liquid nitrogen cooled chamber might be helpful to keep sample in the oxidized state and follow the intermediates of cNOR reaction with oxygen and nitric oxide.

## 6.2 Electrochemical study of cNOR WT and Fe<sub>B</sub> lacking enzyme

UV-vis potentiometric titrations were carried out in the electrochemical cell to determine the red-ox potentials of the heme cofactors of the wild type and mutated enzymes. The O<sub>2</sub> and NO catalytic activity of the cNOR, immobilized on glassy carbon electrodes, was investigated by means of protein film voltammetry.

### 6.2.1 Potentiometric titration of cNOR WT and Fe<sub>B</sub> lacking enzyme

UV/Vis red-ox titrations in the thin-layer electrochemical cell were performed at protein concentration of 0.8 mM in 100 mM phosphate buffer pH 7.5.

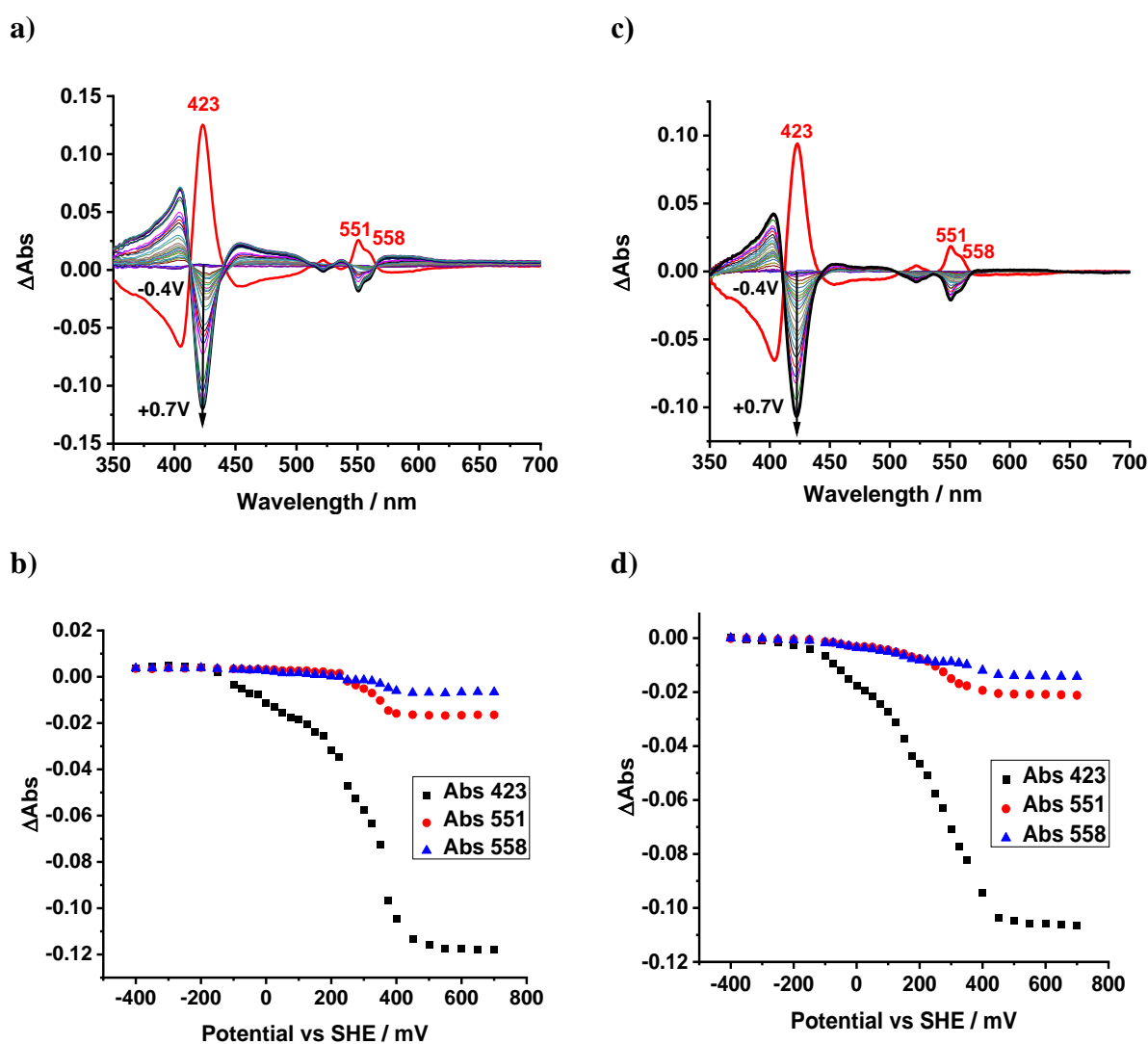


Figure 6.6. Oxidative UV-Vis titration curves of cNOR WT (a, b) and Variant without non-heme iron Fe<sub>B</sub> (c, d) in buffer pH 7.5 (100 mM KPi, 100 mM KCl, 0.05% DDM)

The analysis of the data includes plotting of the changes of differential absorption at particular wavelength versus applied potential (Fig.6.6 b-d).

In order to determine the redox potentials of the heme cofactors, the first derivative of the titration curves at particular wavelength (Soret band at 523 nm and Q-bands at 551 and 558 nm) were computed and fitted to the multi-component Gaussian and de-convoluted for the contributions of three hemes (Fig. 6.7).

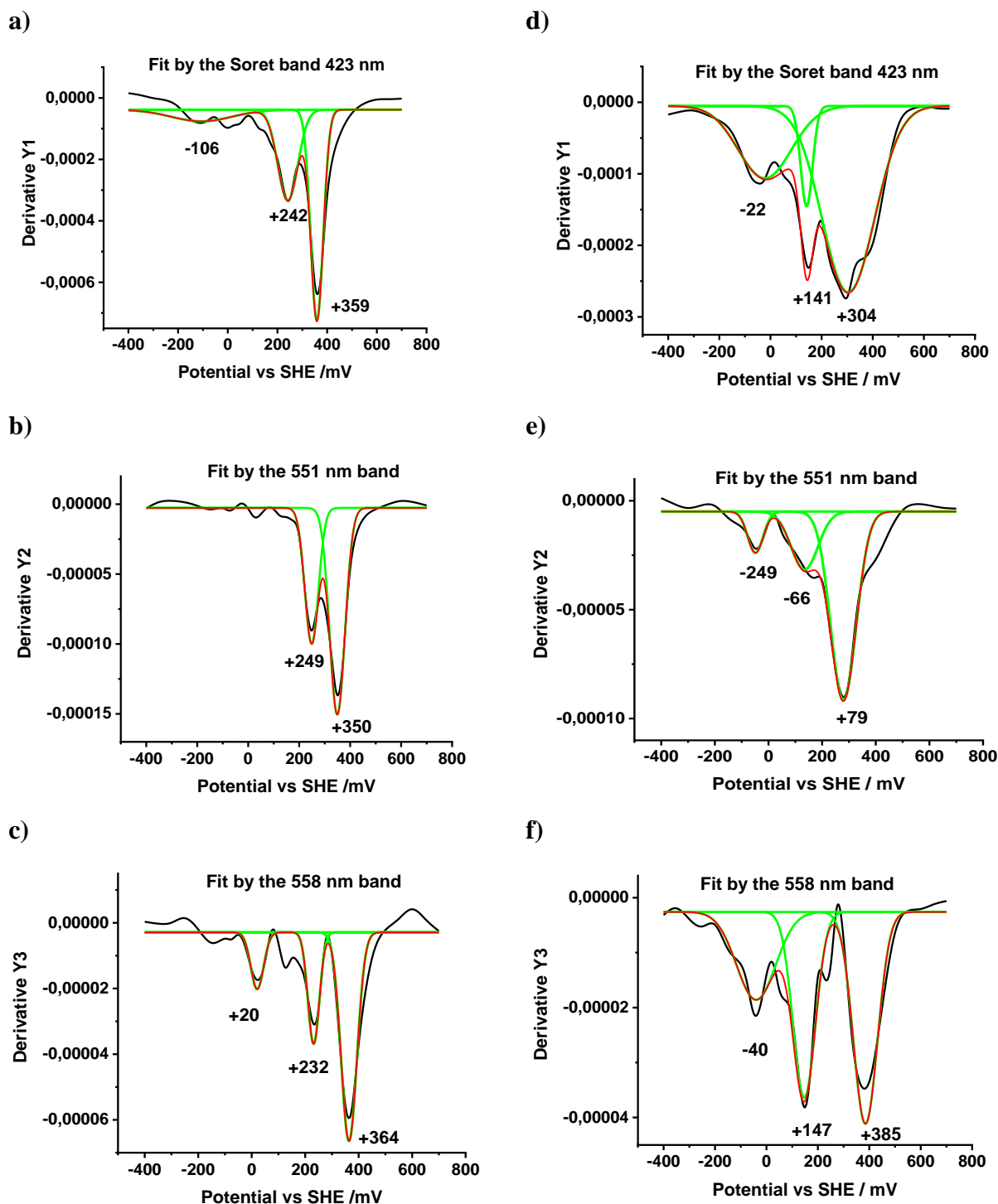


Figure 6.7. Multi-component analysis: Gaussian fitting of the 1<sup>st</sup> derivative of the titration curves at 423 nm, 551 nm, 558 nm for WT (a, b, c) and Variant cNOR (d, e, f); **black** – 1<sup>st</sup> derivative of the absorbance at certain wavelength, **red** – final fitted curve, **green** – separated contributions from the redox heme cofactors.

In table 6.3 the mean value of the mid-point potentials obtained from two potentiometric titrations of wild type and variant cNOR are shown and compared with the data reported in literature. The most negative mid-point potential  $E_m$  is assigned to the heme  $b_3$ , while contributions between +150 and +250 vs SHE are related to the heme  $b$  and  $c$ . The separation of these low-spin hemes was made on the basis of the knowledge from the engineered *P. denitrificans* NOR in membranes<sup>92</sup>. It was shown that mutated cNOR membranes containing only  $b$ -type heme had an  $\alpha$ -band with maximum at 558 nm, whereas from the membranes with  $c$ - and  $b$ -type hemes two peaks with almost equal intensities at 550 and 558 nm were resolved. Therefore, here for the wild type cNOR the attribution of the  $E_m$  of the low-spin heme  $b$  was made based on the biggest fraction in differential absorbance at 558 nm band, while at 551 nm absorbance considered to rise mostly due to  $c$ -type heme.

Table 6.3. Red-ox potentials (vs SHE) of the WT and Fe<sub>B</sub> lacking Variant of cNOR determined by potentiometric titration, standard error of the measurement  $\pm 20$  mV.

Potential vs SHE, mV	Fe <sub>B</sub> lacking Variant pH 7.5, <i>P. denitrificans</i>	WT pH 7.5, <i>P. denitrificans</i>	WT <sup>89</sup> pH 7.5, <i>P. denitrificans</i>	WT <sup>300</sup> pH 7.5, <i>P. stutzeri</i>
heme $b_3$	-64	-50	+60 (CT band)	-
heme $c$	+133	+246	+310	+280
heme $b$	+320	+356	+345	+322

From the potentiometric titration, it is observed that the mid-point potential of the heme  $b_3$  is 100 mV more negative, -50 mV (WT) and -64 mV (M) vs SHE, than reported in literature, +60 mV vs SHE<sup>89</sup>. Here, the redox potential for the heme  $b_3$  was obtained from the deconvolution of the Soret band and  $\alpha$ -bands rather than charge transfer (CT) band at 595 nm used by the Butland's group. This low intensity band is not visible in the thin layer electrochemical cell used here.

From the comparison of the wild type and Fe<sub>B</sub> lacking variant of cNOR, the absence of the Fe<sub>B</sub> in structure resulted in a greater shift of the redox potential of the two low-spin hemes rather than heme  $b_3$ . The redox potential of the heme  $c$  was downshifted by 110 mV and that of the heme  $b$  by 36 mV in the variant. It was unexpected to observe that the mutation affected only slightly the potential of the heme  $b_3$  (by 14mV), which was in the range of the standard error of the method. The stronger potential shift for the heme  $c$ , a cofactor that is further away from heme  $b_3$ , in the Fe<sub>B</sub>-less variant can happen due to structural changes in the enzyme coming from the absence of the non-heme cofactor and chaperons NorQ and NorD. Another remarkable finding from the potentiometric titration is an extremely negative potential of the

heme *b*<sub>3</sub> for both proteins. Giving that heme-copper oxidases and cNOR are evolutionally related, it is instructive to compare obtained results for cNOR with *cbb*<sub>3</sub> oxidase. For the *cbb*<sub>3</sub> oxidases the low potential of the heme *b*<sub>3</sub> is suggested to be related to the presence of a highly conserved glutamic acid residue in H-bond interaction with the His ligand of the heme<sup>288</sup>. The group of Shiro suggested that acid residues Glu-215, Glu-280 in the cNOR from *P.aeruginosa* could generate an electro-negative environment at the catalytic center that could be an explanation for the very negative potential of the heme *b*<sub>3</sub><sup>295,296</sup>. The group of Varotsis proposed that the low potential of heme *b*<sub>3</sub> is required to create a large thermodynamical barrier to the reduction of the low-spin heme *b* and, as a result, to prevent the formation of the dead-end heme *b*<sub>3</sub><sup>2+</sup>-NO species<sup>299</sup>. A similar mechanism was proposed for the fully-reduced cyt *cbb*<sub>3</sub> NO reaction<sup>148</sup>.

### 6.2.2 Probing electrocatalytic activity of cNOR on carbon electrodes

The catalytic reactivity of the cNOR wild type was investigated and compared with the Fe<sub>B</sub> lacking variant by means of protein film voltammetry. This method is based on the immobilization of the studied enzyme on the surface of rotating disk electrode for direct electrochemical measurements. In this study a sample of cNOR prepared in pH 7.5 KPi buffer was deposited directly onto a glassy carbon electrode (GCE) surface which allows studying redox reactions in a wide potential range from +0.6 to -0.8 V (vs SHE). All measurements were performed in a standard three-electrode cell where the modified GCE was set as the working electrode, and a platinum wire and Ag/AgCl were the counter and reference electrodes, respectively. All potentials reported in this section were converted vs SHE.

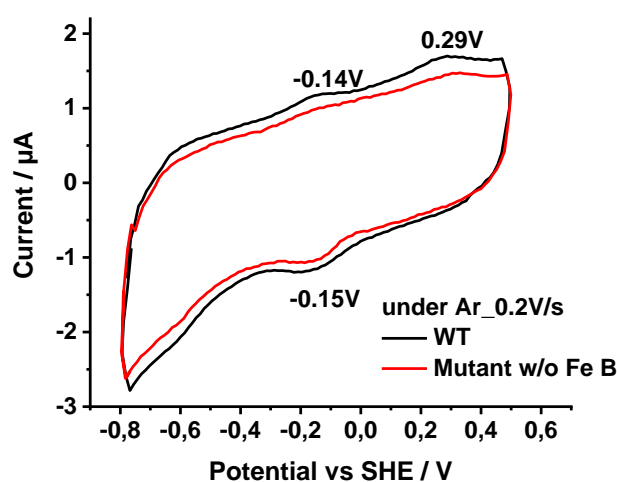


Figure 6.8. Cyclic voltammograms of cNOR wild type and Fe<sub>B</sub> lacking variant immobilized on the glassy carbon electrode at pH 7.5, with a scan rate of 0.02 V/s.

At first, the cyclic voltammograms of the WT cNOR and non-heme iron Fe<sub>B</sub> lacking variant were recorded in non-catalytic conditions, without addition of the physiological substrate nitric oxide in solution, and under an argon atmosphere (Fig. 6.8). In this experiment, the direct electrochemical response from two protein redox centers was observed for both WT and variant. The formal redox potentials were determined and assigned to the high-spin *heme b*<sub>3</sub> (cathodic peak at -0.15 V and anodic peaks at -0.14V) and *heme c* (anodic peak at +0.29V) based on the data reported in literature<sup>301,302</sup>. For both protein samples the signal of the non-heme Fe<sub>B</sub> was not detected.

Table 6.4. Redox potentials reported for nitric oxide reductase biosensors.

Protein/ electrode	E, V (SHE)	Cofactor	Ref
NOR from <i>Paracoccus denitrificans</i> /pyrolytic graphite electrode	-0.127	<i>heme b</i> <sub>3</sub>	302
NOR from <i>Pseudomonas nautica</i> /rotating graphite disk electrode	-0.369 -0.162 +0.043 +0.208	Fe <sub>B</sub> <i>heme b</i> <sub>3</sub> <i>heme b</i> <i>heme c</i>	301
NOR from <i>Marinobacter hydrocarbonoclasticus</i> /pyrolytic graphite electrode	-0.394 -0.087 +0.133 +0.336	Fe <sub>B</sub> <i>heme b</i> <sub>3</sub> <i>heme b</i> <i>heme c</i>	303
NOR/ rotating glassy carbon disk electrode	-0.140 WT +0.290 WT  -0.150 Variant +0.294 Variant	<i>heme b</i> <sub>3</sub> <i>heme c</i>  <i>heme b</i> <sub>3</sub> <i>heme c</i>	this study

\*Potential values reported vs SCE and Ag/AgCl were converted vs SHE to allow comparison between studies.

It is known that cNORs have catalytic activity towards O<sub>2</sub>, in addition to NO reduction to N<sub>2</sub>O<sup>302,304</sup>. In this step, we investigated the electrocatalysis of cNOR with O<sub>2</sub> and NO in the presence of the substrates (Fig. 3.8). Experiments in the presence of O<sub>2</sub> were carried out in the open cell using oxygenated buffer solution, whereas NO was introduced as aliquots of the MAHMA NONOate stock solution in 10mM NaOH, the NO donor compound.



The onset of O<sub>2</sub> catalytic reduction is approximately at +0.1V and the half-wave potentials E<sub>m</sub> of this reaction are determined at -0.11 V for the WT and -0.15 V for the mutated enzyme (Fig. 6.9a), which is close to the potential of the *heme b*<sub>3</sub> that composes the active site of the enzyme. Following the catalytic NO reduction, the development of a characteristic sigmoidal curve with E<sub>m</sub> at -0.550 V (WT) and -0.563 V (Fe<sub>B</sub> less variant) was observed (Fig. 6.9b). These values are very close to those reported in literature for the cNOR from the *Pseudomonas nautica*, -0.560 vs SHE<sup>301</sup>.

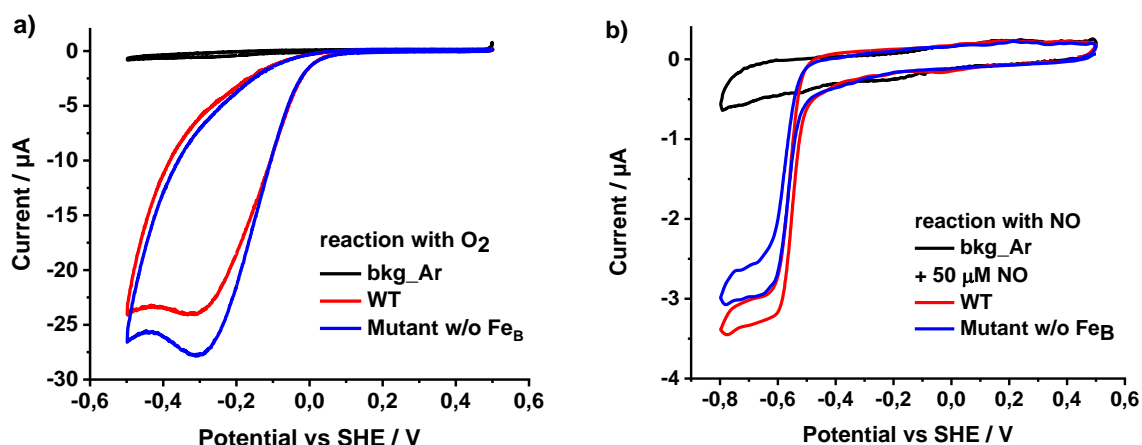
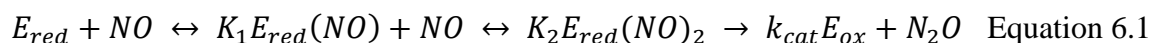


Figure 6.9. Cyclic voltammograms of cNOR WT (red line), Fe<sub>B</sub> less variant (blue line) immobilized on the glassy carbon electrode in the presence of O<sub>2</sub> (a) and NO (b), black line shows the protein response without any substrate in the anaerobic atmosphere, experimental conditions: 0.02 V/s, 1000 rpm, pH 7.5 phosphate buffer.

In the next step, the enzyme activity towards NO reduction of WT cNOR and variant without non-heme iron Fe<sub>B</sub> was evaluated. Concentration dependent experiments were carried out under anaerobic conditions with protein deposited on the GCE surface. It was shown that addition of the NO solution to the bare electrode without any cNOR immobilized on the surface does not result in a catalytic wave or increase in the catalytic current, that happens only with electrodes modified with enzyme WT or variant (Fig. 6.10 a, b).

The increase in the catalytic current at -0.8 V was plotted vs concentration of NO (Fig. 6.9 c, d) and fitted to the steady-state kinetics of cNOR developed by Girsch and de Vries<sup>140</sup>.



$$v = \frac{v_{max}}{1 + K_2 \left( \frac{1}{[NO]} + \frac{K_1}{[NO]^2} \right)} \quad \text{Equation 6.2}$$

In this model it is assumed that two molecules of NO bind one by one with to the enzyme with two equilibrium dissociation constants  $K_1, K_2$ . The equation 6.2 was used to fit the NO binding kinetics and estimate the  $v_{max}$ .

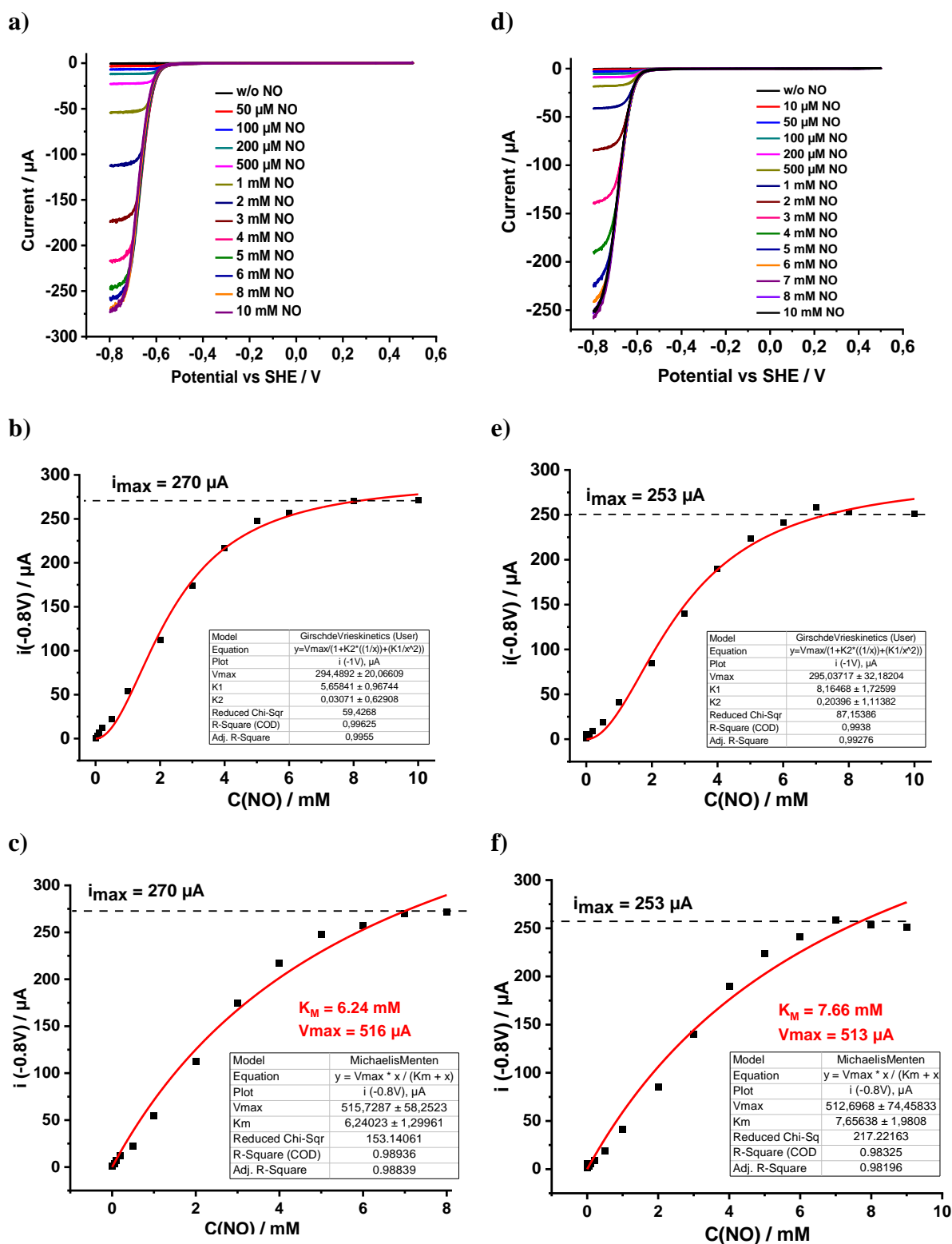


Figure 6.10. Concentration dependent NO reduction on the glassy carbon electrode modified with cNOR WT (a) and Fe<sub>B</sub> less variant (d) at 0.02 V/s, 1000 rpm, pH 7.5. The reaction rate vs NO concentration Girsch and de Vries fit (b,e) and Michaelis-Menten fit (c,f).

Interestingly, for the wild type and Fe<sub>B</sub> lacking variant the kinetic curves have a clear saturation point at 7 mM NO. It may be explained by the limitations of the method used, the real concentration of NO in the experimental chamber may vary from the expected, the real-time NO concentration detection is required. After the 7mM the activity is slightly decreased to less than 5% due to the possible desorption of the protein from the electrode surface. Overall, the character of the steady-state reaction does not follow the conventional Michaelis-Menten kinetics and giving the values of  $v_{max}$  around 500-520  $\mu\text{A}$ , so the Girsch and de Vries model was used. The maximum catalytic current for both immobilized proteins was reached at NO concentration which is far over the physiological levels, whereas many kinetic studies with cNOR have shown the inhibition of the NO catalysis at the concentration higher than 10  $\mu\text{M}$ <sup>140,305</sup> linked to the NO binding to the oxidized heme  $b_3$ . Here, we do not observe the NO inhibition of the oxidized state because in performed experiments protein is maintained in the reduced state by the applied potential.

The turnover number was calculated from the  $v_{max}$  obtained from the kinetics curves and protein coverage estimated at different scan rates from the -0.15V peak of heme  $b_3$  in the absence of the substrate under argon atmosphere. Both enzymes showed a high catalytic activity towards the NO reduction with respective turnover numbers of  $2859 \pm 712$  units/s for wild type and  $2842 \pm 961$  units/s for the variant. On the contrary to these results, the group of Pr. Pia Ädelroth who kindly provided us with the Fe<sub>B</sub> lacking variant of cNOR in the steady-state turnover experiment showed the significant drop in the catalytic activity down to 8% affected by the missing Fe<sub>B</sub><sup>17</sup>. In the abovementioned assay the cytochrome c was used as the electron donor that passes the electrons to the cNOR one by one. On contrary, in our protein film voltammetry assay, the electron supply is more efficient, whereas Fe<sub>B</sub> may not be required. In case of favorable orientation of the enzymes on the electrode surface, we suppose that electrons can be transferred to the protein active center directly from the electrode surface avoiding the natural electron transfer chain from cytochrome c (cyt  $c \rightarrow$  heme  $c \rightarrow$  heme  $b \rightarrow$  heme  $b_3 \leftrightarrow$  Fe<sub>B</sub>), thus neglecting the inhibition of the NO reduction caused by inefficient internal electron transfer.

### 6.3 Conclusions

In this chapter, the spectral characterization of the cNOR from *Paracoccus denitrificans* by the UV-Vis, IR and Raman spectroscopies was made. The protein structural integrity was confirmed by the UV-Vis spectra, showing the presence of all three heme redox centers. However, the charge transfer band about 600 nm was not observed in the electrochemical cell in the wild type cNOR, nor in the variant without Fe<sub>B</sub>. The redox induced FTIR data analysis of the amide I band confirmed the similar environment of the heme cofactors in both enzymes and revealed the small but significant differences in the region of the vibrational modes of the protonated Glu/Asp acidic residues. This difference points towards a change of the microenvironment as a response to the absence of the non-heme iron center in the active site. Nevertheless, it is hard to attribute this difference to the Glu residue which is a direct ligand to the Fe<sub>B</sub>, for that the study with the mutated residue of interest, Glu to Asp, would be in help. From the Raman experiments, all heme contributions in both cNOR samples were present. In order to follow the catalytic reaction with NO and O<sub>2</sub>, the applied technique requires modifications to ensure the oxidized state of the enzyme, for example, in the optical flow cell with coupled temperature and potential control.

The electrochemical methods allowed us to determine the mid-point potentials of the heme cofactors in the wild type and Fe<sub>B</sub> depleted variant. The extremely negative redox potential of -50 mV and -64 mV vs SHE was determined for the heme *b*<sub>3</sub> in the wild type and variant, respectively. The significant effect of the depletion of the Fe<sub>B</sub> on the low-spin heme *c* was unexpected but probably due to the conformational changes in the enzyme. Giving the differences between these enzymes in FTIR differential spectra in the region of the Glu/Asp, and knowledge of the influence of these acidic residues on the redox potential of the heme cofactors<sup>288,295,296</sup>, it is recommended to the probe electrocatalytic properties of the variant with mutated Glu that is ligated to the Fe<sub>B</sub> in further studies.

The electrochemical study showed that direct electron transfer of cNOR immobilized on the glassy carbon electrode was attained for the wild type and Fe<sub>B</sub> lacking variant. As a result, in non-catalytic conditions the formal redox potentials of the two protein metallic centers were determined, giving +290 V for heme *c* and -0.158 V vs SHE for heme *b*<sub>3</sub>. Similar values were obtained for the protein without Fe<sub>B</sub>. The electrocatalytic activity in the presence of oxygen and nitric oxide was probed by cyclic voltammetry. It was observed that the absence of the non-heme iron center does not perturb the binding and reduction of the oxygen in the Fe<sub>B</sub> depleted variant, which is in line with the activity experiment with these enzymes<sup>17,302,304</sup>.

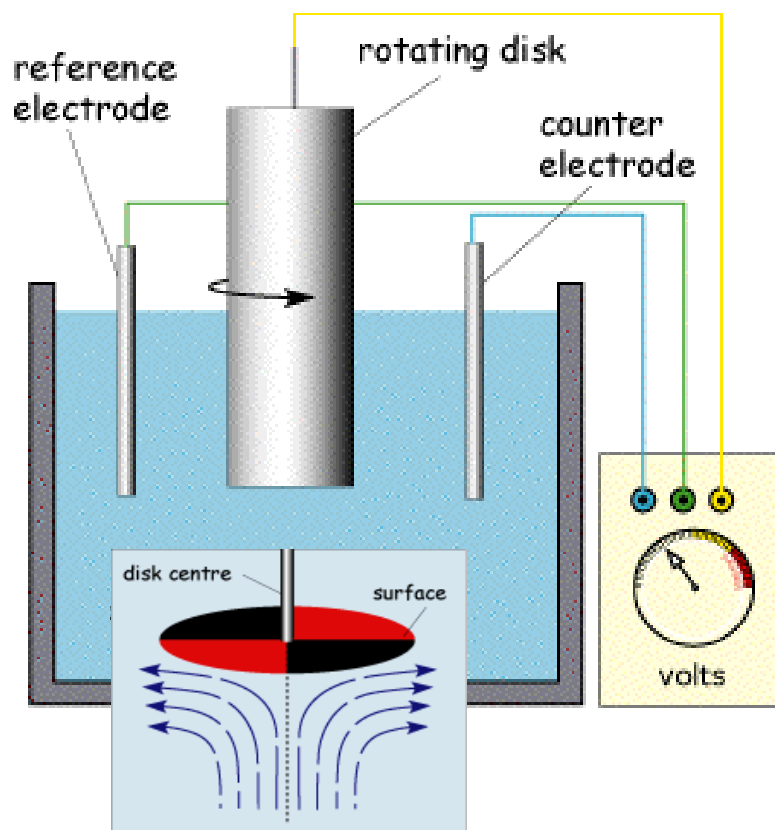
The respective half-wave potentials of the catalytic reduction were evaluated. The results in the concentration-dependent experiment with the NO electrocatalysis also showed the high functionality of the wild type and cNOR variant without Fe<sub>B</sub> with turnover numbers ( $k_{\text{cat}}$ ) of  $2859 \pm 712$  units/s and  $2842 \pm 961$  units/s, respectively. Giving the fact that even in the absence of the Fe<sub>B</sub> the catalytic reduction of NO still takes place, these results work in favor of the trans and cis:*b*<sub>3</sub> catalytic mechanisms, where either one or both NO molecules are believed to bind to the heme *b*<sub>3</sub>. However, the extremely high catalytic activity for both immobilized proteins can be linked to the experiment setup where with the favorable orientation on the electrode surface, electrons are directly transferred to active site, avoiding the natural electron transfer chain. Importantly, the inhibition of the oxidized state of the enzyme by NO is not observed because in performed experiments protein is maintained in the reduced state by the applied potential, which is not the case in traditional assays where the variant was observed to be much less active<sup>17</sup>. The obtained results suggest to probe the electrocatalytic reaction of cNOR with the controlled orientation of the protein on the electrode surface, for instance, through the His-Tag linker.

# Annex

## A. Instrumentation

### A.1 Electrochemical equipment

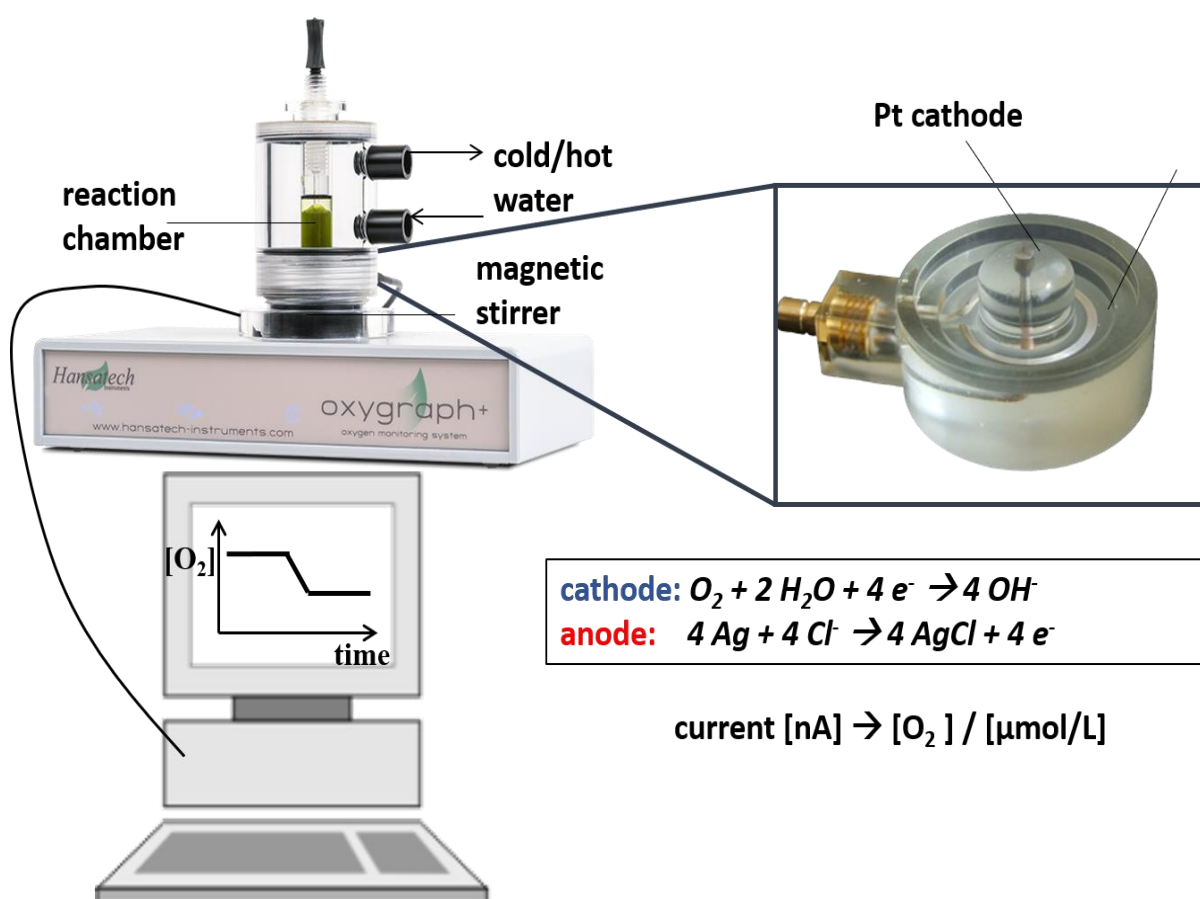
A standard three electrode cell was used in all electrochemical experiments (Scheme A.1). The working electrode (WE) was either a gold disk rotating electrode RGE or a glassy carbon electrode GCE. The reference electrode (RE) was a commercial Ag/AgCl (3M KCl) electrode (+208 mV vs SHE). The counter electrode (CE) was a platinum wire. The role of the CE is to prevent the polarization of the reference electrode, as the potential at WE was maintained between WE and RE, and the current is measured in the circuit between WE and CE. Unless otherwise stated, the ion strength of the supporting electrolyte was 0.1 M which allows avoiding such mass transport component as the charge migration. The voltammetric measurements were performed with a Princeton Applied Research VERSASTAT 4 potentiostat.



Scheme A.1. The three-electrode electrochemical cell for the cyclic voltammetry <sup>306</sup>.

## A.2 Clark electrode

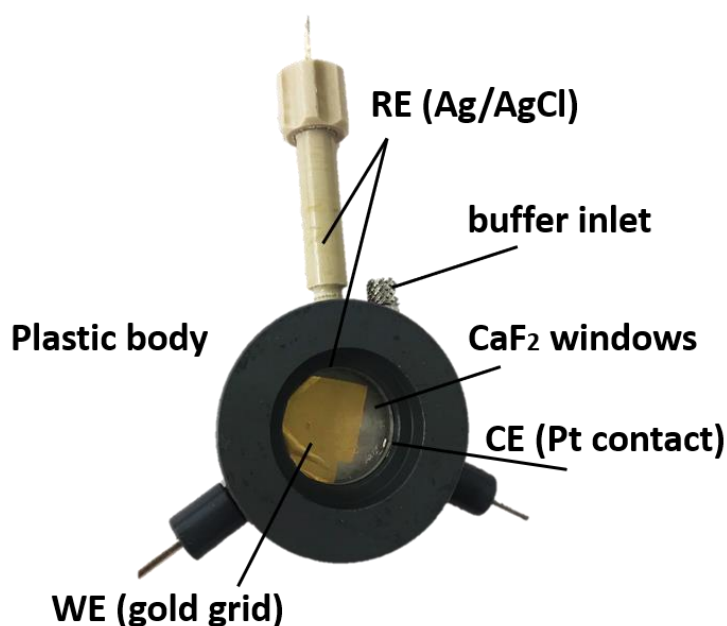
The additional measurements of the activity of the *bd* oxidases were conducted with chemical sensor Clark electrode on isolated proteins or in membranes. The set up and principle is shown in Scheme A.2. The sensor is a Pt disk cathode (WE) and Ag ring anode (CE). The electrodes are immersed in the supporting electrolyte and isolated from the reaction chamber through a thin Teflon membrane. This membrane is permeable to molecular oxygen and allows this gas to reach the cathode, where it is electrolytically reduced. The sensor is enclosed in the plastic vessel filled with a buffer with the sample. The continuous stirring of the solution is provided. The result signal of chronoamperometric experiment is a steady-state current that is proportional to the dissolved oxygen concentration. Depending on the protein oxygen consumption activity the quantity of oxygen in the closed system can be measured.



Scheme A.2. Clark-type oxygen electrode<sup>307</sup>

### A.3 Thin-layer electrochemical cell

The potentiometric titration and FTIR redox induced spectroscopic experiments were performed in an optically transparent thin-layer electrochemical cell<sup>308</sup> was used (Scheme A.3). It is a three-electrode cell confined between two CaF<sub>2</sub> windows (transparent in UV/Vis and MIR region of the spectrum) and set into the polymer body. A 6 μm-thick 70% optically transparent gold grid acts as a working electrode which is in electrical contact with a platinum counter electrode and an Ag/AgCl reference electrode. The gold grid was incubated overnight with a 1:1 solution of 1mM cysteamine and 1mM mercaptopropionic acid. It is proposed that the mixture of positively and negatively charged thiols serve to prevent the adsorption of the protein on the gold surface. A cocktail of 17 mediators was added to the protein sample with a final concentration of 25 μM (*see appendix C.3*). The protein solution of around 5 μL is deposited on the gold grid and the cell is closed with CaF<sub>2</sub> windows, then filled with buffer containing 100mM KCl. In this cell the protein solution forms a layer of 10-15 μm, which is comparable to diffusion layer so that it does not require stirring. The cell is inserted either in UV-Vis or IR spectrometer and connected to the potentiostat. The loss of protein in 24 h is as low as 5% and it is due to capillary forces and small contact area with the buffer. Since the cell is a thin-layer cell, it allows decreasing water signal which shows strong absorption bands in MIR spectral region. On the other hand, the protein solution should be concentrated enough up to 500-800 μM to reach satisfying signal-to-noise ratio.

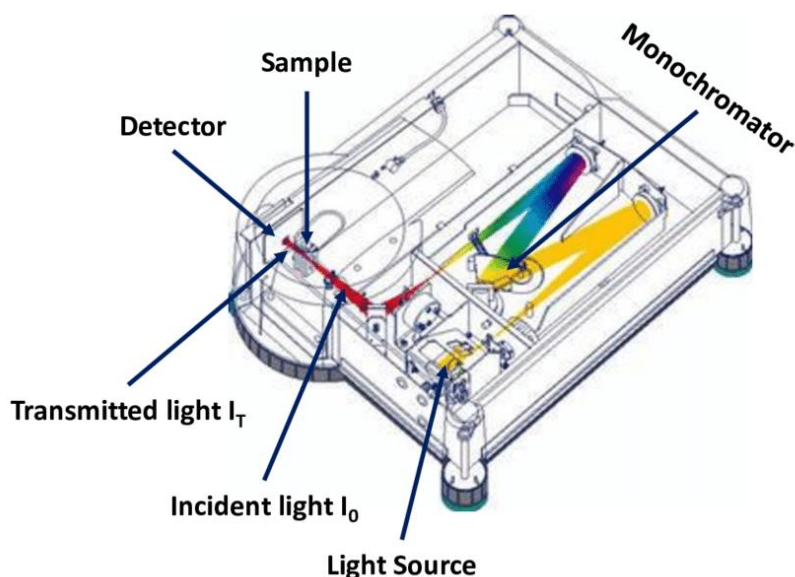


Scheme A.3. The thin-layer electrochemical cell



## A.4 UV-vis spectrometer

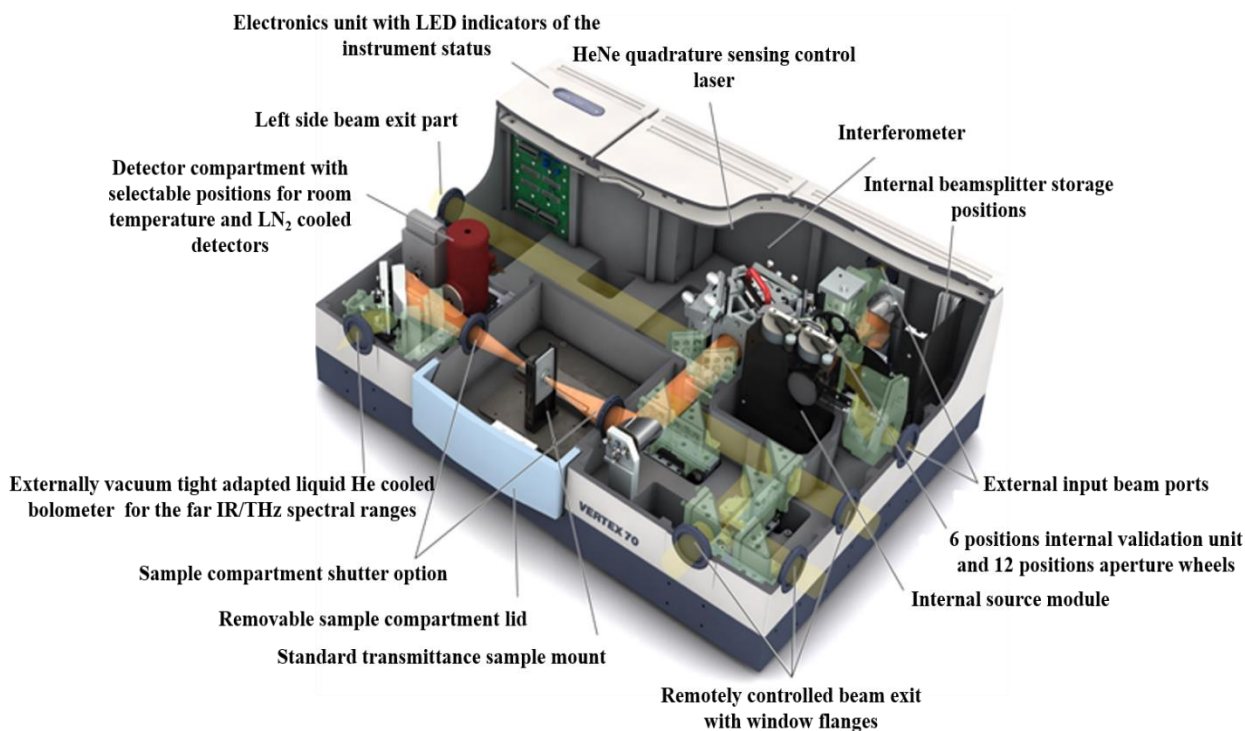
In UV-Vis experiments a dual-beam spectrophotometer VARIAN Cary 300 in single beam mode was employed (Scheme A.4). The sources are a deuterium lamp for UV region (350-800nm) and xenon lamp (190-350 nm) for the visible region of the spectrum. The slit width was 1 nm. This spectrometer is based on scanning monochromator. The measurements were conducted either in an optical glass cuvette (1 cm length) or with a thin-layer cell (described above).



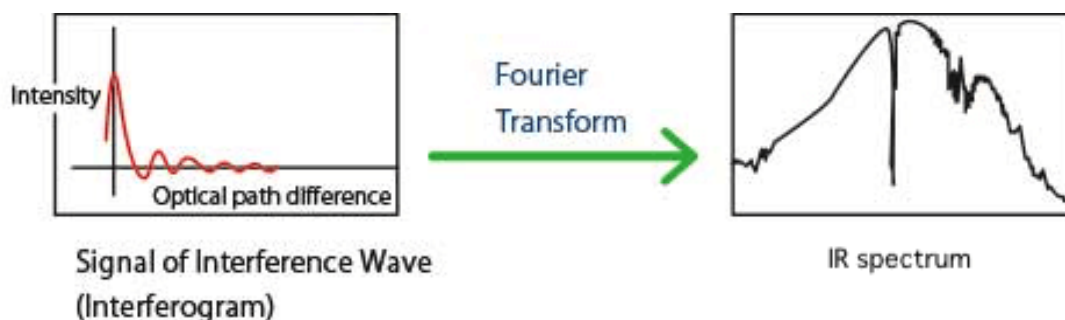
Scheme. A.4. The optical path in the UV/Vis spectrometer.

## A.5 Fourier transform IR spectrometer

The MIR spectra were collected with a Vertex 70 Spectrometer from Bruker Optiks (Karsruhe). The light source is a globar (CSi) heated up to 1300 K. The optical system includes the Michelson interferometer (*vide infra*) with KBr beam splitter and He-Ne calibrating laser (632 nm) (Scheme A.5). The detector is a MCT (mercury cadmium telluride HgCdTe) which is cooled down with liquid nitrogen. Each spectrum included accumulation of 256 scans with 40 kHz scan rate. The resolution  $\Delta\kappa$  is determined from the maximal amplitude of the movable mirror, which is 0.25 cm the standard spectrometer, so that  $\Delta\kappa=1/\delta$ , where  $\delta$  is the maximal difference of the pathlength, giving  $4\text{ cm}^{-1}$ .



Scheme. A.5. The FTIR spectrometer Vertex 70 from Bruker Optics <sup>234</sup>.



Scheme A.6. From Fourier Transform interferogram to the IR spectrum.

In Fourier Transform IR spectrometer, an IR source is interfered with itself at shifting path lengths as at the semi-transparent mirror (“beam splitter”) it splits into two coherent beams: one beam goes to the fixed mirror then the second one is directed to the moving mirror, these beams meet again at detector resulting in interferogram signal as a function of time. This interferogram is a sum of the interferograms at all wavelengths except the ones that were absorbed, and then by Fourier transform it is presented as a function of frequency in  $\text{cm}^{-1}$  seen as an absorbance spectrum.

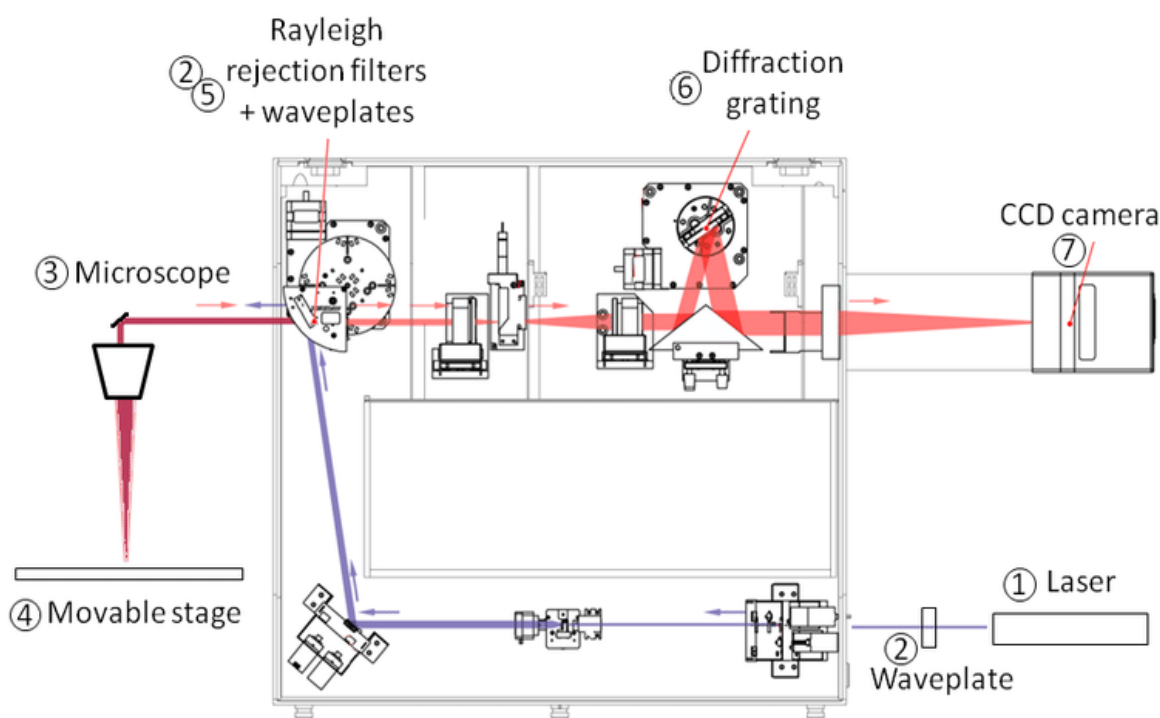
FTIR has several advantages because of the replacement of dispersive monochromator with an interferometer. Firstly, the increase of the signal-to-noise ratio is dramatically improved due to a slit-free optical design allowing more light to pass in the system (Jacquinot’s

advantage). Secondly, the data obtained at multiple wavelengths simultaneously without the need for scanning using a moving grating/prism (Fellgett's advantage). Thirdly, the avoidance of the mechanical movements of the calibrating laser (Connes' advantage).

## A.6 Raman spectrometer

A Renishaw InVia Reflex Raman spectrometer was used in this project. The optical system of the dispersive type spectrometer includes (Scheme A.7): an argon ion laser with excitation wavelengths at 457 (9 mW) and 514 nm (12.5mW), Leica focalising optics, 4 notch filters (for Rayleigh scattering cut off), the slit, dispersive monochromator (grating: 2400 /cm) with a charge coupled device (CCD) detector.

The samples were recorded in the form of dry film on CaF<sub>2</sub> windows (transparency in 83333-1111 cm<sup>-1</sup>) or as solution in the borosilicate capillary. The collection of the Raman scattering emission is conducted under 180° (backscattering), resolution is 1 cm<sup>-1</sup>.



Scheme. A.7. The optical path in the Raman spectrometer, reproduced from <sup>234</sup>.

## B. Protocols

### B.1 Preparation and purification of the studied protein samples

#### B.1.1 Production and of the *E. coli* cytochrome *bd*-I and *bd*-II oxidase

The proteins were kindly extracted and purified by the group of Prof. T. Friedrich (University of Freiburg, Germany). The one of many batches of *bd*-I oxidase was prepared by myself under the guidance of Tatjana Gerasimova. The purification protocol includes metal affinity chromatography IMAC (His-tag). Cyt *bd*-I from *E. coli* strain CBO- pET28b(+):*cydA<sub>h</sub>BX* , (with 'h' describing the position of the His-tag at the C-terminus of CydA) was prepared as previously described <sup>55</sup>. The protein in 20 mM MOPS, 20 mM NaCl, 0.003% LMNG, pH 7.0 was stored at a final concentration of 10 mg/ml. Cyt *bd*-II from *E. coli* strain CBO-AppC<sub>h</sub>BX was prepared as previously described <sup>78</sup> and stored at 20 mg/ml in the same buffer as mentioned above complemented with 0.5 mM PMSF.

#### B.1.2 Purification and generation of mutants E445D and R448N of cyt *bd*-I oxidase

Cyt *bd*-I and the E445D and R448N variants were prepared from *E. coli* strain CBO-CydA<sub>h</sub>BX strain and the appropriate mutants strains as previously described <sup>55</sup>. The preparations in 20 mM MOPS, 20 mM NaCl, 0.003% LMNG, pH 7.0 were stored at a final concentration of 10 mg/ml. The *bd*-I E445D and R448N variants were made as described <sup>55,78</sup> using the primers listed in Table B.1.

Table B.1. Sequences of mutagenic primer, point mutations are shown in bold and silent mutations to generate a new restriction site in italics.

Oligonucleotide	Sequence 5'-3'
CydA E445D_fwd	GAAGCGGGCTGGTTCGTGGCT <b>G</b> ATTATGGGCGCCAACCGTGGGCTATC
CydA E445D_rev	GATAGCCCACGGTTGGCGCCATAATCAGCCACGAACCAGCCCGCTTC
CydA R448N_fwd	CTGGTTCGTGGCTGAATATGGCA <b>AA</b> CCAACCATGGGCTATCGGTGAAGTG
CydA R448N_rev	CACTTCACCGATAGCCCATGGTTGGTTGCCATATTCAGCCACGAACCAG

#### B.1.3 Production and of the D58E and D58L variants of the cytochrome *bd*-I and E58D mutants of the *bd*-II oxidase

The *bd*-I Asp58<sup>B</sup>Glu and the *bd*-II Glu58<sup>B</sup>Asp variants were made as described <sup>55,78</sup> using the primers listed in Table B.2.

Table B.2. Oligonucleotides used in this work. Homologous areas are marked bold. The sequences are given in 5'->3' direction.

Oligonucleotide	Sequence 5'-3'
appB E58D_fwd	ACAGCGTTGGT <b>GCCCACTGGGATGGCAACCAGGTCTGGTTGAT</b>
appB E58D_rev	ATCAACCAGACCTGGTTGCCATCCCAGTGGGGCACCAACGCTGT
CydB D58E_fwd	TCCATAGCACCACACTGGGAAGGTAACCAGGTTTGGCTG
CydB D58E_rev	CAGCCAAACCTGGTTACCTTCCCAGTGTGGTGCTATGGA

#### B.1.4 The preparation and purification of cNOR from *P. denitrificans*

The cNOR wild type and Fe<sub>B</sub> less variant were kindly provided by Sofia Appelgren from the group of Pr. Pia Ädelroth in Stockholm University. The detailed production and purification protocol is described below.

The cNOR protein was produced from the pNOREX plasmid containing the cNOR gene cluster norCBQDEF<sup>92</sup>, modified with the QuickChange Site-Directed Mutagenesis method. For WT cNOR, a C-terminal 6-His-tag was introduced on norB, and for the Fe<sub>B</sub> lacking mutant, the accessory genes norQDEF were cut out by the introduction of restriction sites<sup>9</sup>.

The pNOREX constructs were transformed into *E. coli* JM109, together with the plasmid pEC86, encoding cyt *c* maturation factors. The cells were grown in 800 mL TB media. After induction with 1 mM IPTG, the cultures were incubated at 30°C with 180 rpm shaking for 5 hours, followed by 5 h of incubation at 18°C without agitation, and then returning to 30°C, 180 rpm for 8 h before harvesting<sup>304</sup>. Cells were harvested by centrifugation and resuspended in 100 mM TRIS/HCl, pH 7.6, 50 mM KCl, 1 mM PMSF, followed by cell disruption at 22 kpsi (Emulsiflex C3 Homogenizer) and centrifugation. The membrane pellet was suspended in 100 mM TRIS/HCl, pH 7.6, 50 mM KCl, 1% DDM and solubilized (1 h, 4°C, rotating), followed by centrifugation. The supernatant was mixed with 20 mM imidazole and 1/10 volume of NTA-agarose (1 h, 4°C, rotating). The sample was applied to a gravity-controlled column and washed with 5 column volumes of 50mM TRIS/ HCl, pH 7.6, 200 mM KCl, 0.05% DDM, 50 mM imidazole, followed by elution with 3 column volumes of 50mM TRIS/HCl, pH 7.6, 200 mM KCl, 0.05% DDM, 250 mM imidazole. The eluted protein was concentrated by centrifugal filters (100 kDa cut-off). The imidazole concentration was decreased to >1 mM by repeated concentration and dilution with 50 mM TRIS/HCl, pH 7.6, 200 mM KCl, 0.05% DDM<sup>9</sup>.

## B.2 Catalytic activity measurement in solution for *bd* oxidases and its mutants

### B.2.1 NADH oxidase activity of the *bd* oxidases measured in membranes

The NADH oxidase activity of the membranes of the parental strain of cytochrome *bd*-I oxidase and the R448N and E445D mutant strains was measured with a Clark-type oxygen electrode (Oxyview System, Hansatech Instruments) as previously described <sup>267</sup>. Briefly, the 5  $\mu$ L membrane suspensions (~50 mg/mL) were added to 2 mL buffer (20 mM MOPS pH 7.0, 20 mM NaCl) and heated up to 30 °C. This strain (CBO-CydA<sub>h</sub>BX strain) is lacking *bd*-II type oxidase, the activity of the bo<sub>3</sub> oxidase was inhibited by an addition of 2  $\mu$ L of 1 M KCN to the buffer. The reaction was initiated by an addition of 5  $\mu$ L NADH (10 mM). The rates were corrected for the non-enzymatic rate that was less than 1% of the rate of the enzymatic reaction. Each data point was assayed in triplicates from three different biological samples. The data treatment was performed with kind help of Tatjana Gerasimova (group of Pr. T. Friedrich, Freiburg University, Germany).

### B.2.2 The duroquinol: oxygen oxidoreductase activity of isolated *bd* oxidases

The duroquinol: dioxygen oxidoreductase activity of isolated *E. coli* *bd*-I and *bd*-II oxidase were determined by monitoring the O<sub>2</sub> consumption with a Clark-type oxygen electrode (Oxyview System, Hansatech Instruments). Activity was measured at 30 °C and solution filled into Clark electrode was stirred. The reaction chamber was filled with 2 mL buffer (20mM MOPS, 20mM NaCl, 0.003% LMNG, pH 6.0-9.0), 10  $\mu$ L DTT (1 M) and 5  $\mu$ L duroquinone in ethanol (100 mM) and incubated for 1 min. 10  $\mu$ L protein in LMNG buffer (2 mg/mL) resulting in a final concentration of 95.25 nM protein were added to start the reaction. The rates were corrected for the non-enzymatic reaction. The pH value of the buffers was checked at the beginning and the end of the experiment. The data treatment was performed with kind help of Jan Kägi (group of Pr. T. Friedrich, Freiburg University, Germany).

## B.3 Protein film voltammetry immobilization protocols

### B.3.1 Protein sample pretreatment for the PFV

After the purification all the studied enzymes contained detergent in the buffer that adversely perturbed the stability of the protein films on the electrode surface, therefore, buffer was exchanged to the 100mM phosphate at the appropriate pH. The filter (Amicon) was prewashed with water and corresponding exchange buffer for 10 min at 7500 rpm. The protein samples were washed at 4°C in the corresponding conditions (see Table B.1). The

final volume of the filtrate was 17-21  $\mu\text{L}$ , and the concentration obtained was around 65  $\mu\text{M}$ . This protein stock sample was further diluted to the 10  $\mu\text{M}$  concentration for the direct deposition on the electrode.

*Table B.3. The summarized conditions of the buffer exchange for the proteins probed in protein film voltammetry on gold or glassy carbon rotating electrodes.*

Protein sample	cyt <i>bd-I</i> wild type	cyt <i>bd-II</i> wild type	cyt <i>bd-I</i> E445D	cyt <i>bd-I</i> R448N	cNOR wild type	cNOR w/o Fe <sub>B</sub>
Washed solution	5 $\mu\text{L}$ , 265 $\mu\text{M}$	20 $\mu\text{L}$ , 64 $\mu\text{M}$	7 $\mu\text{L}$ , 170 $\mu\text{M}$	7 $\mu\text{L}$ , 170 $\mu\text{M}$	30 $\mu\text{L}$ , 42 $\mu\text{M}$	19 $\mu\text{L}$ , 66 $\mu\text{M}$
Buffer as-prepared	20mM MOPS, pH 7.0, 20mM NaCl, 0.003% MNG	20mM MOPS, pH 7.0, 20mM NaCl, 0.003% MNG	20mM MOPS, pH 7.0, 20mM NaCl, 0.003% MNG	20mM MOPS, pH 7.0, 20mM NaCl, 0.003% MNG	50 mM Tris/HCl, pH 7.6, 200 mM KCl and 0.05 % DDM	50 mM Tris/HCl, pH 7.6, 200 mM KCl and 0.05 % DDM
Exchange buffer	KPi 100 mM, pH7	KPi 100 mM, pH7	KPi 100 mM, pH7	KPi 100 mM, pH7	KPi 100 mM, pH7.5	KPi 100 mM, pH7.5
Filter cutoff, kDa	50	50	50	50	30	30
Rotation speed, rpm	7500	7500	7500	7500	7500	7500
Number of centrifugation cycles	2	2	4	4	2	2
Time of centrifugation cycle	45 min	45 min	45 min	45 min	45 min	45 min

In case of the cytochrome *bd-I* oxidase, the stock protein solution was incubated with lipids (PE or PG) and UQ<sub>1</sub> when the Aurachins inhibition was tested. The lipids were separately diluted in an ethanol-chloroform (1/3) solution of 36  $\mu\text{M}$  concentration. The required quantity of the lipid solution was added to dry was deposited on the bottom of a cone-like glass vessel and dried under argon stream. The final concentration of lipids was 2.5%, molar percentage comparing to the final concentration of protein (10  $\mu\text{M}$ ). At the same time 0.1 mM solution of ubiquinone in ethanol was added. On the next step, the protein stock solution was added to the lipids and incubated overnight, diluted with phosphate buffer next morning and was ready to use for electrode modification.

### B.3.2 Pretreatment of the gold rotating electrodes

The rotating gold electrode (4.5 mm in diameter) was mechanically polished with 0.3  $\mu\text{m}$  aluminium oxide powder, washed and sonicated for 5 min. Then it was electrochemically pretreated in 0.1 M  $\text{H}_2\text{SO}_4$ : 1) + 2V, 5 s; 2) -0.35 V, 10 s, 100 points; 3) CV: 100 scans, 4 V/s, -0.35...1.5 V; 4) verification CV: 2 cycles, 0.1 V/s, -0.35...1.5 V. The electrode was dried by Ar stream and was ready for the modification with gold nanoparticles concentrated solution.

### B.3.3 Preparation of gold NPs with average diameter of 14-16 nm

The gold nanoparticles were prepared according to the method proposed by Turkevich<sup>309</sup> and refined by Frens<sup>310</sup>. To the 125 mL of boiling 1 mM solution of  $\text{HAuCl}_4$  the 12.5 mL of 38.8 mM sodium citrate was added, all time the magnetic stirrer was employed. It was left to boil for 15 minutes and then cooled down at room temperature. Later the average size of obtained gold nanoparticles (GNPs) was verified by UV/Vis spectroscopy from the ratio of the plasmon resonance band to the background absorption at 450 nm using the table B.4<sup>311</sup>. Before each modification of the rotation electrode, the concentrated solution of GNPs was freshly prepared by centrifugation at 10 000 rpm during 30 min where 95% of the supernatant was removed.

Table B.4. Ratio of the absorbance of GNPs at the surface plasma resonance peak  $A_{\text{spr}}$  to the absorbance at the plateau of the peak at 450 nm  $A_{450}$  in dependence the particle diameter<sup>311</sup>.

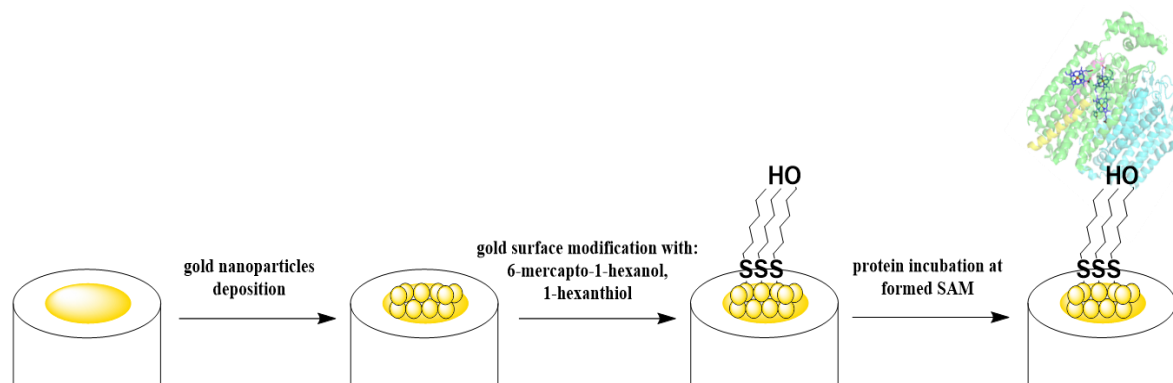
$A_{\text{spr}}/A_{450}$	d / nm	$A_{\text{spr}}/A_{450}$	d / nm	$A_{\text{spr}}/A_{450}$	d / nm
1.10	3	1.56	12	1.96	40
1.19	4	1.61	14	2.00	45
1.27	5	1.65	16	2.03	50
1.33	6	1.69	18	2.07	55
1.38	7	1.73	20	2.10	60
1.42	8	1.80	25	2.12	65
1.46	9	1.86	30	2.15	70
1.50	10	1.92	35	2.17	75

### B.3.4 Immobilization protocol for *bd*-I and *bd*-II on the gold disk electrode

The 7  $\mu\text{L}$  of centrifuged gold NPs were deposited on the gold electrode surface. After drying at room temperature, the 20 control cycles at 0.1 V/s scan rate in the range from -0.2 to 1.55 V vs Ag/AgCl were performed to see an increase the current after modification. Then, the electrode was immersed in a thiol mixture prepared in ethanol with a concentration (1 mM) and incubated for an hour. Electrode then was washed with ethanol from the excess of non-bound thiols, dried and tested in the control experiment (without protein) at 0.02 V/s and 1000 rpm in the +0.3 to -0.65V vs Ag/AgCl potential range. The measurements of the background



were conducted in buffer with 100 mM ion strength. The protein solution was then drop casted and left on the electrode at 4°C for 4 hours.



Scheme B.1. The immobilization scheme of the cytochrome *bd-I* oxidase on the surface of the gold electrode (pdb file 6rko)<sup>10,312</sup>.

### B.3.5 Immobilization protocol for cNOR on the glassy carbon electrode

The electrode (4.5 mm in diameter) was mechanically polished with 0.3  $\mu\text{m}$  aluminium oxide powder and washed in the ultrasonic bath. Then without any pretreatment, the 5  $\mu\text{L}$  of 10  $\mu\text{M}$  cNOR sample was deposited on the surface of electrode, covered with a cap and stored in the fridge +4°C for 4 hours. The excess of protein was washed with buffer and was ready to use in the electrochemical study. In this study, a sample of cNOR was washed from the excess of the detergent in the phosphate buffer of pH 7.5 and then was deposited directly onto a glassy carbon electrode (GCE) surface for 4 hours which allows studying redox reactions in a wide potential range from +0.6 to -0.8 V (vs SHE).

### B.3.6 Inhibition assay with Aurachin derivatives for cytochrome *bd-I* oxidase

In cyclic voltammetry experiments, the aliquot of 20 mM solution of tested inhibitor in DMSO was injected into 20 mL buffer (KPi 100 mM, pH 7) in which rotating disk electrode was immersed.

### B.3.7 Inhibition of the oxygen reduction catalytic reaction of *bd* oxidases by nitric oxide

The NO inhibition of the *bd* oxidases and mutants was tested over one hour. Giving that MAHMA NONOte releasing two equivalents of NO, the aliquot of 10mM solution of MAHMA NONate was added to the buffer solution and CVs were recorded immediately after introduction of NO and every 10 min.

## B.4 Spectroelectrochemistry in the thin-layer cell

### B.4.1 The working electrode (semitransparent gold grid) modification

The gold grid was modified with thiols mixture (1:1) of 1mM MPA and 1mM MEA (1 mM) one night before the experiment in the thin-layer film. After each experiment the gold grid was cleaned from the residual protein sample by sonication (10 min, 2 times). After each 4<sup>th</sup> experiment due to passivation of the protein the grid was washed with piranha / aqua regia solution (300  $\mu$ l HNO<sub>3</sub> (65%), 3000  $\mu$ l H<sub>2</sub>O<sub>2</sub> (33%) and 3x600  $\mu$ l H<sub>2</sub>SO<sub>4</sub> (96%)).

### B.4.2 The conditions of the potentiometric titrations

For the UV-Vis redox titrations the protein samples were first concentrated in the original buffer up to the 600-800  $\mu$ M in the filter (Amicon), and then, washed in the exchange buffer twice. The phosphate buffer pH 7 for *bd* oxidase and pH 7.5 for cNOR wild type and mutants with 100 mM KCl and 0.02 % DDM was used for the exchange. All washing procedure were performed at 4°C and 7500 rpm. The temperature of the titration experiment was 13°C. The resolution of the spectra was 1 nm.

In the titration experiment the heme content of each batch of cytochrome *bd* protein was verified using chemical reduction. The air-oxidised protein solution 2  $\mu$ l was diluted in 900  $\mu$ l buffer solution in the quartz-cuvette and reduced with dithionite. The concentration was calculated based on  $\Delta\epsilon$  values determined for specific wavelengths<sup>313</sup>. The calculations employed the formula:

$$C = \frac{(A_{\lambda_1}^{red} - A_{\lambda_2}^{red}) - (A_{\lambda_1}^{ox} - A_{\lambda_2}^{ox})}{\Delta\epsilon_{\lambda_1, \lambda_2}^{red-ox}} = \frac{(A_{\lambda_1}^{red} - A_{\lambda_1}^{ox}) - (A_{\lambda_2}^{red} - A_{\lambda_2}^{ox})}{\Delta\epsilon_{\lambda_1, \lambda_2}^{red-ox}}$$

where C – protein concentration, A – absorption at specific wavelength  $\lambda$  and for red or ox state.

### B.4.3 Red-ox induced FTIR spectroscopy conditions

For FTIR then protein concentration and buffer exchange were performed as described in previous section. The organic buffers such as MOPS were replaced by phosphate because their signals are seen in the same region of the infrared spectrum as for the protein Amide I band. All the experiments in thin-layer electrochemical cell were conducted with a connected cooling system at 5°C. The 256 spectra were accumulated in each cycle and averaged. More than 40 averaged spectra were averaged to obtain the final ox-red differential spectrum. The resolution of the spectra was 4 cm<sup>-1</sup>. The conditions of measurement are described in details in table B.5.

Table B.5. Conditions of the redox-induced differential FTIR experiments.

Experimental parameter	cyt <i>bd</i> -I and <i>bd</i> -II from <i>E. coli</i>	cNOR from <i>P. denitrificans</i>
Potential range, mV (vs Ag/AgCl)	-500 / +500	-600 / +500
Buffer	100 mM KPi, pH 7.0, 100 mM KCl, 0.02% DDM	100 mM KPi, pH 7.5, 100 mM KCl, 0.02% DDM
Equilibration time, s	120	300

## B.5 Spectroscopic study of proteins

### B.5.1 MAHMA NONOate kinetics

From the product description, the half-life of MAHMA NONOate is 2.7 min at 22°C in 0.1 M phosphate buffer (pH 7.4). The intact MAHMA NONOate has a characteristic band at 267 nm, permitting quantitation of the half-time in aqueous solutions with different pH values<sup>314</sup>. In details, the stock solution of MAHMA NONOate in 0.01M NaOH (stable at pH higher than 9) was added to the phosphate buffer in glass cuvette reaching the final concentration of 100 μM. The absorption spectra were recorded every 15s in the range 240-350 nm. The rate of the NO release was determined by following the disappearance of the band at 267 nm. In each measurement the clear first-order kinetics was observed and the rate constant was obtained, all experiments were repeated three times.

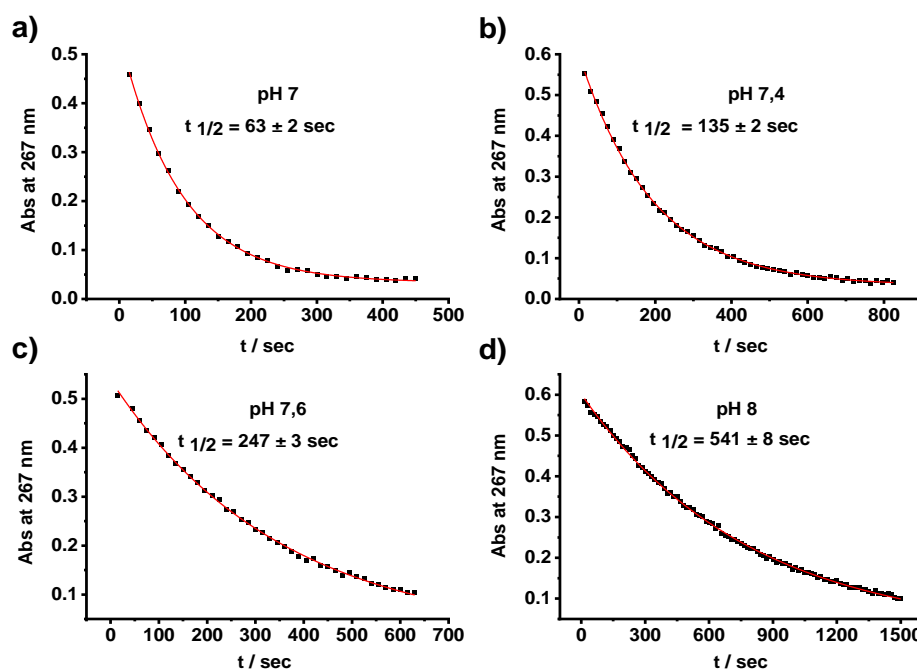


Figure B.1. Kinetics of MAHMA NONOate decomposition in the phosphate buffer solutions and determination of the half-life by the following of the disappearance of the characteristic UV absorption band of NONOate at 267 nm a)-d)

### B.5.2.NO binding experiment for *bd* oxidases

For the 5  $\mu\text{M}$  solution of *bd* oxidase (*bd*-I, *bd*-II, D58E and E58D variants) the air-oxidized (as prepared) and dithionite-reduced spectra vs. background of KPi buffer. The 3 $\mu\text{L}$  of freshly prepared sodium dithionite solution of 2 mM was added, to control the slight change in pH after introduction of the reductant agent. Then, the aliquot of 10 mM MAHMA NONOate stock solution in 0.01 NaOH was introduced to the studied protein, quickly mixed and for an hour to record visible spectra every minute. In cuvette with the volume of 400  $\mu\text{L}$ , the final concentrations were 5  $\mu\text{M}$ , 15  $\mu\text{M}$  and 500  $\mu\text{M}$  for the studied *bd* oxidase, sodium dithionite and NO, respectively. The pH of the solution was verified in the end of each experiment.

### B.5.3 Pretreatment of the cNOR samples for Raman spectroscopy

Dried films and a protein solution (2  $\mu\text{l}$ ) were used. The wild type and mutant of cNOR were exchanged buffer from 50 mM Tris/HCl, pH 7.6, 200 mM KCl and 0.05 % DDM to 100 mM KPi pH 7.6. In experiment with NO, the NO-releasing compound (MAHMA NONOate) was added to the 10  $\mu\text{M}$  cNOR solution with the 100-equivalent excess (1:100 / cNOR: NO), and after 2 minutes the RR spectra were recorded at 514 nm laser excitation.

A x50 magnification was applied for all experiments. Several spectrum accumulations from 3 different spots were collected. The resolution of the spectra was 1  $\text{cm}^{-1}$ . For additional conditions of the experiments see table B.6.

Table B.6. Conditions of the RR measurements.

Experimental parameters	cNOR wild type and mutant	
	Dry film on CaF <sub>2</sub>	Solution in Borosilicate capillary
State of sample	Dry film on CaF <sub>2</sub>	Solution in Borosilicate capillary
Studied concentration, $\mu\text{M}$	10	10
Excitation wavelength, nm	514, 457	514
Number of spectrum accumulations	~30	~60

## C. Materials

### C.1 Chemicals

Sodium citrate, hydrogen tetrachloroaurate trihydrate, sulfuric acid, ubiquinone-1, MAHMA NONOate, 1-mercaptohexanol (MCH), 1-hexanethiol (HT), mercaptopropionic acid (MPA), mercaptohexanoic acid (MHA) and mercaptoundecanoic acid (MUA) were purchased from Sigma; potassium phosphate dibasic trihydrate from Fischer BioReagents; potassium chloride from Fischer BioReagents; sodium hydroxide from SDS; sodium dithionite from Fluka BioChemika; n-dodecyl- $\beta$ -D-maltoside (DDM) from Thermo Scientific; mercaptopropionic acid and cysteamine (MEA) from TCI, 1,2-dioleoyl-sn-glycero-3-phospho-(1'-rac-glycerol) (sodium salt) (PG) and 1,2-dimyristoyl-sn-glycero-3-phosphoethanolamine (PE) were provided by Avanti Polar Lipids. H<sub>2</sub>O<sub>2</sub> (33%) and H<sub>2</sub>SO<sub>4</sub> (96%) were purchased from Sigma-Aldrich, HNO<sub>3</sub> (65%) - from Fluka, aluminum oxide powder – from Buehler.

The aurachin D derivatives were synthesized by the group of Dr. Speicher (Saarland University, Saarbrücken, Germany), using the Conrad-Limpach cyclization<sup>315</sup>. These compounds can be efficiently synthesized in a few steps, HQNO was purchased from Enzo Life Sciences Inc.

### C.2 Mediators for the electrochemical cell

The mediator solutions (see Table C.1) were prepared by two successive dilutions. The weighted mass was diluted with 1.25 ml of corresponding solvent ( $C_1 = 0.01 \text{ mM}$ ) and well-mixed in shaker. Then, the 20  $\mu\text{l}$  of the  $C_1$  solution were then diluted more with 780  $\mu\text{l}$  solvent and were shaken during 15 min ( $C_2 = 0.25 \text{ mM}$ ). Finally, all mediators were mixed together by taking 1  $\mu\text{l}$  of each solution, thus, with final concentration of 25  $\mu\text{l}$  of each compound. With this concentration the contribution of the mediators to the spectra is negligible. The mediators were chosen to cover the whole potential range from -400 to +800 mV (vs SHE)<sup>316</sup>.

Table C.1. List of 19 mediators used in the differential redox-induced spectroscopy measurements. All mediators are low-weight redox active compounds.

Compound	E <sup>0</sup> , mV (vs SHE)	Solvent	Producer
ferrocenylmethyltrimethylammoniumiodide	806	ethanol	Strem chemicals
1,1'-ferrocenedicarboxylic acid	635	ethanol	Fluka
potassiumhexacyanoferrate(II) trihydrate	411	water	Riedel-de-Haen
1,1'-dimethylferrogene	332	ethanol	Aldrich
Quinhydrone	269	ethanol	Fluka
Tetrachloro-1,4-benzoquinone ( <i>p</i> -Chloranil)	271	acetone	Aldrich
N,N,N',N'-tetramethyl- <i>p</i> -phenylenediamine Dihydrochloride	261	water	Fluka
2,6-dichlorophenolindophenol sodium salt hydrate	208	ethanol	Biochemika
hexaammineruthenium(III)chloride	191	water	Aldrich
anthraquinone-2-sulfonic acid sodium salt	176	water	Aldrich
1,4 naphthoquinone hydrate	136	ethanol	Aldrich
Anthraquinone	91	ethanol	Aldrich
5-hydroxy-1,4-naphthoquinone	41	ethanol	Aldrich
Duroquinone	1	ethanol	Sigma
Menadione	-21	acetone	Sigma
2-hydroxyl-1,4-naphthoquinone	-134	ethanol	Sigma
9,10-antraquinone-2,6-dizulfonic acid disodium salt	-234	ethanol	Sigma
Neutral Red	-316	ethanol	Sigma-Aldrich
methyl viologen dichloride hydrate	-429	water	Aldrich

### C.3 Software

The data was processed by means of Origin Lab Pro 9.5, VersaStudio, Microsoft Office, and Opus Brucker. For the protein structure visualization PyMOL was used.

Calculation of pK<sub>a</sub> values and of electrostatic surface potentials were performed with PropKa3 by the Dr. Daniel Wohlwend (the group of Prof. T. Friedrich at University of Freiburg, Germany) as described in literature<sup>317,318</sup> using the pdb models 6RKO (*E. coli* *bd*-I) and 7OY2 (*E. coli* *bd*-II). Electrostatic surface potentials were calculated using the APBS plugin as implemented in PyMOL (version 2.4.1)<sup>318</sup>. Solvent channels in the proteins were probed with the PyMOL plugin CAVER (version 3.0.3) at a minimal radius of 0.9 Å<sup>319,320</sup>.

## D.1 Abbreviations and structures of 20 common amino acids

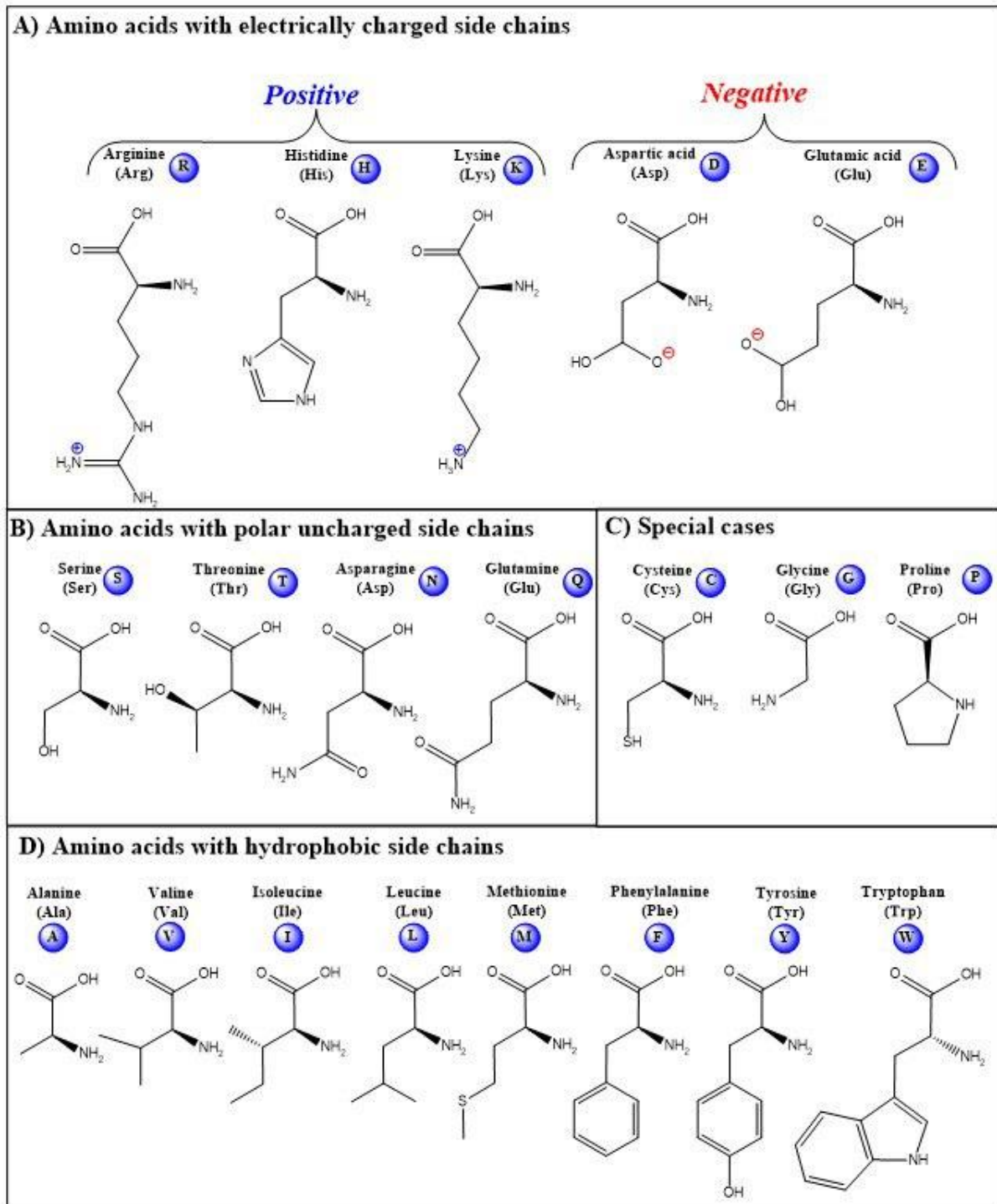


Figure B.2. The structures of the 20 common amino acids

## E.1 The titration curves of the E445D variant of the cytochrome *bd-I* oxidase

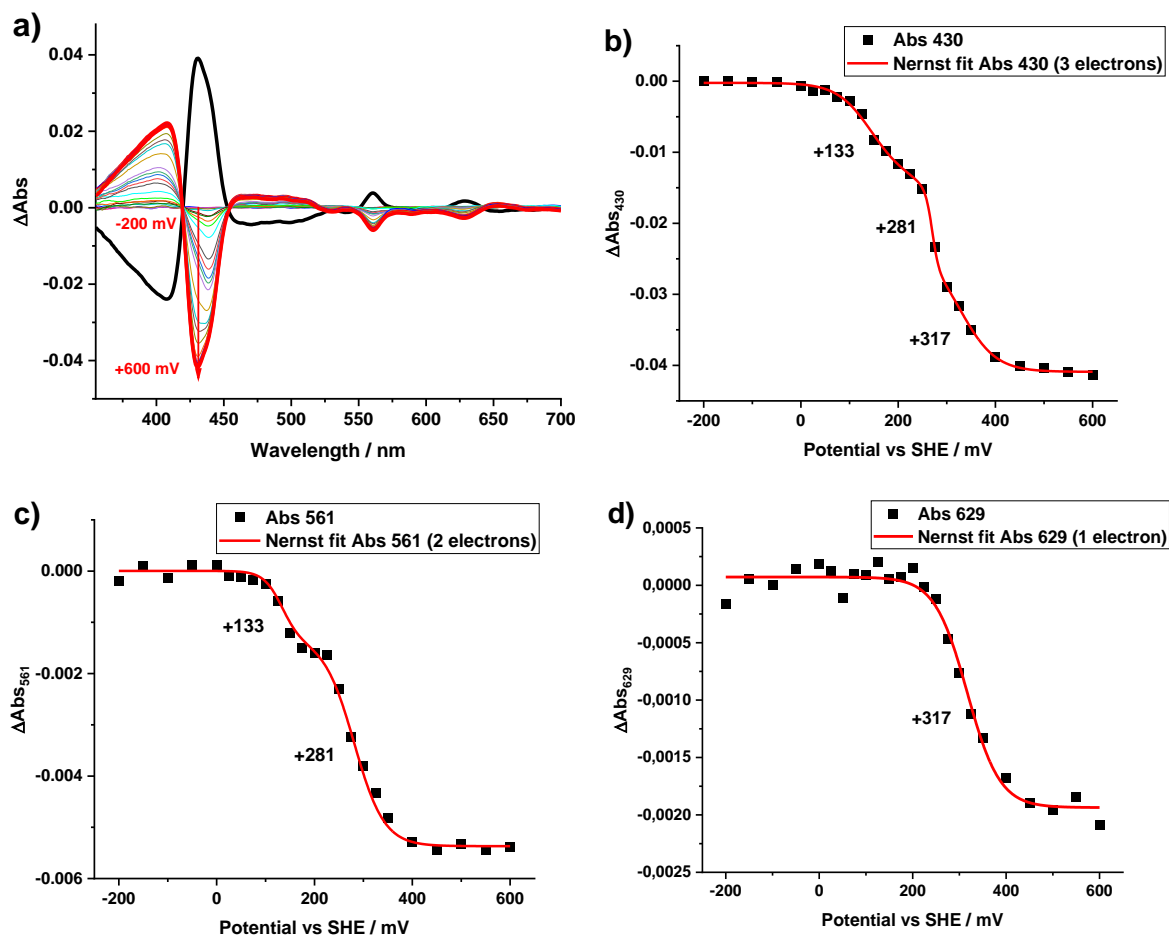


Figure E.1. a) Oxidative titration of *bd-I* E445D variant in the range of +600/-200 mV vs. SHE, b) The differential absorbance of *bd-I* R448N at Soret band, 430 nm, plotted versus applied potential, c) Determination of the hemes *b* potential from differential UV/Vis spectra at 561 nm with modified Nernst equation, d) Determination of the heme *d* potential from differential UV/Vis spectra at 629 nm with modified Nernst equation.



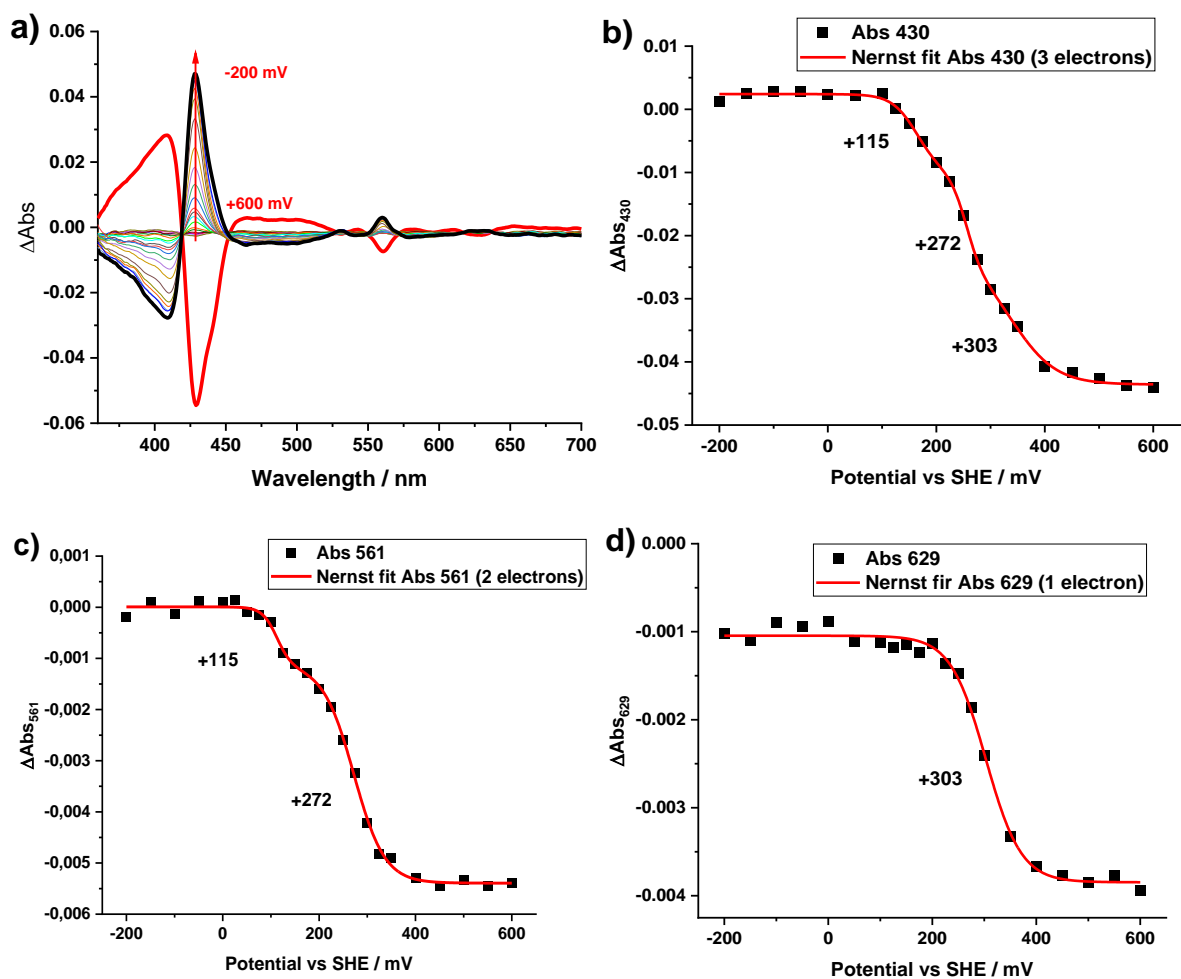


Figure E.2. a) Example of the reductive titration of *bd-I* E445D variant in the range of +600/-400 mV vs. SHE, b) The differential absorbance of *bd-I* R448N at Soret band, 430 nm, plotted versus applied potential, c) Determination of the hemes *b* potential from differential UV/Vis spectra at 561 nm with modified Nernst equation, d) Determination of the heme *d* potential from differential UV/Vis spectra at 629 nm with modified Nernst equation.

# References

---

1. Yin, H. & Flynn, A. D. *Drugging Membrane Protein Interactions. Annual Review of Biomedical Engineering* vol. 18 (2016).
2. Jünemann, S. Cytochrome bd terminal oxidase. *Biochim. Biophys. Acta - Bioenerg.* **1321**, 107–127 (1997).
3. Theßeling, A. *et al.* Homologous bd oxidases share the same architecture but differ in mechanism. *Nat. Commun.* **10**, 1–7 (2019).
4. Safarian, S. *et al.* Structure of a bd oxidase indicates similar mechanisms for membrane-integrated oxygen reductases. *Science (80-. )*. **352**, 583–586 (2016).
5. Borisov, V. B. *et al.* Cytochrome bd protects bacteria against oxidative and nitrosative stress: A potential target for next-generation antimicrobial agents. *Biochem.* **80**, 565–575 (2015).
6. Grund, T. N. *et al.* Mechanistic and structural diversity between cytochrome bd isoforms of *Escherichia coli*. *Proc. Natl. Acad. Sci. U. S. A.* **118**, (2021).
7. Takeda, H., Nomura, T. & Yokota, A. Selected Paper Timing of NO Binding and Protonation in the Catalytic Reaction of Bacterial Nitric Oxide Reductase as Established by Time-Resolved Spectroscopy. 825–833 (2020) doi:10.1246/bcsj.20200038.
8. Matsumura, H. *et al.* Mechanism of substrate inhibition in cytochrome-c dependent NO reductases from denitrifying bacteria (cNORs). *J. Inorg. Biochem.* **231**, (2022).
9. Kahle, M., ter Beek, J., Hosler, J. P. & Ädelroth, P. The insertion of the non-heme Fe B cofactor into nitric oxide reductase from *P. denitrificans* depends on NorQ and NorD accessory proteins. *Biochim. Biophys. Acta - Bioenerg.* **1859**, 1051–1058 (2018).
10. Fournier, E. *et al.* Creation of a gold nanoparticle based electrochemical assay for the detection of inhibitors of bacterial cytochrome bd oxidases. *Bioelectrochemistry* **111**, 109–114 (2016).
11. Moss, D., Nabedryk, E., Breton, J., Mantele, W. & Moss, D. A. *Redox-linked conformational changes in proteins detected by a combination of infrared spectroscopy and protein electrochemistry Evaluation of the technique with cytochrome c. Eur. J. Biochem* vol. 187 (1990).
12. Vos, M. H., Borisov, V. B., Liebl, U., Martin, J. L. & Konstantinov, A. A. Femtosecond resolution of ligand-heme interactions in the high-affinity quinol oxidase bd: A di-heme active site? *Proc. Natl. Acad. Sci. U. S. A.* **97**, 1554–1559 (2000).
13. Safarian, S. *et al.* Active site rearrangement and structural divergence in prokaryotic respiratory oxidases. *Science (80-. )*. **366**, 100–104 (2019).
14. Belevich, I., Borisov, V. B., Bloch, D. A., Konstantinov, A. A. & Verkhovsky, M. I. Cytochrome bd from *Azotobacter vinelandii*: Evidence for high-affinity oxygen binding. *Biochemistry* **46**, 11177–11184 (2007).
15. Mogi, T. & Miyoshi, H. Properties of cytochrome bd plastoquinol oxidase from the cyanobacterium *Synechocystis* sp. PCC 6803. *J. Biochem.* **145**, 395–401 (2009).
16. Borisov, V. B. *et al.* Interactions between heme d and heme b595 in quinol oxidase bd from *Escherichia*

- coli: A photoselection study using femtosecond spectroscopy. *Biochemistry* **41**, 1654–1662 (2002).
17. Kahle, M., Blomberg, M. R. A., Jareck, S. & Ädelroth, P. Insights into the mechanism of nitric oxide reductase from a FeB-depleted variant. *FEBS Lett.* **593**, 1351–1359 (2019).
  18. Margareta R. A. Blomberg and Per E. M. Siegbahn & Department. Mechanism for N<sub>2</sub>O Generation in Bacterial Nitric Oxide Reductase: A Quantum Chemical Study. *Biochemistry* **51**, 5173–5186 (2012).
  19. Signes, A. & Fernandez-Vizarra, E. Assembly of mammalian oxidative phosphorylation complexes I–V and supercomplexes. *Essays Biochem.* **62**, 255–270 (2018).
  20. Nolfi-Donagan, D., Braganza, A. & Shiva, S. Mitochondrial electron transport chain: Oxidative phosphorylation, oxidant production, and methods of measurement. *Redox Biol.* **37**, 101674 (2020).
  21. Saraste, M. Oxidative phosphorylation at the fin de siecle. *Science (80-. )*. **283**, 1488–1493 (1999).
  22. Sousa, J. S., D’Imprima, E. & Vonck, J. Mitochondrial respiratory chain complexes. *Subcell. Biochem.* **87**, 167–227 (2018).
  23. Peter Mitchell. Coupling of Phosphorylation to Electron and Hydrogen Transfer by a Chemi-Osmotic type of Mechanism. *Nature* **191**, 144–148 (1961).
  24. Hamilton, W. A. Bioenergetics of sulphate-reducing bacteria in relation to their environmental impact. *Biodegradation* **9**, 201–212 (1998).
  25. Hein, S. & Simon, J. Bacterial nitrous oxide respiration: electron transport chains and copper transfer reactions. *Adv. Microb. Physiol.* **75**, 137–175 (2019).
  26. John, M., Schmitz, R. P. H., Westermann, M., Richter, W. & Diekert, G. Growth substrate dependent localization of tetrachloroethene reductive dehalogenase in *Sulfurospirillum multivorans*. *Arch. Microbiol.* **186**, 99–106 (2006).
  27. Richardson, D. J. Bacterial respiration: a flexible process for a changing environment. *Microbiology* **146** ( Pt 3, 551–571 (2000).
  28. Schägger, H. Respiratory chain supercomplexes of mitochondria and bacteria. *Biochim. Biophys. Acta - Bioenerg.* **1555**, 154–159 (2002).
  29. Lobo-Jarne, T. & Ugalde, C. Respiratory chain supercomplexes: Structures, function and biogenesis. *Semin. Cell Dev. Biol.* **76**, 179–190 (2018).
  30. Brzezinski, P., Moe, A. & Adeloith, P. Structure and Mechanism of Respiratory III-IV Supercomplexes in Bioenergetic Membranes. *Chem. Rev.* **121**, 9644–9673 (2021).
  31. Skulachev, V. P., Bogachev, A. V. & Kasparinsky, F. O. *Principles of bioenergetics. Principles of Bioenergetics* vol. 9783642334 (2013).
  32. Kampjut, D. & Sazanov, L. A. Structure of respiratory complex I – An emerging blueprint for the mechanism. *Curr. Opin. Struct. Biol.* **74**, 102350 (2022).
  33. Friedrich, T., Hooser, F., Mérono, L. & Harter, C. On the mechanism of respiratory complex I. *Biochim. Biophys. Acta - Bioenerg.* **1863**, 148602 (2022).
  34. On the mechanism of respiratory complex I - ScienceDirect.  
<https://www.sciencedirect.com/science/article/abs/pii/S000527282200072X?via%3Dihub>.
  35. Zickermann, V. *et al.* Architecture of complex I and its implications for electron transfer and proton pumping. *Biochim. Biophys. Acta - Bioenerg.* **1787**, 574–583 (2009).
  36. Brandt, U. Energy converting NADH:quinone oxidoreductase (complex I). *Annu. Rev. Biochem.* **75**, 69–

- 92 (2006).
37. Huang, S. & Millar, A. H. Succinate dehydrogenase: The complex roles of a simple enzyme. *Curr. Opin. Plant Biol.* **16**, 344–349 (2013).
  38. Moosavi, B., Berry, E. A., Zhu, X. L., Yang, W. C. & Yang, G. F. The assembly of succinate dehydrogenase: a key enzyme in bioenergetics. *Cell. Mol. Life Sci.* **76**, 4023–4042 (2019).
  39. Cecchini, G. Function and structure of complex II of the respiratory chain. *Annu. Rev. Biochem.* **72**, 77–109 (2003).
  40. Crofts, A. R. The cytochrome bc<sub>1</sub> complex: Function in the context of structure. *Annu. Rev. Physiol.* **66**, 689–733 (2004).
  41. Cramer, W. A., Hasan, S. S. & Yamashita, E. The Q cycle of cytochrome bc complexes: A structure perspective. *Biochim. Biophys. Acta - Bioenerg.* **1807**, 788–802 (2011).
  42. Ndi, M., Marin-Buera, L., Salvatori, R., Singh, A. P. & Ott, M. Biogenesis of the bc<sub>1</sub> Complex of the Mitochondrial Respiratory Chain. *J. Mol. Biol.* **430**, 3892–3905 (2018).
  43. Hederstedt, L. Diversity of Cytochrome c Oxidase Assembly Proteins in Bacteria. *Microorganisms* **10**, (2022).
  44. Pérez-Mejías, G., Díaz-Quintana, A., Guerra-Castellano, A., Díaz-Moreno, I. & De la Rosa, M. A. Novel insights into the mechanism of electron transfer in mitochondrial cytochrome c. *Coord. Chem. Rev.* **450**, (2022).
  45. Michel, H. Cytochrome c oxidase: Catalytic cycle and mechanisms of proton pumping—A discussion. *Biochemistry* **38**, 15129–15140 (1999).
  46. Richter, O. M. H. & Ludwig, B. Cytochrome c oxidase—structure, function, and physiology of a redox-driven molecular machine. *Rev. Physiol. Biochem. Pharmacol.* **147**, 47–74 (2003).
  47. Unden, G. & Bongaerts, J. Alternative respiratory pathways of Escherichia coli: Energetics and transcriptional regulation in response to electron acceptors. *Biochim. Biophys. Acta - Bioenerg.* **1320**, 217–234 (1997).
  48. Cook, G. M., Greening, C., Hards, K. & Berney, M. *Energetics of Pathogenic Bacteria and Opportunities for Drug Development. Advances in Microbial Physiology* vol. 65 (Elsevier Ltd., 2014).
  49. Kaila, V. R. I. & Wikström, M. Architecture of bacterial respiratory chains. *Nat. Rev. Microbiol.* **19**, 319–330 (2021).
  50. Jormakka, M., Törnroth, S., Byrne, B. & Iwata, S. Molecular basis of proton motive force generation: Structure of formate dehydrogenase-N. *Science (80-. ).* **295**, 1863–1868 (2002).
  51. Jormakka, M., Byrne, B. & Iwata, S. Protonmotive force generation by a redox loop mechanism. *FEBS Lett.* **545**, 25–30 (2003).
  52. Alvarez-Paggi, D. *et al.* Multifunctional Cytochrome c: Learning New Tricks from an Old Dog. *Chem. Rev.* **117**, 13382–13460 (2017).
  53. Huang, Y., Reimann, J., Lepp, H., Drici, N. & Ädelroth, P. Vectorial proton transfer coupled to reduction of O<sub>2</sub> and NO by a heme-copper oxidase. *Proc. Natl. Acad. Sci. U. S. A.* **105**, 20257–20262 (2008).
  54. Matsumura, H. *et al.* Mechanism of substrate inhibition in cytochrome-c dependent NO reductases from denitrifying bacteria (cNORs). *J. Inorg. Biochem.* **231**, (2022).

55. Theßeling, A. *et al.* Homologous bd oxidases share the same architecture but differ in mechanism. *Nat. Commun.* **10**, 1–7 (2019).
56. Friedrich, T., Wohlwend, D. & Borisov, V. B. Recent Advances in Structural Studies of Cytochrome bd and Its Potential Application as a Drug Target. *Int. J. Mol. Sci.* **23**, (2022).
57. Wiseman, B. *et al.* Structure of a functional obligate complex III<sub>2</sub>IV<sub>2</sub> respiratory supercomplex from *Mycobacterium smegmatis*. *Nat. Struct. Mol. Biol.* **25**, 1128–1136 (2018).
58. Ying, Y. & Park, D. An electron transfer path connects subunits of a mycobacterial respiratory supercomplex. **8923**, 6–7 (2018).
59. Sun, C. *et al.* Structure of the alternative complex III in a supercomplex with cytochrome oxidase. *Nature* **557**, 123–126 (2018).
60. Sousa, F. L. *et al.* The superfamily of heme-copper oxygen reductases: Types and evolutionary considerations. *Biochim. Biophys. Acta - Bioenerg.* **1817**, 629–637 (2012).
61. Pereira, M. M., Santana, M. & Teixeira, M. A novel scenario for the evolution of haem-copper oxygen reductases. *Biochim. Biophys. Acta - Bioenerg.* **1505**, 185–208 (2001).
62. Murali, R., Gennis, R. B. & Hemp, J. Evolution of the cytochrome bd oxygen reductase superfamily and the function of CydAA' in Archaea. *ISME J.* **15**, 3534–3548 (2021).
63. Murali, R., Hemp, J. & Gennis, R. B. Evolution of quinol oxidation within the heme-copper oxidoreductase superfamily. *Biochim. Biophys. Acta - Bioenerg.* **1863**, 148907 (2022).
64. Shinzawa-Itoh, K. *et al.* Monomeric structure of an active form of bovine cytochrome c oxidase. *Proc. Natl. Acad. Sci. U. S. A.* **116**, 19945–19951 (2019).
65. Yoshikawa, S. & Shimada, A. Reaction mechanism of cytochrome c oxidase. *Chem. Rev.* **115**, 1936–1989 (2015).
66. Richter, O. M. H. & Ludwig, B. Electron transfer and energy transduction in the terminal part of the respiratory chain - Lessons from bacterial model systems. *Biochim. Biophys. Acta - Bioenerg.* **1787**, 626–634 (2009).
67. Iwata, S., Ostermeier, C., Ludwig, B. & Michel, H. Structure at 2.8 Å resolution of cytochrome c oxidase from *paracoccus denitrificans*. *Nature* vol. 376 660–669 (1995).
68. Li, J. *et al.* Cryo-EM structures of *Escherichia coli* cytochrome bo<sub>3</sub> reveal bound phospholipids and ubiquinone-8 in a dynamic substrate binding site. *Proc. Natl. Acad. Sci. U. S. A.* **118**, (2021).
69. Yap, L. L. *et al.* The quinone-binding sites of the cytochrome bo<sub>3</sub> ubiquinol oxidase from *Escherichia coli*. *Biochim. Biophys. Acta - Bioenerg.* **1797**, 1924–1932 (2010).
70. Noor, M. R. & Soulimane, T. Structure of caa<sub>3</sub> cytochrome c oxidase - A nature-made enzyme-substrate complex. *Biol. Chem.* **394**, 579–591 (2013).
71. Tiefenbrunn, T. *et al.* High resolution structure of the ba<sub>3</sub> cytochrome c oxidase from *thermus thermophilus* in a lipidic environment. *PLoS One* **6**, (2011).
72. Soulimane, T. *et al.* Structure and mechanism of the aberrant ba<sub>3</sub>-cytochrome c oxidase from *Thermus thermophilus*. *EMBO J.* **19**, 1766–1776 (2000).
73. Das, T. K. *et al.* Active site structure of the aa<sub>3</sub> quinol oxidase of *Acidianus ambivalens*. *Biochim. Biophys. Acta - Bioenerg.* **1655**, 306–320 (2004).
74. Gomes, C. M. *et al.* Heme-copper oxidases with modified D- and K-pathways are yet efficient proton

- pumps. *FEBS Lett.* **497**, 159–164 (2001).
75. Blomberg, M. R. A. The mechanism for oxygen reduction in the C family cbb3 cytochrome c oxidases - Implications for the proton pumping stoichiometry. *J. Inorg. Biochem.* **203**, 110866 (2020).
  76. Blomberg, M. R. A. & Ädelroth, P. Mechanisms for enzymatic reduction of nitric oxide to nitrous oxide - A comparison between nitric oxide reductase and cytochrome c oxidase. *Biochim. Biophys. Acta - Bioenerg.* **1859**, 1223–1234 (2018).
  77. Reimann, J., Flock, U., Lepp, H., Honigmann, A. & Ädelroth, P. A pathway for protons in nitric oxide reductase from *Paracoccus denitrificans*. *Biochim. Biophys. Acta - Bioenerg.* **1767**, 362–373 (2007).
  78. Grauel, A. *et al.* Structure of *Escherichia coli* cytochrome bd-II type oxidase with bound aurachin D. *Nat. Commun.* **12**, (2021).
  79. Safarian, S. *et al.* The cryo-EM structure of the bd oxidase from *M. tuberculosis* reveals a unique structural framework and enables rational drug design to combat TB. *Nat. Commun.* **12**, (2021).
  80. Hemp, J. & Gennis, R. B. Diversity of the Heme-Copper superfamily in archaea: Insights from genomics and structural modeling. *Results Probl. Cell Differ.* **45**, 1–31 (2008).
  81. Morris, R. L. & Schmidt, T. M. Shallow breathing: Bacterial life at low O<sub>2</sub>. *Nat. Rev. Microbiol.* **11**, 205–212 (2013).
  82. Garcia-Horsman, J. A., Barquera, B., Rumbley, J., Ma, J. & Gennis, R. B. The superfamily of heme-copper respiratory oxidases. *J. Bacteriol.* **176**, 5587–5600 (1994).
  83. Aoyama, H. *et al.* The Whole Structure of the 13-Subunit Oxidized Cytochrome c Oxidase at 2.8 Å. *Science (80-. ).* **272**, 1136–1144 (1995).
  84. Trojan, D. *et al.* Microaerobic Lifestyle at Nanomolar O<sub>2</sub> Concentrations Mediated by Low-Affinity Terminal Oxidases in Abundant Soil Bacteria. *mSystems* **6**, (2021).
  85. Durand, A. *et al.* Biogenesis of the bacterial cbb3 cytochrome c oxidase: Active subcomplexes support a sequential assembly model. *J. Biol. Chem.* **293**, 808–818 (2018).
  86. Zumft, W. G. Nitric oxide reductases of prokaryotes with emphasis on the respiratory, heme-copper oxidase type. *J. Inorg. Biochem.* **99**, 194–215 (2005).
  87. Hino, T. *et al.* Structural Basis of Biological N<sub>2</sub>O Generation by Bacterial Nitric Oxide Reductase. **330**, 1666–1671 (2010).
  88. Moe, P. Nitric Oxide Reductase from *Paracoccus denitrificans* Contains an Oxo-Bridged Heme / Non-Heme Diiron. 9344–9345 (2000).
  89. Rolda, M. D. *et al.* A Low-Redox Potential Heme in the Dinuclear Center of Bacterial Nitric Oxide Reductase : Implications for the Evolution of Energy-Conserving Heme - Copper. 13780–13786 (1999).
  90. Blomberg, M. R. A. Can reduction of NO to N<sub>2</sub>O in cytochrome c dependent nitric oxide reductase ( cNOR ) proceed through a trans-mechanism ? (2016) doi:10.1021/acs.biochem.6b00788.
  91. Matsumura, H. *et al.* Mechanism of substrate inhibition in cytochrome-c dependent NO reductases from denitrifying bacteria ( cNORs ). **231**, (2022).
  92. Butland, G., Spiro, S., Watmough, N. J. & Richardson, D. J. Two Conserved Glutamates in the Bacterial Nitric Oxide Reductase Are Essential for Activity but Not Assembly of the Enzyme. **183**, 189–199 (2001).
  93. Sharma, V. & Wikström, M. A structural and functional perspective on the evolution of the heme-

- copper oxidases. *FEBS Lett.* **588**, 3787–3792 (2014).
94. Borisov, V. B. *et al.* Aerobic respiratory chain of *Escherichia coli* is not allowed to work in fully uncoupled mode. *Proc. Natl. Acad. Sci. U. S. A.* **108**, 17320–17324 (2011).
  95. Borisov, V. B. *et al.* Interaction of the bacterial terminal oxidase cytochrome bd with nitric oxide. *FEBS Lett.* **576**, 201–204 (2004).
  96. Giuffrè, A., Borisov, V. B., Mastronicola, D., Sarti, P. & Forte, E. Cytochrome bd oxidase and nitric oxide: From reaction mechanisms to bacterial physiology. *FEBS Lett.* **586**, 622–629 (2012).
  97. Jones-Carson, J., Husain, M., Liu, L., Orlicky, D. J. & Vázquez-Torres, A. Cytochrome bd-dependent bioenergetics and antinitrosative defenses in *Salmonella* pathogenesis. *MBio* **7**, (2016).
  98. Mason, M. G. *et al.* Cytochrome bd confers nitric oxide resistance to *Escherichia coli*. *Nat. Chem. Biol.* **5**, 94–96 (2009).
  99. Forte, E., Siletsky, S. A. & Borisov, V. B. In *Escherichia coli* ammonia inhibits cytochrome bo<sub>3</sub> but activates cytochrome bd-i. *Antioxidants* **10**, 1–15 (2021).
  100. Guo, K. & Gao, H. Physiological Roles of Nitrite and Nitric Oxide in Bacteria: Similar Consequences from Distinct Cell Targets, Protection, and Sensing Systems. *Adv. Biol.* **5**, 1–10 (2021).
  101. Fu, H. *et al.* Crp-dependent cytochrome bd oxidase confers nitrite resistance to *Shewanella oneidensis*. *Environ. Microbiol.* **15**, 2198–2212 (2013).
  102. Borisov, V. B. & Forte, E. Impact of hydrogen sulfide on mitochondrial and bacterial bioenergetics. *Int. J. Mol. Sci.* **22**, (2021).
  103. Forte, E. & Giuffrè, A. How bacteria breathe in hydrogen sulfide-rich environments. *Biochem. (Lond.)* **38**, 8–11 (2016).
  104. Korshunov, S., Imlay, K. R. C. & Imlay, J. A. The cytochrome bd oxidase of *Escherichia coli* prevents respiratory inhibition by endogenous and exogenous hydrogen sulfide. *Mol. Microbiol.* **101**, 62–77 (2016).
  105. Forte, E. *et al.* The Terminal Oxidase Cytochrome bd Promotes Sulfide-resistant Bacterial Respiration and Growth. *Sci. Rep.* **6**, 1–8 (2016).
  106. Borisov, V. B. & Forte, E. Terminal Oxidase Cytochrome bd Protects Bacteria Against Hydrogen Sulfide Toxicity. *Biochem. 2020 861* **86**, 22–32 (2021).
  107. Forte, E., Borisov, V. B., Vicente, J. B. & Giuffrè, A. Cytochrome bd and Gaseous Ligands in Bacterial Physiology. in *Advances in Microbial Physiology* vol. 71 171–234 (Academic Press, 2017).
  108. Borisov, V. B. *et al.* Cytochrome bd oxidase from *Escherichia coli* displays high catalase activity: An additional defense against oxidative stress. *FEBS Lett.* **587**, 2214–2218 (2013).
  109. Giuffrè, A., Borisov, V. B., Arese, M., Sarti, P. & Forte, E. Cytochrome bd oxidase and bacterial tolerance to oxidative and nitrosative stress. *Biochimica et Biophysica Acta - Bioenergetics* vol. 1837 1178–1187 (2014).
  110. Paulus, A., Rossius, S. G. H., Dijk, M. & De Vries, S. Oxoferryl-porphyrin radical catalytic intermediate in cytochrome bd oxidases protects cells from formation of reactive oxygen species. *J. Biol. Chem.* **287**, 8830–8838 (2012).
  111. Borisov, V. B. *et al.* Cytochrome bd protects bacteria against oxidative and nitrosative stress: A potential target for next-generation antimicrobial agents. *Biochemistry (Moscow)* vol. 80 565–575

- (2015).
112. Al-Attar, S. *et al.* Cytochrome bd Displays Significant Quinol Peroxidase Activity. *Sci. Rep.* **6**, 1–12 (2016).
  113. Borisov, V. B., Forte, E., Siletsky, S. A., Sarti, P. & Giuffrè, A. Cytochrome bd from *Escherichia coli* catalyzes peroxy-nitrite decomposition. *Biochim. Biophys. Acta - Bioenerg.* **1847**, 182–188 (2015).
  114. Kalia, N. P. *et al.* Carbon metabolism modulates the efficacy of drugs targeting the cytochrome bc<sub>1</sub> complex in *Mycobacterium tuberculosis*. *Sci. Rep.* **9**, 1–9 (2019).
  115. Beebout, C. J., Sominsky, L. A., Eberly, A. R., Van Horn, G. T. & Hadjifrangiskou, M. Cytochrome bd promotes *Escherichia coli* biofilm antibiotic tolerance by regulating accumulation of noxious chemicals. *npj Biofilms Microbiomes* **7**, (2021).
  116. Schildkraut, J. A. *et al.* RNA Sequencing Elucidates Drug-Specific Mechanisms of Antibiotic Tolerance and Resistance in *Mycobacterium abscessus*. *Antimicrob. Agents Chemother.* **66**, (2022).
  117. Wang, W. *et al.* Cryo-EM structure of mycobacterial cytochrome bd reveals two oxygen access channels. *Nat. Commun.* **12**, 6–13 (2021).
  118. Safarian, S. *et al.* Active site rearrangement and structural divergence in prokaryotic respiratory oxidases. *Science (80-. )*. **366**, 100–104 (2019).
  119. Borisov, V. B., Gennis, R. B., Hemp, J. & Verkhovskiy, M. I. The cytochrome bd respiratory oxygen reductases. *Biochim. Biophys. Acta - Bioenerg.* **1807**, 1398–1413 (2011).
  120. Nikolaev, A. *et al.* Electrocatalytic evidence of the diversity of the oxygen reaction in the bacterial bd oxidase from different organisms. *Biochim. Biophys. Acta - Bioenerg.* **1862**, 148436 (2021).
  121. Sakamoto, J. *et al.* Gene structure and quinol oxidase activity of a cytochrome bd-type oxidase from *Bacillus stearothermophilus*. *Biochim. Biophys. Acta - Bioenerg.* **1411**, 147–158 (1999).
  122. Mogi, T. *et al.* Probing the ubiquinol-binding site in cytochrome bd by site-directed mutagenesis. *Biochemistry* **45**, 7924–7930 (2006).
  123. Matsumoto, Y. *et al.* Mass spectrometric analysis of the ubiquinol-binding site in cytochrome bd from *Escherichia coli*. *J. Biol. Chem.* **281**, 1905–1912 (2006).
  124. Borisov, V. B., Forte, E., Sarti, P. & Giuffrè, A. Catalytic intermediates of cytochrome bd terminal oxidase at steady-state: Ferryl and oxy-ferrous species dominate. *Biochim. Biophys. Acta - Bioenerg.* **1807**, 503–509 (2011).
  125. Belevich, I., Borisov, V. B. & Verkhovskiy, M. I. Discovery of the true peroxy intermediate in the catalytic cycle of terminal oxidases by real-time measurement. *J. Biol. Chem.* **282**, 28514–28519 (2007).
  126. Borisov, V. B. & Forte, E. Bioenergetics and Reactive Nitrogen Species in Bacteria. *Int. J. Mol. Sci.* **23**, (2022).
  127. Belevich, I. *et al.* Time-resolved electrometric and optical studies on cytochrome bd suggest a mechanism of electron-proton coupling in the di-heme active site. *Proc. Natl. Acad. Sci. U. S. A.* **102**, 3657–3662 (2005).
  128. Borisov, V. B., Belevich, I., Bloch, D. A., Mogi, T. & Verkhovskiy, M. I. Glutamate 107 in subunit I of cytochrome bd from *Escherichia coli* is part of a transmembrane intraprotein pathway conducting protons from the cytoplasm to the heme b<sub>595</sub>/heme d active site. *Biochemistry* **47**, 7907–7914 (2008).
  129. Jasaitis, A. *et al.* Electrogenic reactions of cytochrome bd. *Biochemistry* **39**, 13800–13809 (2000).



130. Zumft, W. G. Cell biology and molecular basis of denitrification. *Microbiol. Mol. Biol. Rev.* **61**, 533–616 (1997).
131. Bruckdorfer, R. The basics about nitric oxide. *Molecular Aspects of Medicine* vol. 26 3–31 (2005).
132. Weiss, G. & Schaible, U. E. Macrophage defense mechanisms against intracellular bacteria. *Immunol. Rev.* **264**, 182–203 (2015).
133. Kahle, M. & Kahle, M. *Assembly and Function of Nitric Oxide Reductase from Paracoccus denitrificans* *Assembly and Function of Nitric Oxide Reductase from Paracoccus denitrificans*. (2019).
134. Forte, E. *et al.* The cytochrome cbb3 from *Pseudomonas stutzeri* displays nitric oxide reductase activity. *Eur. J. Biochem.* **268**, 6486–6491 (2001).
135. Giuffrè, A. *et al.* The heme-copper oxidases of *Thermus thermophilus* catalyze the reduction of nitric oxide: Evolutionary implications. *Proc. Natl. Acad. Sci. U. S. A.* **96**, 14718–14723 (1999).
136. Borisov, V. B. *et al.* Interaction of the bacterial terminal oxidase cytochrome *bd* with nitric oxide. *FEBS Lett.* **576**, 201–204 (2004).
137. Sarti, P., Forte, E., Mastronicola, D., Giuffrè, A. & Arese, M. Cytochrome c oxidase and nitric oxide in action: Molecular mechanisms and pathophysiological implications. *Biochim. Biophys. Acta - Bioenerg.* **1817**, 610–619 (2012).
138. Moënné-Loccoz, P. Spectroscopic characterization of heme iron-nitrosyl species and their role in NO reductase mechanisms in diiron proteins. *Nat. Prod. Rep.* **24**, 610–620 (2007).
139. Moënné-Loccoz, P. & De Vries, S. Structural characterization of the catalytic high-spin heme b of nitric oxide reductase: A resonance Raman study. *J. Am. Chem. Soc.* **120**, 5147–5152 (1998).
140. Girsch, P. & De Vries, S. Purification and initial kinetic and spectroscopic characterization of NO reductase from *Paracoccus denitrificans*. *Biochim. Biophys. Acta - Bioenerg.* **1318**, 202–216 (1997).
141. Kumita, H. *et al.* NO reduction by nitric-oxide reductase from denitrifying bacterium *Pseudomonas aeruginosa*: Characterization of reaction intermediates that appear in the single turnover cycle. *J. Biol. Chem.* **279**, 55247–55254 (2004).
142. Matsumura, H., Hayashi, T., Chakraborty, S., Lu, Y. & Moënné-Loccoz, P. The production of nitrous oxide by the heme/nonheme diiron center of engineered myoglobins (FeBMbs) proceeds through a trans-iron-nitrosyl dimer. *J. Am. Chem. Soc.* **136**, 2420–2431 (2014).
143. Ye, R. W., Averill, B. A. & Tiedje, J. M. Denitrification: Production and consumption of nitric oxide. *Appl. Environ. Microbiol.* **60**, 1053–1058 (1994).
144. Butler, C. S., Seward, H. E., Greenwood, C. & Thomson, A. J. Fast cytochrome bo from *Escherichia coli* binds two molecules of nitric oxide at CU(B). *Biochemistry* **36**, 16259–16266 (1997).
145. Blomberg, M. R. A. & Siegbahn, P. E. M. Why is the reduction of NO in cytochrome c dependent nitric oxide reductase (cNOR) not electrogenic? *Biochim. Biophys. Acta - Bioenerg.* **1827**, 826–833 (2013).
146. Pinakoulaki, E., Stavarakis, S., Urbani, A. & Varotsis, C. Resonance Raman detection of a ferrous five-coordinate nitrosylheme b3 complex in cytochrome cbb3 oxidase from *Pseudomonas stutzeri*. *J. Am. Chem. Soc.* **124**, 9378–9379 (2002).
147. De Vries, S., Suharti & Pouvreau, L. A. M. Nitric Oxide Reductase: Structural Variations and Catalytic Mechanism. *Biol. Nitrogen Cycle* 57–66 (2007) doi:10.1016/B978-044452857-5.50005-9.
148. Pinakoulaki, E., Gemeinhardt, S., Saraste, M. & Varotsis, C. Nitric-oxide reductase: Structure and

- properties of the catalytic site from resonance Raman scattering. *J. Biol. Chem.* **277**, 23407–23413 (2002).
149. Forte, E., Giuffrè, A., Huang, L. S., Berry, E. A. & Borisov, V. B. Nitric oxide does not inhibit but is metabolized by the cytochrome bcc-aa3 supercomplex. *Int. J. Mol. Sci.* **21**, 1–12 (2020).
150. Butler, C. S. *et al.* Cytochrome bo3 from *Escherichia coli*: The binding and turnover of nitric oxide. *Biochem. Biophys. Res. Commun.* **296**, 1272–1278 (2002).
151. Stubauer, G., Giuffrè, A., Brunori, M. & Sarti, P. Cytochrome c oxidase does not catalyze the anaerobic reduction of NO. *Biochem. Biophys. Res. Commun.* **245**, 459–465 (1998).
152. Chen, J., Xie, P., Huang, Y. & Gao, H. Complex Interplay of Heme-Copper Oxidases with Nitrite and Nitric Oxide. *Int. J. Mol. Sci.* **23**, (2022).
153. Brown, G. C. & Cooper, C. E. Nanomolar concentrations of nitric oxide reversibly inhibit synaptosomal respiration by competing with oxygen at cytochrome oxidase. *FEBS Lett.* **356**, 295–298 (1994).
154. Cooper, C. E. *et al.* Nitric oxide and peroxynitrite cause irreversible increases in the  $K_m$  for oxygen of mitochondrial cytochrome oxidase: In vitro and in vivo studies. *Biochim. Biophys. Acta - Bioenerg.* **1607**, 27–34 (2003).
155. Mason, M. G., Nicholls, P., Wilson, M. T. & Cooper, C. E. Nitric oxide inhibition of respiration involves both competitive (heme) and noncompetitive (copper) binding to cytochrome c oxidase. *Proc. Natl. Acad. Sci. U. S. A.* **103**, 708–713 (2006).
156. Torres, J., Cooper, C. E. & Wilson, M. T. A common mechanism for the interaction of nitric oxide with the oxidized binuclear centre and oxygen intermediates of cytochrome c oxidase. *J. Biol. Chem.* **273**, 8756–8766 (1998).
157. Arjona, D., Wikström, M. & Ädelroth, P. Nitric oxide is a potent inhibitor of the cbb3-type heme-copper oxidases. *FEBS Lett.* **589**, 1214–1218 (2015).
158. Stevanin, T. M. *et al.* Flavohemoglobin Hmp affords inducible protection for *Escherichia coli* respiration, catalyzed by cytochromes bo' or bd, from nitric oxide. *J. Biol. Chem.* **275**, 35868–35875 (2000).
159. Giuffrè, A., Borisov, V. B., Arese, M., Sarti, P. & Forte, E. Cytochrome bd oxidase and bacterial tolerance to oxidative and nitrosative stress. *Biochim. Biophys. Acta - Bioenerg.* **1837**, 1178–1187 (2014).
160. Shepherd, M. *et al.* The cytochrome bd-I respiratory oxidase augments survival of multidrug-resistant *Escherichia coli* during infection. *Sci. Rep.* **6**, 1–10 (2016).
161. Beebout, C. J. *et al.* Respiratory heterogeneity shapes biofilm formation and host colonization in uropathogenic *Escherichia coli*. *MBio* **10**, 1–16 (2019).
162. Hyduke, D. R., Jarboe, L. R., Tran, L. M., Chou, K. J. Y. & Liao, J. C. Integrated network analysis identifies nitric oxide response networks and dihydroxyacid dehydratase as a crucial target in *Escherichia coli*. *Proc. Natl. Acad. Sci. U. S. A.* **104**, 8484–8489 (2007).
163. Pullan, S. T. *et al.* Nitric oxide in chemostat-cultured *Escherichia coli* is sensed by Fnr and other global regulators: Unaltered methionine biosynthesis indicates lack of S nitrosation. *J. Bacteriol.* **189**, 1845–1855 (2007).
164. Jones-Carson, J., Husain, M., Liu, L., Orlicky, D. J. & Vázquez-Torres, A. Cytochrome bd-dependent

- bioenergetics and antinitrosative defenses in Salmonella pathogenesis. *MBio* **7**, 1–10 (2016).
165. Richardson, A. R., Dunman, P. M. & Fang, F. C. The nitrosative stress response of *Staphylococcus aureus* is required for resistance to innate immunity. *Mol. Microbiol.* **61**, 927–939 (2006).
166. Shi, L. *et al.* Changes in energy metabolism of *Mycobacterium tuberculosis* in mouse lung and under in vitro conditions affecting aerobic respiration. *Proc. Natl. Acad. Sci. U. S. A.* **102**, 15629–15634 (2005).
167. Moore, C. M., Nakano, M. M., Wang, T., Ye, R. W. & Helmann, J. D. Response of *Bacillus subtilis* to nitric oxide and the nitrosating agent sodium nitroprusside. *J. Bacteriol.* **186**, 4655–4664 (2004).
168. Borisov, V. B., Forte, E., Giuffrè, A., Konstantinov, A. & Sarti, P. Reaction of nitric oxide with the oxidized di-heme and heme-copper oxygen-reducing centers of terminal oxidases: Different reaction pathways and end-products. *J. Inorg. Biochem.* **103**, 1185–1187 (2009).
169. Borisov, V., Arutyunyan, A. M., Osborne, J. P., Gennis, R. B. & Konstantinov, A. A. Magnetic circular dichroism used to examine the interaction of *Escherichia coli* cytochrome bd with ligands. *Biochemistry* **38**, 740–750 (1999).
170. Borisov, V. B. *et al.* Redox control of fast ligand dissociation from *Escherichia coli* cytochrome bd. *Biochem. Biophys. Res. Commun.* **355**, 97–102 (2007).
171. Sarti, P. *et al.* Nitric oxide and cytochrome c oxidase: Mechanisms of inhibition and NO degradation. *Biochem. Biophys. Res. Commun.* **274**, 183–187 (2000).
172. Borisov, V. B. *et al.* Nitric oxide reacts with the ferryl-oxo catalytic intermediate of the CuB-lacking cytochrome bd terminal oxidase. *FEBS Lett.* **580**, 4823–4826 (2006).
173. Giuffrè, A. *et al.* Reaction of nitric oxide with the turnover intermediates of cytochrome c oxidase: Reaction pathway and functional effects. *Biochemistry* **39**, 15446–15453 (2000).
174. Meunier, B., Madgwick, S. A., Reil, E., Oettmeier, W. & Rich, P. R. New Inhibitors of the Quinol Oxidation Sites of Bacterial Cytochromes bo and bd. *Biochemistry* **34**, 1076–1083 (1995).
175. Radloff, M. *et al.* Short-chain aurachin D derivatives are selective inhibitors of *E. coli* cytochrome bd-I and bd-II oxidases. *Sci. Rep.* **11**, 1–9 (2021).
176. Makarchuk, I. *et al.* The Inhibition Study of Cytochrome bd Oxidase Using the Enzyme-Based Electrochemical Sensor. 45 (2021) doi:10.3390/csac2021-10555.
177. Kalia, N. P. *et al.* Exploiting the synthetic lethality between terminal respiratory oxidases to kill *Mycobacterium tuberculosis* and clear host infection. *Proc. Natl. Acad. Sci. U. S. A.* **114**, 7426–7431 (2017).
178. Mascolo, L. & Bald, D. Cytochrome bd in *Mycobacterium tuberculosis*: A respiratory chain protein involved in the defense against antibacterials. *Prog. Biophys. Mol. Biol.* **152**, 55–63 (2020).
179. WHO. *Tuberculosis Reports. Global Tuberculosis Report* vol. 188 (2021).
180. Hoehl, S. *et al.* Evidence of SARS-CoV-2 Infection in Returning Travelers from Wuhan, China. *N. Engl. J. Med.* **382**, 1278–1280 (2020).
181. Lu, P. *et al.* The cytochrome bd-type quinol oxidase is important for survival of *Mycobacterium smegmatis* under peroxide and antibiotic-induced stress. *Sci. Rep.* **5**, 1–10 (2015).
182. Lu, P. *et al.* The anti-mycobacterial activity of the cytochrome bcc inhibitor Q203 can be enhanced by small-molecule inhibition of cytochrome bd. *Sci. Rep.* **8**, 1–7 (2018).
183. Lee, B. S. *et al.* Dual inhibition of the terminal oxidases eradicates antibiotic-tolerant *Mycobacterium*

- tuberculosis . *EMBO Mol. Med.* **13**, 1–16 (2021).
184. Harikishore, A., Chong, S. S. M., Ragunathan, P., Bates, R. W. & Grüber, G. Targeting the menaquinol binding loop of mycobacterial cytochrome bd oxidase. *Mol. Divers.* **25**, 517–524 (2021).
185. Hopfner, S. M. *et al.* Structure guided generation of thieno[3,2-d]pyrimidin-4-amineMycobacterium tuberculosis bdoxidase inhibitors. *RSC Med. Chem.* **12**, 73–77 (2021).
186. Eddowes, M. J. & Hill, H. A. O. Novel method for the investigation of the electrochemistry of metalloproteins: Cytochrome c. *J. Chem. Soc. Chem. Commun.* 771b – 772 (1977)  
doi:10.1039/C3977000771b.
187. Tarasevich, M. R., Yaropolov, A. I., Bogdanovskaya, V. A. & Varfolomeev, S. D. Electrocatalysis of a cathodic oxygen reduction by laccase. *J. Electroanal. Chem.* **104**, 393–403 (1979).
188. Fourmond, V. & Léger, C. An introduction to electrochemical methods for the functional analysis of metalloproteins. in *Practical Approaches to Biological Inorganic Chemistry* 325–373 (Elsevier, 2020).  
doi:10.1016/B978-0-444-64225-7.00009-2.
189. Liu, J. *et al.* Metalloproteins containing cytochrome, iron-sulfur, or copper redox centers. *Chem. Rev.* **114**, 4366–4369 (2014).
190. Armstrong, Fraser A.; Heering, Hendrik A.; Hirst, Judy. Reaction of complex metalloproteins studied by protein-film .*Chemical Society Reviews.* [doi 10.1039%2FCS9972600169] **26**, 169–179 (1997).
191. Murata, K. *et al.* A simple fabrication method for three-dimensional gold nanoparticle electrodes and their application to the study of the direct electrochemistry of cytochrome c. *Electroanalysis* **22**, 185–190 (2010).
192. Laviron, E. General expression of the linear potential sweep voltammogram in the case of diffusionless electrochemical systems. *J. Electroanal. Chem.* **101**, 19–28 (1979).
193. Page, C. C., Moser, C. C., Chen, X. & Dutton, P. L. Natural engineering principles of electron tunnelling in biological oxidation-reduction. *Nature* **402**, 47–52 (1999).
194. Gray, H. B. & Winkler, J. R. Electron tunneling through proteins. *Q. Rev. Biophys.* **36**, 341–372 (2003).
195. Meharena, Y. T., Oertel, P., Bhaskar, B. & Poulos, T. L. Engineering ascorbate peroxidase activity into cytochrome c peroxidase. *Biochemistry* **47**, 10324–10332 (2008).
196. Léger, C. & Bertrand, P. Direct electrochemistry of redox enzymes as a tool for mechanistic studies. *Chem. Rev.* **108**, 2379–2438 (2008).
197. Sasaki, Y. C. *et al.* Two-dimensional arrangement of a functional protein by cysteine-gold interaction: Enzyme activity and characterization of a protein monolayer on a gold substrate. *Biophys. J.* **72**, 1842–1848 (1997).
198. Armstrong, F. A. Protein film voltammetry: Revealing the mechanisms of biological oxidation and reduction. in *Russian Journal of Electrochemistry* vol. 38 49–62 (Springer, 2002).
199. Sassolas, A., Blum, L. J. & Leca-Bouvier, B. D. Immobilization strategies to develop enzymatic biosensors. *Biotechnol. Adv.* **30**, 489–511 (2012).
200. Marcus, R. A. & Sutin, N. Electron transfers in chemistry and biology. *Biochim. Biophys. Acta - Rev. Bioenerg.* **811**, 265–322 (1985).
201. Jenner, L. P. & Butt, J. N. Electrochemistry of surface-confined enzymes: Inspiration, insight and opportunity for sustainable biotechnology. *Current Opinion in Electrochemistry* vol. 8 81–88 (2018).

202. Dominguez-Benetton, X., Srikanth, S., Satyawali, Y., Vanbroekhoven, K. & Pant, D. Enzymatic electrosynthesis: An overview on the progress in enzyme-electrodes for the production of electricity, fuels and chemicals. *Journal of Microbial and Biochemical Technology* vol. 5 (2013).
203. Chen, P. & McCreery, R. L. Control of Electron Transfer Kinetics at Glassy Carbon Electrodes by Specific Surface Modification. *Anal. Chem.* **68**, 3958–3965 (1996).
204. Haccoun, J., Piro, B., Noël, V. & Pham, M. C. The development of a reagentless lactate biosensor based on a novel conducting polymer. *Bioelectrochemistry* **68**, 218–226 (2006).
205. Nadzhafova, O., Etienne, M. & Walcarius, A. Direct electrochemistry of hemoglobin and glucose oxidase in electrodeposited sol-gel silica thin films on glassy carbon. *Electrochem. commun.* **9**, 1189–1195 (2007).
206. Adeloju, S. B. & Lawal, A. T. Fabrication of a bilayer potentiometric phosphate biosensor by cross-link immobilization with bovine serum albumin and glutaraldehyde. *Anal. Chim. Acta* **691**, 89–94 (2011).
207. Chin, Q. *et al.* Molecular monolayers and interfacial electron transfer of *Pseudomonas aeruginosa* azurin on Au(111). *J. Am. Chem. Soc.* **122**, 4047–4055 (2000).
208. Bellare, M. *et al.* Electrochemical Signal-triggered Release of Biomolecules Functionalized with His-tag Units. *Electroanalysis* **31**, 2274–2282 (2019).
209. Ataka, K. *et al.* Oriented attachment and membrane reconstitution of his-tagged cytochrome c oxidase to a gold electrode: In situ monitoring by surface-enhanced infrared absorption spectroscopy. *J. Am. Chem. Soc.* **126**, 16199–16206 (2004).
210. Willner, B., Katz, E. & Willner, I. Electrical contacting of redox proteins by nanotechnological means. *Curr. Opin. Biotechnol.* **17**, 589–596 (2006).
211. Yates, N. D. J., Fascione, M. A. & Parkin, A. Methodologies for “Wiring” Redox Proteins/Enzymes to Electrode Surfaces. *Chemistry - A European Journal* vol. 24 12164–12182 (2018).
212. Roy, I. & Gupta, M. N. Bioaffinity Immobilization. in 107–116 (Humana Press, 2006). doi:10.1007/978-1-59745-053-9\_10.
213. Giess, F., Friedrich, M. G., Heberle, J., Naumann, R. L. & Knoll, W. The protein-tethered lipid bilayer: A novel mimic of the biological membrane. *Biophys. J.* **87**, 3213–3220 (2004).
214. Jeuken, L. J. C. *et al.* Redox enzymes in tethered membranes. *J. Am. Chem. Soc.* **128**, 1711–1716 (2006).
215. Meyer, T. *et al.* Evidence for distinct electron transfer processes in terminal oxidases from different origin by means of protein film voltammetry. *J. Am. Chem. Soc.* **136**, 10854–10857 (2014).
216. Wang, J. Nanomaterial-based amplified transduction of biomolecular interactions. *Small* **1**, 1036–1043 (2005).
217. Luo, X., Morrin, A., Killard, A. J. & Smyth, M. R. Application of nanoparticles in electrochemical sensors and biosensors. *Electroanalysis* **18**, 319–326 (2006).
218. Xiao, Y., Patolsky, F., Katz, E., Hainfeld, J. F. & Willner, I. Plugging into enzymes: Nanowiring of redox enzymes by a gold nanoparticle. *Science (80-. )*. **299**, 1877–1881 (2003).
219. Wang, L. & Wang, E. Direct electron transfer between cytochrome c and a gold nanoparticles modified electrode. *Electrochem. commun.* **6**, 49–54 (2004).
220. Zhu, M. *et al.* Novel nitric oxide microsensor and its application to the study of smooth muscle cells.

- Anal. Chim. Acta* **455**, 199–206 (2002).
221. Raj, C. R., Okajima, T. & Ohsaka, T. Gold nanoparticle arrays for the voltammetric sensing of dopamine. *J. Electroanal. Chem.* **543**, 127–133 (2003).
  222. Melin, F. & Hellwig, P. Redox Properties of the Membrane Proteins from the Respiratory Chain. *Chemical Reviews* vol. 120 10244–10297 (2020).
  223. Northrop, D. B. On the meaning of  $K_m$  and  $V/K$  in enzyme kinetics. *J. Chem. Educ.* **75**, 1153–1157 (1998).
  224. Rodriguez, J. M. G., Hux, N. P., Philips, S. J. & Towns, M. H. Michaelis-Menten Graphs, Lineweaver-Burk Plots, and Reaction Schemes: Investigating Introductory Biochemistry Students' Conceptions of Representations in Enzyme Kinetics. *J. Chem. Educ.* (2019) doi:10.1021/acs.jchemed.9b00396.
  225. Whiteley, C. G. Enzyme kinetics: Partial and complete competitive inhibition. *Biochem. Educ.* **25**, 144–146 (1997).
  226. Brandt, R. B., Laux, J. E. & Yates, S. W. Calculation of inhibitor  $K_i$  and inhibitor type from the concentration of inhibitor for 50% inhibition for Michaelis-Menten enzymes. *Biochem. Med. Metab. Biol.* **37**, 344–349 (1987).
  227. Reed, M. C., Lieb, A. & Nijhout, H. F. The biological significance of substrate inhibition: A mechanism with diverse functions. *BioEssays* **32**, 422–429 (2010).
  228. Copeland, R. A. *Evaluation of Enzyme Inhibitors in Drug Discovery: A Guide for Medicinal Chemists and Pharmacologists: Second Edition. Evaluation of Enzyme Inhibitors in Drug Discovery: A Guide for Medicinal Chemists and Pharmacologists: Second Edition* (2013). doi:10.1002/9781118540398.
  229. Williams, J. W. & Morrison, J. F. *The Kinetics of Reversible Tight-Binding Inhibition. Methods in Enzymology* vol. 63 (1979).
  230. Kuzmič, P. *et al.* High-throughput screening of enzyme inhibitors: Automatic determination of tight-binding inhibition constants. *Anal. Biochem.* **281**, 62–67 (2000).
  231. Yung-Chi, C. & Prusoff, W. H. Relationship between the inhibition constant ( $K_I$ ) and the concentration of inhibitor which causes 50 per cent inhibition ( $I_{50}$ ) of an enzymatic reaction. *Biochem. Pharmacol.* **22**, 3099–3108 (1973).
  232. Murphy, D. J. Determination of accurate  $K_I$  values for tight-binding enzyme inhibitors: An in silico study of experimental error and assay design. *Anal. Biochem.* **327**, 61–67 (2004).
  233. Henderson, P. J. A linear equation that describes the steady-state kinetics of enzymes and subcellular particles interacting with tightly bound inhibitors. *Biochem. J.* **127**, 321–333 (1972).
  234. What is Kasha's Rule? <https://www.edinst.com/us/blog/what-is-kashas-rule/>.
  235. Förster2004\_Chapter\_UVVISSpectroscopy.
  236. Gill, S. C. & von Hippel, P. H. Calculation of protein extinction coefficients from amino acid sequence data. *Anal Biochem* **182(2)**, 319–326 (1989).
  237. Williams, M. A. *Protein-ligand interactions: Fundamentals. Methods in Molecular Biology* vol. 1008 (2013).
  238. Parker F.S. *Applications of infrared spectroscopy in biochemistry, biology, and medicine.* (Springer Science & Business Media, 2012).
  239. Marcelli, A., Cricenti, A., Kwiatek, W. M. & Petibois, C. Biological applications of synchrotron

- radiation infrared spectromicroscopy. *Biotechnology Advances* vol. 30 1390–1404 (2012).
240. Barth, A. Infrared spectroscopy of proteins. *Biochimica et Biophysica Acta - Bioenergetics* vol. 1767 1073–1101 (2007).
241. Miller, L. M., Bourassa, M. W. & Smith, R. J. FTIR spectroscopic imaging of protein aggregation in living cells. *Biochimica et Biophysica Acta - Biomembranes* vol. 1828 2339–2346 (2013).
242. Melin, F. & Hellwig, P. Recent advances in the electrochemistry and spectroelectrochemistry of membrane proteins. *Biol. Chem.* **394**, 593–609 (2013).
243. Hellwig, P. *et al.* Involvement of glutamic acid 278 in the redox reaction of the cytochrome c oxidase from *Paracoccus denitrificans* investigated by FTIR spectroscopy. *Biochemistry* **37**, 7390–7399 (1998).
244. Wolpert, M. & Hellwig, P. Infrared spectra and molar absorption coefficients of the 20 alpha amino acids in aqueous solutions in the spectral range from 1800 to 500 cm<sup>-1</sup>. *Spectrochim. Acta - Part A Mol. Biomol. Spectrosc.* **64**, 987–1001 (2006).
245. Caserta, G. *et al.* Unusual structures and unknown roles of FeS clusters in metalloenzymes seen from a resonance Raman spectroscopic perspective. *Coord. Chem. Rev.* **452**, 214287 (2022).
246. Spiro, T. G., Czernuszewicz, R. S. & Li, X. Y. Metalloporphyrin structure and dynamics from resonance raman spectroscopy. *Coord. Chem. Rev.* **100**, 541–571 (1990).
247. Li, X. Y., Czernuszewicz, R. S., Kincaid, J. R., Su, Y. O. & Spiro, T. G. Consistent porphyrin force field. 1. Normal-mode analysis for nickel porphine and nickel tetraphenylporphine from resonance Raman and infrared spectra and isotope shifts. *J. Phys. Chem.* **94**, 31–47 (1990).
248. Rush, T. S. *et al.* Computational Modeling of Metalloporphyrin Structure and Vibrational Spectra: Porphyrin Ruffling in NiTPP. *J. Phys. Chem. B* **104**, 5020–5034 (2000).
249. Spiro, T. G. & Strekas, T. C. Resonance Raman Spectra of Heme Proteins. Effects of Oxidation and Spin State. *J. Am. Chem. Soc.* **96**, 338–345 (1974).
250. Spiro, T. G. & Burke, J. M. Protein Control of Porphyrin Conformation. Comparison of Resonance Raman Spectra of Heme Proteins with Mesoporphyrin IX Analogs. *J. Am. Chem. Soc.* **98**, 5482–5489 (1976).
251. Heibel, G. E. *et al.* Comparative Resonance Raman Study of Cytochrome c Oxidase from Beef Heart and *Paracoccus denitrificans*. *Biochemistry* **32**, 10866–10877 (1993).
252. Gerscher, S., Hildebrandt, P., Buse, G. & Soulimane, T. The active site structure of ba3 oxidase from *Thermus thermophilus* studied by resonance Raman spectroscopy. *Biospectroscopy* **5**, 53–63 (1999).
253. Yin, H. & Flynn, A. D. Drugging Membrane Protein Interactions. *Annu. Rev. Biomed. Eng.* **18**, 51–76 (2016).
254. Corbett, D. *et al.* *Listeria monocytogenes* Has Both Levels , and Both Are Important in Infection. *MBio* **85**, 1–13 (2017).
255. Jones-Carson, J., Husain, M., Liu, L., Orlicky, D. J. & Vázquez-Torres, A. Cytochrome bd-dependent bioenergetics and antinitrosative defenses in *Salmonella* pathogenesis. *MBio* **7**, (2016).
256. Koul, A. *et al.* Delayed bactericidal response of *Mycobacterium tuberculosis* to bedaquiline involves remodelling of bacterial metabolism. *Nat. Commun.* **5**, 3369 (2014).
257. Meyer, T. *et al.* Evidence for distinct electron transfer processes in terminal oxidases from different origin by means of protein film voltammetry. *J. Am. Chem. Soc.* **136**, 10854–10857 (2014).

258. Trasatti, S. & Petrii, O. A. International Union of Pure and Applied Chemistry Physical Chemistry Division Commission on Electrochemistry: Real Surface Area Measurements in Electrochemistry. *Pure Appl. Chem.* **63**, 711–734 (1991).
259. Vericat, C., Vela, M. E., Benitez, G., Carro, P. & Salvarezza, R. C. Self-assembled monolayers of thiols and dithiols on gold: new challenges for a well-known system. *Chem. Soc. Rev.* **39**, 1805–1834 (2010).
260. Makarchuk, I. *et al.* Identification and optimization of quinolone-based inhibitors against cytochrome bd oxidase using an electrochemical assay. *Electrochim. Acta* **381**, 138293 (2021).
261. Nikolaev, A. *et al.* Stabilization of the highly hydrophobic membrane protein, cytochrome bd oxidase, on metallic surfaces for direct electrochemical studies. *Molecules* **25**, (2020).
262. Fujita, K. *et al.* Mimicking protein-protein electron transfer: Voltammetry of *Pseudomonas aeruginosa* azurin and the *Thermus thermophilus* CuA domain at  $\omega$ -derivatized self-assembled-monolayer gold electrodes. *J. Am. Chem. Soc.* **126**, 13954–13961 (2004).
263. Liko, I. *et al.* Dimer interface of Bovine cytochrome c oxidase is influenced by local posttranslational modifications and lipid binding. *Proc. Natl. Acad. Sci. U. S. A.* **113**, 8230–8235 (2016).
264. Lee, A. G. How lipids affect the activities of integral membrane proteins. *Biochim. Biophys. Acta - Biomembr.* **1666**, 62–87 (2004).
265. Musatov, A. & Robinson, N. C. Bound cardiolipin is essential for cytochrome c oxidase proton translocation. *Biochimie* **105**, 159–164 (2014).
266. Léger, C., Jones, A. K., Albracht, S. P. J. & Armstrong, F. A. Effect of a dispersion of interfacial electron transfer rates on steady state catalytic electron transport in [NiFe]-hydrogenase and other enzymes. *J. Phys. Chem. B* **106**, 13058–13063 (2002).
267. Theßeling, A., Burschel, S., Wohlwend, D. & Friedrich, T. The long Q-loop of *Escherichia coli* cytochrome bd oxidase is required for assembly and structural integrity. *FEBS Lett.* **594**, 1577–1585 (2020).
268. Dueweke, T. J. & Gennis, R. B. Proteolysis of the Cytochrome d Complex with Trypsin and Chymotrypsin Localizes a Quinol Oxidase Domain. *Biochemistry* **30**, 3401–3406 (1991).
269. Miyoshi, H., Takegami, K., Sakamoto, K., Mogi, T. & Iwamura, H. Characterization of the ubiquinol oxidation sites in cytochromes bo and bd from *Escherichia coli* using aurachin C analogues. *J. Biochem.* **125**, 138–142 (1999).
270. Mogi, T. *et al.* Antibiotics LL-Z1272 identified as novel inhibitors discriminating bacterial and mitochondrial quinol oxidases. *Biochim. Biophys. Acta - Bioenerg.* **1787**, 129–133 (2009).
271. Galván, A. E. *et al.* Microcin J25 inhibits ubiquinol oxidase activity of purified cytochrome bd-I from *Escherichia coli*. *Biochimie* **160**, 141–147 (2019).
272. Zhang, J., Oettmeier, W., Gennis, R. B. & Hellwig, P. FTIR spectroscopic evidence for the involvement of an acidic residue in quinone binding in cytochrome bd from *Escherichia coli*. *Biochemistry* **41**, 4612–4617 (2002).
273. Kita, K., Konishi, K. & Anraku, Y. Terminal oxidases of *Escherichia coli* aerobic respiratory chain. II. Purification and properties of cytochrome b558-d complex from cells grown with limited oxygen and evidence of branched electron-carrying systems. *J. Biol. Chem.* **259**, 3375–3381 (1984).
274. Inglese, J. *et al.* Quantitative high-throughput screening: A titration-based approach that efficiently



- identifies biological activities in large chemical libraries. *Proc. Natl. Acad. Sci. U. S. A.* **103**, 11473–11478 (2006).
275. Arutyunyan, A. M. *et al.* Strong excitonic interactions in the oxygen-reducing site of bd-type oxidase: The Fe-to-Fe distance between hemes d and b595 is 10 Å. *Biochemistry* **47**, 1752–1759 (2008).
276. Hill, J. J., Alben, J. O. & Gennis, R. B. Spectroscopic evidence for a heme-heme binuclear center in the cytochrome bd ubiquinol oxidase from *Escherichia coli*. *Proc. Natl. Acad. Sci. U. S. A.* **90**, 5863–5867 (1993).
277. Hellwig, P. Infrared spectroscopic markers of quinones in proteins from the respiratory chain. *Biochim. Biophys. Acta - Bioenerg.* **1847**, 126–133 (2015).
278. Yang, K. *et al.* Glutamate 107 in subunit I of the cytochrome bd quinol oxidase from *Escherichia coli* is protonated and near the heme d/heme b595 binuclear center. *Biochemistry* **46**, 3270–3278 (2007).
279. Wenz, T. *et al.* Role of phospholipids in respiratory cytochrome bc<sub>1</sub> complex catalysis and supercomplex formation. *Biochim. Biophys. Acta - Bioenerg.* **1787**, 609–616 (2009).
280. Lorence, R. M., Miller, M. J., Borochoy, A., Faiman-Weinberg, R. & Gennis, R. B. Effects of pH and detergent on the kinetic and electrochemical properties of the purified cytochrome d terminal oxidase complex of *Escherichia coli*. *Biochim. Biophys. Acta (BBA)/Protein Struct. Mol.* **790**, 148–153 (1984).
281. Bloch, D. A., Borisov, V. B., Mogi, T. & Verkhovsky, M. I. Heme/heme redox interaction and resolution of individual optical absorption spectra of the hemes in cytochrome bd from *Escherichia coli*. *Biochim. Biophys. Acta - Bioenerg.* **1787**, 1246–1253 (2009).
282. Zhang, J., Hellwig, P., Osborne, J. P. & Gennis, R. B. Arginine 391 in subunit I of the cytochrome bd quinol oxidase from *Escherichia coli* stabilizes the reduced form of the hemes and is essential for quinol oxidase activity. *J. Biol. Chem.* **279**, 53980–53987 (2004).
283. Lübben, M., Prutsch, A., Mamat, B. & Gerwert, K. Electron transfer induces side-chain conformational changes of glutamate-286 from cytochrome bo<sub>3</sub>. *Biochemistry* **38**, 2048–2056 (1999).
284. Valentine, J. S., Sheridan, R. P., Allen, L. C. & Kahn, P. C. Coupling between oxidation state and hydrogen bond conformation in heme proteins. *Proc. Natl. Acad. Sci. U. S. A.* **76**, 1009–1013 (1979).
285. Ye, T., Kaur, R., Wen, X., Bren, K. L. & Elliott, S. J. Redox properties of wild-type and heme-binding loop mutants of bacterial cytochromes c measured by direct electrochemistry. *Inorg. Chem.* **44**, 8999–9006 (2005).
286. Michel, L. V. *et al.* Heme attachment motif mobility tunes cytochrome c redox potential. *Biochemistry* **46**, 11753–11760 (2007).
287. Bowman, S. E. J. & Bren, K. L. Variation and analysis of second-sphere interactions and axial histidinate character in c -type cytochromes. *Inorg. Chem.* **49**, 7890–7897 (2010).
288. Melin, F. *et al.* The unusual redox properties of C-type oxidases. *Biochim. Biophys. Acta - Bioenerg.* **1857**, 1892–1899 (2016).
289. Hori, H., Tsubaki, M., Mogi, T. & Anraku, Y. EPR Study of NO Complex of bd-type Ubiquinol Oxidase from *Escherichia coli*. *J. Biol. Chem.* **271**, 9254–9258 (1996).
290. Borisov, V. B. *et al.* Nitric oxide reacts with the ferryl-oxo catalytic intermediate of the Cu<sub>B</sub>-lacking cytochrome bd terminal oxidase. *FEBS Lett.* **580**, 4823–4826 (2006).
291. Behr, J., Hellwig, P., Mäntele, W. & Michel, H. Redox dependent changes at the heme propionates in

- cytochrome c oxidase from *Paracoccus denitrificans*: Direct evidence from FTIR difference spectroscopy in combination with heme propionate <sup>13</sup>C labeling. *Biochemistry* **37**, 7400–7406 (1998).
292. Kägi, J. *et al.* E. coli cytochrome bd-I requires Asp58 in the CydB subunit for catalytic activity. *FEBS Lett.* **596**, 2418–2424 (2022).
293. Sato, N. *et al.* Structures of reduced and ligand-bound nitric oxide reductase provide insights into functional differences in respiratory enzymes. *Proteins Struct. Funct. Bioinforma.* **82**, 1258–1271 (2014).
294. Hendriks, J. *et al.* The active site of the bacterial nitric oxide reductase is a dinuclear iron center. *Biochemistry* **37**, 13102–13109 (1998).
295. Hino, T. *et al.* Structural basis of biological N<sub>2</sub>O generation by bacterial nitric oxide reductase. *Science (80-. )*. **330**, 1666–1670 (2010).
296. Hino, T., Nagano, S., Sugimoto, H., Tosha, T. & Shiro, Y. Molecular structure and function of bacterial nitric oxide reductase. *Biochim. Biophys. Acta - Bioenerg.* **1817**, 680–687 (2012).
297. Hellwig, P. *et al.* Electrochemical and ultraviolet/visible/infrared spectroscopic analysis of heme a and a<sub>3</sub> redox reactions in the cytochrome c oxidase from *Paracoccus denitrificans*: Separation of heme a and a<sub>3</sub> contributions and assignment of vibrational modes. *Biochemistry* **38**, 1685–1694 (1999).
298. Hellwig, P., Barquera, B. & Gennis, R. B. Direct evidence for the protonation of aspartate-75, proposed to be at a quinol binding site, upon reduction of cytochrome bo<sub>3</sub> from *Escherichia coli*. *Biochemistry* **40**, 1077–1082 (2001).
299. Pinakoulaki, E. & Varotsis, C. Resonance raman spectroscopy of nitric oxide reductase and cbb3 Heme-Copper oxidase. *J. Phys. Chem. B* **112**, 1851–1857 (2008).
300. Zumft, W. G., Braun, C. & Cuypers, H. Nitric oxide reductase from *Pseudomonas stutzeri*, a novel cytochrome bc complex Phospholipid requirement, electron paramagnetic resonance and redox properties. *Eur. J. Biochem.* **219**, 481–490 (1994).
301. Cordas, C. M., Duarte, A. G., Moura, J. J. G. & Moura, I. Electrochemical behaviour of bacterial nitric oxide reductase - Evidence of low redox potential non-heme FeB gives new perspectives on the catalytic mechanism. *Biochim. Biophys. Acta - Bioenerg.* **1827**, 233–238 (2013).
302. Cordas, C. M. *et al.* Nitric oxide reductase: Direct electrochemistry and electrocatalytic activity. *ChemBioChem* **7**, 1878–1881 (2006).
303. Gomes, F. O. *et al.* Electroanalytical characterization of the direct *Marinobacter hydrocarbonoclasticus* nitric oxide reductase-catalysed nitric oxide and dioxygen reduction. *Bioelectrochemistry* **125**, 8–14 (2019).
304. Flock, U., Watmough, N. J. & Ädelroth, P. Electron/proton coupling in bacterial nitric oxide reductase during reduction of oxygen. *Biochemistry* **44**, 10711–10719 (2005).
305. Lachmann, P., Huang, Y., Reimann, J., Flock, U. & Ädelroth, P. Substrate control of internal electron transfer in bacterial nitric-oxide reductase. *J. Biol. Chem.* **285**, 25531–25537 (2010).
306. <https://www.ceb.cam.ac.uk/research/groups/rg-eme/Edu/hydrodynamic-voltammetry>.
307. Fork, D. C. Oxygen Electrode. *Methods Enzymol.* **24**, 113–122 (1972).
308. Moss, D., Nabedryk, E., Breton, J. & Mantele, W. Redox-linked conformational changes in proteins detected by a combination of infrared spectroscopy and protein electrochemistry: Evaluation of the

- technique with cytochrome *c*. *Eur. J. Biochem.* **187**, 565–572 (1990).
309. Turkevich, J., Stevenson, P. C. & Hillier, J. A study of the nucleation and growth processes in the synthesis of colloidal gold. *Discuss. Faraday Soc.* **11**, 55–75 (1951).
310. G. FRENS. Controlled Nucleation for the Regulation of the Particle Size in Monodisperse Gold Suspensions. *Nat. Phys. Sci.* **241**, 20–22 (1973).
311. Wolfgang Haiss, Nguyen T. K. Thanh, Jenny Aveyard, and D. G. F. Determination of Size and Concentration of Gold Nanoparticles from UV-Vis Spectra. *Anal. Chem.* **79**, 4215–4221 (2007).
312. Melin, F. *et al.* Direct electrochemistry of cytochrome bo<sub>3</sub> oxidase at a series of gold nanoparticles-modified electrodes. *Electrochem. commun.* **26**, 105–108 (2013).
313. Borisov, V. B. & Verkhovsky, M. I. Oxygen as Acceptor. *EcoSal Plus* **6**, (2015).
314. Hrabie, J. A., Klose, J. R., Wink, D. A. & Keefer, L. K. New Nitric Oxide-Releasing Zwitterions Derived from Polyamines Joseph. *J. Org. Chem* **58**, 1472–1476 (1993).
315. Dejon, L. & Speicher, A. Synthesis of aurachin D and isoprenoid analogues from the myxobacterium *Stigmatella aurantiaca*. *Tetrahedron Lett.* **54**, 6700–6702 (2013).
316. Hellwig, P., Scheide, D., Bungert, S., Mantele, W. & Friedrich, T. FT-IR spectroscopic characterization of NADH:Ubiquinone oxidoreductase (complex I) from *Escherichia coli*: Oxidation of FeS cluster N2 is coupled with the protonation of an aspartate or glutamate side chain. *Biochemistry* **39**, 10884–10891 (2000).
317. Olsson, M. H. M., SØndergaard, C. R., Rostkowski, M. & Jensen, J. H. PROPKA3: Consistent treatment of internal and surface residues in empirical p K a predictions. *J. Chem. Theory Comput.* **7**, 525–537 (2011).
318. SØndergaard, C. R., Olsson, M. H. M., Rostkowski, M. & Jensen, J. H. Improved treatment of ligands and coupling effects in empirical calculation and rationalization of p K a values. *J. Chem. Theory Comput.* **7**, 2284–2295 (2011).
319. Jurrus, E. *et al.* Improvements to the APBS biomolecular solvation software suite. *Protein Sci.* **27**, 112–128 (2018).
320. Chovancova, E. *et al.* CAVER 3.0: A Tool for the Analysis of Transport Pathways in Dynamic Protein Structures. *PLoS Comput. Biol.* **8**, 23–30 (2012).

# Étude spectroélectrochimique de la réactivité de la cytochrome *bd* oxydase et des systèmes apparentés avec de petites molécules

## Résumé

Dans le présent projet, la réactivité de protéines de la chaîne respiratoire d'origine bactérienne, la cytochrome *bd* oxydase de *E. coli* et la cNOR de *P. denitrificans*, avec des petites molécules a été étudiée. Les oxydases *bd* sont une famille d'oxydases terminales qui assurent la respiration bactérienne dans des conditions microaérobie par réduction de l'oxygène en eau. On estime également qu'elle participe à la résistance aux médicaments et à la protection bactérienne contre les facteurs de stress environnementaux. Le capteur électrochimique basé sur l'oxydase du cytochrome *bd*-I immobilisée sur la surface des nanoparticules d'or modifiées avec des thiols SAM a été adapté pour l'étude d'inhibition. Le criblage de la bibliothèque de dérivés d'Aurachin D a été réalisé avec succès et l'inhibiteur le plus puissant a été déterminé. Dans le cadre de ce travail, une caractérisation spectroélectrochimique UV-Vis et FTIR des oxydases homologues *bd*-I et *bd*-II a aussi été réalisée. La réactivité avec l'oxygène ainsi que la fixation et la libération de l'oxyde nitrique en fonction du pH ont été étudiées pour les oxydases *bd* de type sauvage et plusieurs mutants.

Un autre système enzymatique étudié dans ce travail était la cNOR. La spectroscopie infrarouge et la voltampérométrie à film protéique sur des électrodes en carbone vitreux ont été utilisées pour mettre en évidence les différences de propriétés catalytiques des enzymes avec l'oxyde nitrique et l'oxygène en fonction des caractéristiques structurelles.

Mot-clés: *bd* oxydase, cNOR, UV-Vis, FTIR, spectroélectrochimie, biocapteur, électrocatalyse

## Résumé en anglais

In the present project the reactivity of respiratory chain proteins of bacterial origin, cytochrome *bd* oxidase from *E. coli* and cNOR from *P. denitrificans*, with small molecules were studied. *Bd* oxidases is a family of terminal oxidases that ensures bacterial respiration in microoxic conditions by reduction of oxygen to water. It was also found to participate in the drug-resistance and bacterial protection against adverse environmental stressors. The electrochemical sensor based on cytochrome *bd*-I oxidase immobilized on the surface of the gold nanoparticles modified with SAM thiols was adapted for inhibition study. The screening of the library of Aurachin D derivatives, was successfully performed and the most potent inhibitor was determined. As another part of this work, UV-Vis and FTIR spectroelectrochemical characterization of the homologues *bd*-I and *bd*-II oxidases was carried out. The reactivity with oxygen as well as nitric oxide binding and release as the function of pH was studied for the wild type *bd* oxidases and several mutants.

Another enzymatic system investigated in this work was the cNOR. The infrared spectroscopy method and the protein film voltammetry on glassy carbon electrodes were employed to highlight the differences in catalytic properties of the enzymes with nitric oxide and oxygen in relation to the structural features.

Keywords: *bd* oxidase, cNOR, UV-Vis, FTIR, spectroelectrochemistry, biosensor, electrocatalysis